Thèse de doctorat en cotutelle de

l'**Université Paris VI - Pierre et Marie Curie**

Spécialité
ED 517 "Particules, Noyaux, Cosmos"

présentée par
M. Nils Kristian HUSKE

pour obtenir le grade de
DOCTEUR de l'UNIVERSITÉ PIERRE ET MARIE CURIE

Dissertation in Co-Betreuung der

Universität Bielefeld - Fakultät für Physik

GRK 881 "*Quantum Fields and Strongly Interacting Matter*"

vorgelegt von
Herrn Nils Kristian Hüske

zur Erlangung des Grades
DOKTOR RER. NAT. der UNIVERSITÄT BIELEFELD

Sujet de la thèse / Titel der Dissertation:

THE HIGGS BOSON IN THE STANDARD MODEL: THEORETICAL CONSTRAINTS AND A DIRECT SEARCH IN THE WH CHANNEL AT THE TEVATRON

NILS KRISTIAN HÜSKE

soutenue le 10 Sept. 2010 à Paris

devant le jury composé de:

verteidigt am 10. Sept. 2010 in Paris

vor der Jury bestehend aus:

M.	Gregorio BERNARDI,	Directeur de thèse
M.	Dominik SCHWARZ,	Directeur de thèse
M.	Nicolas BORGHINI,	Rapporteur
M.	Laurent VACAVANT,	Rapporteur
M.	Jean-François GRIVAZ,	Examinateur
M.	Reynald PAIN,	Président du jury

SUPERVISORS:

Gregorio BERNARDI, Directeur de recherche CNRS
Dominik SCHWARZ, Professor Universität Bielefeld

INSTITUTIONS:

Université Paris VI - Pierre et Marie Curie
4 Place Jussieu
75005 Paris, France

Universität Bielefeld - Fakultät für Physik
Universitätsstraße 25
33615 Bielefeld, Deutschland

0 FOREWORD

The physics of the Higgs boson and especially the search for this elusive particle have been the inspiration and motivation of research for scientists for decades now. Its central part in the context of the origin of mass has given rise to a public interest in its discovery not only since Leon Lederman referred to the Higgs boson as the *God Particle* in 1993.

In recent years, physicists have finally come close to the experimental possibility of discovering this last missing building block of matter in the Standard Model of particle physics. With the mass of the Higgs boson being theoretically unknown, a search is generally a difficult task. Indirect limits from electroweak precision measurements suggest that a light Higgs boson around 120 GeV is favored. Direct searches at the LEP experiment were able to set a lower limit on the mass of the Higgs boson, yet unsuccessful in proving its existence, at 114.4 GeV at 95% confidence level (CL). The Tevatron accelerator at Fermilab with its two detector experiments CDF and DØ approaches an amount of collected data that could allow to reach sensitivity for observing the Higgs boson over a broad range of potential mass points. In 2008 physicists from both experiments were able to exclude the region of 162–166 GeV at 95% CL as a Higgs boson mass for the first time since the LEP exclusion in 2001. Combining direct and indirect constraints on the Higgs boson mass yields a region of 114.4–186 GeV as the preferred region for a Higgs boson in the Standard Model.

Even if the mass of the Higgs boson is not predictable from theory, it is however closely linked to the fate of the Standard Model. There are two possible scenarios: The Higgs boson mass could predict the Standard Model to be a theory only valid in describing phenomena at the electroweak energy scale, giving rise to a vast amount of theories for physics beyond the Standard Model, such as Grand Unified Theories. It could, on the other hand, prove the Standard Model to be valid up to highest energy scales such as the Planck scale, therefore giving rise to theories of cosmological inflation that could use the Higgs boson as an explanation for the earliest stages in the expansion of our Universe. However, the minimally coupled Higgs boson of the Standard Model cannot be the particle responsible for cosmological inflation. But we are free to investigate how to couple the Higgs boson to gravity. It has

been shown recently that a non-minimally coupled Higgs boson gives rise to a physically well motivated scenario of cosmological inflation.
This present work will give an insight into both of the above mentioned aspects of Higgs boson physics, a *direct search* in one of the most favored channels at low mass, namely the associated production with a W boson, and a study on *theoretical implications* on the validity of the Standard Model at highest energy scales and the link to models of cosmological inflation.

To be pedagogical in the description of this work and to give the reader the most logical approach to the topic, this dissertation is divided into three parts:

I Theory The first part will, in its first chapter, describe the theoretical basics of the Standard Model and the mechanism that gives rise to the existence of the Higgs boson. Following, the theoretical basis for Higgs searches at the Tevatron will be laid out, especially for the search presented in the second part of this work. In the second chapter, the dependence of the validity of the Standard Model on the Higgs mass will be evaluated. Implications on models of cosmological inflation using the Higgs boson to explain the evolution of the very early Universe will be studied in conclusion of this part.

II Experiment The second part which represents the main part of this dissertation will describe the direct search for a low mass Higgs boson in associated production with a W boson. It will start by describing the general environment of the search, namely the DØ experiment at Fermilab, and continue by explaining how we get from proton–antiproton collisions to well described physics variables that finally will allow us, in the absence of a signal excess, to constrain limits on the Higgs boson production cross section on a dataset of 5.3 fb^{-1} of integrated luminosity.

III Conclusion and Outlook This final part will summarize the work presented in this dissertation and put it into context of the research in this field in the years to come. Furthermore, the combination of results across Tevatron experiments and the recently started operation of the LHC at CERN will be presented.

Results of this dissertation have been included in work recently published in a conference note as a preliminary result based on a subset of the analyzed data [1] and soon to be submitted to Physics Letters B [2]. This work also contributed to the recent Tevatron Higgs exclusion [3].

It is not so much our friends' help that helps us
as the confident knowledge that they will help us.

— Epicurus (341 - 270 BC), *Greek philosopher*

ACKNOWLEDGMENTS

First of course I want to thank my advisors *Gregorio Bernardi* and *Dominik Schwarz* for the opportunity of performing this research work and for lots of good advice and support over the course of the last three years.
Next my thanks go to the other members of my thesis committee, *Reynald Pain* in his function as president of the committee as well as head of the LPNHE Paris, *Nicolas Borghini* and *Laurent Vacavant* (who in particular provided many thoughtful comments to my manuscript) as rapporteurs of my thesis and of course *Jean-François Grivaz* as member of the committee.
Furthermore, I want to thank all my colleagues at the DØ experiment, at the LPNHE Paris and at the University of Bielefeld. In particular, I want to thank the whole WH team for the great and hard but always pleasant work over these last years. I want to thank *Jeremie Lellouch* for getting me started on my work at Fermilab, as well as *Ken Herner*, *Mike Cooke* and *Duncan Brown* for their help while working on this analysis. Very special thanks to Yuji Enari for his continuous support and never ending patience. It was always a pleasure to work with him, regardless of the time of day or night. I want to thank *Jonathan Brown* with whom I shared the same fate over the last two years ;) as well the other grad students at Fermilab.

I am grateful for the help, support and friendship of many people during these last three years and I want to thank a few of them in particular as they were in one way or another related to this work. I want to thank *Florian Dehmelt* for his continuous friendship and support throughout this time. I want to thank *Simon Sitt* for all his support and friendship and our many discussions over a good cup of coffee at the lab. I want to thank *Martin Frank* for putting things back into perspective and for many discussions about physics and life and all the rest.

Finally and most importantly I want to thank my parents *Karin and Helmut Hüske*. Without them I would not be where and who I am today. Their unconditional support and love is and will always be one of the cornerstones of my life.

CONTENTS

LIST OF FIGURES

Part I

THEORY

1 THE STANDARD MODEL OF PARTICLE PHYSICS

1.1 INTRODUCTION

Describing the constituents of matter and their interactions has been a goal of humankind for centuries. Already in the sixth century BC the first ideas about the smallest units forming larger structures arose in India [4]. Around 450 BC Democritus coined the term 'atom' [5] which is still in use today. It was not until 1967, leaving out many major milestones of discovery in nuclear and particle physics of course, that our understanding of how to describe elementary particles drastically improved. Combining electromagnetic and weak interaction incorporating the Higgs mechanism, the Standard Model of particle physics (SM) was born. Until today, it is able to describe experimental phenomena in the world of the small and elusive elementary particles that modern experiments are now able to identify and measure[1]. We will explain the Standard Model in all necessary detail to understand its significance and the significance of the work presented in this thesis for the field of modern particle physics. This chapter will introduce the elementary particles and their interactions described by the SM. Following, the necessity of the Higgs mechanism in the context of electroweak symmetry breaking and the creation of mass will be outlaid. The chapter concludes with an overview over Higgs searches, in particular at the Tevatron collider.

1.2 ELEMENTARY PARTICLES

As mentioned before, the SM describes the elementary particles and their interactions. Before going into detail on the interactions (see Sec. 1.3) we will first line out the elementary particles and their structure. The constituents of matter can be grouped in two big families, fermions and bosons obeying different statistical laws. Bosons are particles with an integer spin number and are often associated with quantum fields that are responsible for particle interactions. Bosons obey the Bose-Einstein statistics. The boson family consists of elementary bosons which are the carriers of the fundamental forces (see Table 1) and composite bosons

1 We disregard flaws of the Standard Model in explaining e.g. neutrino masses and other hints of new phenomena beyond the Standard Model.

which are any kind of particles with integer spin, e.g. pions (consisting of a quark and an anti-quark).

Force	Electromagnetic	Weak	Strong	Gravity
Boson	γ	W^+, W^-, Z	gluon	graviton

Table 1: The elementary bosons - carriers of the forces.

Fermions are particles with a half integer spin number. They are the constituents of known matter in the Universe. Fermions obey the Fermi-Dirac statistics and the Pauli exclusion principle which states that two fermions can never be in the same quantum physical state, i.e. do never have the same quantum numbers. Fermions are divided into two main families, leptons and quarks, both divided into three generations. The lepton family consists of electrons e, muons μ and tauons τ which all carry an electric charge -1. They all have corresponding neutrinos ν which are massless[2] and free of charge. The quarks also split up into three generations (up, down), (charm, strange) and (top, bottom) which carry electric charges of (2/3, -1/3). Table 2 sums up some important quantum numbers for the leptons and quarks of the three generations.

	1. Gen	2. Gen	3. Gen	Q	B	L
Leptons	e	μ	τ	-1	0	1
	ν_e	ν_μ	ν_τ	0	0	1
Quarks	up	charm	top	2/3	1/3	0
	down	strange	bottom	-1/3	1/3	0

Table 2: The three fermion generations. All these elementary fermions have spin 1/2, electric charge Q, baryon number B and lepton number L.

All particles whether elementary or composite have antiparticles. That is, particles with identical properties but opposite sign of their quantum numbers and electric charge.

1.3 FUNDAMENTAL FORCES

Interaction among elementary particles can be classified into one of four fundamental forces: the electromagnetic force, the weak force, the strong force and gravity.

2 In the theory of the SM neutrinos are massless, yet there is evidence that neutrinos do have a mass [6]. For the purpose of this work neutrinos can be assumed to be massless.

1.3.1 *Electromagnetic Force*

The electromagnetic force is the force responsible for all electromagnetic processes, its mediator is the photon. The symmetry group describing this interaction is U(1), the coupling strength is described by the electromagnetic coupling constant $\alpha \sim 1/137$. As the force mediating photons travel with the speed of light and do not decay, its range is ∞.

1.3.2 *Weak Force*

The weak force is responsible for nuclear processes like the β decay, its mediators are the massive gauge bosons $W^{\pm}$, Z. The symmetry group for this interaction is SU(2), the typical field strength is about a factor of 10^{-11} of that of the electromagnetic force and 10^{-13} of the typical field strength of the strong force. The typical range is of the order 10^{-3} fm. The coupling constant g of the weak interaction is defined by the equation

$$\frac{G_F}{\sqrt{2}} = \frac{g^2}{8M_W^2} \tag{1.1}$$

where M_W is the mass of the W boson and $G_F = 1.16637 \cdot 10^{-5}$ GeV^{-2} is the Fermi constant. The weak force is the only interaction that can change flavor (the different elementary fermion generations are called flavors, so changing an e into a μ or an (up, down) into a (charm, strange) doublet would be a flavor changing process). Weak interactions can also violate parity symmetry P as well as charge conjugation parity symmetry CP [7].
The electromagnetic and weak interaction can be unified in the electroweak theory (see Sec. 1.4).

1.3.3 *Strong Force*

The strong force is responsible for two kinds of phenomena. Interactions between quarks mediated via gluons, and the binding force between protons and neutrons inside of nuclei. The latter is, however, a 'long distance' residual of the first case. The symmetry group of the strong force is SU(3), its coupling strength is of $\mathcal{O}(1)$, thus the name strong force, compared to the other fundamental forces. The typical range of this force is of the order 1.5 fm. The remarkable thing about the strong force is that it does not fade with distance but instead becomes stronger. As a consequence, quarks are "confined". They can never exist separately. As they move apart the strong force becomes stronger with distance. If their kinetic energy becomes large enough to separate them, a

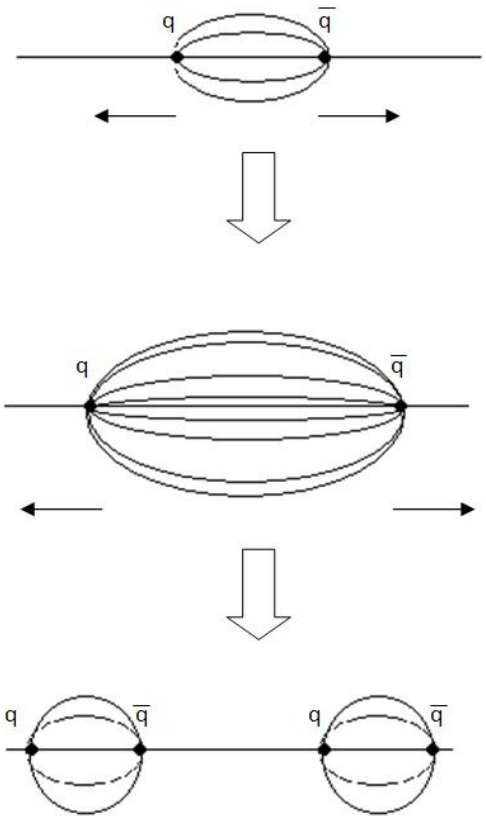

Figure 1: Confinement of Quarks: Two quarks move away from each other. The strong force binding them together increases with distance, illustrated by the strings in between them. If their kinetic energy is, however, large enough to separate them, a new quark and antiquark pair is created from the vacuum.

quark and an anti-quark pair are created from the vacuum. See Fig. 1 for an illustration of this fact.

1.3.3.1 *Quark colors*

The theory of quarks and their interactions is fully described in Quantum Chromodynamics (QCD) (see e.g. [8] for an introduction to QCD). The fact that quarks are never observed separately and only in pairs of two or three quarks (due to the confinement), forming hadrons, leads to a new quantum number. The corresponding concept is called 'color' charge of the quarks. There are three colors (arbitrarily chosen as red, green and blue) and their corresponding anticolors. In Nature, only color neutral objects appear. That is, objects formed by red, green and blue (which by definition equals neutral) or objects made of a certain color and its anticolor. Gluons, the mediators of the quark interactions are two-colored objects.

1.3.3.2 *Quark mixing, the CKM Matrix*

To conserve the universality of the weak interaction, Nicola Cabibbo introduced a concept that later led to the Cabibbo-Kobayashi-Maskawa matrix. This matrix describes the probability of a certain quark to decay into another. Mathematically, it connects a vector of down-like quark mass eigenstates to a vector of the down-like interaction partners of the up-like quarks:

$$\begin{pmatrix} |d'\rangle \\ |s'\rangle \\ |b'\rangle \end{pmatrix} = \begin{pmatrix} |V_{ud}| & |V_{us}| & |V_{ub}| \\ |V_{cd}| & |V_{cs}| & |V_{cb}| \\ |V_{td}| & |V_{ts}| & |V_{tb}| \end{pmatrix} \begin{pmatrix} |d\rangle \\ |s\rangle \\ |b\rangle \end{pmatrix} \tag{1.2}$$

The most recent values for the matrix elements of the CKM matrix can be found from the particle data group [9]:

$$V_{CKM} = \begin{pmatrix} 0.97419 \pm 0.00022 & 0.2257 \pm 0.0010 & 0.00359 \pm 0.00016 \\ 0.2256 \pm 0.0010 & 0.97334 \pm 0.00023 & 0.0415^{+0.0010}_{-0.0011} \\ 0.00874^{+0.00026}_{-0.00037} & 0.0407 \pm 0.0010 & 0.999133^{+0.000044}_{-0.000043} \end{pmatrix} \tag{1.3}$$

The CKM matrix in general has a complex phase $e^{i\delta}$ where δ is the Kobayashi-Maskawa phase [10] which is responsible for all CP violating phenomena in flavor changing processes in the Standard Model [9]. CP violation was Kobayashi's and Maskawa's initial motivation for an expansion of the original 2×2 Cabbibo matrix.

1.3.4 *Gravity*

General relativity is the fundamental theory of gravity. There is, however, no fundamental theory of quantum gravity yet and it is in particular not described by the Standard Model. The range of this force is ∞ and it is weaker than the other forces ($F_C(\text{H-Atom})/F_G(\text{H-Atom}) = \frac{e^2}{G_N m_p m_e} \gg 1$ with F_C the Coulomb force coming from the electroweak force, F_G the gravitational force, e the elementary charge, $G_N = 6.67 \cdot 10^{-11} m^3 kg^{-1} s^{-2}$ the gravitational constant, m_p and m_e the mass of the proton and electron, respectively). We will add further details in the relevant places in later chapters as gravity becomes important again at the Planck scale.

1.4 ELECTROWEAK THEORY AND SPONTANEOUS SYMMETRY BREAKING

In 1979 the work of Abdus Salam, Sheldon Glashow and Steven Weinberg was rewarded with the Nobel Prize in Physics "for

their contributions to the theory of the unified weak and electromagnetic interaction between elementary particles" [11]. They founded a theory which unifies the electromagnetic and weak interactions into one theoretical description called the electroweak interaction. Experimentally, the existence of the electroweak force was established by the discovery of neutral currents in neutrino scattering and the discovery of the W and Z bosons (by the UA1 and UA2 experiments at CERN in 1983). According to the symmetry groups of the two interactions, the new symmetry group of the combined interaction is $SU(2)_L \times U(1)_Y$. The gauge bosons of this group are the photon and the W and Z bosons. The index L indicates that only left-handed fermions interact weakly. Y denotes the weak hypercharge defined as $Y \equiv 2(Q - T_3)$ where Q is the electric charge and T_3 is the third component of the weak isospin. T_3 is a conserved quantum number within the weak interaction. The Lagrangian describing the interactions of the fermions and the bosons has the following form

$$\begin{aligned}\mathcal{L}_{ew} = &-\frac{1}{4}\mathbf{G}^{\mu\nu}\cdot\mathbf{G}_{\mu\nu} - \frac{1}{4}F^{\mu\nu}F_{\mu\nu} \\ &+ \sum_k \bar{\Psi}_k i\gamma^\mu D_\mu \Psi_k \end{aligned} \tag{1.4}$$

$\mathbf{G}_{\mu\nu}$ denotes the field tensor

$$\mathbf{G}_{\mu\nu} = \partial_\mu W_\nu - \partial_\nu W_\mu + ig[W_\mu, W_\nu] \tag{1.5}$$

with $W_\mu = \frac{\tau^l}{2} W^l_\mu$, W^l_μ being an isotriplet of gauge fields and $\frac{\tau^l}{2}$ being the generators of the weak symmetry group SU(2), where τ^l denotes the Pauli matrices. The dot product denotes a scalar product in SU(2) space. The field tensor $F_{\mu\nu} = \partial_\mu B_\nu - \partial_\mu B_\nu$ where B_μ is the vector field associated with the U(1) hypercharge Y.

Ψ_k is the fermion spinor given by the doublets

$$\Psi_k = \begin{pmatrix} \nu_{kL} \\ e_{kL} \end{pmatrix} \text{ or } \begin{pmatrix} u_{kL} \\ d'_{kL} \end{pmatrix} \tag{1.6}$$

in SU(2) space for the left handed fields of the *k*th fermionic family of leptons and quarks and by the SU(2) singlets

$$\Psi_k = e_{kR} \quad \text{or} \quad q_{kR} \tag{1.7}$$

for the right handed partners. Here, the index *k* denotes (ν_e, *e*), (ν_μ, μ) and (ν_τ, τ) in the case of leptons and (u,d'), (c,s') and (t,b') in the case of quarks.

Interactions between fermions and gauge bosons are defined by the covariant derivatives

$$D_\mu \Psi_k = \left(\partial_\mu + ig\frac{\tau^l}{2} W_\mu^l + ig'\frac{1}{2} y_k B_\mu \right) \Psi_k \tag{1.8}$$

with y_k being the hypercharge of Ψ_k. g is the coupling strength of the weak isotriplet gauge field W_μ^l to the fermion spinor, g' is the coupling strength of the vector field B_μ to the fermion spinor.

The following equations identify the terms in the Lagrangian of Eq. 1.4, $W_\mu^l$and B_μ, with the gauge bosons, $W^\pm$ and Z_μ, and the photon field A_μ:

$$W_\mu^\pm = \frac{1}{\sqrt{2}} \left(W_\mu^1 \mp W_\mu^2 \right) \tag{1.9}$$

$$Z_\mu = -\sin\theta_W B_\mu + \cos\theta_W W_\mu^3 \tag{1.10}$$

$$A_\mu = \cos\theta_W B_\mu + \sin\theta_W W_\mu^3 \tag{1.11}$$

where $\theta_W = g/\sqrt{g^2 + g'^2}$ is the Weinberg angle which is a measure for the mixing of the W_μ^l and B_μ terms.
So far, the electroweak Lagrangian correctly describes the interactions between the fermions and between fermions and gauge bosons. However, this Lagrangian can only describe massless particles which is not what we observe in Nature.

1.4.1 *The Higgs mechanism*

To solve the problem of theoretically massless bosons and fermions, the Higgs mechanism offers a gauge invariant way of introducing the concept of mass to such "massless" theory. Adding a simple mass term like $m_W^2 W_\mu^\dagger W^\mu$ would violate gauge invariance, so we need instead to introduce an additional SU(2) doublet

$$\phi = \begin{pmatrix} \phi^+ \\ \phi^0 \end{pmatrix} \tag{1.12}$$

where ϕ^+ and ϕ^0 are complex fields defined by their real components $\phi_1, \ldots, \phi_4$:

$$\phi^+ = \frac{\phi_1 + i\phi_2}{\sqrt{2}} \tag{1.13}$$

$$\phi^0 = \frac{\phi_3 + i\phi_4}{\sqrt{2}}. \tag{1.14}$$

The corresponding Lagrangian has the form

$$\mathcal{L}_\phi = (D_\mu \phi)^\dagger (D^\mu \phi) - V(\phi) \tag{1.15}$$

with $V(\phi)$ the potential of the field defined as

$$V(\phi) = \mu^2 \phi^\dagger \phi - \lambda \left(\phi^\dagger \phi\right)^2. \tag{1.16}$$

This potential has a minimum for $\mu^2 < 0$ at (1.18)

$$\phi^\dagger \phi = \phi^{+*}\phi^+ + \phi^{0*}\phi^0 = \frac{\phi_1^2 + \phi_2^2 + \phi_3^2 + \phi_4^2}{2} \tag{1.17}$$

$$= \frac{-\mu^2}{2\lambda} = \frac{v^2}{2}. \tag{1.18}$$

Only because for $\mu^2 < 0$ the potential $V(\phi)$ has a minimum at $\phi \neq 0$, a non-zero ground state of the vacuum, spontaneous symmetry breaking can occur. For $\mu^2 > 0$, $V(\phi)$ has its minimum at $\phi = 0$ and no spontaneous symmetry breaking would even occur, therefore we do not further consider this case as we would end up where we started, a theory with massless particles.
Looking at Eq. 1.17 we see that the choice of the minimum is not unique, so we have to choose a direction in SU(2) space, leaving us with the vacuum ground state ϕ_0,

$$\phi_0 = \frac{1}{\sqrt{2}} \begin{pmatrix} 0 \\ v \end{pmatrix} \tag{1.19}$$

which corresponds to the choice $\phi_1 = \phi_2 = \phi_4 = 0$ and $\phi_3 = v$. Looking at Eq. 1.15, the terms from the derivative contain a contribution proportional to $W_\mu^- W_\nu^+ v^2 g^2$ which can be identified with a mass term:

$$\begin{aligned} & m_W^2 \propto g^2 v^2 \\ & \Rightarrow v^2 = \frac{4 m_W^2}{g^2} = 246\,\text{GeV} \end{aligned} \tag{1.20}$$

The full Lagrangian of the electroweak theory incorporating the Higgs mechanism has the form [12]:

$$\begin{aligned} \mathcal{L}_{ew} = & -\frac{1}{4}\mathbf{G}^{\mu\nu} \cdot \mathbf{G}_{\mu\nu} - \frac{1}{4} F^{\mu\nu} F_{\mu\nu} \\ & + m_W^2 W_\mu^\dagger W^\mu \left(1 + \frac{\varphi}{v}\right)^2 \\ & + \frac{1}{2} m_z^2 Z_\mu Z^\mu \left(1 + \frac{\varphi}{v}\right)^2 \\ & + \sum_k \bar{\Psi}_k i\gamma^\mu D_\mu \Psi_k + \mathcal{L}_Y \\ & + \frac{1}{2}(\partial^\mu \varphi)(\partial_\mu \varphi) - \frac{1}{2} m_H^2 \varphi^2 \left(1 + \frac{\varphi}{v} + \frac{1}{4}\left(\frac{\varphi}{v}\right)^2\right). \end{aligned} \tag{1.21}$$

m_W and m_Z are the masses of the W and Z bosons, respectively. φ is the scalar Higgs field and v its vacuum expectation value. $F_{\mu\nu}$ can now be identified with the electromagnetic field $F_{\mu\nu} = \partial_\mu A_\nu - \partial_\nu A_\mu$. $\mathcal{L}_Y$ is the Yukawa term of the Lagrangian that generates the Fermion masses by coupling to the Higgs field:

$$\begin{aligned}\mathcal{L}_Y = &-(g_e \bar{e}_R e_L + g_\mu \bar{\mu}_R \mu_L + g_\tau \bar{\tau}_R \tau_L \\ &+ g_d \bar{d}_R d_L + g_s \bar{s}_R s_L + g_b \bar{b}_R b_L \\ &+ g_u \bar{u}_R u_L + g_c \bar{c}_R c_L + g_t \bar{t}_R t_L + \text{h.c.}) \frac{v}{\sqrt{2}} \left(1 + \frac{\varphi}{v}\right)\end{aligned} \tag{1.22}$$

1.5 QUANTUM CHROMODYNAMICS

The theory of Quantum Chromodynamics (QCD) describes the strong force, i.e. the dynamics of quarks and gluons, the mediators of the strong force. The QCD Lagrangian is of the following form [13]

$$\mathcal{L}_{QCD} = -\frac{1}{4} G^{\mu\nu}_a G^a_{\mu\nu} + i \sum_{j=1}^{n} \bar{\psi}^\alpha_j \gamma^\mu (D_\mu)_{\alpha\beta} \psi^\beta_j \tag{1.23}$$

$$- \sum_{j=1}^{n} m_j \bar{\psi}^\alpha_j \psi_{j,\alpha} \tag{1.24}$$

where $G^a_{\mu\nu} = -\partial_\mu A^a_\nu \partial^\mu A^\nu_a + g_{QCD} f_{abc} A^b_\mu A^c_\nu$ ($a = 1, \ldots, 8$) are the Yang-Mills field strengths and the A^a_μ are the gluon fields. ψ_j is the quark field of flavor j. The covariant derivative acting on the quark color components is defined as $(D_\mu)_{\alpha\beta} = \partial_{\alpha\beta}\partial_\mu - ig \sum_a \frac{1}{2} \lambda^a_{\alpha\beta} A^a_\mu$ where α, β are the color indices and $\lambda^a_{\alpha\beta}$ are the eight 3×3 color matrices, also often referred to as the *Gell-Mann* matrices. f_{abc} are the real structure constants and g_{QCD} is the QCD gauge coupling that sets the strength of the gluon self interaction.

1.6 THE STANDARD MODEL

The Standard Model is the combination of the previously discussed theories of electroweak and strong interaction. Its Lagrangian has the symmetry group $SU(3)_c \times SU(2)_L \times U(1)_Y$ where c denotes the color index of QCD, L denotes the fact that only left-handed fermions participate in the weak interaction and Y represents the hypercharge. After spontaneous symmetry breaking, at energies smaller $\sim \mathcal{O}(100\,\text{GeV})$ which is the mass scale of the W and Z bosons, part of this symmetry group is reduced. $SU(2)_L \times U(1)_Y$ becomes $U(1)_{em}$ which is the usual group of classical QED.

In total, the SM contains 19 free parameters, which is a main reason for the criticism that the SM cannot be a truly fundamental theory. One of these parameters is the mass of the Higgs boson, which is not determined by theory. Proving its existence is a crucial step in proving the validity of the SM.
Given the vacuum expectation value of the field

$$\langle \phi \rangle = \frac{1}{\sqrt{2}} \begin{pmatrix} 0 \\ v \end{pmatrix} \tag{1.25}$$

perturbative calculations around the vacuum at $\phi = \pm v$ lead to a space time dependent field fluctuation φ

$$\phi = \frac{1}{\sqrt{2}} \begin{pmatrix} 0 \\ v + \varphi \end{pmatrix} \tag{1.26}$$

which is interpreted as the Higgs boson. The Higgs potential after symmetry breaking becomes [14]

$$V(\phi) = -\frac{\mu^4}{4\lambda} - \mu^2 \varphi^2 + \lambda v \varphi^3 + \frac{\lambda}{4} \varphi^4 \tag{1.27}$$

The tree level mass of the Higgs boson can then be read from the second term in V

$$m_H = \sqrt{-2\mu^2} = \sqrt{2\lambda} v \tag{1.28}$$

As λ is a free parameter, the mass of the Higgs boson has a priori no constraints from SM theory.

2 THE HIGGS BOSON

2.1 CONSTRAINTS ON THE HIGGS BOSON MASS

The hunt for the Higgs boson will be explained in much detail in the second part of this work (see Chapter 4) discussing the search in associated production with a W boson in the low mass region (< 150 GeV). This chapter will give an introduction into the general framework of making predictions and possibly exclusions of certain mass regions of the Higgs boson. This section will go over other direct searches previously performed at the LEP experiment at CERN, summarize indirect constraints from electroweak precision measurements of other quantities such as the top quark or the mass of the W boson and conclude with the theoretical framework of Higgs boson production at the Tevatron and the reasoning for choosing a specific event topology, and production and decay channel for the Higgs search presented in the later chapters of this work.

2.1.1 *Direct Searches at LEP*

The hunt for the Higgs boson has been an active field of research for the last twenty years. The Large Electron-Positron Collider (LEP) at CERN has been searching for direct evidence in electron positron collisions from 1989 until it was shut down in 2000 to be replaced by the Large Hadron Collider which just recently started operating. LEP operated at a final center of mass energy of 209 GeV. The main search channel was the Higgsstrahlung process $e^+e^- \to HZ$ with smaller contributions from WW/ZZ fusion ($e^+e^- \to \nu_e\bar{\nu}_e H/e^+e^-H$). These direct Higgs boson searches performed at LEP could exclude the mass range for the Standard Model Higgs boson up to a mass of $m_H > 114.4$GeV at a CL of 95% (Fig. 2).

2.1.2 *Indirect constraints from EW Precision Measurements*

There are several ways to get constraints on the Higgs mass despite the general lack of prediction from theory, the first of which comes from one-loop electroweak radiative corrections. The Higgs boson contributes to radiative corrections on the top quark and W boson masses. Therefore, precision measurements of electroweak parameters, like the top quark and W boson masses or the Weinberg angle θ_W of the W and Z boson mixing

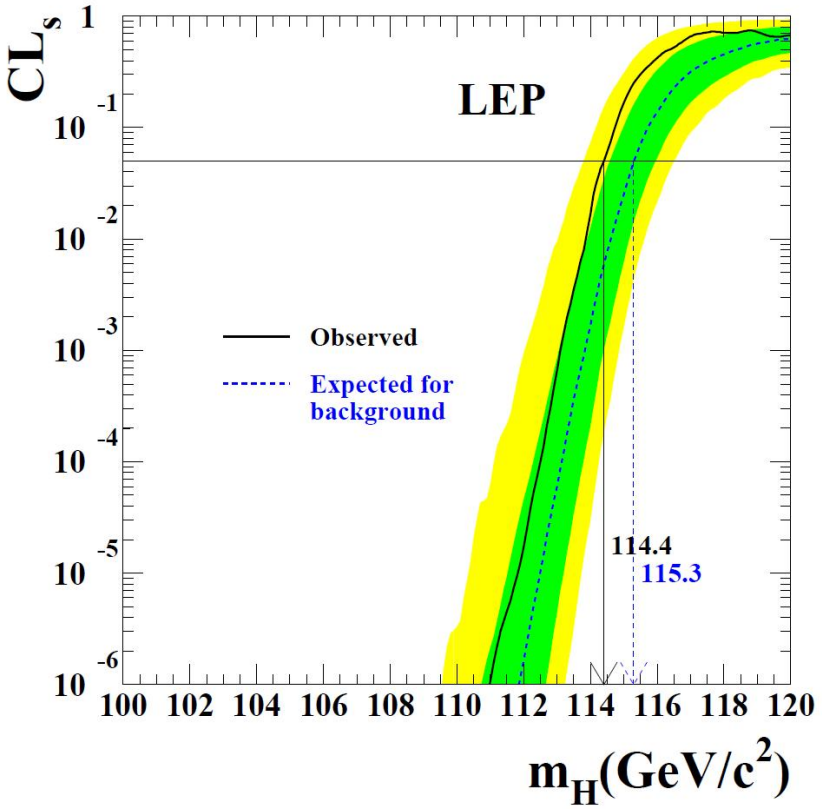

Figure 2: Confidence level for the signal plus background hypothesis. Solid line: observation; dashed line: median background expectation. The green (dark) and yellow (light) shaded bands around the median expected line correspond to the 68% and 95% probability bands. The intersection of the horizontal line for $CL_s = 0.05$ with the observed curve is used to define the 95% confidence level lower bound on the mass of the Standard Model Higgs boson. [15]

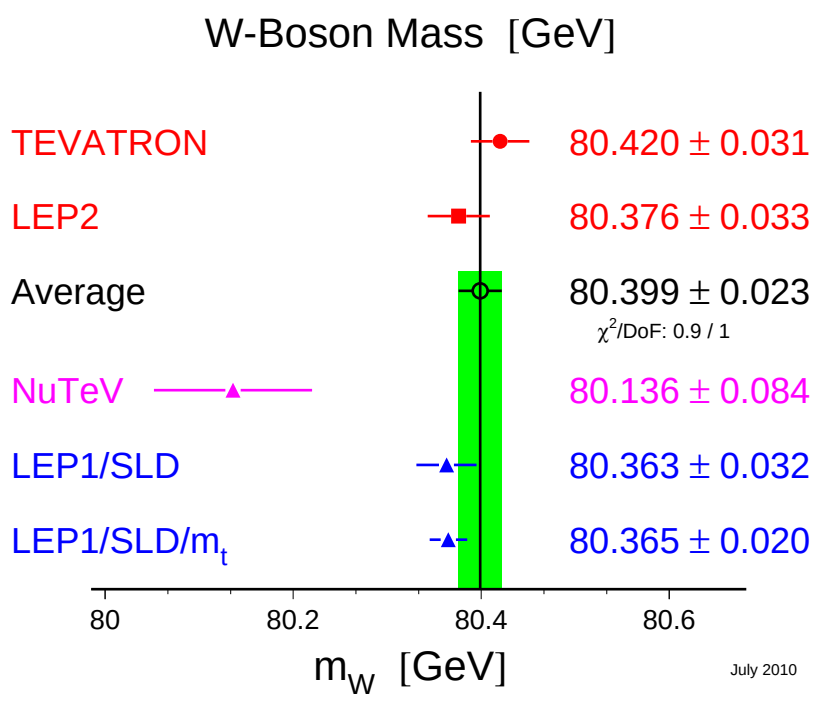

Figure 3: Measurements of the W mass at the LEP and Tevatron collider and their combined average. [16]

can put constraints on the Higgs boson mass. An important quantity is the electroweak parameter ρ

$$\rho = \frac{m_W^2}{m_Z^2}(1 - \sin^2\theta_W) = 1 + \Delta r. \tag{2.1}$$

Expressing Δr in terms of the top quark, W and Higgs boson masses yields

$$\Delta r = \frac{3G_F}{8\pi^2\sqrt{2}} m_t^2 + \frac{\sqrt{2}G_F}{16\pi^2} m_t^2 \left[\frac{11}{3} \ln\left(\frac{m_H^2}{m_W^2}\right) + \cdots\right] + \cdots \tag{2.2}$$

and therefore relates m_t, m_W and m_Z with m_H. Experiments at the LEP and Tevatron colliders have measured the top quark (Tevatron only) and W and Z boson masses with high precision. Fig. 3 shows measurements and the combined average for the W mass, Fig. 4 shows the same plot for the top quark mass, respectively.

Combining all this information leads to a $\Delta\chi^2$ fit of the Higgs boson mass (Fig. 5). The preferred value for the Higgs boson mass is therefore at 87 GeV (corresponding to the minimum of the fitting curve), with an uncertainty of +35 GeV and -26 GeV (at a 68% CL[1], derived from $\Delta\chi^2 = 1$ for the black line, not taking

1 See Sec. 7.4 for details on confidence limits.

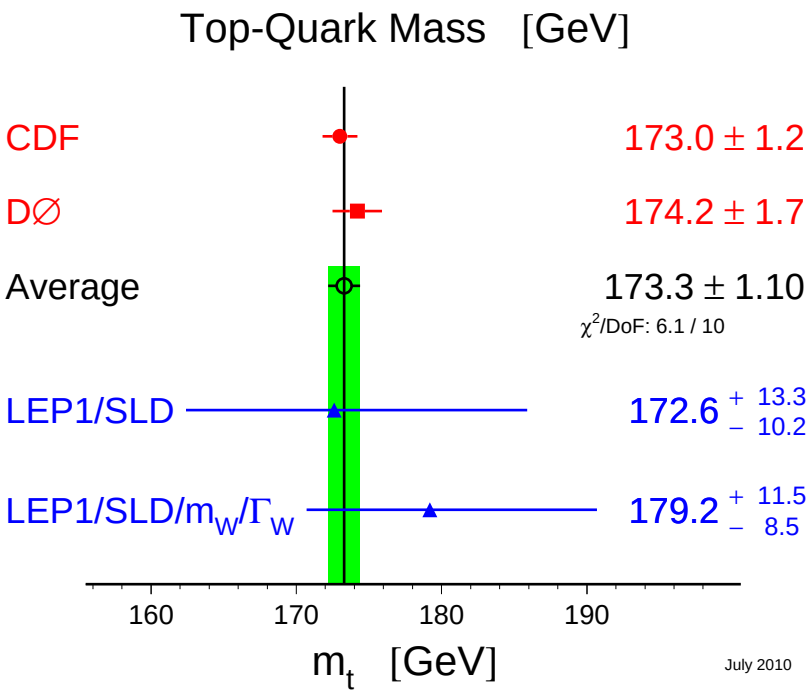

Figure 4: Measurements of the top quark mass at the LEP and Tevatron collider and their combined average. [16]

into account the theoretical uncertainty shown as a blue band in the plot). This is not a proof that the SM Higgs boson actually exists. However, if it exists, it gives an idea for the mass range in which we expect it.
From precision electroweak measurements alone, we obtain a single sided upper limit on the Higgs boson mass of $m_H < 157$ GeV at 95% CL, derived from $\Delta\chi^2 = 2.7$ for the blue band in the plot, when including both the experimental and the theoretical uncertainties. When the direct exclusion from the LEP experiment ($m_H > 114.4$ GeV) is included in the calculation, this limit increases to $m_H < 186$ GeV (the LEP exclusion is represented by the lower yellow band in Fig.5).

2.1.3 *Combining Direct and Indirect Constraints*

The information from direct exclusions at LEP and Tevatron and indirect constraints from electroweak precision measurements can be combined in a global statistical interpretation of the results, as presented in [17] using the GFitter package [18]. This combination yields a preferred Higgs boson mass of $m_H = 119.1^{+13.5}_{-4.0}$ GeV. The corresponding fit, taking into account theoretical and experimental uncertainties and the excluded mass regions from both experiments is shown in Fig. 6. This result favors a low mass Higgs boson.

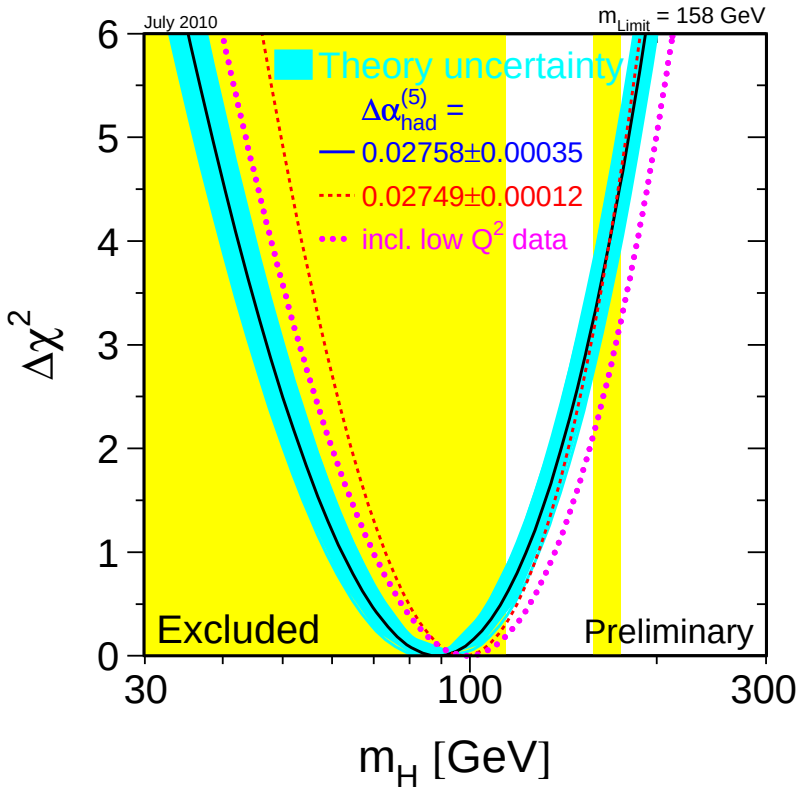

Figure 5: $\Delta\chi^2$ fit to the Higgs boson mass from electroweak precision measurements. The blue band represents theoretical uncertainties to the fit. The lower yellow band represents the LEP exclusion up to a Higgs mass of 114.4 GeV, the yellow band to the right represents the Tevatron exclusion of Higgs masses between 162-166 GeV. Both exclusions are made at a 95% CL. [16]

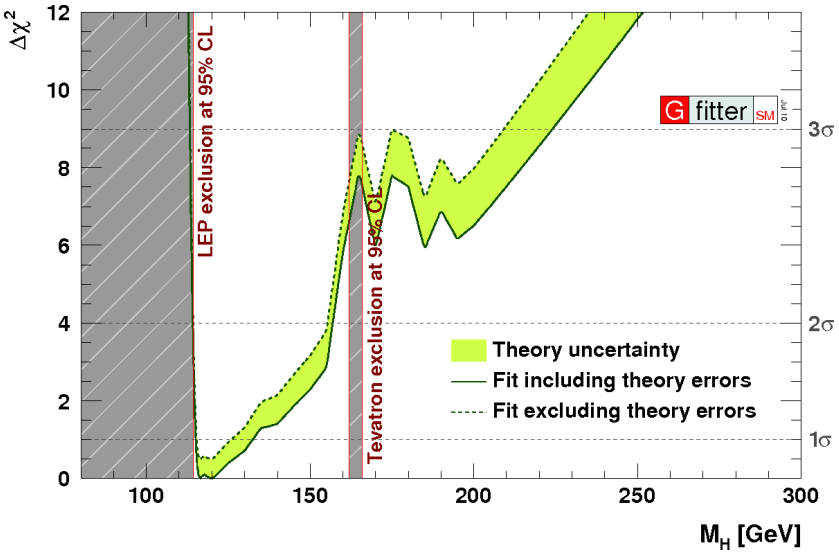

Figure 6: $\Delta\chi^2$ fit to the Standard Model Higgs boson mass from electroweak precision measurements using the Gfitter package. The solid (dashed) lines give the results when including (ignoring) theoretical errors. This fit yields a preferred Higgs boson mass of $m_H = 119.1^{+13.5}_{-4.0}$ GeV. [18]

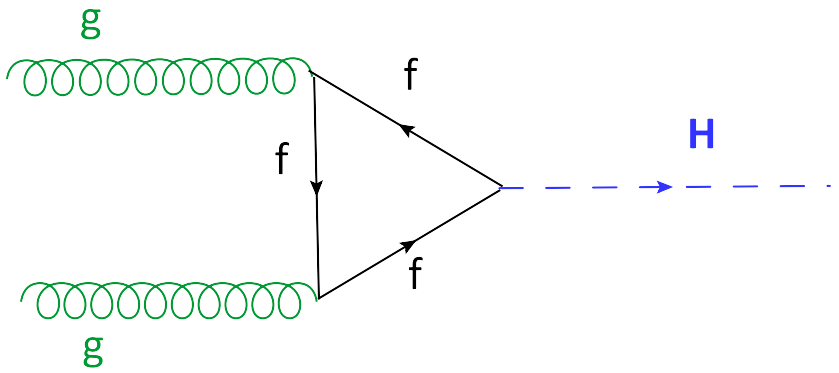

Figure 7: Feynman diagram for gluon fusion Higgs boson production.

2.2 HIGGS SEARCHES AT THE TEVATRON

At the Tevatron, protons and antiprotons are brought to collision at a center of mass energy of 1.96 TeV. For the production of SM Higgs bosons, this leads to four dominant production channels and the corresponding Feynman diagrams:

1. Gluon–gluon fusion, Fig. 7.
2. Vector boson fusion, Fig. 8.
3. Associated production with a W boson, Fig. 9.
4. Associated production with a Z boson, Fig. 9.

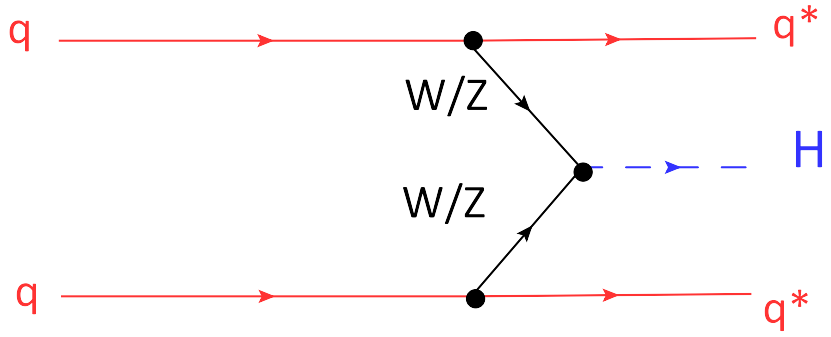

Figure 8: Feynman diagram for vector boson fusion Higgs boson production.

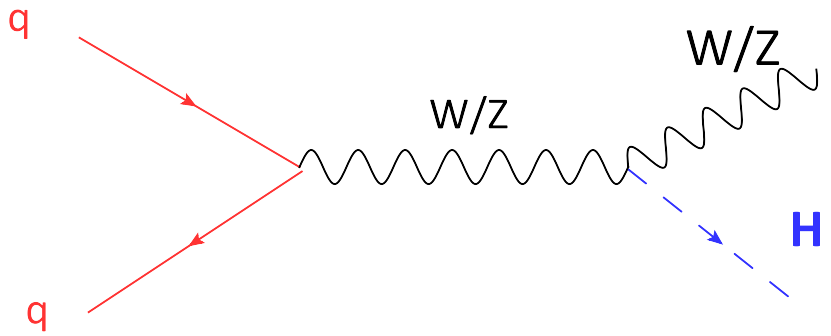

Figure 9: Feynman diagram for production of a Higgs boson in association with a W boson.

Fig. 10 illustrates the production rates for the different channels at the Tevatron. Gluon–gluon fusion is the dominant channel over the whole mass range having however one major drawback that will become clear once we look at decay channels. The second best channels for Higgs production at the Tevatron, almost one order of magnitude smaller, are the associated productions with a W or a Z boson. These channels are in fact the most prominent ones for Higgs searches at low mass.

Fig. 11 shows the equivalent plot for decay rates comparing branching ratios of the SM Higgs boson. In the low mass region < 140 GeV the Higgs boson dominantly decays into a pair of b quarks. At high mass $140 < M_H < 200$ GeV the dominant decay channel is the decay into a pair of W bosons. We know from the LEP and Tevatron exclusion and indirect constraints that the Higgs boson is favored to be in the low mass region. Therefore, we look again at final states containing a pair of b quarks. Considering now a Higgs boson production via gluon–gluon fusion (which has a cross section of ~ 1 pb), we see the emerging problem of backgrounds from direct $b\bar{b}$ production which has a production cross section of $10\,\mu b$. Therefore, it is almost impossible to detect a Higgs boson signature in this channel. Associated production offers the possibility to nonetheless

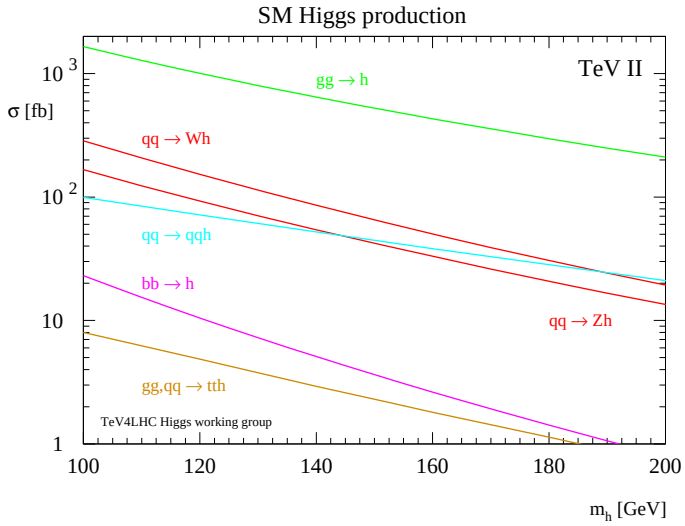

Figure 10: Production cross sections for the SM Higgs boson at the Tevatron. The dominant production channels for SM Higgs production are gluon-gluon fusion (green), associated production with a W/Z boson (red) and vector boson fusion (cyan). [19]

conduct a Higgs boson search at low mass. The additional signature of the decaying W or Z boson helps identifying the desired event topology in the final state and reducing the backgrounds.

With a preferred Higgs mass in the low mass region (as seen in Sec.2.1.3) and the highest production cross section in the WH channel, as a channel with manageable background contributions, the search for a Higgs boson in the $WH \to \ell\nu b\bar{b}$ channel is the most logical choice at a Tevatron experiment. The direct search in this channel on a dataset of $5.3 fb^{-1}$ will be presented in Ch.7.

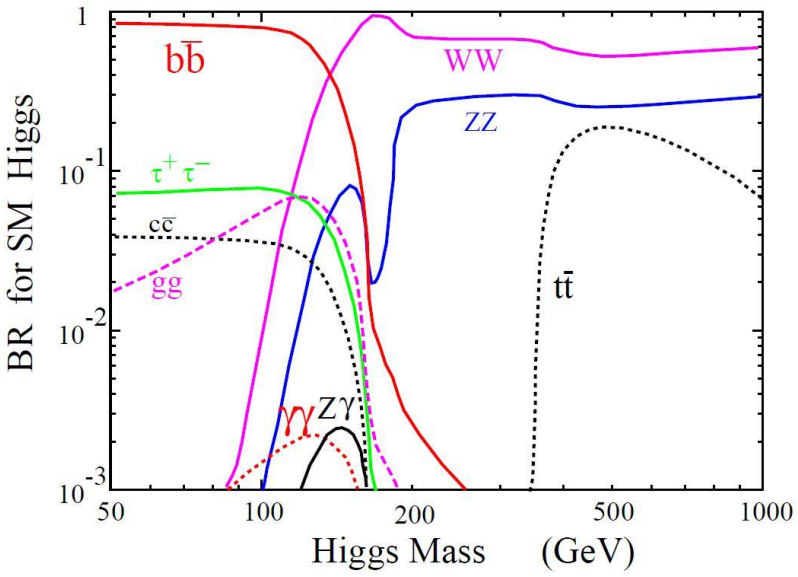

Figure 11: Branching ratios for the SM Higgs boson at the Tevatron. The dominant decay channel at low mass is the decay into a pair of b quarks (red) and into a pair of W bosons at high mass (pink). [20]

3

IMPLICATIONS OF THE HIGGS BOSON MASS FOR THE EXTRAPOLATION OF THE STANDARD MODEL TO HIGHEST ENERGIES AND FOR COSMOLOGY

To be able to assess the domain of validity of the Standard Model, it is interesting to test the validity of the Higgs mechanism up to high energy scales. If we imagine that the SM was actually valid up to the scale of Grand Unified Theories (GUTs) ($\mathcal{O}(10^{16}\mathrm{GeV})$) or even the Planck scale ($\mathcal{O}(10^{19})\mathrm{GeV}$), this would immediately rise another interesting question. Namely, its direct implications to the field of GUTs and cosmology. An SM valid up to these scales could in the first case effectively rule out several theoretically developed GUTs, as it could, in the latter case, be the foundation of theories of inflation using the Higgs as the inflaton (the particle giving rise to inflation). We will discuss these possible consequences in more detail in Sec. 3.3.2.
The possibility of making these predictions only arises with the study of the renormalization group equations (RGEs) of some fundamental parameters of the Standard Model. This chapter will start by explaining the meaning of renormalization in general, then go over the use of RGEs, explain algorithms used to solve these equations and then present the work performed. We want to have a look at the quark Yukawa couplings as a measure of the coupling strength of the Higgs boson to the quarks. This will be a crucial step in predicting possible consequences arising for cosmology. For years, text books and articles have been simplifying their calculations with the claim that all other quark Yukawa couplings are negligible compared to the top quark coupling. We will show whether this claim holds true, not only using latest experimental values for the masses of the quarks, but also studying the behavior of the couplings up to high scales and therefore important for cosmology. Finally, we will look at the validity of the SM which strongly depends on the Higgs boson mass, describe different scenarios for the fate of the SM and conclude with implications for theories of cosmological inflation.

3.1 RENORMALIZATION

When the theory of quantum electrodynamics was developed in the 1930's the problem arose that many integrals in the perturbative[1] calculations were divergent. In Feynman diagrams, closed

1 See e.g. [21] for an introduction to perturbation theory.

loops can represent virtual particles. To calculate the amplitude of the loop process, all possible combinations of energy and momentum traveling around the loop have to be integrated over. The virtual particles can have almost arbitrarily large momenta. These cases can also involve ultraviolet (UV) divergences (often logarithmically divergent). To get rid of these divergences when integrating up to ∞, a cutoff Λ is introduced into the calculation. This method is called *regularization* of the theory. This is a valid approach as long as it is assured that the scale of the cutoff is sufficiently large, no symmetries of the theory are violated and results for physical measurements do not depend on Λ.

So how do we make the newly introduced cutoff vanish from the equations of the theory?
This brings us to the term of 'running couplings'. The coupling constants which appear in the Lagrangian are often called 'bare couplings'. Experiments always measure the sum of the bare couplings and all contributions from loop interactions. Absorbing large and Λ dependent corrections to measured quantities into the couplings is called 'renormalization' of the theory. An arbitrary scale μ is introduced so that couplings only depend on this scale and (at least for $\mu \gg m$) not on the physical mass of any particles under study. For this to become a useful approach we need to know how the running coupling evolves as a function of the scale μ. This leads to the so-called 'β functions' of renormalization theory or 'renormalization group equations' (RGEs)[2]. These are essentially derivatives of the renormalized couplings with respect to μ. The β functions then allow to get equations at a physical measurable scale (e.g. $\mu = m_Z$ where m_Z is the mass of the Z boson, a typical energy scale for accelerator experiments). We now have a theory which allows us to make predictions for measurable quantities at arbitrary energy scales avoiding any logarithmic divergences arising from loop corrections. This powerful tool makes it possible to match theoretical predictions with experimental results and make theoretical predictions of physics at high energy scales. These predictions are interesting from the cosmological point of view for models of cosmic inflation as well as for the validity of the SM and the possibility of new physical phenomena at scales $\gg$ electroweak scale.

3.2 EVOLUTION OF THE QUARK YUKAWA COUPLINGS

Eq. 3.1 is the general form of an up-like Yukawa coupling renormalization group equation at one loop [23]:

2 See [22] for a hands-on description of how to derive the β functions.

$$16\frac{\pi^2}{g_u}\frac{dg_u}{ds} = \frac{3}{2}g_u^2 - \frac{3}{2}\sum_i g_i^2|V_{ui}|^2 + \sum_n g_n^2 - \frac{3}{4}\left(3g^2 + g'^2\right) - \frac{2}{3}g'^2 - 8g_{QCD}^2, \tag{3.1}$$

where $s = \ln(\mu/m_Z)$, $i = (d, s, b)$ runs over all down-like quark flavors and n runs over all quark flavors, including colors, as well as all lepton flavors. The index u can be read as a placeholder for any of the up-like quarks $(u, c$ or $t)$. g_u is the up-like quark Yukawa coupling, g, g' and g_{QCD} are the gauge couplings. V_{ui} is the ui*th* element of the CKM matrix [9]. Accordingly, Eq. 3.2 is the RGE for a down-like quark Yukawa coupling g_d, where $j = (u, c, t)$ runs over all up-like quark flavors and n runs over all quark flavors, including colors, as well as all lepton flavors. The index d can be read as a placeholder for any of the down-like quarks $(d, s$ or $b)$.

$$16\frac{\pi^2}{g_d}\frac{dg_d}{ds} = \frac{3}{2}g_d^2 - \frac{3}{2}\sum_j g_j^2|V_{jd}|^2 + \sum_n g_n^2 - \frac{3}{4}\left(3g^2 + g'^2\right) + \frac{1}{3}g'^2 - 8g_{QCD}^2. \tag{3.2}$$

To get the final form of the coupled differential equations for the top, bottom, charm and strange quark Yukawa couplings, we neglect the coupling of the up and down quark as well as the lepton couplings. Judging from their masses, the τ would be of the same order of magnitude as the charm quark and the μ of the order of the strange quark. The assumptions to neglect these couplings in the sum of Eqn. 3.1 and 3.2 will be justified by the outcome of this analysis, as the couplings scale with the masses of the corresponding particles. Eqn. 3.3 - 3.6 are the emerging quark Yukawa coupling RGEs.

$$16\frac{\pi^2}{g_t}\frac{dg_t}{ds} = \frac{9}{2}g_t^2 + \left(3-\frac{3}{2}(V_{tb})^2\right)g_b^2 + \left(3-\frac{3}{2}(V_{ts})^2\right)g_s^2 - \left(\frac{9}{4}g^2+\frac{17}{12}g'^2+8g_{QCD}^2\right) \tag{3.3}$$

$$16\frac{\pi^2}{g_b}\frac{dg_b}{ds} = \frac{9}{2}g_b^2 + \left(3-\frac{3}{2}(V_{tb})^2\right)g_t^2 + \left(3-\frac{3}{2}(V_{cb})^2\right)g_c^2 - \left(\frac{9}{4}g^2+\frac{5}{12}g'^2+8g_{QCD}^2\right) \tag{3.4}$$

$$16\frac{\pi^2}{g_c}\frac{dg_c}{ds} = \frac{9}{2}g_c^2 + \left(3-\frac{3}{2}(V_{cb})^2\right)g_b^2 + \left(3-\frac{3}{2}(V_{cs})^2\right)g_s^2 - \left(\frac{9}{4}g^2+\frac{17}{12}g'^2+8g_{QCD}^2\right) \tag{3.5}$$

$$16\frac{\pi^2}{g_s}\frac{dg_s}{ds} = \frac{9}{2}g_s^2 + \left(3-\frac{3}{2}(V_{ts})^2\right)g_t^2 + \left(3-\frac{3}{2}(V_{cs})^2\right)g_c^2 - \left(\frac{9}{4}g^2+\frac{5}{12}g'^2+8g_{QCD}^2\right) \tag{3.6}$$

Solving these equations also requires the knowledge of the three gauge coupling RGEs for g, g' and g_{QCD} at one loop [24], Eqn. 3.7 - 3.9.

$$16\pi^2\frac{dg}{ds} = -\frac{19}{6}g^3 \tag{3.7}$$

$$16\pi^2\frac{dg'}{ds} = \frac{41}{6}g'^3 \tag{3.8}$$

$$16\pi^2\frac{g_{QCD}}{ds} = -7g_{QCD}^3 \tag{3.9}$$

Eq. 3.3 - 3.9 are simultaneously solved using a Runge-Kutta method with adaptive step size. We explain this method in some detail in Excerpt 3.2.1.

3.2.1 *Excerpt: Runge-Kutta method*

The problem of solving ordinary differential equations (ODEs) is a common problem in many fields of science. Computer science provides us with simple yet powerful algorithms to solve these equations in approximative ways up to a desired accuracy. Among these algorithms the Runge-Kutta method is probably the most common one. If we are to solve a system of N coupled first order differential equations for the functions $y_i, i = 1, 2, \ldots, N$ in the general form

$$\frac{dy_i(x)}{dx} = f_i'(x, y_1, \ldots, y_N) \tag{3.10}$$

where the functions f_i' are the known derivatives of the y_i's, the Runge-Kutta method [25] is an advancement of the Euler method. The Euler method of solving ODEs is to evolve a solution from a point x_n to $x_{n+1} \equiv x_n + L$ through the interval L:

$$y_{n+1} = y_n + Lf'(x_n, y_n). \tag{3.11}$$

This clearly has the disadvantage of using the derivative at the beginning of the interval to evolve the equation through the whole interval. The Runge-Kutta method, however, advances only to the midpoint of the interval, takes the derivative at that point and uses this information for the evolution throughout the whole interval:

$$\begin{aligned} l_1 &= Lf'(x_n, y_n) \\ l_2 &= Lf'(x_n + \frac{1}{2}L, y_n + \frac{1}{2}l_1) \\ y_{n+1} &= y_n + l_2 + \mathcal{O}(L^3) \end{aligned} \tag{3.12}$$

The error term shows that this method is of second order. To further advance this technique we go to the fourth order Runge-Kutta method:

$$\begin{aligned} l_1 &= Lf'(x_n, y_n) \\ l_2 &= Lf'(x_n + \frac{1}{2}L, y_n + \frac{1}{2}l_1) \\ l_3 &= Lf'(x_n + \frac{1}{2}L, y_n + \frac{1}{2}l_2) \\ l_4 &= Lf'(x_n + L, y_n + l_3) \\ y_{n+1} &= y_n + \frac{l_1}{6} + \frac{l_2}{3} + \frac{l_3}{3} + \frac{l_4}{6} + \mathcal{O}(L^5) \end{aligned} \tag{3.13}$$

The accuracy of the fourth order method is generally higher than the second order method. To further increase the accuracy of the solution without largely increasing the computing time the size of the interval can be changed adaptively. This is called adaptive step size control. In every step the desired accuracy (this generally means that the quantities described by the differential equations are within their allowed errors) is compared to the accuracy of the last step performed in the calculation. If the achieved accuracy of the solution in the interval of the step size is worse that the desired accuracy, the step will be repeated with smaller step size. In case the achieved accuracy is better than the desired, the next step will be performed with a larger step size. This way, interesting or 'wilder' intervals will get smaller step sizes and therefore the same accuracy as intervals in which the differential

equations behave more 'smooth' which means that larger step sizes are sufficient.

In Fig. 12a the evolution of the quark Yukawa couplings is shown up to the Planck scale in a linear-log scale, Fig. 12b shows the same plot in log-log scale.
These plots were made using the quark masses listed in Table 3.

Quark	mass [GeV] $\pm$ error	Ratio to the top quark mass
Top	$171.3 \pm 1.1 \pm 1.2$	1
Bottom	$4.2^{+0.17}_{-0.07}$	40.8 ± 1.10
Charm	$1.27^{+0.07}_{-0.11}$	134.8 ± 9.87
Strange	$0.105^{+0.025}_{-0.035}$	1646.2 ± 521.90

Table 3: Quark masses and their errors from the 2009 PDG booklet update [26], and their ratios in comparison to the top quark mass.

Fig. 13 shows the ratio of the top quark Yukawa coupling to the other quark Yukawa couplings on a log-log scale. The bottom coupling is about a factor of 40 smaller than the top coupling, the charm coupling more than a factor of 100 and the strange coupling more than a factor of 1000, respectively. Comparing these numbers to the ratios in Table 3, we clearly see that the couplings scale with their masses to a good approximation.

These plots allow to back up the general assumption that compared to the top quark Yukawa coupling the other quark Yukawa couplings are negligible due to their low mass.

The running of the gauge couplings can equally be simulated up to the Planck scale. Fig. 14 shows the evolution of g, g' and g_{QCD}. Around a scale of $\mathcal{O}(17)$GeV the gauge couplings get very close but do not unify. According to GUTs, the couplings could unify in a case where the SM is not an accurate theory up to energies of the Planck scale. The next section will elaborate on this topic.

3.3 VALIDITY OF THE STANDARD MODEL

The mass of the Higgs boson is a crucial parameter for the validity of the SM. There are two possible scenarios that limit the Higgs sector of the SM from surviving up to the scale of the reduced Planck mass ($m_{Pl} = \frac{1}{\sqrt{8\pi G}} = 2.43 \times 10^{18}$GeV, where G is the gravitational constant). At this scale (maybe even earlier) quantum gravity effects are believed to appear [27, 28]. In the first scenario, for a large Higgs mass $m_H \geqslant 170$GeV, the RGEs lead to a quartic Higgs self coupling that becomes too large to

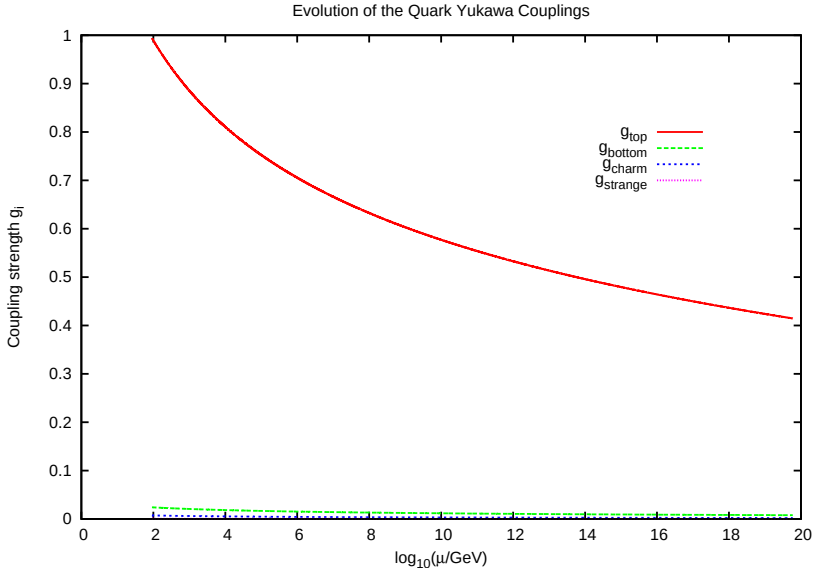

(a) Evolution of the quark Yukawa couplings. Lin-log scale.

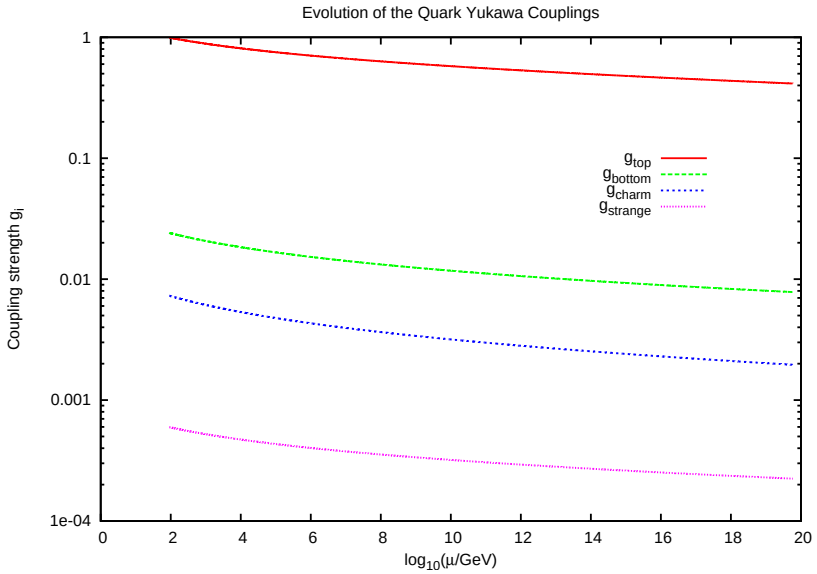

(b) Evolution of the quark Yukawa couplings. Log-log scale.

Figure 12: The evolution of the quark Yukawa couplings is shown over the cutoff scale Λ (the electroweak scale is of $\mathcal{O}(10^2 GeV)$, the Planck scale of $\mathcal{O}(10^{19} GeV)$.

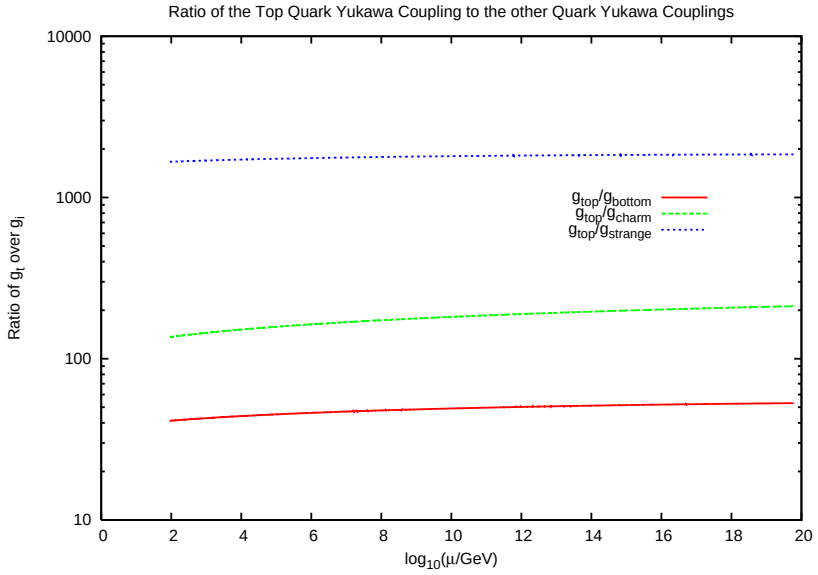

Figure 13: Ratio of the top quark Yukawa coupling over the bottom, charm and strange quark Yukawa couplings plotted over the renormalization scale μ (the electroweak scale is of $\mathcal{O}(10^2 GeV)$, the Planck scale of $\mathcal{O}(10^{19} GeV)$.

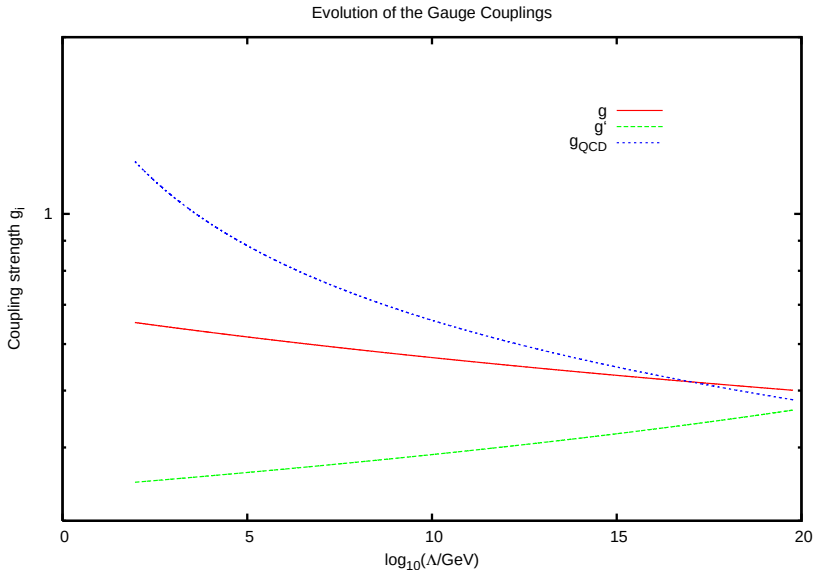

Figure 14: Evolution of the gauge couplings g, g' and g_{QCD} up to the Planck scale of $\mathcal{O}(10^{19} GeV)$.

be accurately described by perturbation theory. This is often denoted as the non-perturbative regime for the Higgs coupling λ occurring at some scale $\Lambda < m_{Pl}$ yielding either a new kind of non-perturbative physics at a scale $\sim \Lambda$ or new physics at a scale $< \Lambda$ that keeps λ from becoming divergent [29].
If, however, m_H is rather small ($\leqslant$ 130GeV), the RGEs will cause λ to become negative for some Higgs field value $\Lambda < m_{Pl}$. In this scenario the electroweak vacuum would only be a local minimum and there would be an additional new minimum at a scale $> \Lambda$ which would be potentially dangerous as it would make the vacuum become unstable (see also Sec. 3.3.2).

3.3.1 *Calculating the Higgs mass bounds*

In the SM conventions the renormalization group improved effective potential for the real Higgs field φ can be written in the 't Hooft-Landau gauge and the $\overline{\text{MS}}$ renormalization scheme as [30]:

$$V[\mu(s), g_i(s), \varphi(s)] \equiv V_0 + V_1 + \dots, \tag{3.14}$$

with g_i running over all couplings. V_0 and V_1 denote the tree level potential and the one-loop correction. They are given by

$$V_0 = -\frac{1}{2}m^2(s)\varphi^2(s) + \frac{1}{4!}\lambda(s)\varphi^4(s) + \Omega_C \tag{3.15}$$

$$V_1 = \sum_i \frac{n_i}{(8\pi)^2} m_i^4(\varphi)\left[\log\frac{m_i^2(\varphi)}{\mu^2} - c_i\right] \tag{3.16}$$

where the sum goes over all Higgs dependent masses $m_i(\varphi)$ (W, Z, Higgs and Goldstone bosons, fermions) having n_i degrees of freedom (with a negative value for fermions). c_i denotes a factor $5/6$ for gauge bosons and $3/2$ for scalars and fermions. Ω_C is a constant term for the cosmological constant which is of no further interest in our calculations and will be neglected in the following. A good approximation for the effective Higgs potential at highest energies is, according to a paper from J. Ellis et al. [29],

$$V(\varphi) = \frac{\lambda(\varphi)}{4!}\varphi^4, \tag{3.17}$$

with the argument that the effective Higgs potential V is scale independent and therefore allows to fix the renormalization scale μ at will for different values of the Higgs field φ. As we mainly focus on large values of the field, it is justified to set μ equal to φ. Hereby, also the bilinear term becomes negligible. The running quartic Higgs coupling $\lambda(\varphi)$ absorbs the large logarithms and

includes a one loop finite non logarithmic piece. For now, we will follow the train of thought of the quoted paper presenting the results leading to significant statements about the validity of the SM. In Sec. 3.3.1.1, we will however present some criticism to the approximations made.

The RGE for λ [24] reads:

$$16\pi^2\frac{d\lambda}{ds} = \frac{27}{4}g^4 + \frac{9}{2}g'^2g^2 - 9\lambda g^2 + \frac{9}{4}g'^4 - 36g_t^4 + 4\lambda^2 - 3g'^2\lambda + 12g_t^2\lambda \tag{3.18}$$

To calculate the perturbativity bound (where perturbation theory for λ starts to fail) we take a look at two conditions, $\lambda_{pb}(\Lambda) = \pi, 2\pi$ [31]. These two values correspond to a two loop correction to the one loop β function of λ of approximately 25% (where the perturbative expansion is still meaningful) and a two loop correction of about 50% [29], respectively, represented by the blue (bold) upper lines in Fig. 15.

The stability bound, the region where the electroweak vacuum becomes unstable, is marked by the shaded bands at the bottom of Fig. 15. The SM potential of the Higgs field develops an additional deeper minimum at a scale Λ, higher than the electroweak scale. This implies that $\lambda(\mu)$ becomes negative at a certain scale $\mu \leqslant \Lambda$ causing the possible instability of the potential.
In between the two scenarios the SM does survive up to highest energy scales. In this region the SM would actually be valid up to the Planck scale ($\mathcal{O}(10^{29})$). Sec. 3.3.2 lines out the possible consequences.

However, of the possible Higgs masses that could lead to such a survival scenario, there are already some excluded mass regions from direct Higgs searches. The gray zones in Fig. 15 represent the LEP exclusion from 2003 (Higgs mass excluded up to 114 GeV at a 95% confidence level (CL)) and the Tevatron exclusion from March 2009 (Higgs mass excluded between 160 and 170 GeV at 95% CL).

Fig. 16 illustrates the behavior of the quartic Higgs coupling λ for the different scenarios depending on the Higgs mass. Perturbation theory starts failing from a mass of 170 GeV upwards where λ becomes larger with increasing scale. Therefore it can soon no longer be treated as a small parameter that can be described by perturbation theory. If the Higgs mass is lower than 130 GeV λ will soon become negative at a scale $\Lambda < m_{Pl}$. Only in the region between the two scenarios outlined above, λ remains positive yet small and therefore the SM would remain to be a valid theory up to m_{Pl}.

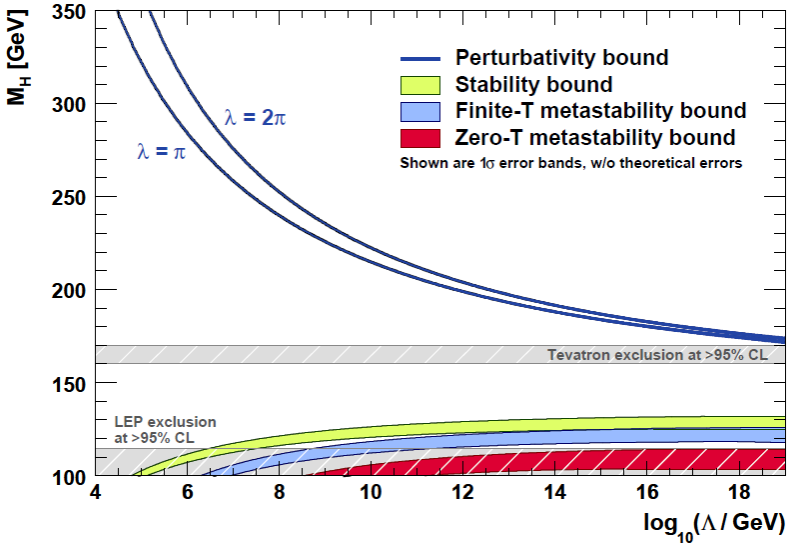

Figure 15: This plot is taken from [29]. It shows at which scale Λ the SM RGEs cause the quartic Higgs coupling λ to become too large to be described by perturbation theory and at which scale the electroweak vacuum becomes unstable, depending on the mass of the Higgs boson. The upper blue (bold) lines represent the perturbativity bound for $\lambda = \pi$ (lower line) and $\lambda = 2\pi$ (upper line). The vacuum stability bounds are represented by the three bands at the bottom of the plot. The green (light shaded) band represents the absolute vacuum stability bound, the blue and red (medium and dark shaded) bands represent the less restrictive finite and zero temperature metastability bounds, respectively (not discussed in this work). The gray covered bands represent the LEP [32] and Tevatron [33] exclusions for the Higgs boson mass.

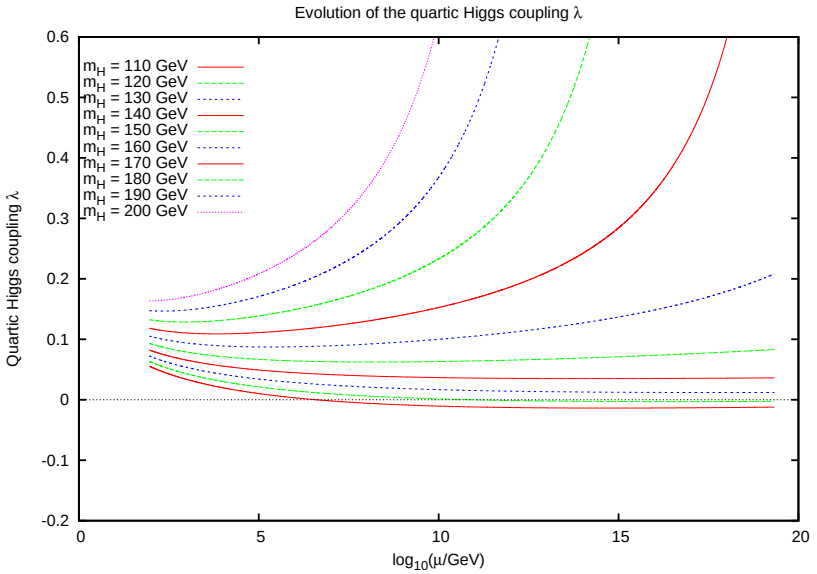

Figure 16: The behavior of the quartic Higgs coupling λ is illustrated depending on different Higgs masses. For Higgs masses between 110 and 120 GeV λ becomes negative at scales between 10^7 to 10^{10} GeV. In the region between 130 and 160 GeV λ remains positive and relatively small (so perturbation theory still applies) up to the Planck scale $\sim \mathcal{O}(10^{19})$. For Higgs masses greater than 170 GeV λ diverges and can no longer be described by perturbation theory. The divergence starts at lower scales in cases with a higher Higgs mass.

3.3.1.1 *Criticism*

The approximation made earlier in Sec. 3.3.1 in reducing the effective Higgs potential to its tree level component, see Eq. 3.17, seems justified at first sight, following the above mentioned reasoning for high values of the potential. We, however, explicitly calculate the ratio of the tree level component to the full potential including the one loop correction to check the validity of the assumption.

$$\text{ratio} = \frac{V_0}{V_0 + V_1} \,, \tag{3.19}$$

where V_0 and V_1 are the tree level and one loop contributions to the Higgs potential from Eq. 3.15 - 3.16.
Fig. 17 shows the result for scenarios using different Higgs masses. Comparing this plot to Fig. 16 unveils that in cases where the quartic Higgs coupling λ is well behaving, i.e. does not diverge or become negative, the assumption is justified since the ratio of the tree level component to the full potential calculated at one loop is around 90 to 100%. In the Higgs mass region where λ becomes negative at a certain scale Λ and the SM electroweak vacuum might become unstable ($m_H \leqslant 130$ GeV), the ratio develops a singularity. In this case the calculation would have to be conducted at higher order than tree level to be on the safe side. Looking at cases of higher Higgs masses (> 170 GeV) in which perturbation theory is no longer applicable to λ, it shows that the ratio drops to a plateau at around 50%. This indicates that the assumption of neglecting the one loop correction to the potential is not fully justified anymore.

3.3.2 *Implications for cosmology and new physics beyond the SM*

In general, we can divide the results of this section into three regions for the Standard Model:

1. Vacuum stability bound, lower Higgs mass region
2. Survival region, medium Higgs mass region
3. Perturbative bound, higher Higgs mass region

For all three cases, one statement holds generally true. The Standard Model is a highly successful theory at the electroweak scale. Many measurements have proven its accuracy in describing and predicting particle physics processes with high precision and its potential in predicting the existence of elementary and composed particles. However, there are hints of new phenomena

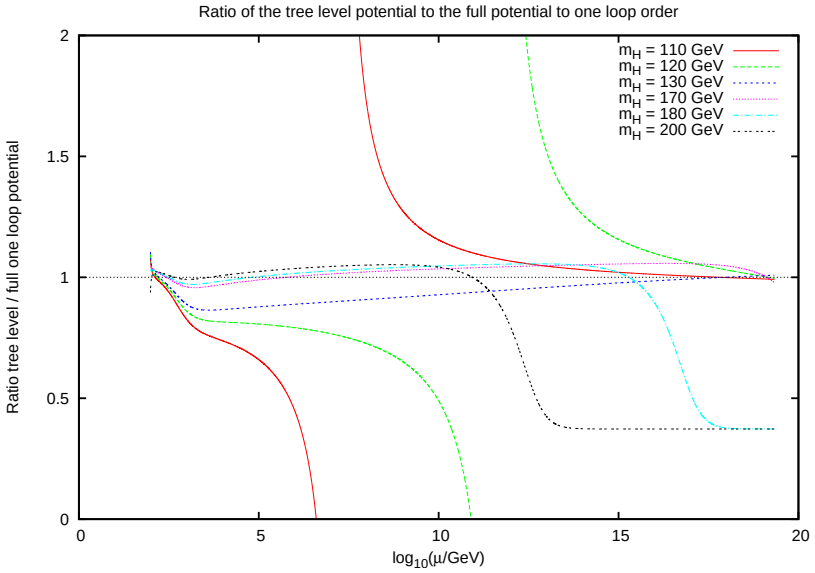

Figure 17: Ratio of the tree level component of the effective Higgs potential to the full potential including one loop corrections $\frac{V_0}{V_0+V_1}$. Scenarios for different Higgs masses are shown.

beyond the physics of the SM. It fails, for example in describing the origin of neutrino oscillation and neutrino masses. Also cosmology gives us indications of physics that we are unable to explain as of today. Within the SM there is no way of explaining Dark Matter from the velocity dispersion of galaxies in the Coma cluster in 1934, or Dark Energy to account for the missing mass and energy in the Universe found only about ten years ago by the means of Supernovae of high redshift being greater than expected[3].

The implications for new physics beyond the SM physics in the first case were already briefly mentioned above. The minimum of the effective Higgs potential at the electroweak scale (non zero ground state of the vacuum) can become unstable against collapse due to decay via quantum or thermal fluctuations into the new deeper minimum at some higher scale Λ. The vacuum state at the electroweak scale obviously has a lifetime $\geqslant$ the age of the universe $t_0 \approx 13.73 \pm 0.12$billion years [35] and new physics at a scale $< \Lambda$ could prevent the new minimum from even existing.

In the third region, perturbation theory fails as λ becomes large at a scale Λ. This could be understood with new non perturbative physics at $\sim \Lambda$ or new physics at some scale $< \Lambda$ that prevents the quartic Higgs coupling from becoming large.

3 See e.g. [34] for an introduction to topics like cosmology, Dark Matter and Dark Energy.

Region number two seems 'boring' for the future of particle physics since it does not imply any hint on new physics beyond the Standard Model. From a cosmological point of view, however, a Higgs mechanism surviving up to the Planck scale could back up some interesting cosmological models of inflation.

3.3.3 *Cosmological inflation*

Explaining the origin and evolution of our Universe is not an easy task. Starting from standard big bang cosmology, we end up with several problems that cannot be explained satisfactorily so far. From modern observation we assume the Universe to be homogeneous, patches of the Universe that have not even been in causal contact yet, show the same homogeneity and cosmic background radiation. This can only be explained with a high degree of fine tuning in case of a classical expansion which is obviously not a very natural explanation.
Cosmological inflation explains the evolution of the very early Universe as a change of state in a scalar field of a very flat potential, called the inflaton field. The inflaton field is spatially homogeneous and has a finite energy density. If the field changes slowly enough towards lower energy densities it builds up negative pressure and acts similar to a cosmological constant, therefore leading to an accelerated expansion of the Universe. If the field is the dominant component in the Universe, the expansion will go exponentially. After slowly rolling down the almost flat potential energy hill (inflation phase), the field reaches a steeper hill, inflation ends and an effect called reheating occurs. Reheating causes the large potential energy of the inflaton field to decay into particles and fill the universe with radiation. Today's observable matter in the Universe origins from quantum fluctuations at a time in the very early Universe before inflation occurred. Thereby, inflation solves the homogeneity problem, as well as the flatness problem and the absence of magnetic monopoles. Modern measurements have proven the Universe to be flat to high precision which then would be due to the fact that we only see a very small patch of the Universe on which scale it would naturally appear flat.
A similar argument holds true for the magnetic monopoles. From theory, there is no explanation for why there are no magnetic monopoles to observe on Earth or any hints in the observable Universe. Inflation, however, would have caused the magnetic monopoles present in the early Universe to be scattered far away from each other during the slow roll inflation phase. Therefore, we do not see any in the observable Universe. Further details on inflationary models can be found in Refs. [36, 37, 38, 39, 40, 41].

Finding a solid candidate for the inflaton field is one of the main concerns of inflationary theories. A Standard Model Higgs field could in principle be such a candidate if the SM remains valid up to the scale at which inflation occurs (> Planck scale). The observed amplitude of the initial perturbations in the early Universe, that caused the CMB radiation, require an extremely flat potential for the inflaton field (slow roll). We can calculate the criterion for λ to satisfy the assumption of a slow roll potential starting from the Hubble constant $H \equiv \frac{\dot{a}}{a}$ satisfying the equation

$$H^2 = \frac{8\pi G}{3}(\frac{1}{2}\dot{\varphi}^2 + V(\varphi)), \tag{3.20}$$

where φ is the inflaton field satisfying the differential equation

$$\ddot{\varphi}^2 + 3H\dot{\varphi} + V_{,\varphi} = 0. \tag{3.21}$$

The metric is defined by $ds^2 = -dt^2 + a^2(t)d\vec{x}^2$. Introducing the criteria for slow roll,

$$\dot{\varphi}^2 \ll V \text{ and } |\ddot{\varphi}| \ll 3H|\dot{\varphi}|, \tag{3.22}$$

we are left with simplified equations

$$H^2 \approx \frac{8\pi G}{3}V(\varphi), \tag{3.23}$$

$$3H\dot{\varphi} \approx V_{,\varphi}. \tag{3.24}$$

Assuming V to be a quartic potential (as $|\phi| \gg 100$ GeV here)

$$V \approx \frac{\lambda}{4}\varphi^4 \tag{3.25}$$

$$\Rightarrow H \approx \sqrt{\frac{8\pi G}{3}}\sqrt{\frac{\lambda}{4}}\varphi^2, \tag{3.26}$$

leading to a solution for the field

$$\varphi \approx \varphi_{sr} e^{-\sqrt{\frac{\lambda}{6\pi}}\left(\frac{t-t_{sr}}{t_{Pl}}\right)} \tag{3.27}$$

where $t_{Pl} = \sqrt{G}$ is the Planck time, t_{sr} and ϕ_{sr} are the time and field value when slow roll starts. For the slow roll regime of inflation, φ is assumed to be almost constant $\varphi \approx \varphi_{sr}$.
Therefore, the exponent of e has to be $\ll 1$ in order to allow for an extended period of $H \approx$ const.. From WMAP 7-year data [35] it is possible to set an upper limit on H from an upper limit on the power spectrum of gravitational waves $P_{gw} \sim \frac{H^2}{M_{Pl}^2}$. From

this, we obtain the upper limit $Ht_{Pl} \leqslant 3 \cdot 10^{-6}$ (see [42] for the principle of the calculation). The number of *e*-foldings[4] has to be big enough to allow for the Universe to reach its current size. This puts a lower limit on the number of *e*-foldings $N > 50$ if inflation happens close to the Planck scale. Also, the time $\Delta t = t - t_{sr}$ from the start of the slow roll phase of inflation to today times the Hubble rate has to be at least as big as the number of *e*-foldings, $N < H\Delta t$. Combining this information gives

$$50 < N < H\Delta t = Ht_{Pl}\frac{\Delta t}{t_{Pl}} < 3 \cdot 10^{-6}\frac{\Delta t}{t_{Pl}} \tag{3.28}$$

from which directly follows $\Delta t < 10^{-7} t_{Pl}$. This will require the quartic Higgs coupling λ to be $\leqslant 10^{-13}$ which would again be an extreme fine tuning of the theory. If, however, the Higgs field would couple non-minimally to gravity,

$$\mathcal{L}_{\text{non-minimal}} = \xi \phi^\dagger \phi R \tag{3.29}$$

where ϕ is the Higgs field and R is the gravitational Ricci tensor, this coupling would relax the requirement of the quartic Higgs coupling to be small (see [43]). Therefore, this could provide a very natural way of explaining inflation without introducing new particles or fields [44], given that the SM survives as a valid theory up to the inflationary scale and that the SM Higgs boson itself exists in the appropriate mass range. Considering the fact that new physics could alter the RGEs, this mass range could be as large as $120 < m_H < 180$ GeV, or to be more conservative (judging from the SM results only) $130 < m_H < 160$ GeV.

4 A time in which the Universe expands by a factor of *e*

Part II

EXPERIMENT

4

THE WH ANALYSIS

After understanding the importance of the Higgs boson not only for the Standard Model of particle physics but also for theories of cosmological inflation in Part I of this dissertation, we will now approach the topic of directly searching for the Higgs boson in proton antiproton collisions. As we have learned in Chapter 1, the preferred mass range for the SM Higgs boson is at relatively low mass $< 135 GeV$. Today, there are two colliders capable of exploring this mass range: the Tevatron based at Fermilab near Chicago, USA and the Large Hadron Collider (LHC) at CERN near Geneva, Switzerland. The Tevatron has been in operation since 1988, and can reach the mass range interesting for Higgs physics after the RunII upgrade in 2001. The LHC just recently started its operation in 2009 and, even though operating at higher collision energies, it will take some time to accumulate data and match the higher design luminosity. Therefore, at the time this work was performed, the Tevatron was the only place in the world to conduct a direct search for the Higgs boson.

The analysis presented in this work is searching for Higgs boson production in association with a W boson, which is the channel with the highest production cross section times branching ratio yields in the low mass range (neglecting gluon-gluon fusion due to its high backgrounds). The analysis is based on a dataset of 5.3 fb^{-1} of integrated luminosity. Previous searches on the associated production of a W boson together with a Higgs boson have been presented, the most recent one on a subset of the data used in this analysis (5.0 fb^{-1}) using a Neural Network multivariate technique to increase signal sensitivity [1]. The analysis presented here uses a Random Forest approach to increase sensitivity even more. Thorough understanding of the detector is crucial to understanding the underlying physics of this analysis. Therefore, we will start by describing the framework in which we perform physics analyses, namely the Tevatron accelerator and the DØ detector. We will then go into detail about the reconstruction of physics objects from data and the simulation of physics processes in Monte Carlo simulations to be able to fully understand and describe the physics measured in the detector. In the final analysis chapter, we will then put the pieces together to explain how we reconstruct the objects we are looking for, namely the W boson and the Higgs boson to see whether we have an excess of signal in our final analysis variables. To optimize sensi-

tivity, we split the analysis in different subchannels throughout, divided by final states and data taking periods. We separate into an electron and a muon channel, corresponding to the decay of the W boson into a lepton (electron, muon or tauon, decaying subsequently in an electron or muon) and the corresponding neutrino. We also divide into two and three jets originating from the decaying Higgs boson, in two b quark jets with an additional gluon jet in the three jet case, respectively. The different data taking periods will be described in the following. We further apply a procedure known as *b tagging* of the jets originating from the hadronization of b quarks and finally apply a *Random Forest* to the tagged samples.

We evaluate the output of every channel separately and assure that we have good agreement between data and simulation. We then combine the sensitivity of every subchannel in our final results which, in the absence of a signal, is a limit setting procedure on the production cross section times branching ratio of the SM Higgs boson in the WH channel.

5

EXPERIMENTAL APPARATUS

The dataset that we use in this analysis comes from mainly two different data taking periods. The first sample corresponds to data taken until summer 2006 when the Tevatron and both detector experiments were shut down for upgrading purposes. This sample corresponds to an integrated luminosity of 1.04 (1.08) fb^{-1} for the electron (muon) subsample and is referred to as the RunIIa data sample.
The second sample corresponds to a data taking period between June 2006 and June 2009, it is referred to as the RunIIb data sample. It has an integrated luminosity of 4.28 (4.28) fb^{-1}. The total integrated luminosity of the combined data sample is 5.32 fb^{-1} and 5.36 fb^{-1} for the electron and muon channel, respectively. This dataset has passed certain criteria on the quality of the data and has been cleaned of data taking periods in which data taking was corrupted in the detector. The uncertainty on the measured luminosity is 6.1% [45].
The two data samples are treated separately to properly account for the changes in detector response due to important detector and trigger upgrades. The main difference in treatment comes from different samples of simulated events, often called Monte Carlo (MC) samples, and different correction factors that are applied to these MC samples (see Sec. 6.4).
In this chapter, we will explain the details of the DØ detector hardware that delivers the data for our analysis. We will continue with a detailed description of the reconstruction of physics objects from the detector information.

5.1 FERMILAB

Accelerating particles to high energies $\sim \mathcal{O}(TeV)$ and bringing them to collision is the key tool of particle physics to study the constituents of matter and their interactions as well as to search for new particles yet to observe. At Fermilab, officially called Fermi National Accelerator Laboratory (FNAL), located about 50 km west of Chicago in the United States of America, founded in 1967 as a particle physics laboratory, these collisions take place between protons and antiprotons in the Tevatron collider. Fermilab has been home to many discoveries of which the most famous ones were the discovery of the bottom quark in 1977, the top quark in 1995 and the neutrino of the third leptonic family, the τ neutrino in 2000.

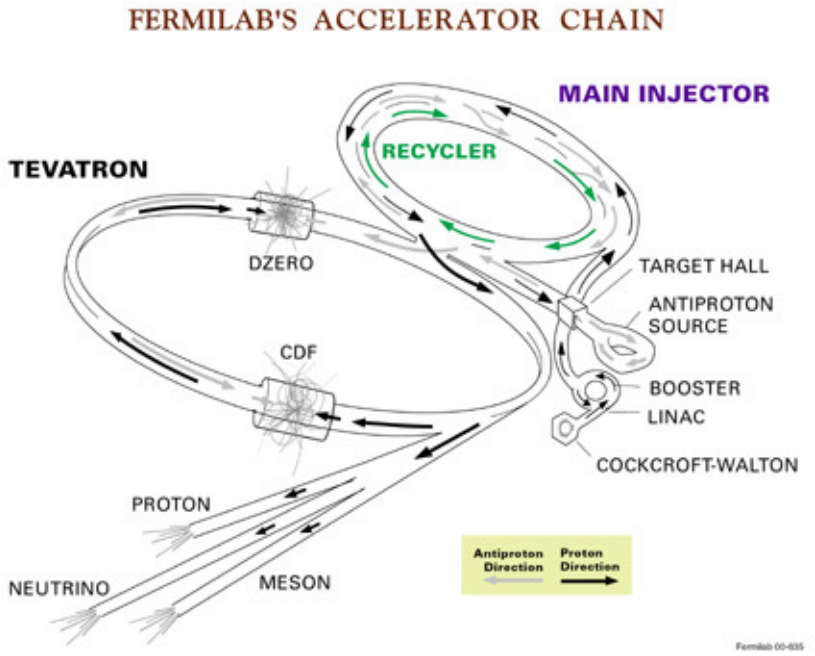

Figure 18: Schematic view of the accelerator chain leading to the 1.96 TeV beam inside the Tevatron [46].

The Tevatron started its work in 1988 as a proton antiproton collider at a center of mass energy of 1.0 TeV (hence the name). Two experiments are located along the accelerator ring, the Collider Detector at Fermilab (CDF) and DØ detector (named after its location on the Tevatron ring), at points where the circulating proton and antiproton beams are brought to collision. Since an accelerator and detector upgrade in 2000 the Tevatron operates at a center of mass energy of 1.96 TeV and has been the world's most powerful particle accelerator until the launch of the Large Hadron Collider (LHC) at CERN in Geneva, Switzerland in 2009, operating at 7 TeV. We will outline the accelerator chain in following section. We will then go into detail about the DØ detector and all its subsystems.

5.2 ACCELERATOR CHAIN

The well known Tevatron collider is only the last step in a chain of accelerators creating the proton and antiproton beams and bringing them to their final collision energy inside the Tevatron ring. Fig. 18 shows a schematic of the accelerator chain that creates the beam. We will follow the protons through this chain.

COCKROFT-WALTON ACCELERATOR Negatively charged H^- atoms are created by ionizing Hydrogen atoms from H_2 Hydrogen gas. The molecules in the gas are split up into single Hydrogen atoms by adding an additional electron in a magnetron source. In this

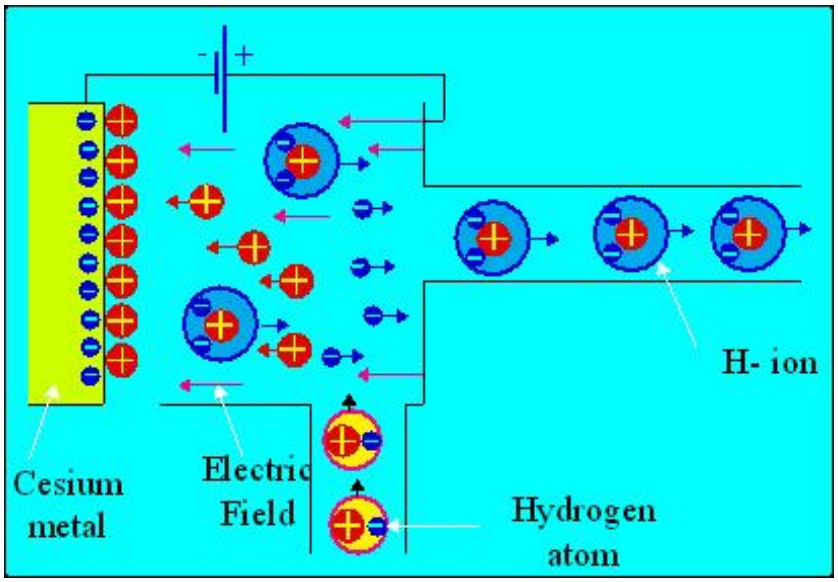

Figure 19: Schematic view of the magnetron source. The Hydrogen atoms from the H_2 gas separate into protons and electrons. The protons dock to the wall of Cesium until they pick up two electrons and can escape from the magnetron [47].

device, the Hydrogen atoms from the gas strip off their electron and dock to a wall of Cesium metal (see Fig. 19). Because of the low work function of the Cesium, the proton will eventually pick up two electrons allowing the thereby created H^- ion to escape.

The magnetron source leads directly into the Cockroft-Walton accelerator. In this accelerator, capacitors are charged in parallel from an AC source to then be discharged in series to create an acceleration of 750 keV for the H^- ions while they travel through the device. Fig. 20 shows a picture of the Cockroft-Walton accelerator.

LINAC The linear accelerator (LINAC) picks up the H^- ions at an energy of 750 keV to further accelerate them. The working principle of a LINAC is shown in Fig. 21. The ions enter a vacuum drift tube that consists of radio frequency (RF) cavities and gaps between them. Charged particles traveling through such an alignment are accelerated by the attraction of the electromagnetic field in between the cavities while they are protected from the field inside the cavity. The field is alternated with a certain frequency so that the charged particles get accelerated and grouped into bunches at the same time. Particles that are slightly ahead of the bunch will feel less acceleration and particles that are slightly behind will feel a stronger field. The LINAC used at Fermilab has a length of 130 m and it accelerates the protons up to an energy of 400 MeV. The ion bunches exiting the LINAC are separated by 5 ns. When leaving the LINAC, the H^- ions are stripped off

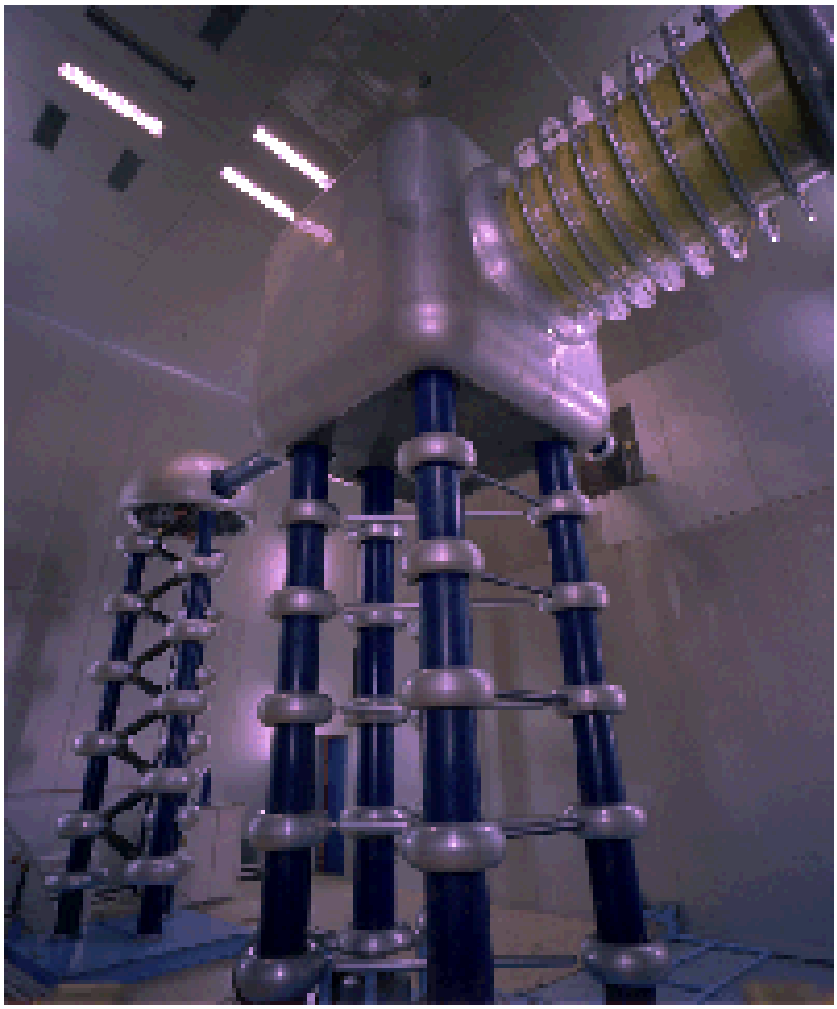

Figure 20: Picture of the Cockroft-Walton accelerator in which the ionized Hydrogen atoms are accelerated by capacitors discharged in series up to an energy of 750 keV. This accelerator feeds the H^- ions into the LINAC and is the first point of acceleration.

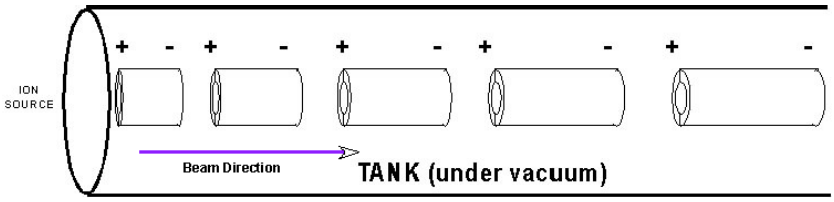

Figure 21: Schematic of the LINAC. Hydrogen ions (H^-) enter from the magnetron to be accelerated by RF cavities of alternating field polarization up to an energy of 400 MeV [48].

their electrons by passing the ions through a carbon foil and the pure protons continue their way through the accelerator chain. Further acceleration using a LINAC is unpractical because of the length needed for the acceleration. Therefore, the next step of acceleration will be a synchrotron.

BOOSTER The Booster is a synchrotron with a circumference of 475 m. It brings the 400 MeV protons up to an energy of 8 GeV. Inside the Booster, RF cavities accelerate the protons by 500 kV per turn, the frequency must therefore change at a rate of 1 GHz/s to be able to further accelerate the protons.

MAIN INJECTOR Exiting the Booster, the protons enter the Main Injector which obtains his name from the fact that after further accelerating the protons, it delivers the beam into the Tevatron. The Main Injector is also a synchrotron at a circumference of 3.3 km. It creates a proton beam at 120 GeV to be injected into the antiproton source which creates the beam of antiprotons. The Main Injector also accelerates both beams of protons and antiprotons to an energy of 150 GeV to be injected into the Tevatron.

ANTIPROTON BEAM The beam of 120 GeV protons from the Main Injector is used to create antiprotons. Fig. 22 shows a schematic of the antiproton source.

The proton beam is fired on a Nickel target producing many outgoing secondary particles at the Target Station. A lithium lens together with a magnetic field focus the beam of created particles and filter out the produced antiprotons. The antiprotons are passed to the Debuncher. The function of the Debuncher, also a synchrotron in the shape of a triangle with a radius of 90 m (see Fig. 23), is to smooth the distribution in energy of the antiprotons to produce an 8 GeV beam. Unfortunately, in this energy smoothing procedure the bunch structure of the beam is lost. Therefore, the beam from the Debuncher is passed to the Accumulater. Designed like the Debuncher as a triangular shaped synchrotron, with a radius of 75 m, the Accumulator restores the

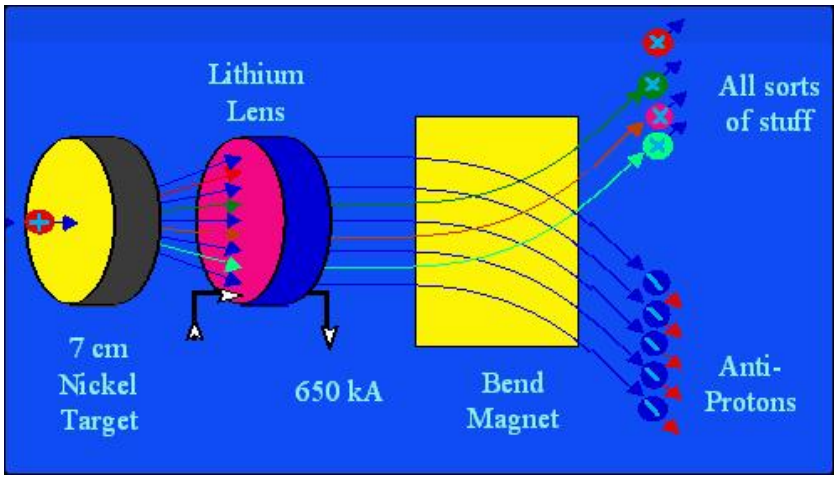

Figure 22: Schematic view of the antiproton source. The incoming proton beam creates many outgoing secondary particles from the collision with the Nickel target, such as pions, kaons, muons and also antiprotons. The antiprotons are filtered out using a lithium lens and a magnetic field [49].

bunch structure of the beam. Both, Debuncher and Accumulator use stochastic cooling to keep the antiprotons on track. Stochastic cooling is a procedure in which the beam width is controlled by monitoring and correcting the amplitude of the beam. Fig. 23 shows a sketch of the antiproton facility. More details on the antiproton beam can be found in Ref. [50]. The antiproton beam is subsequently accelerated in the Main Injector to an energy of 150 GeV, as mentioned above.

RECYCLER As the previous paragraph might have implied, the production of antiprotons is not an easy procedure. Therefore, the Main Injector tunnel contains a second storage ring, called the Recycler to which a fraction of the unused antiprotons can be transferred at the end of a store [1]. They are kept at an energy of 8 GeV until they are filled into the Main Injector again. The Recycler also serves as an additional storage of antiprotons to increase the initial luminosity of a store over the initial design capacity of the Main Injector.

TEVATRON The final piece in the chain of acceleration is the Tevatron accelerator ring, also a synchrotron, with a circumference of 6.28 km. Over 1000 superconducting magnets at field strengths of 4 T are used to keep the protons and antiprotons on their tracks. Both beams are accelerated from their initial energies of 150 GeV from the Main Injector level up to 980 GeV, resulting

1 A store is the name for a filling of the Tevatron with enough protons and antiprotons to collide beams for a time between typically 12-36 hours. Within this time, no additional particles are inserted into the Tevatron.

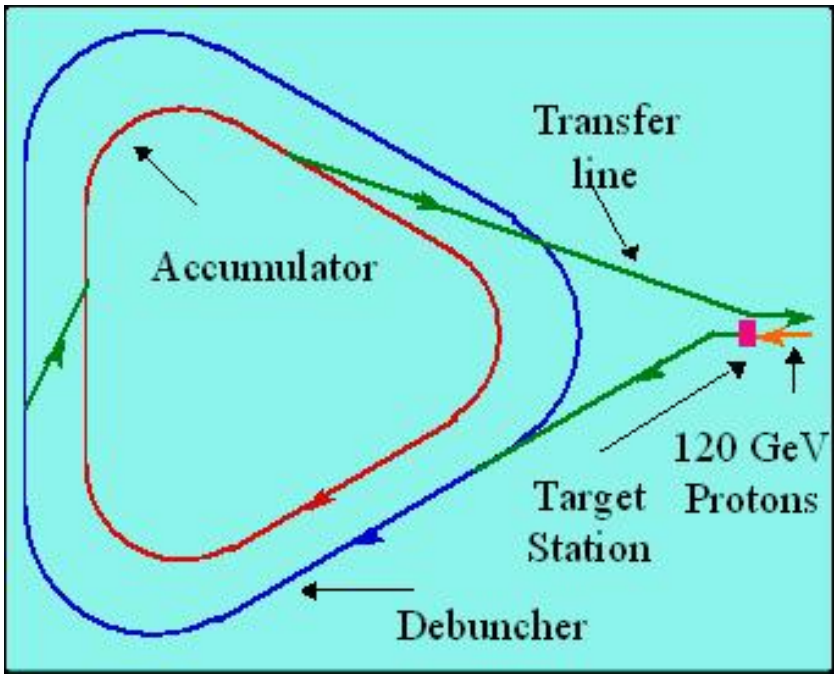

Figure 23: Sketch of the antiproton facility showing the way of the antiproton beam from its creation at the Target Station, over the Debuncher, through the Accumulator out into the transfer line that leads into the Main Injector [49].

in proton-antiproton collisions at an energy of 1.96 TeV. The two beams, circulating in opposite directions, are structured into 36 bunches which each contain around $3 \cdot 10^{11}$ protons and $6 \cdot 10^{10}$ antiprotons. The bunches are separated by 396 ns and grouped into three superbunches with a luminous region of about 26 cm in longitudinal size at the interaction points. The Tevatron currently delivers instantaneous luminosities of up to 375 $(\mu b\, s)^{-1}$. The ring is grouped into six sections, denoted A-F with subsections 0-3. The beams are brought to collision in two distinct points, the first one at the B0 point on the ring, which is the location of the CDF detector, the second one at D0, the location of the DØ detector.

5.3 THE DØ DETECTOR

The DØ detector is designed to be a multiple purpose detector for a variety of physics analyses. It is constructed to analyze the outcome of $p\bar{p}$ collisions at the TeV scale, especially to reconstruct physics objects with high transverse momentum ($\mathcal{O}(1-100\text{GeV})$). Today's detector differs from the initial design due to the detector upgrade between the RunI (1992 - 1996) and RunII (2002 - today) data taking periods of the Tevatron. As we only use data from the RunII data taking period, we will detail the upgraded design of the detector in the following. For a description of the initial detector design see Ref. [51]. The current design is described in detail in Ref. [48]. The DØ detector is 20 m long and 13 m high. It has an angular coverage of almost 4π.
The coordinate system used to describe the detector and reconstructed objects inside the detector consists of the spherical coordinates r, θ, ϕ with θ being measured with respect to the beam axis, $\theta = 0°$ is defined to be aligned with the proton beam direction and $\theta = 180°$ is aligned with the antiproton beam direction. The origin of the coordinate system coincides with the center of the detector which is also the nominal interaction point. The z axis is parallel to the beam axis inside the detector where $z > 0$ corresponds to $\theta = 0°$ and $z < 0$ corresponds to $\theta = 180°$. However, instead of using the polar angle θ, we use the so called pseudorapidity η defined as

$$\eta = -\ln\left[\tan\left(\frac{\theta}{2}\right)\right] \tag{5.1}$$

The pseudorapidity approximates the true rapidity y in the limit $m/E \to 0$. y is defined as

$$y = \frac{1}{2}\log\frac{E + p_z}{E - p_z}. \tag{5.2}$$

For an object with polar angle $\theta = 90°$ the pseudorapidity η equals 0, whereas $\eta \to \infty$ for $\theta \to 0°$. Pseudorapidity can be calculated with respect to a reconstructed physics object or with respect to the origin of the detector in which case it is denoted by η_{det}.
To define distances between objects in this coordinate system, we use the angular distance ΔR defined as

$$\Delta R = \sqrt{(\Delta\eta)^2 + (\Delta\phi)^2} \tag{5.3}$$

where $\Delta\eta$ and $\Delta\phi$ are the differences in value of the η and ϕ coordinates for the two objects in question.

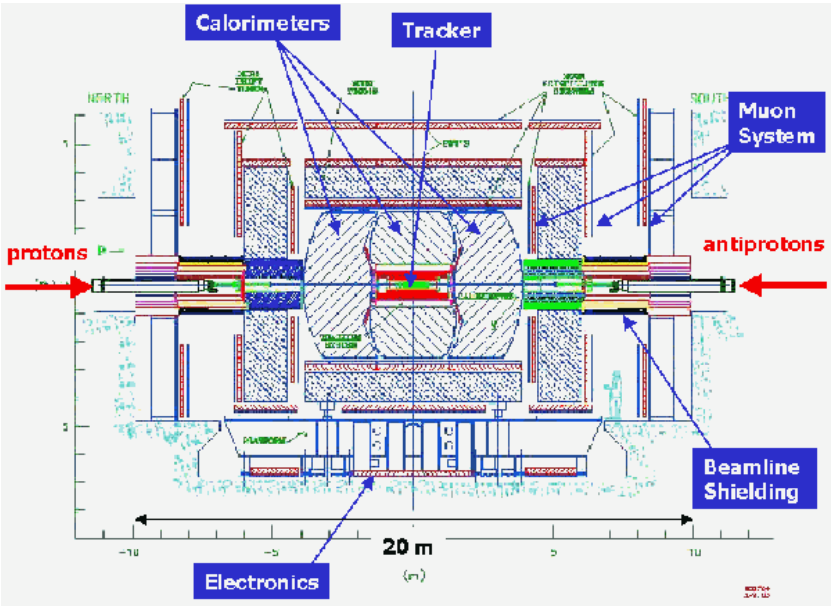

Figure 24: Schematic side view of the DØ detector with its different layers of subdetectors. Starting from the tracking system as the innermost layer, over the solenoid creating a 2T magnetic field, the electromagnetic and hadronic calorimeter as well as the different layers of the muon system with the toroid between the two outermost layers [52].

Fig. 24 shows a schematic of the DØ detector in which all the different layers of subdetectors as well as the magnets can be seen, Fig. 25 shows a photograph from the south end of the detector before closing the forward muon chamber wall and the toroid.

5.3.1 *Tracking System*

The subdetector closest to the nominal interaction point at the center of the detector is the tracking system. It is designed to measure trajectories of charged particles originating from the primary (and possibly secondary) interaction vertices. It consists of two different systems, the Silicon Microstrip Tracker (SMT) as the innermost layer and the Central Fiber Tracker (CFT) surrounding the SMT. Both are within the 2T magnet field of a solenoid. Fig. 26 shows a cross sectional view of the central tracking system in the $x-z$ plane. SMT and CFT together provide a resolution of 35µm for the reconstruction of the primary vertex along the beam axis. They make it possible to tag a jet originating from a b quark with a resolution in the distance of closest approach to the beam axis [2] of 15µm in the $r-\phi$ plane for particles with

2 The distance of closest approach of an object to the beam axis is often called *impact parameter*

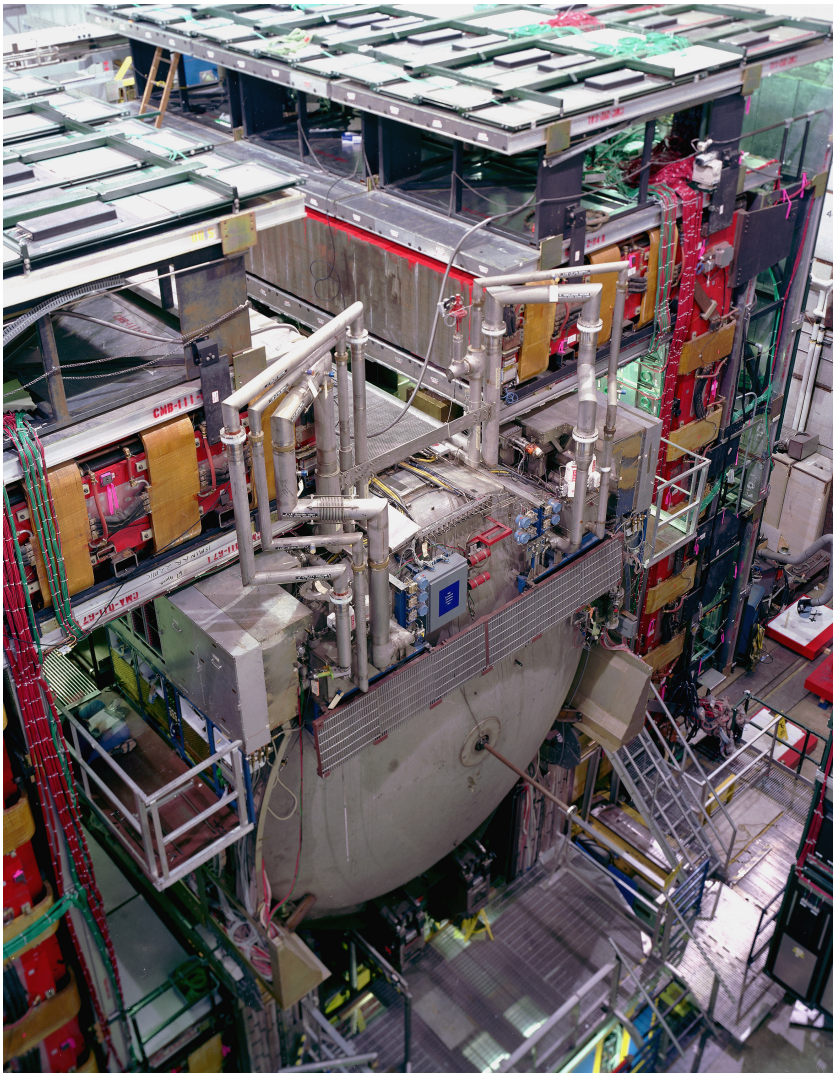

Figure 25: Picture from the southside of the DØ detector. The gray vessel in the center is the cryostat surrounding the liquid argon calorimeter with a pipe structure on top to regulate cooling and pressure. In its middle, the brown beam pipe sticks out. Surrounding the calorimeter, three layers of muon chambers incorporate the red toroid. [53].

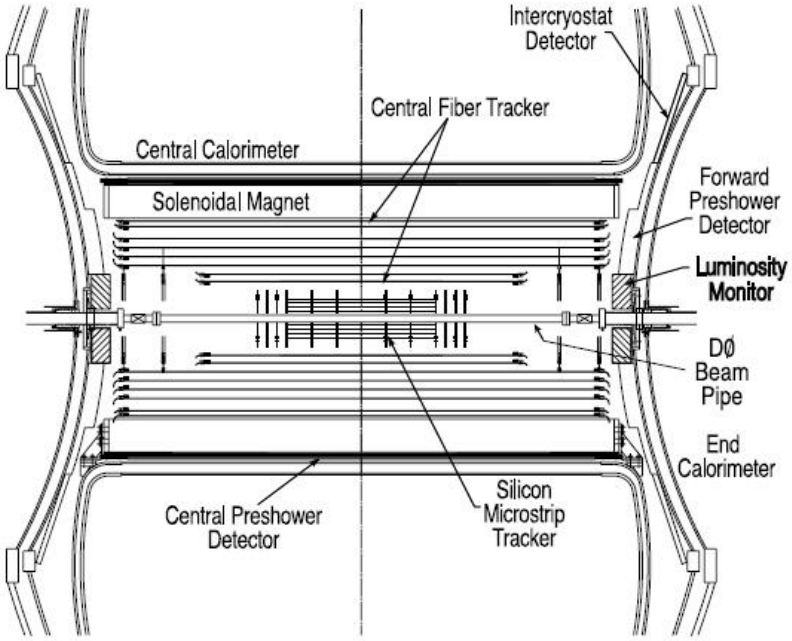

Figure 26: Cross sectional view of the tracking system. At the innermost layer, the SMT surrounds the beam pipe followed by the CFT. Both are enclosed in the solenoid that provides a magnetic field of 2T. The positions of the central calorimeter, the luminosity monitor as well as the preshower detectors can also be seen [48].

transverse momentum $p_T > 10$ GeV in the central direction $\eta = 0$ perpendicular to the beam axis.

SILICON MICROSTRIP TRACKER The SMT surrounds the beam pipe inside the DØ detector in which the protons and antiprotons are brought to collision. The beam pipe is a 0.508 mm thick beryllium pipe that has a diameter of 38.1 mm. The SMT consists of barrel and disk modules of silicon microstrip sensors that surround the whole beam pipe. Fig. 27 shows a schematic of the barrel and disk module alignment around the beam pipe which covers almost the full η range of the detector. In the central region (low η), both barrel and disk modules are used, whereas in the forward region only disk modules are used. Within $|z| < 38.2$ cm of the interaction point, barrels and disks cover the region of proton–antiproton collisions with a width of $\sigma_z = 26$ cm (which corresponds to the luminous region at the interaction point). The centers of the barrel modules are located at $|z| = 6.2$, 19.0 and 31.8 cm, the disk modules are located at $|z| = 12.5$, 25.3, 38.2, 43.1, 48.1 and 53.1 cm. While barrels primarily measure the $r - \phi$ coordinate, disks measure $r - z$ as well as $r - \phi$. Vertices for particles in the high η range are reconstructed in three dimensions by the disks whereas vertices of particles at small values of η

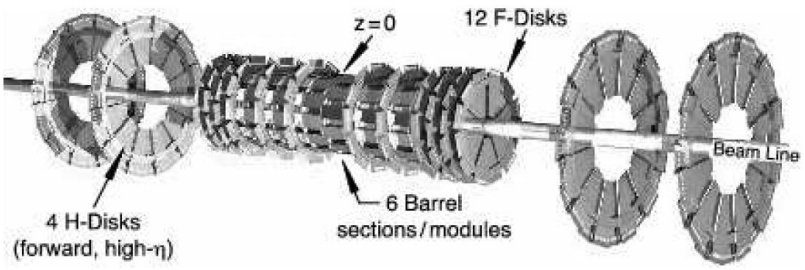

Figure 27: Three-dimensional view of the silicon microstrip tracker. Barrel and disk alignments cover the central region. Larger disks assure coverage in the forward region [48].

are measured in the barrels and the central fiber tracker. In r direction, the central disk modules range from 2.6 to 10.0 cm, the barrel detectors range from 2.7 to 7.6 cm. The forward disk modules extend from 9.5 to 26.0 cm in r.

Each of the barrels consists of four layers of silicon readouts. Silicon modules inside of barrels are called ladders. 12 ladders form the first and second layer while the third and fourth layer are made of 24 ladders. Each layer consists of two sublayers. Layer two and four use single sided detectors in all barrels using only axial microstrips, whereas layer one and three of the central four barrels use double sided double metal detectors which allow for a three-dimensional reconstruction of tracks by using axial and stereo strips with a stereo angle of 2°. The outermost barrels use double sided detectors.
Disk modules consist of wedge-shaped detectors, central modules consist of 12 wedges made of double sided detectors with a stereo angle of 30°, forward modules consist of 24 single sided wedges aligned back to back in pairs providing a stereo angle of 15°.
The working principle of the silicon microstrip detectors is to register a current from the ionizing effect of charged particles traveling through the detector. In between the microstrips of the detector, a charged particle creates electron–hole pairs in the so-called depletion zones. An electric field applied to this zone separates the charges which then become measurable in the microstrips allowing for a reconstruction of the spatial position of the track of the charged particle. The SMT consists of a total of almost 800,000 readout channels.
To compensate for aging effects of the silicon and to ameliorate the resolution in terms of p_T and impact parameter, a new layer of silicon detectors was inserted closest to the beam pipe in a maintenance shutdown of detector operations in 2006.

CENTRAL FIBER TRACKER The CFT consists of two inner cylinders and six outer cylinders that surround the SMT in a radial

range of $20-52$ cm. The two inner cylinders are spatially limited by the distance between the forward disks of the SMT and therefore have a length of 1.66 m, whereas the outer cylinders have a length of 2.52 m thereby covering the whole beam pipe which has a length of 2.37 m. Four layers of scintillating fibers, each fiber having a diameter of 835µm, are mounted to each of the concentric cylinders. The fiber core is made of polystyrene doped with paraterphenyl which acts as an organic fluorescent dye. Two layers of fibers are aligned axially on the cylinders and the other two layers are aligned at +3° (odd cylinder layers) and -3° (even cylinder layers) in ϕ. The fibers are connected to clear fiber waveguides that transfer the light from charged particles passing through the scintillating material to visible light photon counters. They convert the light into an electronic signal with an efficiency of 75%, producing up to 65,000 electrons per photon. Only one of the ends of the fiber is connected to a photon counter, the other end is coated with sputtered aluminum reflecting about 90% of photons.
The CFT contributes the most to the overall momentum resolution for tracks with $|\eta| < 1.7$, by itself it has a spatial resolution of 100µm.

5.3.2 *Magnets*

The DØ detector uses two different types of magnets to create a magnetic field inside which charged particles will travel on bent trajectories. Surrounding the tracking detectors, a superconducting solenoid creates a 2T field. Fig. 29 shows a plot of the field strength created by the solenoid. Due to the solenoidal field, charged particles travel on curved trajectories inside the tracking system, allowing for a high resolution in the measurement of momentum and charge of these particles.

An iron toroid surrounds the calorimeter between the first and second layer of the muon system. It consists of a central region with a field strength of 1.8 T and forward regions covering the north and south end of the detector with a magnetic field of 1.9 T. The magnetic field of the toroid allows for a momentum and charge measurement of the muons measured in the muon system, independently of the information from the tracking system.
Fig. 28 shows a perspective view of the DØ detector illustrating the position of the two magnets.

5.3.3 *Preshower System*

The preshower system is located between the tracking system and the calorimeter. It is split up in two regions, the central

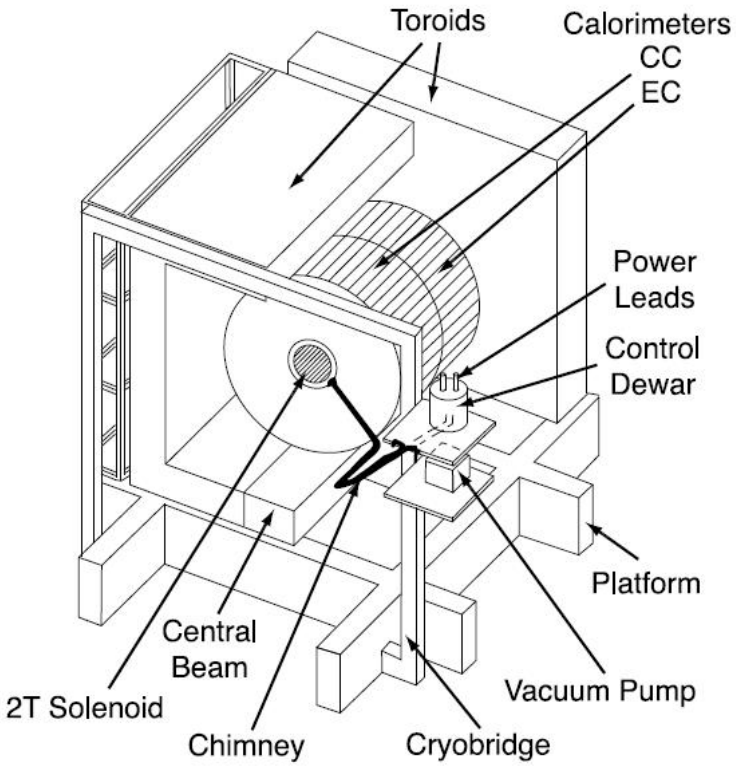

Figure 28: Perspective view of the DØ detector showing the location of the solenoid magnet at the inner core of the detector and the toroid surrounding the calorimeter [48].

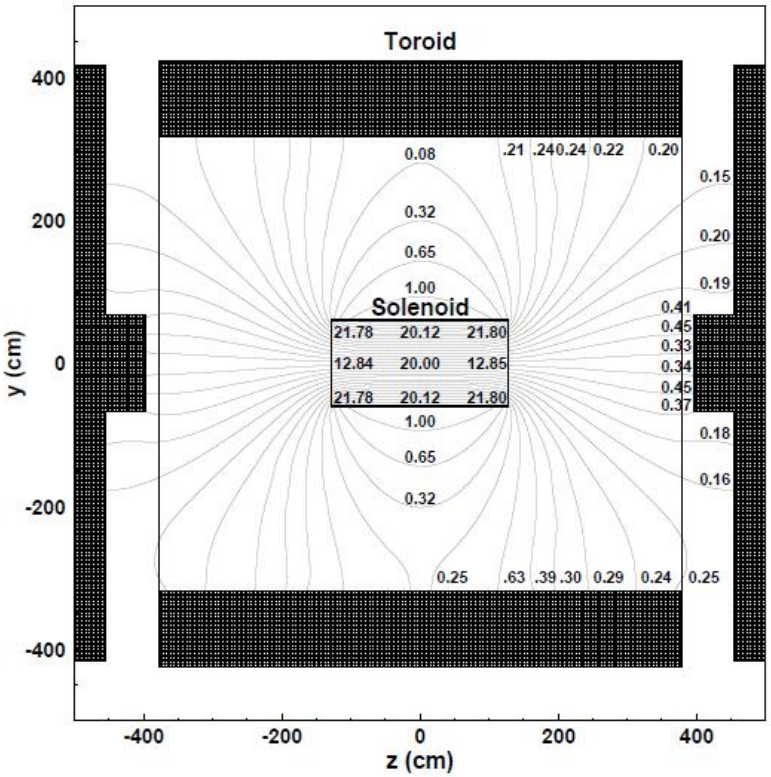

Figure 29: Magnetic field created by the solenoid (measured in kG). The toroid is shown for scale in this plot. The toroid surrounds the calorimeter, field strengths are only shown for the solenoidal magnetic field. The solenoid surrounds the tracking system around the beam pipe [48].

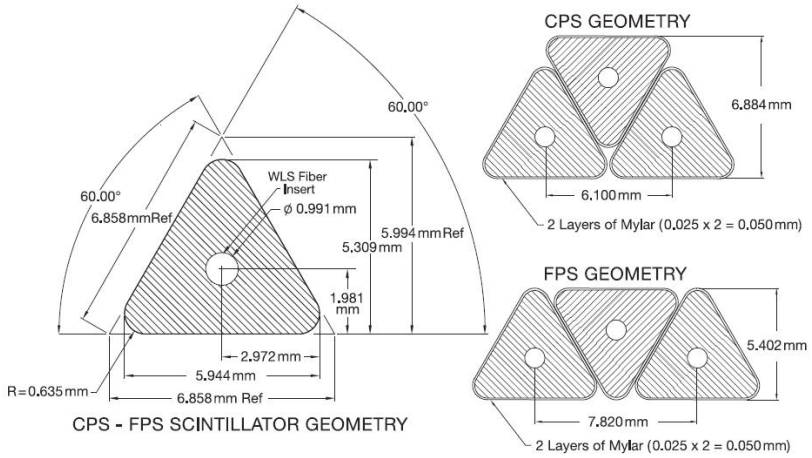

Figure 30: Schematic of the preshower detector elements. Scintillating strips are aligned in wedges. The geometry of a wedge element is shown on the left and the alignment in the central and forward preshower detectors is shown on the right [48].

preshower detector (CPS), located between the solenoid and the central calorimeter, covering a range in pseudorapidity of $|\eta| < 1.3$ and two forward preshower detectors (FPS), located at the surface of the north and south calorimeter end caps, covering $1.5 < |\eta| < 2.5$. The preshower detectors are the binding element between tracking system and calorimeter. Their main purpose is to ameliorate the identification of electrons and to make it easier to reduce background signals for the triggering as well as the reconstruction of physics objects by enhancing spatial matching between tracks in the inner tracking system and showers in the calorimeter. Both, central and forward preshower detectors, are made of triangular shaped scintillators whose working principle is very similar to the scintillators used in the CFT. The CPS consists of three concentric cylindrical layers of strips made of polystyrene plastic, doped with 1% paraterphenyl and 150 parts per million of diphenyl stilbene. Each layer has a total of 1280 strips. The layers are oriented along the z axis and at stereo angles of about $\pm 24°$. The three layers are mounted to a lead radiator that has a length of about one radiation length X_0 [3].
The FPS consists of two times two layers of strips aligned around an absorber (made of lead and stainless steel) with a length corresponding to $2X_0$.
Fig. 30 shows the geometry of the scintillator strips of the CPS and FPS.

3 X_0 is defined as the mean distance inside a certain material over which an electron emits energy by means of bremsstrahlung until only a fraction of $1/e$ of its initial energy remains. This becomes clear from the equation of energy loss for an electron traveling a distance x in matter: $E = E_0 e^{-x/X_0}$.

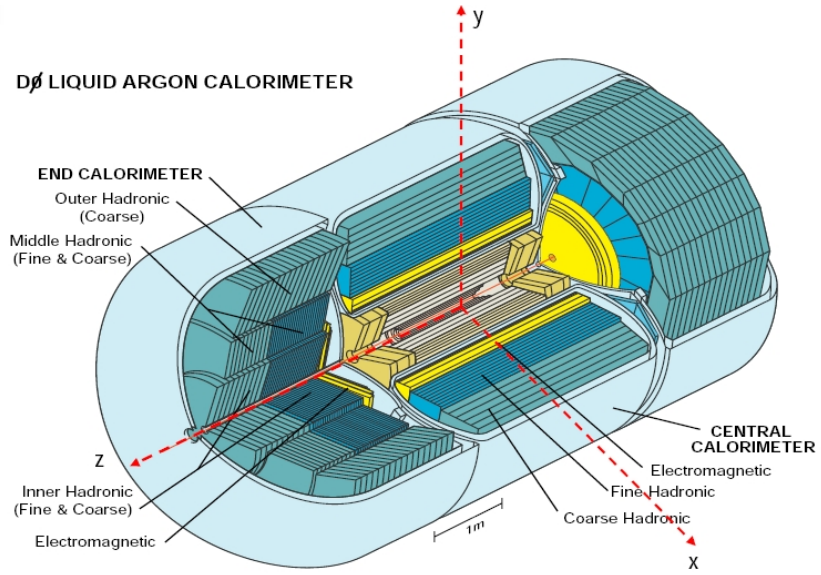

Figure 31: Schematic view of the different layers of the calorimeter. The plot shows the structure of all three segments, the two endcaps and the central calorimeter. The calorimeter encloses the tracking alignments around the beam pipe. Its first shell is the electromagnetic layer, followed by the fine and coarse hadronic layer. It is made of cells that use liquid argon as the central medium and uranium as an absorber [48].

5.3.4 *Calorimeter*

The calorimeter is the largest of the subdetector systems in the DØ detector. It surrounds the tracking system and the preshower system. The purpose of the calorimeter is to detect all electromagnetic objects, foremost electrons, photons and hadronic showers. Using the information from the calorimeter also makes it possible to account for objects that do not interact with matter, such as neutrinos, by reconstructing missing energy in an event by means of conservation of momentum. The calorimeter consists of two main regions, the central calorimeter (CC) covering a region of $|\eta| < 1.1$ and two end cap calorimeters (EC) at the north and south end of the CC covering $1.4 < |\eta| < 4$. The DØ calorimeter is a sampling calorimeter that uses liquid argon (lAr) as the sensitive medium, therefore all three calorimeter parts are located inside their own cryostats keeping the temperature at a constant value of 90 K. Also the pressure inside the liquid argon is constantly monitored and regulated.
Fig. 31 shows a schematic of the calorimeter in which the EC and CC parts can be seen, also displaying the different layers inside the calorimeter modules. Going from the inside to the outside, four electromagnetic layers are followed by three fine hadronic layers and one coarse hadronic layer. All layers have

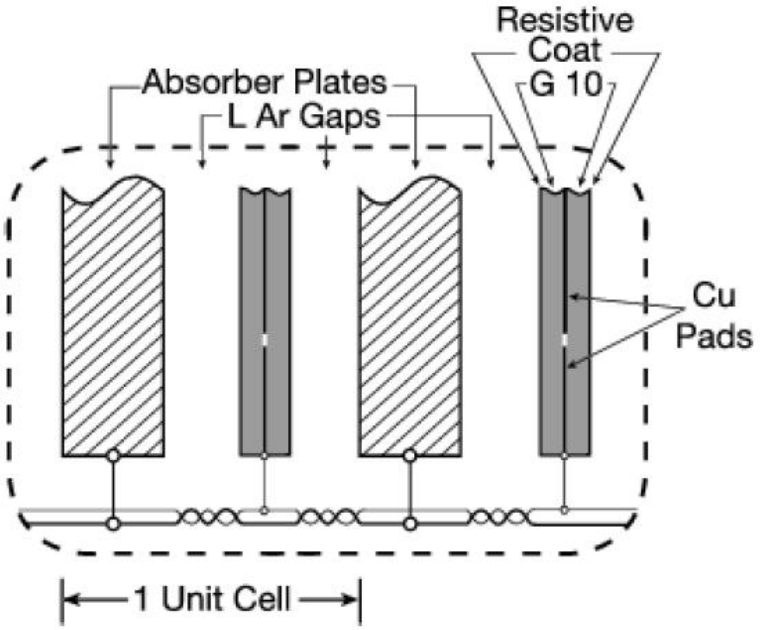

Figure 32: Schematic of a calorimeter cell. In each cell, two uranium absorber plates are used to slow down and stop particles passing through. Copper pads are used to measure the energy deposited in the calorimeter. Liquid argon serves as the transporting medium of the charges created by the ionizing effect of particles affected by the absorbers [48].

a cell structure. Inside a cell, absorber plates are used to cause particles passing through to lose their energy in the calorimeter by showers resulting from interacting with the absorbing material. These absorber plates are made of depleted uranium in the electromagnetic layers with a thickness of 3 mm in the CC and 4 mm in the EC. The hadronic layers use 46.5 mm thick copper plates in the CC and equally thick stainless steel plates in the EC region to increase the effect of slowing down and stopping particles originating from hadronizations. Fig. 32 illustrates the layout of a calorimeter cell. The showers created in the absorber plates produce particles that ionize atoms in the liquid argon filled gap. An electric field of 2 kV between the absorber plate and a signal board at the other end of the cell is used to determine the difference in voltage as a measure of energy deposited in the cell. The mean collection time of the deposited charge is 450 ns and therefore longer than the mean bunch crossing time of 396 ns causing a pile-up of energy inside the calorimeter. This effect is taken into account in the online and offline reconstruction of physics objects.

The cells of the calorimeter are grouped into pseudo-projective towers as Fig. 33 illustrates. The blocks in the drawing represent the longitudinal division of the towers. The towers are called

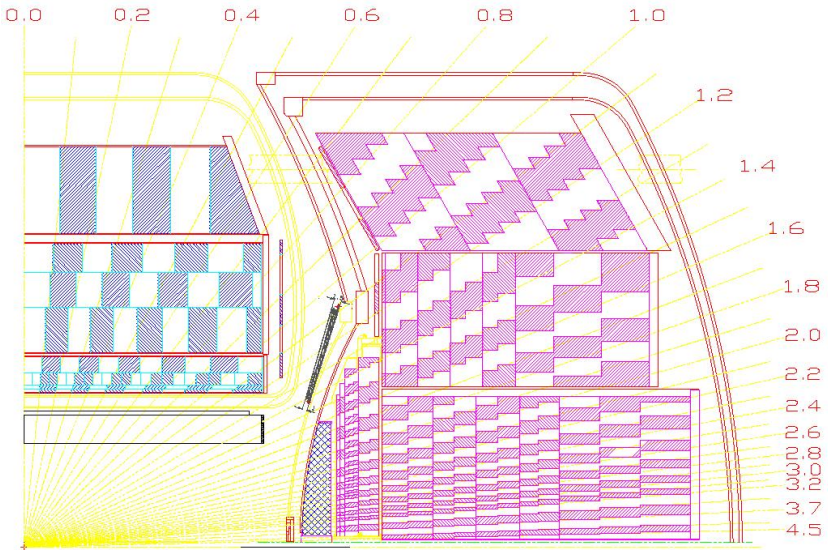

Figure 33: Schematic of a segment of the DØ calorimeter regions showing the transverse and longitudinal segmentation patterns. The shaded regions indicate towers of cells grouped together for signal readout. The rays mark pseudorapidity intervals pointing outwards from the center of the detector [48].

pseudo-projective because the centers of cells lie on rays of constant pseudorapidity projecting from the nominal interaction point to the outside of the detector while the cell boundaries are oriented perpendicular to the absorber plates.

The typical size of electromagnetic showers in the transverse direction is of the order of 1 cm and 10 cm for hadronic showers, therefore the readout cells are of the same size. In $\eta - \phi$ space the size of the towers in both EM and hadronic layers is $\Delta\eta \times \Delta\phi = 0.1 \times 0.1$. To allow for a more precise location of EM shower barycenters, the third EM layer has a segmentation of $\Delta\eta \times \Delta\phi = 0.05 \times 0.05$. Towards higher values of η the cell size increases to avoid very small cells.

The calorimeter has a total of 47,032 physical readout channels that transport their signal coming from the readout cells to the preamplification system mounted at the top of the cryostat. The cables used for the readout signal have a low impedance of 30 Ω which is matched by the preamplifiers to avoid a signal reflection inside the cable. As the position of the preamplifiers makes it very difficult to conduct repairs, they are equipped with a redundant power supply system that can be switched from the primary to the secondary supply from outside the detector in case of a power supply failure. Each power supply provides power for one of 12 preamplifier boxes that each house 96 motherboards on which 48 preamplifiers are mounted per board. The preamplified signal is transfered to baseline subtraction (BLS) cards via twisted pair cables for analogous signal shaping and finally transmitted via

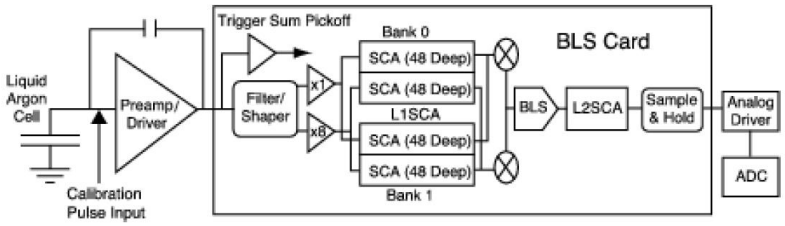

Figure 34: Schematic of the calorimeter readout electronics chain. The signal from the gaps measured in the calorimeter cells is fed into a preamplification system that delivers the signal to the baseline subtraction (BLS) cards. The BLS filters low energetic noise and shapes the signal to enable faster readout times. An analog-to-digital converter (ADC) feeds the signal to the final L3 trigger level [48].

an analog bus system to analog-to-digital converter (ADC) cards which feed the calorimeter signal into the L3 trigger system (see Sec. 5.3.7 for a description of the trigger system). Fig. 34 shows the electronics readout chain for the calorimeter. The BLS cards are, like the preamplifiers, physically located at the inside of the detector, but are more easily accessible for repairs. BLS motherboards are grouped into crates of 12 boards that each contain four daughtercards corresponding to a specific calorimeter tower (corresponding to 48 readout channels). The daughtercards are one of the main sources for the necessity of maintenance accesses of the, in general very smoothly running, DØ detector. In case of a chip failure, the online data reconstruction software will spot readout channels with very high noise levels compared to the average, making it necessary to temporarily exclude a channel from data acquisition. Therefore, at every point in data taking the sanity of the collected data is assured by online monitoring of readouts as well as offline checks before using a certain data taking time for physics analyses.
When the signal passes through the BLS system, low frequency noises and pile-ups are removed from the signal (hence the name baseline subtraction). Pile-up effects are minimized by reducing the collected signal from the gap to the first 260 ns (corresponding to 2/3 of the charge collected by the preamplifier system). The output of a preamplifier is an integral of the measured signal which is characterized by a rise time of ~ 450 ns and a recovery time of 15µs. The shaper in the BLS produces a unipolar signal with a peak around 320 ns and a recovery time of 1.2µs, thereby significantly improving the overall calorimeter response time.

The region between $0.8 < |\eta| < 1.4$ is only poorly covered by the calorimeter. In between the two sections of the calorimeter (CC and EC), there is a zone in the pseudorapidity region of $1.1 < |\eta| < 1.4$ which is not covered by any of the subdetectors

described so far. The inner cryostat detector (ICD) is designed to compensate for the incomplete calorimeter coverage in this η region. The ICD is made of 1.25 cm thick scintillating tiles covering a range of $\Delta\eta \times \Delta\phi = 0.1 \times 0.1$ each and delivering readout to 378 channels. The scintillators use photomultipliers to amplify the signal from ionizing particles inside the scintillating tiles.
Another means of compensating for the not fully covered zone are the so-called massless gap cells. They are essentially an extension of the calorimeter cells and are located inside the central cryostat using its stainless steel wall as the absorber plate. They cover a region of $0.7 < |\eta| < 1.7$. There are also massless gap cells located in the EC modules covering a range of $0.7 < |\eta| < 1.4$.

5.3.5 *Luminosity Monitor*

The DØ detector possesses of two luminosity monitors (LM) located at $z = +140$ cm and $z = -140$ cm as shown in Fig. 35. Each LM consists of 24 plastic scintillation counters built to detect inelastic proton-antiproton collisions. The geometry of the luminosity monitors is shown in Fig. 35, each of the counters extends 15 cm in z direction and covers a pseudorapidity range of $2.7 < |\eta| < 4.4$. Their time of flight resolution is about 0.3 ns allowing to differentiate between particles originating from the nominal interaction point and beam halos. Only particles from inelastic collision events are used to calculate the instantaneous luminosity. To guarantee this, it is first assumed that particles measured in the LM originate from a $p\bar{p}$ event. The z coordinate of the interaction vertex z_{vtx} is estimated from the difference in time of flight: $z_{vtx} = 1/2(t_- - t_+)$ where t_- and t_+ are the time of flight measurements for particles measured in the north and south LM, respectively. By requiring a cut of $z_{vtx} < 100$ cm, only beam-beam collisions are selected. Particles originating from the beam halo traveling along the $\pm z$ axis direction would have $z_{vtx} \approx \mp 140$ cm and are therefore successfully eliminated by the applied cut.
The luminosity is now calculated from the average number of selected events (true inelastic events) per beam crossing $\bar{N}_{LM}$, the beam crossing frequency f and the effective inelastic cross section σ_{LM} taking into account the acceptance and efficiency of the LM detector:

$$\mathcal{L} = f\frac{\bar{N}_{LM}}{\sigma_{LM}} \tag{5.4}$$

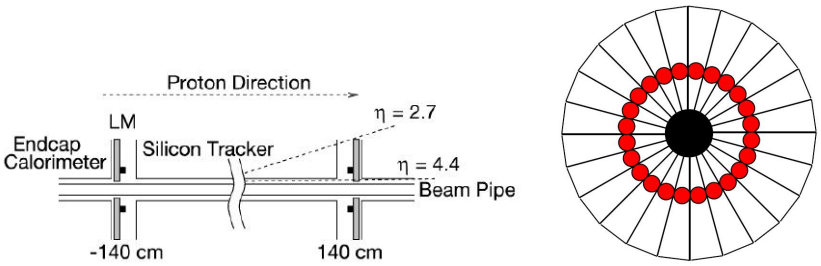

Figure 35: Position (left) and geometry (right) of the luminosity monitor [48].

5.3.6 *Muon System*

Muons are minimal ionizing particles that only deposit a small fraction of their energy in the calorimeter. Therefore, to be able to correctly identify a muon, a muon spectrometer is located outside of the calorimeter. It composes of three layers named A, B and C layers. The muon layer plates are rectangularly surrounding the cylindrical calorimeter. The A layer is located closest to the calorimeter. Between the A and B layers, toroids provide a 1.8 T magnetic field in the central region and a 1.9 T in the forward (north and south) region that offer a way of estimating the muon charge and transverse momentum from the curvature of its tracks which is independent of information from the tracking system. The central part of the muon system covers a range in pseudorapidity of $|\eta| \leqslant 1.0$, the forward muon system located outside of the calorimeter end caps extends the coverage to $|\eta| \leqslant 2.0$.
The central part uses proportional drift tubes (PDTs) and the forward part uses mini drift tubes (MDTs) for the detection of muon tracks. Both are filled with a mixture of gases, the PDTs contain 84% Argon, 8% Methane (CH_4) and 8% Tetrafluoromethane (CF_4), the MDTs contain 90% Tetrafluoromethane and 10% Methane. The MDT tubes are shielded by an iron polyethylene lead cover around the beam pipe in the forward region that reduces the number of muons from beam halo effects.

High voltage wires run through the center of the tubes and collect free charges as a measure of the ionization of a muon passing through the gas. Fig. 36 shows the general principle of a drift tube in measuring the ionization caused by a charged particle. The position of the muon traveling through the muon system can be extrapolated from multiple neighboring tubes and the differences in time of charge collection. Fig. 37 shows a schematic view of two muon layers (a toroidal magnetic field is ignored in the schematic) that show ionization inside the drift tubes (shaded areas), ionization caused by a muon will leave a characteristic trace that can be reconstructed. All three muon layers in the central

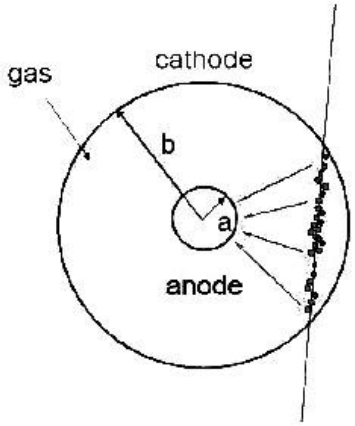

Figure 36: Schematic of a cross sectional view of a drift tube. Ionization of gas atoms inside the tube caused by a charged particle flying through the drift tube is measured as a difference in potential between the outside of the tube and the high voltage wire at the center of the tube [48].

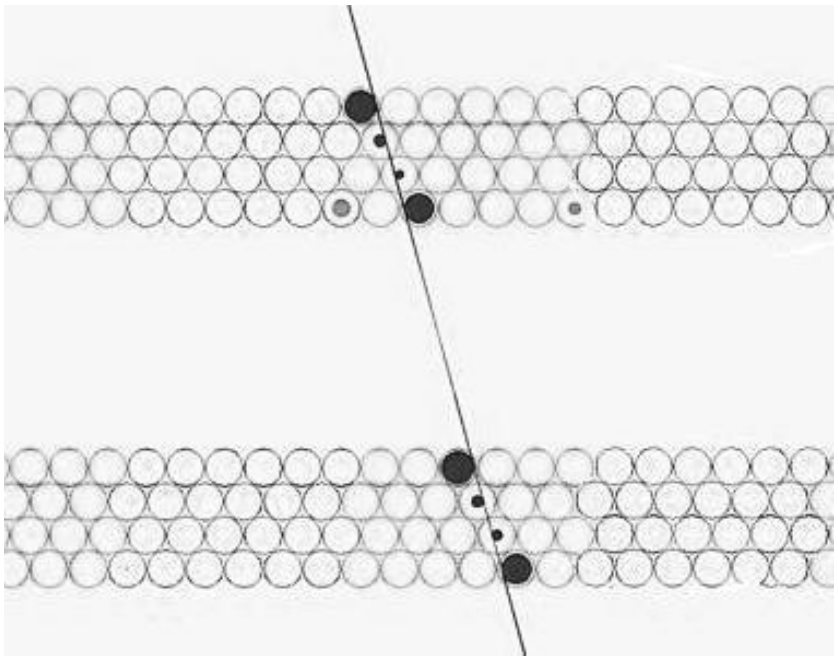

Figure 37: Schematic of two muon layers (without an external magnetic field) each consisting of four layers of drift tubes. Ionization from a muon passing through the detector layers is shown as dark shaded areas inside the tubes. A trace (black line) can then be reconstructed from the coincidence signal of several layers of tubes [48].

and forward region of the muon system consist of three sublayers of drift tubes except for the A layer which has four layers (in the A layer at the bottom of the detector, also only three layers are used due to limited space). The muon system has incomplete coverage at the bottom of the detector due to the presence of support structures in the region $225° < \phi < 310°$. At the inside of the A layers as well as on the surface of the forward layers and the top of the outer muon layers, scintillators are installed. These serve to successfully identify muons and deliver additional information to the triggering system. The scintillators are faster in delivering information whereas the wire tubes are used to precisely determine the position of the muon track. The outer scintillator layers are also used to veto muons from cosmic rays entering the detector.

Fig. 38 shows the alignment and geometry of the muon wire drift tubes and the scintillation detectors.

5.3.7 *Triggers*

The initial rate of data taking inside the DØ detector is 1.7 MHz. This rate is too high to directly record all information to tape due to technical constraints. Therefore, this rate has to be reduced before raw data are being stored for further processing. This requires a sophisticated chain of online processing to bring the continuous data flow down to a final rate of 50 Hz. DØ uses a three-level triggering system taking into account information from all subsystems of the detector to efficiently reduce information to the relevant fraction. A trigger framework delivers information from all subsystems to the different levels of decision making throughout the chain shown in Fig. 39.

- LEVEL 1 (L1) takes into account information from CFT, preshower, calorimeter and muon system. In the calorimeter certain thresholds have to correspond to predefined patterns of energy deposit in the EM and hadronic layers and exceed limits in transverse energy. The central tracking and muon system compare detected tracks for matching information with predefined track patterns and in between the two systems. Also calorimeter tracks are matched with trajectories of charged particles reconstructed by the central track trigger which combines information from the CFT and the preshower detectors. L1 reduces the initial data taking rate from 1.7 MHz to a rate of 2kHz by applying a set of 128 criteria for event selection. It has a buffer size of 4.2μs and is designed to operate at a signal input rate of up to 132 ns.

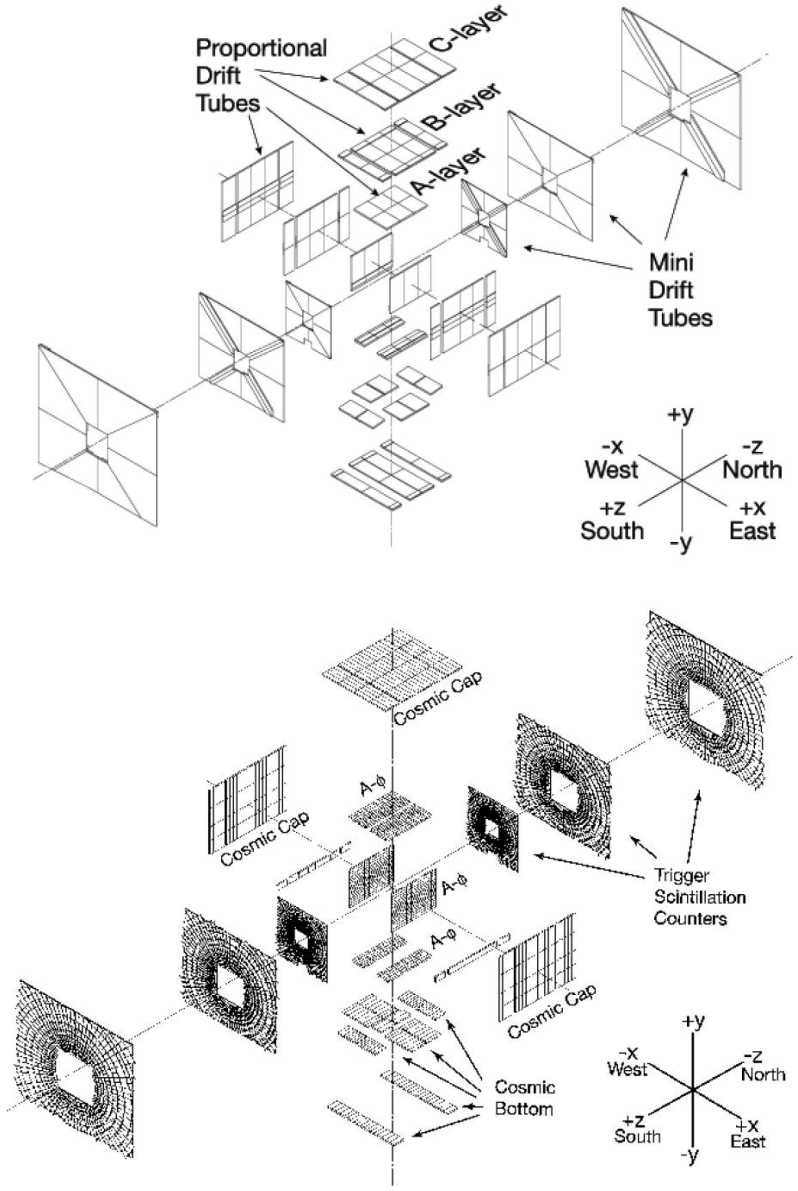

Figure 38: Exploded view of the muon drift tube chambers (*top*) and scintillation detectors (*bottom*) [48].

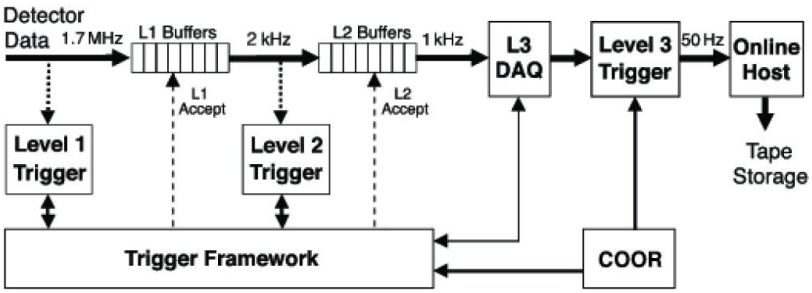

Figure 39: Schematic of the trigger chain from detector data to tape storage. Data have to pass criteria on three levels of triggering reducing the data flow from a rate of 1.7 MHz to 50 Hz going into the storage system [48].

- LEVEL 2 (L2) takes the output of events passing the L1 trigger criteria to apply further scripted selection criteria to reduce the overall data flow rate to 1 kHz. L2 uses basic algorithms for an online reconstruction of physics objects, again taking into account information from all subsystems. Simple physics objects are reconstructed in parallel for each subsystem. Event topologies and correlations between subsystems are then evaluated.

- LEVEL 3 (L3) performs a slightly more sophisticated reconstruction of physics objects from data delivered by the L2 trigger level and the trigger framework. As the computational cost of this step is higher than the preceding trigger levels, L3 calculations are run on a farm of computers. This online reconstruction is similar to the algorithms used for full offline reconstruction described in Sec. 5.4. Correlations between objects are analyzed to fulfill certain requirements in event topology, objects like electrons, muons and missing transverse energy $\not{E}_T$ are reconstructed and variables such as angular separation or invariant mass of objects are calculated for trigger decisions. L3 brings down the rate of data flow to a value of 50 Hz which is subsequently stored on a tape device for further full offline reconstruction and physics analyses.

5.3.8 *Data Quality and Acquisition*

To ensure data quality, the trigger framework incorporates a series of filters of noise suppression at the L3 level. Algorithms that reject dead readout channels or hot calorimeter cells[4] for instance are in place to protect the accumulated collision data. Even before the reconstruction of physics objects from calorimeter

4 Cells that show an unusual high output rate due to a failure in electronics.

data, algorithms reduce the noise level (mostly due to electronics noise) by rejecting energy measured in cells in the calorimeter that have an energy readout below 2.5σ and three-dimensionally isolated cells with a value of less than 4σ (where σ is the RMS of the minimal energy readout threshold of the cell).
During a store, the input rate to the trigger system depends on the luminosity of the $p\bar{p}$ collision which decreases over time. To ensure a constant readout rate at the end of the trigger chain of 50 Hz, prescales are applied to the triggers. Prescales randomly reject 1 out of N events of a certain event type to pass the L1 level. To use the appropriate set of prescales, a store is divided into *runs*, typically lasting two to four hours. Each run uses a set of prescales that corresponds to the current instantaneous luminosity.

5.4 OBJECT RECONSTRUCTION

For a proper reconstruction of the W boson, we need a precise identification of the lepton and the missing energy when the W decays. Also, we need precise reconstruction of jets to be able to identify a Higgs boson decaying into two jets of b quarks. This involves every component of the detector, from the tracker at the innermost shell, over the calorimeter for all sorts of deposited leptonic and hadronic energy, to the muon system as the outermost shell of the detector. So far we have learned about the different detector components and how they work at the hardware level (Sec. 5.3). Now we want to describe how we get from electronic signals in the different subsystems of the DØ detector to reconstructed physics objects that allow precise measurements. We will explain how hits in the silicon detectors are transformed into tracks and energy deposits in the calorimeter cells become electrons or jets of hadronizing quarks and gluons. We will start at the interaction point explaining how tracks are reconstructed (Sec. 5.4.1) that are also the first step to reconstruct vertices (Sec. 5.4.2). Then we will discuss the reconstruction of more complex objects like electrons and muons (Sec. **??**) and finally jets (Sec. 5.4.5). To identify the W in our desired final state topology correctly, we will also need a precise identification of the missing transverse energy $\not\!\!E_T$ (Sec. 5.4.6). Once we are able to reconstruct jets, we also want to identify those jets that originate from a b quark (Sec. 5.6), a crucial point in the WH analysis in terms of background reduction.

5.4.1 *Tracks*

When a charged particle is created by the hard scatter collisions it is at the innermost part of the DØ detector inside the magnetic field of the solenoid. Propagating its way through, it will travel on a bent trajectory. The track of this charged particle is detected in the Central Fiber Tracker (CFT) and the Silicon Microstrip Tracker (SMT) outlined in Sec. 5.3. The SMT is the innermost part of the DØ detector, the CFT follows as the next layer of the detector. Requiring hits in the SMT and CFT detectors, which are essentially energy deposits of ionizing particles, is the first step in constructing track candidates.
The microstrips of the SMT are the first to absorb charge from the traveling particle. A "hit" in the SMT denotes the creation of electron positron pairs inside a strip caused by the particle piercing through. The solenoidal magnetic field can cause these pairs to drift, which has to be compensated for in the reconstruction algorithm. The center of the hit is then reconstructed as the weighted average over all neighboring strips that have detected a

hit by a particle flying through. To reduce noise, a certain energy threshold is required before counting a hit.
In the CFT, a hit describes the emittance of light from two fibers in each layer. To be able to reconstruct the exact position of the hit in x and y, the fibers are shifted so we can use the timing information of two crossing fibers.
A track is then defined as a sequence of hits throughout the tracking system which is associated with a charged particle. To reconstruct tracks we use two different tracking algorithms:

- The Histogram Track Finding Algorithm (HTF).
- The Alternative Algorithm (AA).

Both algorithms use a so-called Kalman filter technique [54].
The HTF algorithm uses a pattern recognition approach that transfers spatial coordinates x and y into coordinates of curvature $\rho = \frac{qB}{p_T}$ (with q the charge of the particle and B the magnetic field strength) and the direction of the track at the distance of closest approach to the beam ϕ. So every point in real space can be identified with a point in (ρ,ϕ) space. This transformation only serves the purpose of filtering out tracks that do not originate from real particles. The advantage of this transformation becomes evident when comparing random hit patterns in the tracking system with hits coming from a particle trajectory as the latter will produce a peak. After filling this information into a two-dimensional histogram (hence the name of the algorithm) it is passed through a filter process that takes the detector geometry and other important information into account to select good track candidates.
Tracks with only a few hits are rejected as well as tracks with very large errors. For tracks that pass the filter, hits are transformed from r-z space to z_0-C space (where z_0 is the part of the track along the beam axis and C is the track inclination defined as C = dz/dr) to include the longitudinal information still missing for the final reconstruction. This algorithm is optimized to efficiently reconstruct tracks of high transverse momentum ($p_T > 20$ GeV) that are well isolated, in the way typically observed for electrons. Details on this algorithm can be found in Ref. [55]

The AA algorithm follows a path of hits through the tracker to reconstruct tracks. This algorithm is designed to be computationally efficient by reconstructing only a minimal number of track candidates. It starts by selecting three hits in either the SMT or the CFT that pass a series of initial criteria with respect to their angular separation curvature and χ^2. The resulting track candidate is extrapolated layer by layer throughout the tracking system. Hits on the way are added to the track if the increase in χ^2 is smaller than 16. If there are no hits that qualify in a certain

layer, the extrapolation moves to the next layer. The algorithm either stops reconstructing the track at the edge of the detector or when it has to skip three or more layers in a row. If several hits match the requirements of the extrapolation, two track candidates are created and further extrapolated. Details on this algorithm can be found in Ref. [56]

The results from running both track reconstruction algorithms are combined compensating for losses in $\frac{dE}{dx}$ and Coulomb scattering effects. A multidimensional minimization of χ^2 of the track candidates is used and optimal parameters for the track are calculated to build the final selection of tracks. The surviving track candidates are then fully reconstructed in three-dimensional real space. The reconstruction and identification efficiency in data is between 97% and 100% for primary vertices reconstructed up to $|z| < 100$ cm, as measured on a $Z \to \mu^+\mu^-$ candidate event sample.

5.4.2 *Vertices*

When the beams of protons and antiprotons collide, several $p\bar{p}$ collisions may occur within a single bunch crossing. We are interested in processes coming from hard scattering interactions only. There is, however, a large number of elastic and inelastic scattering processes in each bunch crossing which makes it important to correctly identify the exact spatial origin of the physics objects we are interested in, called the primary vertex. Measuring the direction of a physics objects and correctly reconstructing $\not\!\!E_T$ as well as b tagging are all things that rely on the accuracy of the proper reconstruction of the primary vertex. We use a reconstruction algorithm called *adaptive primary vertex algorithm* [57] that rejects tracks from minimum bias interactions and tracks from secondary vertices coming from heavy flavor quark decays and leave us with a final selection of primary vertices.
The algorithm selects all tracks with two or more hits in the SMT if they have a transverse momentum $p_T > 0.5$ GeV. The tracks are then projected along the z axis and grouped in regions of $\Delta z < 2$ cm and are then fitted to a common vertex. This initial selection is the input to a Kalman filter that removes tracks that contribute the most to the χ^2 of the vertex fit until χ^2/NDF[5] drops below 10. The algorithm then orders the tracks by their dca[6] and only tracks with $\frac{\text{dca}}{\sigma(\text{dca})} < 5$ are kept[7]. The remaining tracks are used to determine the final location of the vertex candidates.

5 NDF = number of degrees of freedom
6 dca = distance of closest approach, in this case between the track and the beam position in the transverse plane
7 where σ is the standard deviation

Tracks from minimum bias events typically have significantly lower transverse momenta p_T.

$$P(p_T) = \frac{\int_{\log_{10}(p_T)}^{\infty} F(p_T)dp_T}{\int_{\log_{10}(0.5)}^{\infty} F(p_T)dp_T} \tag{5.5}$$

is the probability that the observed p_T of a certain track is compatible with originating from a minimum bias interaction [58]. $F(p_T)$ denotes a minimum bias track $\log_{10}(p_T)$ spectrum distribution obtained from simulation.
It is therefore possible to assign a probability to all of the vertex candidates to originate from a minimum bias interaction (i.e. not a hard scatter event):

$$PMB = \Pi \sum_{k=0}^{N-1} \frac{-\ln \Pi}{k!} \tag{5.6}$$

where Π is the product of individual probabilities for each of the $N > 0$ tracks with $p_T > 0.5$ GeV associated to the vertex. The vertex with the lowest probability of being a minimum bias event is then selected as the primary vertex of the collision event. The PMB distribution for minimum bias vertices and for selected primary vertices on a small test sample of simulated events are shown in Fig. 40.

5.4.3 *Electron reconstruction and identification*

Electrons are calorimetric objects and deposit all their energy in the electromagnetic (EM) section of the calorimeter. Since the calorimeter consists of two separate areas, the central calorimeter (CC) and the endcap calorimeter (EC) regions, we analyze data separately in the detector pseudo-rapidity range of $|\eta_{detector}| < 1.1$ (CC electron sample) and $1.5 < |\eta_{detector}| < 2.5$ (EC electron sample). We exclude the gap situated between the CC and the EC regions in the pseudo-rapidity range of $1.1 < |\eta_{detector}| < 1.5$. To ensure a proper electron identification we use several criteria. In the following, we list quantities used to determine the quality of an electron:

- EM FRACTION The fraction of energy in the EM calorimeter compared to the total energy in the calorimeter (EM + hadronic part): $f_{EM} = \frac{E_{EM}(0.2)}{E_{tot}(0.4)}$, where $E_{tot}(0.4)$ and $E_{EM}(0.2)$ are the energies inside a cone size of $\Delta R < 0.4$ in the whole calorimeter and $\Delta R < 0.2$ in the EM calorimeter, respectively.

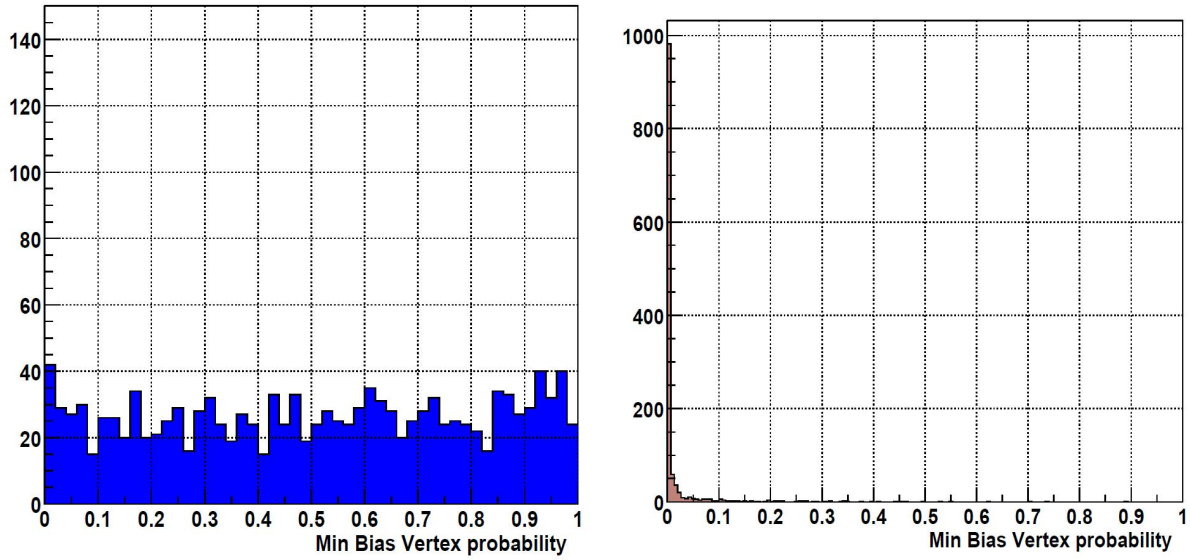

(a) Vertex probability distribution in minimum bias vertices. (b) Vertex probability distribution for primary vertices.

Figure 40: Probability distributions for a vertex to belong to a minimum bias event, measured on a subset of simulated events, for minimum bias vertices (left) and the final selection of primary vertices (right). While minimum bias vertices all show an equal distribution in probability, the final selection of primary vertices shows a very narrow peak around 0 and almost no probability to originate from a minimum bias event.

- ISOLATION FRACTION The fraction of isolated energy deposited in the hadronic calorimeter compared to the energy deposited in the EM calorimeter should be small to indicate that the object in question is of EM and not hadronic nature $f_{iso} = \frac{E_{tot}(0.4)-E_{EM}(0.2)}{E_{EM}(0.2)}$.

- H MATRIX A matrix calculated as the inverse of the covariance matrix of seven EM shower shape variables: The shower energy fraction in each of the first, second, third and fourth EM layers of the calorimeter; the cluster size in $r-\phi$ based on the third EM layer of the calorimeter; the total shower energy; the primary vertex position. To put requirements on this variable, it can be reduced to a one-dimensional χ^2 probability variable: $\chi^2_{HM} = \sum_{ij}(x_i^k - \langle x_i\rangle)H_{ij}(x_j^k - \langle x_j\rangle)$, where x_i is the ith variable and H is the matrix described above.

- ELECTRON LIKELIHOOD This parameter is calculated based on seven variables: the spatial track match χ^2 probability, the ratio of transverse energy over transverse momentum E_T/p_T, the H matrix, the EM Fraction, the distance of closest approach to the primary vertex, the number of tracks in a $\Delta R < 0.05$ cone, the total p_T of tracks in a $\Delta R < 0.4$ cone around the candidate track.

- TRACK ISOLATION This value denotes the total track p_T (for tracks with $p_T^{track} > 0.5$ GeV) in the hollow cone $0.05 < R < 0.4$ around the EM cluster.

Electrons used in the analysis are required to pass the following requirements on the above defined variables:

If the electron deposits its energy in the CC region of the DØ calorimeter it has to pass these requirements:

- $f_{EM} > 0.97$
- $f_{iso} < 0.07$,
- track isolation < 2.5 GeV
- $\chi^2_{HM} < 25$,
- electron likelihood > 0.2

If it is measured in the EC region of the calorimeter, the following requirements are applied:

- $f_{EM} > 0.9$
- $f_{iso} < 0.15$

- $\chi^2_{HM} < 50$,
- electron likelihood > 0.85.

For the estimation of the multijet background (Sec. 6.6.1), we use two electron definitions, the above mentioned requirements define the "tight" selection sample. If the requirement on the electron likelihood is not required, we call the electron selection "loose".

We want to minimize backgrounds containing more than one isolated lepton, as for example final states originating from a Z boson decay or $t\bar{t}$ events. Therefore, we require the event to not contain a second isolated electron with a transverse momentum $p_T > 15$ GeV inside a range of $|\eta| < 2.5$ that passes the loose electron selection criteria.

The efficiency of correctly identifying an electron in data is 75% (60%) for an electron in the CC (EC) region and 85% (70%) in simulation. We apply a correction to simulated events to account for the difference in efficiency between data and simulation. The applied correction is derived as a function of the p_T and η_{det} of the electron and applied on an event by event basis.

5.4.4 *Muon reconstruction and identification*

We reconstruct muons using information from two independent systems, the central tracker and the muon spectrometer. The muon identification is based on reconstructing a track in the muon system which is called a "local muon track". For an object to be identified as a muon, hits in all layers of the muon system inside and outside the toroid are required. To further reject cosmic muons, we apply a timing veto. The superior spatial resolution of the central tracker is used to improve the accuracy of kinematic properties of the muon and to confirm that the muon originates from the primary vertex by using a central track. A special tracking algorithm is used to match the muon and the central track. The basic criteria to identify an object as a muon are:

- Matching muon segments from A and BC layers, as well as a matching central track. This requirement rejects about 10 % of high transverse momentum muons, mainly in the bottom region of the detector where no full muon coverage in the A and BC layers is available.
- Timing veto against muons from cosmic rays: Information from the muon scintillator layers is used together with a

requirement on the travel time in all layers of the muon system for a muon to originate from a real collision event.

In addition, a central track match is required, which asks for $\chi^2/\mathrm{NDF} < 4$ for the central track fit to remove bad tracks.

Muons coming from the leptonic decay of W bosons tend to be isolated from jets and they have a relatively high transverse momentum in comparison to muons originating from semi leptonic decays of heavy flavor hadrons. Such background muons have a lower p_T spectrum and are typically not isolated due to the fragmentation of jets in the partial hadronic decay. Therefore, a first muon isolation criterion can be defined by the spatial separation between a muon and jets in the geometrical plane spanned by the pseudorapidity η and the azimuthal angle φ. The distance between two objects in this plane is defined by the standard ΔR definition. We require the distance between a muon and the nearest jet (with $p_T > 15$ GeV) to be $\Delta R(\mu, \mathrm{Jet}) > 0.5$. Muons passing this selection form the "loose" muon selection sample.

To narrow down our final muon selection to the "tight" selection, the two variables HALO and TRKCONE are introduced as follows:

- HALO(0.1, 0.4) is the scalar sum of transverse calorimeter energy clusters in a hollow cone around the muon between $\Delta R_\mu = 0.1$ and $\Delta R_\mu = 0.4$. Only electromagnetic and fine hadronic calorimeter cells are taken into account in the calculation of this variable, since there is significantly more noise in the coarse hadronic calorimeter.

- TrkCone(0.5) is the scalar sum of the transverse momenta of all tracks within a cone of radius $\Delta R_\mu = 0.5$ around the muon. The track matched to the muon has been excluded from this sum.

We require "tight" muons to pass the following requirements:

- $\mathrm{Halo}(0.1, 0.4) < 2.5$ GeV
- $\mathrm{TrkCone}(0.5) < 2.5$ GeV

Analogously to the electron case, we require the event not to contain additional isolated muons, i.e. being isolated inside a cone of $\Delta R < 0.5$ with a transverse momentum of $p_T > 15$ GeV.

The muon identification efficiency in data (measured on the RunIIa+RunIIb dataset) is 72.2 % [59], its distribution in the (η,ϕ) plane is shown in Fig. 41. The identification efficiency in simulated events is about 3 % higher. We apply efficiency scale factors in the same way as in the case of the electron efficiency scale factors, to compensate for this difference.

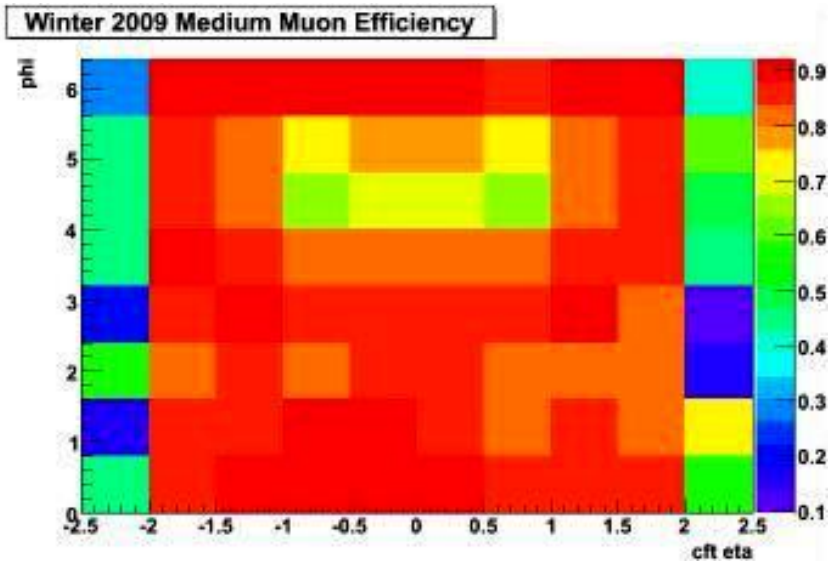

Figure 41: The muon efficiency mainly depends on the angular coverage of the muon system. At the bottom, where there is only poor muon coverage, at coordinates of (η,ϕ) = (-1.0–1.0,4.0–5.5) we see the typical "muon hole" of the DØ detector [59].

5.4.4.1 *Trigger Requirements*

In the *electron* channel, we use the logical OR of two different trigger suites[8], the single EM trigger suite and the EM+JET trigger suite. Single EM triggers "fire" when the recorded event contains an electromagnetic (EM) object that passes all three trigger levels (described in Sec. 5.3). EM+JET triggers are sensitive to events that contain an EM object also including an unspecified number of jets (as described in Sec. 5.4.5. The logical OR denotes that if either of the trigger suites selects the event, it is taken into account for the dataset we are analyzing.
In the muon channel, the logical OR of single muon triggers yields an overall trigger efficiency of only 70% (see Sec. 6.4.1 on how trigger efficiencies are measured). Therefore, we use the muon inclusive trigger (which is equivalent to using a combination of all triggers, thereby not rejecting any events based on trigger information). In Sec. 6.4.1 we explain how triggers are modeled in MC events.

5.4.5 *Jets*

Quarks and gluons are particles that cannot exist freely due to QCD confinement (cf. Chapter 1). We can, however, still observe them in processes originating from high energy collisions in which pairs of quarks and gluons are created. When two quarks separate from each other with high enough energy, new quark

8 Specific trigger terms adapted to different data taking and luminosity periods.

pairs are created from the vacuum. Together, they form hadrons of which some of them decay further. This process is called hadronization and leads to fragmentation when the (in general instable) hadrons decay. This is the creation of what we call *jets*. Jets are calorimetric objects and deposit all their energy in the calorimeter. To ensure that the jets we reconstruct for analyses come from the initial $p\bar{p}$ collision, we require jets to have tracks associated with them. The reconstruction takes place in the following steps:

1. Clusters are built from calorimeter towers with an energy deposit above a certain threshold.
2. Proto-jets are constructed from the clusters.
3. The final jet selection is corrected for double counting.

A good jet reconstruction algorithm allows for the reconstruction of the initial kinematics of the quark or gluon forming that jet and must fulfill a number of requirements. The algorithm has to be relatively infrared and collinear safe. *Infrared safety* means that the algorithm is insensitive to additional soft radiation deposited in the calorimeter. Fig. 42a illustrates this fact.

Collinear safety means that if a hadronic decay deposits energy into several calorimeter towers instead of just one, the jet reconstruction algorithm still has to be able to recognize this energy as belonging to one object inside the calorimeter, even if a single tower does not exceed the minimal energy threshold of the algorithm. Fig. 42b illustrates this on an example that shows that the algorithm must be capable of finding the right jets independent of their ordering in jet p_T.

The DØ algorithm used for the reconstruction of jets is called *RunII Cone Algorithm*. As the name indicates, this algorithm uses cones of energy in the calorimeter to reconstruct jets. As a first step, it selects seeds of energy for potential jet candidates from calorimeter clusters. To build a cluster, an algorithm called *Simple Cone* finds towers with a minimal transverse energy $E_T > 0.5$ GeV. Calorimeter towers within a cone of $\Delta R = 0.3$ and $E_T > 1$ GeV are added to the cluster. In the next step, so-called *proto-jets* are built from the clusters. All clusters within a cone radius of $\Delta R < 0.5$ are grouped into a proto-jet. The algorithm then checks whether neighboring proto-jets could originate from the same hadronization process. If the spatial separation is large enough, both proto-jets are kept as jets, otherwise they are merged into one jet. In the last step, the algorithm loops over all jets to sort out misidentified jets. Those jets with $E_T < 6$ GeV are immediately rejected. Jet candidates then have to pass an additional series of requirements assuring that they originate from hard scattering processes and the following hadronization of quarks or gluons.

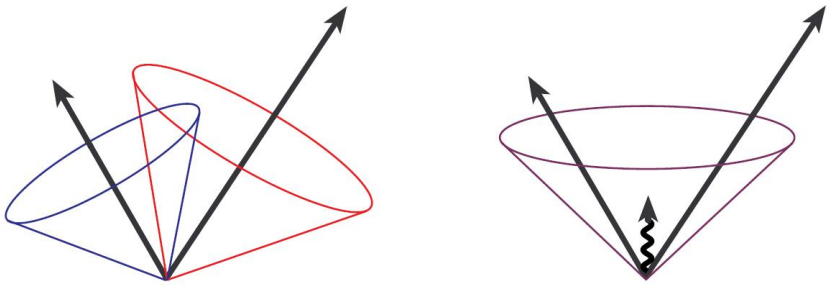

(a) Illustration of infrared sensitivity in cone jet clustering. In this example, jet clustering begins around seed particles, shown here as arrows with length proportional to energy. The presence of soft radiation between two jets may cause a merging of the jets that would not occur in the absence of the soft radiation. The algorithm must be able to identify the soft radiation successfully and separate it from the jet reconstruction.

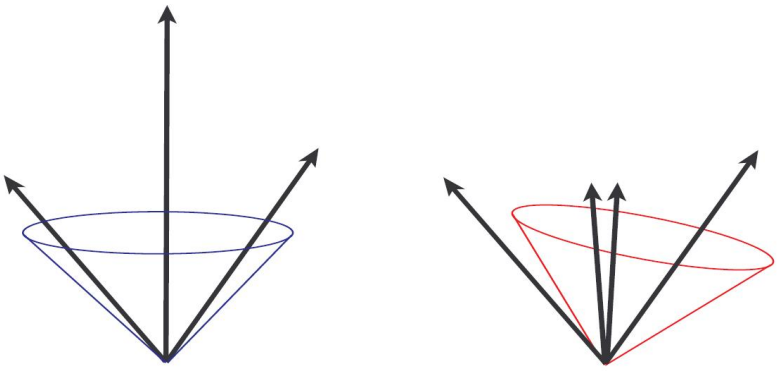

(b) Illustration of collinear safety in algorithms that would be dependent on the ordering in transverse energy E_T of the partons that form a jet. The difference between the two situations is that the central (hardest) parton splits into two almost collinear partons. The separation between the two most distant partons is more than ΔR but less than $2\Delta R$. Thus all of the partons can fall within a single cone of radius ΔR around the central parton(s). However, if the partons are treated as seeds and analyzed with an algorithm not sensitive to E_T ordering of the partons, different jets will be identified in the two situations. On the left, where the single central parton has the largest E_T, a single jet containing all three partons will be found. In the situation on the right, the splitting of the central parton leaves the right-most parton with the largest E_T. Hence this seed is looked at first and a jet may be found containing only the right-most and two central partons. The left-most parton is a jet by itself. In this case the jet number changes depending on the presence or absence of a collinear splitting. This signals an incomplete cancellation of the divergences in the real and virtual contributions to this configuration and renders the algorithm collinear unsafe. This problem should be avoided by making the selection or ordering of seeds and jet cones independent of the E_T of individual particles.

Figure 42: An algorithm for jet reconstruction must fulfill definite requirements to correctly identify a jet. These figures illustrate the criteria of being infrared and collinear safe [60].

The final selection of jets is then kept as *good* jets and can be used in physics analyses. Whenever the term *jets* is used in the following, it refers to such a good jet passing the reconstruction. Sec. 5.5.3 describes necessary corrections to the jet energy scale due to numerous effects.

5.4.6 *Missing Transverse Energy*

The missing transverse energy $\not{E}_T$ can be reconstructed from the net momentum in the x-y plane. The sum of all momenta in the transverse plane at the time at which the collision happens is zero. In the z direction, however, the momentum is unknown, but generally different from zero. This comes from the fact that the partons in the initial state carry different fractions of the proton and antiproton momentum. We could calculate $\not{E}_T$ as the negative sum of vectors of transverse momenta p_T of all particles observed in the detector for a certain collision:

$$\not{E}_T = -\sum_{\text{all cells}} \vec{p_T} \tag{5.7}$$

This equation is based on simple conservation of momentum in the transverse plane, which is exact for the momentum of a neutrino as a massless relativistic particle. If there were other massive particles included in the sum, this equation would only be accurate at high energies at which these particles would become relativistic. In physics analyses, the requirements on the $\not{E}_T$, however, assure that the equation remains a valid approximation even in the case of massive particles contributing to the sum.
What we do in practice to calculate $\not{E}_T$ from detector measurements is to sum up the transverse energy of all calorimeter cells in the electromagnetic (EM) and fine hadronic (FH) part of the calorimeter. We exclude cells from the coarse hadronic (CH) part due to their high noise level. $\not{E}_T$ can only be calculated after the reconstruction of all other physics objects in the event including their proper energy scale correction. The major contribution in terms of energy scale correction comes into play at the reconstruction of jets which also deals with muons inside of jets. The $\not{E}_T$ calculation is also corrected for energy deposits from isolated muons inside the calorimeter. Other calorimetric objects (namely electrons and photons) are included into the calculation of $\not{E}_T$ if their p_T is above a threshold of 5 GeV inside the region of $|\eta| < 2.5$. To sum up this procedure in an equation, we build the sum over all calorimeter cells and then replace those parts of the sum with physics objects that we actually detect in the detector:

$$\not{E}_{x,y} = \sum_{\text{all cells}} E_{x,y} + \sum_{\text{phys obj}} E_{x,y}^{\text{phys obj}} - \sum_{\text{phys cells}} E_{x,y}^{\text{phys cells}}. \tag{5.8}$$

We then calculate the transverse component of the energy that we get out of the above calculation:

$$\not{E}_T = \sqrt{(\not{E}_x)^2 + (\not{E}_y)^2} \tag{5.9}$$

5.5 CORRECTIONS

5.5.1 *Lepton Identification*

The lepton reconstruction efficiency in simulation is higher than in data. This is mostly due to inefficiencies in the tracking system and this effect becomes stronger with tighter lepton identification criteria. To compensate for this discrepancy between data and simulation, we derive the correction factors to reweight our simulated events making them match the data efficiencies. We derive different factors for each lepton type as functions of transverse momentum p_T, η or ϕ of the lepton.

5.5.2 *Lepton Resolution*

Also the lepton energy resolution in simulated events is not the same as in data. It is mostly due to imperfections in the detector that cannot be perfectly simulated, like dead readout channels. We apply a smearing to the energy resolution of simulated events to make the width of the Z boson mass match between data and simulation.

5.5.3 *Jet Energy Scale Correction*

The jets that the RunII Cone Algorithm reconstructs from the energy deposited in the calorimeter does not match the energy of the particles corresponding to these jets. This is due to a series of effects that we have not taken into account during the reconstruction, yet. The calorimeter response to electromagnetic and hadronic particles depositing their energy in the calorimeter cells is being corrected in the following form:

$$E_{\text{jet}} = \frac{E_{\text{jet}}^{\text{measured}} - O}{F_\eta \cdot \mathcal{R} \cdot S}. \tag{5.10}$$

E_{jet} is the energy we finally strive to obtain for physics analyses, whereas $E_{\text{jet}}^{\text{measured}}$ is the energy measured in the calorimeter and

reconstructed as described in Sec. 5.4.5. In the following we explain the applied corrections:

- O is the offset energy that has to be subtracted. Contributions to the offset come from all processes that are not due to the hard scattering interaction in question. It can be additional minimum bias events, additional $p\bar{p}$ interactions, pile up from previous collisions, or processes in the uranium in the calorimeter cells. The offset is measured in minimum bias interactions where the energy of the calorimeter towers within a jet cone radius of $\Delta R < 0.5$ is summed up.
- F_η is the η-dependent correction for differences in calorimeter response. It is measured in photon+jets processes in which the photon and the jet are aligned back-to-back.
- $\mathcal{R}$ is an additional correction of the absolute energy response of the calorimeter. It is measured in the same way as F_η, but after that correction has already been applied. It therefore corrects for losses of energy in regions without calorimeter coverage and for differences in response of the calorimeter between hadrons and electrons or photons.
- S is the correction of the shower shape of the jet. It corrects for parts of the jet shower that are not included in the jet cone and for energies that are accidentally included in the jet. This correction is determined from simulated events.

5.5.4 *Vertex Confirmation*

A criterion to reduce electronic noise or pile-up effects in the jet sample is called vertex confirmation. It is only applied to jets from higher luminosity samples (namely, the RunIIb sample). For a jet to be vertex confirmed, it has to be matched to at least two tracks with

- transverse momentum $p_T > 0.5 GeV$
- dca < 0.5 mm in the transverse plane
- dca < 1.0 mm on the z axis
- a distance in z of < 2 cm.

This ensures for the jet to originate from the primary vertex (in the sense that it was created in the $p\bar{p}$ collision event).

5.6 TAGGING OF B QUARK JETS

For a Higgs with low mass < 135 GeV, the decay into two jets of b quarks (short: b jets) is the dominant decay channel (cf. Chapter 1). Therefore, a correct identification of b jets is a crucial step to gain sensitivity in any low mass Higgs analysis. The jets identified so far give no indication of their flavor or whether they origin from quarks at all. Most of the jets that are being successfully identified as jets come indeed from a V + light jets process (where V stands for a vector boson, W or Z). To vastly reduce this major background of low Higgs mass analyses, we try to identify jets originating specifically from a b quark, a procedure called b tagging.

Pairs of b quarks are produced in hard scattering events in the $p\bar{p}$ collisions. When the two b quarks separate, they will hadronize due to their QCD confinement. A b quark cannot survive by itself and will preferably directly form a B meson. This B meson then travels a certain distance of $\mathcal{O}(1)$ mm before it decays. This decay length corresponds to its average lifetime of $\mathcal{O}(10^{-12})$ s [61] and is much longer than for hadrons formed by light quarks or gluons. The signature of such an event differs from other events not containing b quarks. In the case of b quarks present, jets from the quark hadronization will contain a secondary vertex from the decay of the B meson (see Fig. 43 for an illustration. The secondary vertex is usually displaced by $\mathcal{O}(1)$ mm corresponding to the B meson decay length.

5.6.1 *Taggability*

Before going into the details of tagging b jets, we require jets to fulfill a more general criterion called taggability which requires the identification of the primary vertex corresponding to the jet as well as at least one track jet associated with the (calorimeter) jet. Track jets are essentially jets based on tracking information instead of calorimeter information. To reconstruct track jets, the *Simple Cone* algorithm for the identification of calorimeter towers in the jet reconstruction (cf. Sec. 5.4.5) is applied. In this case, it starts from tracks with a minimal transverse momentum $p_T > 1$ GeV and requires a cone size of $\Delta R < 0.5$ for the track jet candidates. They further have to fulfill the following criteria:

- At least one hit in the SMT system.
- dca (track, primary vertex) < 1.5 mm in the transverse plane.
- dca (track, primary vertex) < 4.0 mm along the z axis.

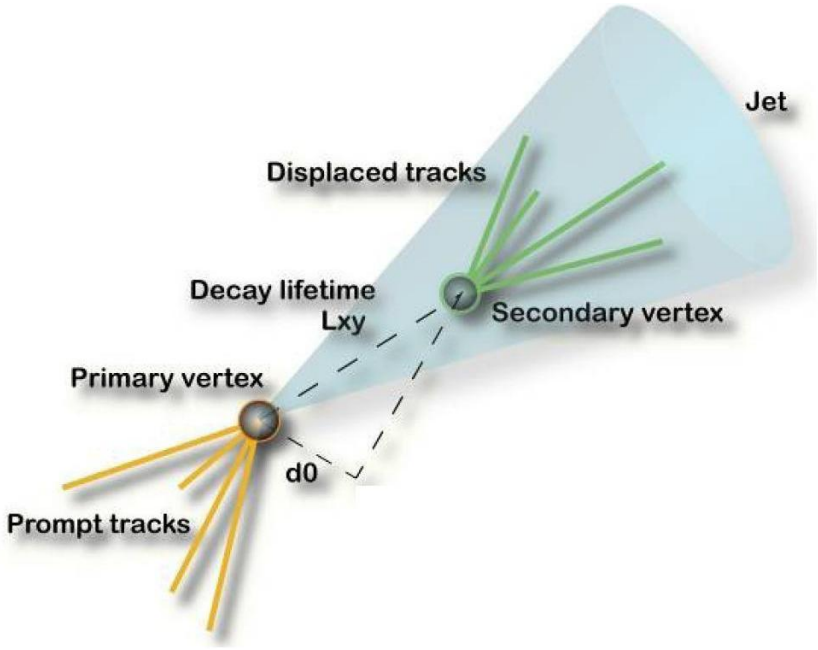

Figure 43: One of the criteria in tagging jets originating from a b quark is to identify a secondary vertex. A b quark will form a B meson that then travels $\mathcal{O}(1)$ mm before it decays. Therefore, jets originating from b quarks will contain a secondary displaced vertex.

These requirements serve to reject long lived[9] particles like kaons. After the track jets have been reconstructed, the calorimeter jets (hadronic jets) are matched to the track jets. Tracks count as matched when they are within a maximal cone radius of $\Delta R < 0.5$ of each other.

5.6.2 *b Tagging*

Now for the actual b tagging of the calorimeter jets, there are four types of objects that play an important role in the b tagging process:

- Tracks formed from charged particles in the CFT or SMT that do not origin from the primary vertex
- A secondary vertex reconstructed from these tracks
- Hadronic jets reconstructed from calorimetric energy
- Identification of a muon inside a jet (as $> 20\%$ of b jets decay semi-muonically)

On the algorithm level, we use four independent approaches of identifying b jets:

9 compared to b quarks

- The Counting Signed Impact Parameters (CSIP) algorithm. This algorithm counts the number of tracks associated with a jet that do not origin from the primary vertex. A track is associated with a jet if $\Delta R(\text{Track}, \text{Jet}) < 0.5$
- The Jet LIfetime Probability tagger (JLIP) algorithm. It combines all information regarding the impact parameters of all tracks associated with the jet to calculate the probability that a jet originates from the primary vertex.
- The Secondary Vertex Tagger (SVT) algorithm. It reconstructs secondary vertices from tracks of charged particles. The criterion for associating a secondary vertex with a jet is $\Delta R(\text{Secondary Vertex}, \text{Jet}) < 0.5$
- The Soft Lepton Tagger algorithm. It tags a jet if it contains a muon.

Although each of these algorithms is capable of tagging b jets by itself, we can get even better tagging results: We combine the output of the algorithms together with other variables (seven in total) capable of identifying b jets inside a Neural Network (NN) b tagging algorithm [62]. This is only possible as the tagging output of the other algorithms is not a hundred percent correlated.

5.6.2.1 *Neural Network Algorithms*

A Neural Network (NN) is a so-called *multivariate technique* used to statistically add the information from many input variables into one output variable. It is used to classify information along the output distribution, for example to separate signal from background in a particle search. In case of the b tagging, the NN is trained to separate W+ *light jets*-like events from W+$b\bar{b}$-like events. A NN output typically is a continuous distribution from 0 to 1 where background-like events (light jets in this case) are shifted towards 0 and signal like events (b quark jets) are shifted towards 1. The way the NN works is that it collects the uncorrelated information between its input variables and combines their separation power. It generally consists of three layers:

1. An input layer containing all variables fed to the NN.
2. One or several hidden layer(s) in which information from the input variables is connected via so-called neurons, nodes that link together the input from certain variables. The number of nodes and links can vary.
3. An output layer in which all links from the hidden layer(s) are brought together in a single neuron

The input x_j to a node in the hidden layer is the linear combination of weighted inputs $w_{ij}y_i$ in the input layer, where w_{ij} is the weight with which the input node is linked to the hidden node and y_i is the input from the variable fed into the NN. The input to a node also takes into account a bias w_{0j} representing the signal strength between the input layer and the hidden layer for this particular node.

$$x_j = w_{0j} + \sum_i w_{ij}y_i. \tag{5.11}$$

This equation holds true for every hidden layer as well as the output layer by replacing the input layer with the preceding layer of the NN. The output of a certain node differs from whether it is in a hidden layer or in the output layer. In a hidden layer, the output o_j of a given node j is a sigmoidal function of its input x_j:

$$o_j = \frac{1}{1 + e^{-x_j}}. \tag{5.12}$$

In the output layer, the final output o_j simply represents the linear combination of its weighted inputs as described in Eq. 5.11:

$$o_j = x_j \tag{5.13}$$

Using at least one hidden layer yields in the fact that the NN output is a continuous function that (if properly normalized) can represent a probability of having a signal between 0 and 1 given a certain known input [63, 64]. Fig. 44 shows a schematic of a neural network.

5.6.2.2 *The b Tagging Neural Network*

In the previous section we have learned about the general concept of a neural network. Now we will get back to the b tagging neural network. Two crucial steps have still to be made to obtain the NN output. The choice of input variables and the training of the NN to assign the weights for the NN to be able to distinguish light jets (u,d,s) from b jets.

INPUT VARIABLES should have a high discrimination power in terms of separating signal and background. Intuitively, the more variables the higher the discrimination power of the NN. At the same time, the complexity and computing time needed to obtain the final output increase with the number of variables. The simplest method is to start with the variables with the highest

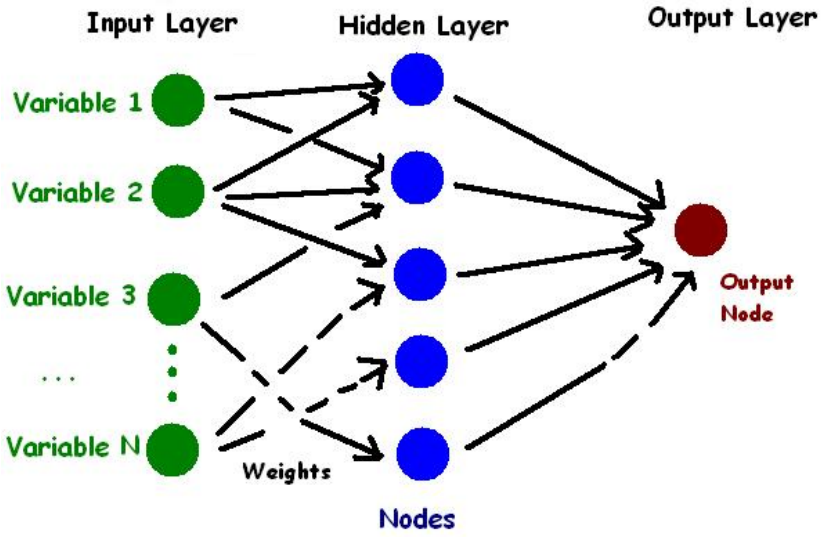

Figure 44: Schematic of a neural network. A certain number N of input variables is fed into a neural network. Weights are assigned to calculate linear combination of input values into one or several hidden layers. The information and separating power of the input variables is combined using linear combinations of sigmoidal functions into a continuous output distribution in the single node in the output layer. Properly normalized between 0 and 1 a NN output represents the probability to have a signal in a given input.

single discriminating power and to add more variables until the amelioration is not longer significant. In the case of the b tagging NN, the total number of input variables is seven, which are listed in the following:

- The decay length significance of the secondary vertex with respect to the primary vertex.
- A linear combination of impact parameter significance variables for a certain number of tracks:
  2(3)s - The number of tracks with a positive[10] impact parameter significance greater than 2 (3).
  2(3)w - The number of tracks with a negative impact parameter significance greater than 2(3) and a maximal angular distance between the track and the jet of $\Delta\phi(\text{track}, \text{jet}) < 1.15$
  Lin-comb $= 6 \times 3s + 4 \times 2s + 3 \times 3w + 2 \times 2w$.
- The probability that the jet originates from the primary vertex.
- χ^2/NDF of the secondary vertex.

10 In the plane transverse to the beam axis, the distance of closest approach to the primary vertex ($d = \vec{d}$) is given the same sign as the scalar product $\vec{d} \cdot \vec{p}_T(\text{jet})$.

- Number of tracks used to reconstruct the secondary vertex.
- The mass of the secondary vertex corrected by the transverse momentum p_T. This is calculated from the combined rest mass of the tracks assuming all the tracks are pions, with a correction for neutral particles.
- Number of reconstructed secondary vertices in the jet.

The distributions of these variables can be seen in Fig. 45 for two different test samples, a sample of $b\bar{b}$ jet events and a sample of light flavored (u,d,s) multijet events (denoted as "QCD" in the plots).
Using more variables than these does not provide further improvement on the identification efficiency. Fig. 46 shows a comparison in terms of identification efficiency over misidentification rate (also called "fake rate") using either five, seven or nine input variables. While going from five to seven input variables still provides additional improvement, at the cost of a higher misidentification rate, going to nine variables does not improve the efficiency any further. The set of nine variables was already chosen by their good separation between b jets and light jets (from a larger initial set of lifetime-related variables). The two additional variables (between the set of seven and nine) are

- the probability that the jet originates from the primary vertex, recalculated after removing the track with the highest significance from the calculation
- a combined variable based on the number of tracks with an impact parameter significance greater than an optimized value.

TRAINING To properly assign the weights in the hidden layers as mentioned before, the NN has to be trained on a subsample of events to be able to separate signal from background. The NN can then be tested on a different subsample to optimize the performance. For training and testing in the case of the b tagging NN, RunIIa MC samples of $t\bar{t}$, Z, multijet events containing light and heavy jets (separately) as well as data subsamples of the RunIIa dataset are used. Fig. 47 displays a performance check on multijet (QCD) test samples. The separation power is demonstrated by sorting signal-like events ($b\bar{b}$) towards 1 and background-like events (called "fake" in the figure) towards 0.

TAGGING REQUIREMENTS We now define two different tagging criteria as a loose and tight requirement on the output distribution of the b tagging NN. As the loose requirement, we define NN > 0.5 and as the tight requirement, we define NN

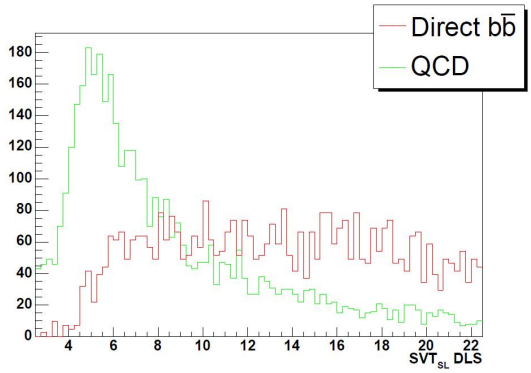

(a) Decay length significance (DLS).

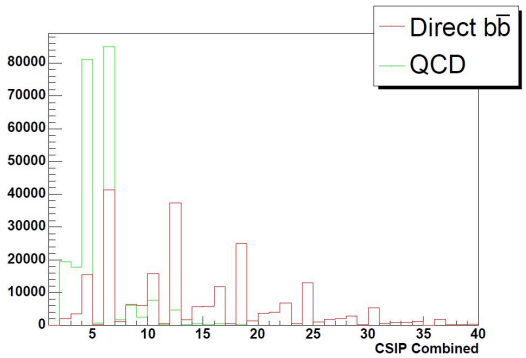

(b) Linear combination of impact parameter variables.

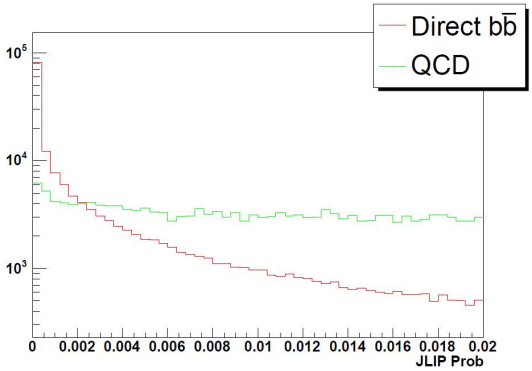

(c) Probability of the jet to originate from the PV.

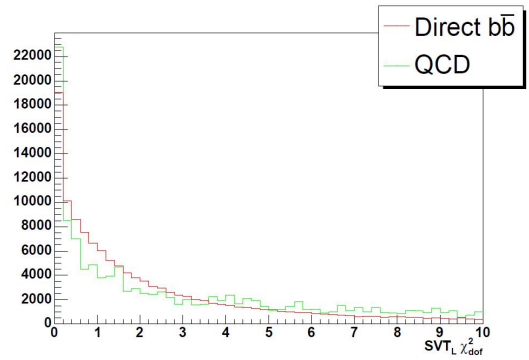

(d) χ^2/NDF of the SV.

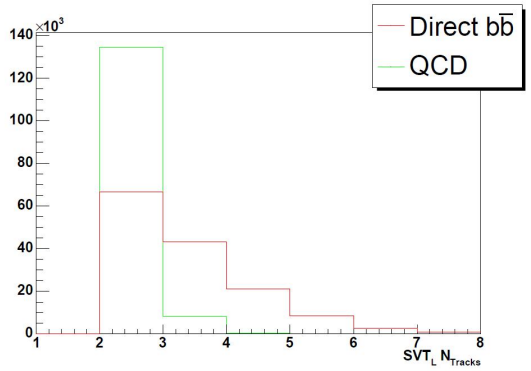

(e) Number of tracks associated with the SV.

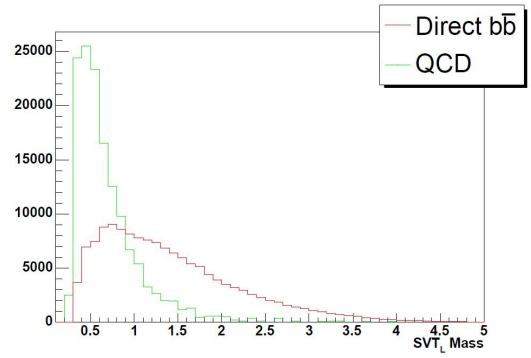

(f) Mass of the SV.

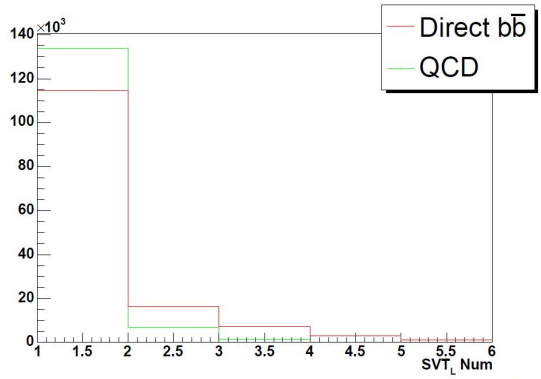

(g) Number of reconstructed vertices in the jet.

Figure 45: Distribution of the input variables of the b tagging NN for a direct $b\bar{b}$ jet events sample (red) and a multijet sample containing light jet events (originating from a u,d,s quark), called "QCD" in the plots (green). The discriminating power of these variables by themselves can be seen by eye. The NN combines their uncorrelated parts for an even higher separation power (see Fig. 47).

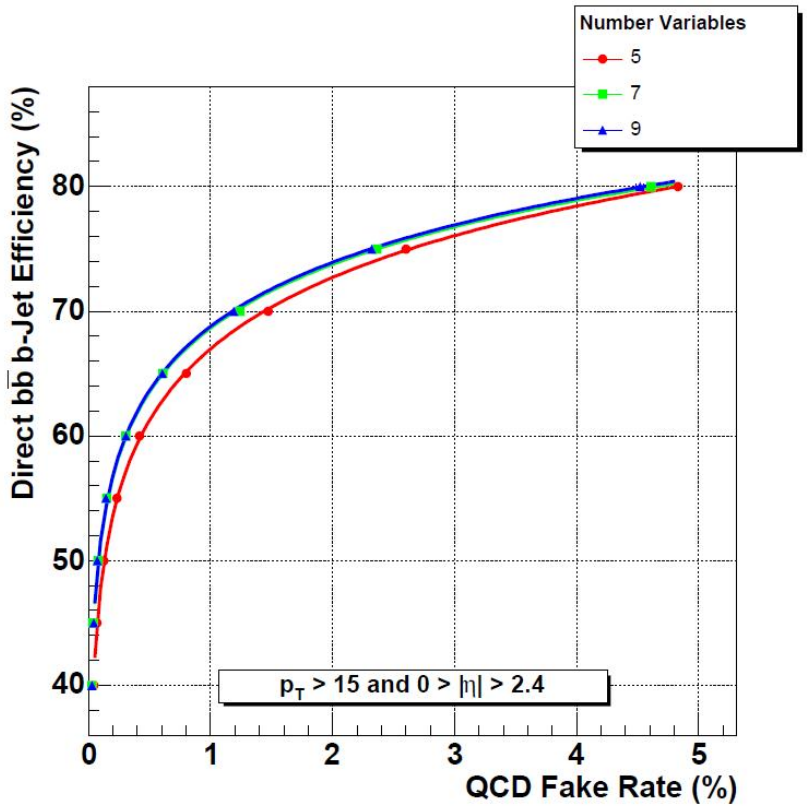

Figure 46: Comparison of efficiency vs. misidentification ("fake") rates for five, seven or nine input variables for the b tagging NN.

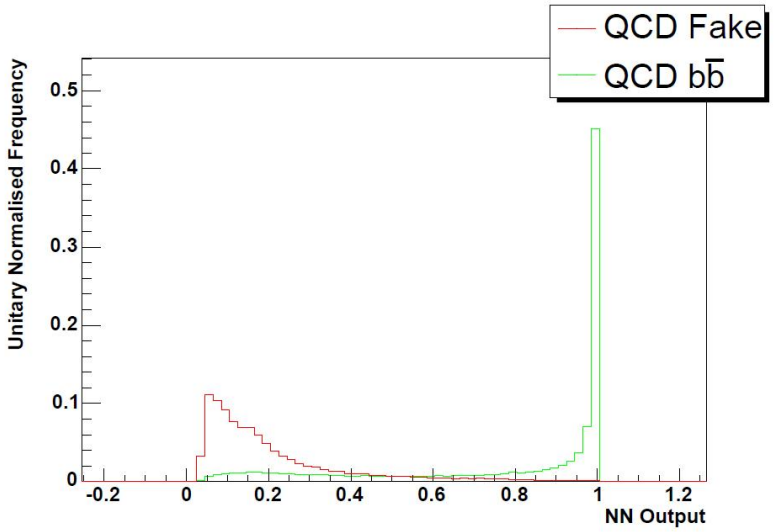

Figure 47: Performance of the b tagging neural network on test samples of multijet $b\bar{b}$ enriched events and multijet events containing light jets (called "fake"). The output proves the separation power of the NN with the $b\bar{b}$ events peaking at 1 and the light jet events accumulated around 0.

> 0.775. These two requirements are optimized to give the best performance in the WH analysis in terms of signal sensitivity.

To create our first sample of events for the final selection, we ask for events to have exactly two jets passing the loose NN b tagging requirement. This sample is then called double tag (DT) sample. For the events failing to pass the double tag selection, we ask for exactly one jet in the event to pass the tight tagging requirement. This sample is then called single tag (ST) sample. Events that do not pass either of the selections, are rejected for the tagging and not further taken into account in the final selection. The ST and DT sample are by construction orthogonal, meaning the do not have any event overlap.

The efficiency of the loose (tight) tagging requirement is 70% (50%). The misidentification rate[11] is 4.5% for the loose requirement and 0.3% for the tight requirement for a jet with $p_T = 50$ GeV [65].

11 The rate at which a light flavored jet or a jet originating from a gluon jet is identified as a b jet

6 MODELING OF PHYSICS PROCESSES

To fully understand the physics in our detector and therefore in our analysis, we must be able to describe the physics processes theoretically and simulate them to the same degree of precision at which we measure data from collision events. For this, we use Monte Carlo (MC) simulations. This modeling works in a way that it repeats the same physical process many times, varying only the initial conditions of the simulation (within their statistical uncertainties). All of the simulated events taken together build a statistics that allows us to make predictions of the true outcome of the physics process. We are able to produce simulated events for all processes that we expect to take place inside the $p\bar{p}$ collisions according to the theory of the Standard Model[1]. We then normalize the obtained event yields of the simulation to data corresponding to the cross section of the process and the luminosity. The simulation of signal events allows us to predict the shape and the kinematic properties of the physics objects we are looking for in the analysis. We apply the same selection cuts as in data and use more advanced techniques to enhance the signal. Matching distributions of the final variables of our analysis for data and MC then allow us to make predictions about the level of understanding of our data. In particle searches, we eventually hope to find deviations in the agreement of data and background simulation that would indicate a signal of the production process of an undiscovered particle.

This chapter will detail the MC generators used to produce the different types of simulated background and signal events (Sec. 6.1) as well as the further processing of the simulated events to compensate for detector effects (Sec. 6.2). We then go into detail about all applied correction factors compensating for mismodeling in simulated events compared to data (Sec. 6.4 for event based corrections and Sec. 6.5 for generator effects). Our modeling of the multijet background events is described in Sec. 6.6.1, followed by jet corrections (Sec. 6.7) and b tagging corrections (6.8) on simulated events.

6.1 GENERATORS

The Monte Carlo events that we use in this analysis were mainly generated with ALPGEN [66] and PYTHIA [67], except for single

1 except for multijet events that we derive from data.

top events that also used CompHEP [68]. These generators are capable of simulating the process from the beginning to the end, starting with initial state radiation in which a quark might emit a gluon and soft interactions of the initial partons, over the simulation of the hard scattering interaction in which the proton and the antiproton collide, up to final state radiation and the hadronization of quarks in the final state.

6.1.1 *PYTHIA*

PYTHIA is an event generator generally used to evaluate processes at leading order in perturbation theory, which means it takes into account only Feynman diagrams at the tree level and does not calculate one-loop corrections or any corrections of higher order. It calculates process cross sections and accounts for QCD radiations by using a parton shower model. This model simulates a shower from an initially high momentum scale down to a certain cut-off scale at which the final state partons form. PYTHIA models color confinement by using a model of strings in between quark pairs. The string carries a potential energy that grows with the distance between the quarks. As soon as there is enough kinetic energy to separate the quarks, a new pair of a quark and an antiquark is created from the vacuum, connected to the ripped ends of the string. The generator iterates this model until only on-shell hadrons remain in the final state. In the MC events used in this analysis, the CTEQ6L1 parton distribution functions (PDFs) were used [69]. The PDFs describe quark and gluon densities of the colliding protons and antiprotons. PYTHIA models the underlying structure of hadronizations very well, but is not as good in modeling multijet events.

6.1.2 *ALPGEN*

ALPGEN calculates the exact matrix element of processes of QCD and EW interactions at the parton level. It calculates processes at leading order (LO) and beyond (W+jets sample) in perturbation theory. The advantage of ALPGEN lies within the simulation of multijet events. Its weakness is, however, the underlying structure of these events, so it is not as good in simulating showering or hadronization. For many simulated processes we use in our analysis, we rely on events generated by an interface of ALPGEN with PYTHIA where ALPGEN generates the events at parton level and PYTHIA is responsible for the proper simulation of hadronization and showering.

6.1.2.1 *MLM Matching*

When a combination of ALPGEN and PYTHIA is used for event generation, it is important to avoid double counting events coming from multijet production. In these events, initially generated by ALPGEN, it is possible that PYTHIA will introduce additional jets into the event by adding gluons to the event that then split into quarks and shower to jets. By using the so-called MLM matching scheme [70] events containing additional jets are removed by clustering gluons and quarks. The jets are matched to partons from the hard scattering interaction so that each parton corresponds to one and only one jet. If this criterion cannot be fulfilled, the matching scheme rejects the event. Only for higher jet multiplicity ($\geqslant 4$), the partons have to be matched to jets, but additional jets are not rejected.

6.1.3 *CompHEP*

CompHEP uses the squared Feynman diagram technique to calculate cross sections and distributions with several particles in the final state. CompHEP is a generator operating at next-to-leading order.

6.2 DETECTOR SIMULATION

After generating simulated events, we process them through a detector simulation software called DØgstar [71] which is short for DØ GEANT Simulation of the Total Apparatus Response. As the name indicates this software is based on GEANT [72], a program of simulating the interaction between particles and matter in a certain specific setup, in this case the material inside the DØ detector. Examples for the simulated effects are electromagnetic showers in the calorimeter or multiple scattering of charged particles in the silicon detectors.
Events processed through DØgstar are fed into a software called DØsim [73] that does the digitization for each subdetector and overlays the simulated events with minimum bias events (taken from data events measured in the detector) to account for soft underlying events or additional inelastic collision events. DØsim also models the pile up in subdetectors like the calorimeter to account for a modified response due to previous bunch crossings, noise and inefficiencies. The final output of this processing chain is a sample of simulated events similar enough to the raw data obtained from the detector to be used in the same analysis framework for reconstruction of physics objects.

6.3 SIMULATED PROCESSES

In the following, we list all simulated processes that play a role in the WH analysis.

- W/Z + LIGHT JETS Production of a W or Z boson in association with light jets. A light jet forms from a light parton such as a light quark (u, d or s) or a gluon. The W boson decays leptonically, into a lepton and a neutrino, the Z boson decays into two leptons. This background is the dominant one to the signal of our analysis before we apply b tagging. This sample is generated with ALPGEN interfaced with PYTHIA for hadronization and showering. See Table 8 - 13 for the number and cross section of generated events.

- W/Z + HEAVY FLAVOR JETS Production of a W or Z boson in association with heavy flavor jets. A heavy flavor jet originates from the hadronization of a c or b quark. In the case of exactly two jets, this background is the dominant one after b tagging. This sample is also generated with ALPGEN interfaced with PYTHIA for hadronization and showering. See Table 8 - 13 for the number and cross section of generated events.

- DOUBLE TOP QUARK Production of a pair of top quarks. Top quarks almost exclusively decay into a W boson and a b quark. We split up this background sample into two cases: The dilepton case in which both W bosons decay leptonically, and the lepton+jets case in which one of the W bosons decays leptonically and the other one decays in a pair of jets. The all-jets final state of this process is accounted for in our estimation of the multijet background from data (see Sec. 6.6.1). The double top background is the dominant one in the case that we look at events with exactly three jets in the final state after applying b tagging. This sample is generated with ALPGEN interfaced with PYTHIA for hadronization and showering, a top mass of $m_T = 172$ GeV was assumed. See Table 6 for the number and cross section of generated events.

- SINGLE TOP QUARK Production of a single top quark, mainly produced in in two different channels, the so-called s and t channels. The s channel describes the fusion of two quarks into a W boson which then decays into a top quark and a $\bar{b}$ quark. The top quark decays into a b quark and a W boson that decays leptonically. The t channel describes the same initial fusion of quarks into a W boson that then interacts with a b quark to produce a top quark. The b quark is produced by a decaying gluon that also produces

a $\bar{b}$. The top quark then again decays into a W that decays leptonically and a b quark. In both cases we end up with an event topology similar to the one in the WH final state. This sample is generated with CompHEP at next-to-leading order, a top mass of $m_T = 172$ GeV was assumed. See Table 7 for the number and cross section of generated events.

- DIBOSON Production of a WW, ZZ or WZ pair. In case the WW pair decays in a lepton+jets way, meaning one of the W's decays leptonically and the other one decays into jets, we are left with an event topology similar to WH production. The same holds true in case of ZZ production where one of the Z's decays into two leptons of which one does not get reconstructed and therefore accounts for missing transverse energy (thereby faking the signature of a W boson) and the other one decays into a pair of quarks. Also for the WZ, we can end up with a topology similar to WH in case the W decays leptonically and the Z decays into a pair of quarks. Also if the W decays into two quarks and the Z decays into leptons of which one of them is not reconstructed. This sample is generated with PYTHIA. See Table 6 for the number and cross section of generated events.

- WH SIGNAL Production of a W boson in association with a Higgs boson[2]. The Higgs boson decays into two b quarks that subsequently form jets. The W boson decays leptonically into a lepton and a corresponding neutrino. We take into account all three lepton flavors. Fig. 48 shows the corresponding Feynman diagram for this production and decay channel. See Table 4 (5) for the number and cross section of generated events for RunIIa (RunIIb).

- OTHER SIGNAL CONTRIBUTIONS We also include signal coming from other processes than WH production. We take into account ZH processes in which the Higgs boson decays into two b quarks, like in WH processes, and the Z boson decays leptonically with one of the leptons not being detected and therefore being misidentified as a neutrino. See Table 4 (5) for the number and cross section of generated events for RunIIa (RunIIb).

6.3.1 *Cross Section Correction*

When simulated events are being generated for analyses, we produce significantly more events than we need to describe the

2 See Sec. 2.2 for details on Higgs boson production at the Tevatron

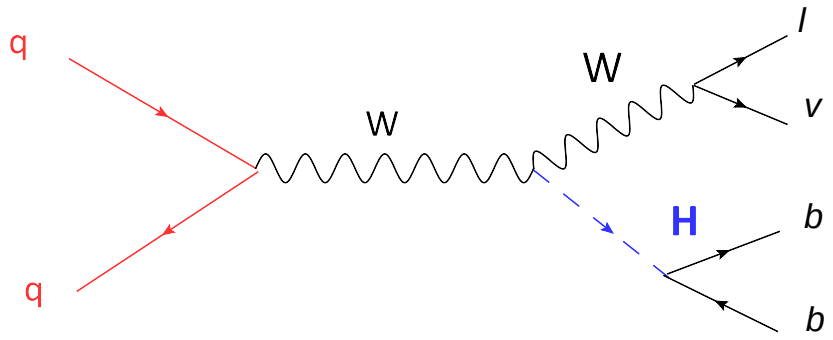

Figure 48: Feynman diagram for production of a Higgs boson in association with a W boson. The W boson decays into a lepton and a neutrino, the Higgs boson decays into two b quarks which subsequently form jets.

data. Especially for processes with rather small production cross sections, the amount of simulated events is by far greater than the amount of events in data. Therefore, we have to make the number of simulated events comparable to the one expected in data by scaling down the simulated events according to their cross section. As mentioned before, most generators used for MC production operate at leading order. For some cross section calculations, the calculation at next-to-leading order (including one-loop Feynman diagrams into the calculations), makes a significant difference. To compensate for this effect, we use a correction factor k between the next-to-leading order (NLO) cross section and the LO cross section of a given physics process:

$$k = \frac{\sigma_{NLO}}{\sigma_{LO}}. \tag{6.1}$$

These factors are then applied to the normalization of our MC samples. Ideally, we would take into account even higher corrections. However, calculating at higher loop corrections becomes significantly more difficult.

6.3.2 *Simulated Event Tables*

The following table summarizes, for all different event samples, split up by parton multiplicity (where the highest parton multiplicity is always an inclusive bin, which means it includes all higher jet multiplicities as well), the number of generated events and the cross section times branching ratio of the process. A k factor is stated in the cases where the cross section is calculated at leading order, to correct to next to leading order. In cases where no k factor is stated, the cross section has already been calculated at NLO, except for the WH cross section which has been calculated at NNLO.

RunIIa MC Process		Generator	# events	$\sigma(\times BR)$[pb]
	$m_H = 100\,GeV$		194715	0.0251
	$m_H = 105\,GeV$		193580	0.0209
	$m_H = 110\,GeV$		199080	0.0173
	$m_H = 115\,GeV$		196937	0.0141
	$m_H = 120\,GeV$		194767	0.0112
$WH \to b\bar{b} + \ell\nu$	$m_H = 125\,GeV$	PYTHIA	193882	0.0087
	$m_H = 130\,GeV$		193045	0.0065
	$m_H = 135\,GeV$		193795	0.0047
	$m_H = 140\,GeV$		197115	0.0032
	$m_H = 145\,GeV$		195850	0.0021
	$m_H = 150\,GeV$		194676	0.0013
	$m_H = 100\,GeV$		394432	0.0046
	$m_H = 105\,GeV$		403338	0.00384
	$m_H = 110\,GeV$		396185	0.00320
	$m_H = 115\,GeV$		400115	0.00263
	$m_H = 120\,GeV$		404973	0.00212
$ZH \to b\bar{b} + \ell\ell$	$m_H = 125\,GeV$	PYTHIA	388415	0.00166
	$m_H = 130\,GeV$		385764	0.00125
	$m_H = 135\,GeV$		387729	0.00091
	$m_H = 140\,GeV$		376238	0.000637
	$m_H = 145\,GeV$		387119	0.000410
	$m_H = 150\,GeV$		387219	0.000249

Table 4: List of the simulated signal processes $WH \to b\bar{b} + \ell\nu$ and $ZH \to b\bar{b} + \ell\ell$ used for RunIIa samples, along with the generator that was used for production, the number of produced events in the sample, for all lepton flavors, and the cross section times branching ratio, for one lepton flavor. ℓ denotes e, μ or τ.

RunIIb MC Process		Generator	# events	$\sigma(\times BR)$[pb]
$WH \to b\bar{b} + \ell\nu$	$m_H = 100\,GeV$	PYTHIA	320322	0.0251
	$m_H = 105\,GeV$		293813	0.0209
	$m_H = 110\,GeV$		316140	0.0173
	$m_H = 115\,GeV$		279087	0.0141
	$m_H = 120\,GeV$		321634	0.0112
	$m_H = 125\,GeV$		278550	0.0087
	$m_H = 130\,GeV$		553407	0.0065
	$m_H = 135\,GeV$		460095	0.0047
	$m_H = 140\,GeV$		495718	0.0032
	$m_H = 145\,GeV$		446339	0.0021
	$m_H = 150\,GeV$		320201	0.0013
$ZH \to b\bar{b} + \ell\ell$	$m_H = 100\,GeV$	PYTHIA	319375	0.0046
	$m_H = 105\,GeV$		279205	0.00384
	$m_H = 110\,GeV$		320038	0.00320
	$m_H = 115\,GeV$		279468	0.00263
	$m_H = 120\,GeV$		322296	0.00212
	$m_H = 125\,GeV$		279466	0.00166
	$m_H = 130\,GeV$		321965	0.00125
	$m_H = 135\,GeV$		279647	0.00091
	$m_H = 140\,GeV$		320005	0.000637
	$m_H = 145\,GeV$		279310	0.000410
	$m_H = 150\,GeV$		316756	0.000249

Table 5: List of the simulated signal processes $WH \to b\bar{b} + \ell\nu$ and $ZH \to b\bar{b} + \ell\ell$ used for RunIIb samples, along with the generator that was used for production, the number of produced events in the sample and the cross section times branching ratio, for one lepton flavor. ℓ denotes e, μ or τ.

data	Process	Generator	# events	k$\times\sigma\times$ BR [pb]
RunIIa	WW inclusive	PYTHIA	1905k	1.03×11.6
	WZ inclusive	PYTHIA	1059k	1.06×3.25
	ZZ inclusive	PYTHIA	590.6k	1.33
RunIIb	WW inclusive	PYTHIA	709.9k	1.03×11.6
	WZ inclusive	PYTHIA	632.3k	1.06×3.25
	ZZ inclusive	PYTHIA	540.3k	1.33

Table 6: List of simulated di-boson processes WW, WZ and ZZ, along with the generator that was used for production, the number of events in the sample and the cross section times branching ratio.

RunIIa MC		Generator	# events	k × (σ×BR)[pb]
$t\bar{t} \to b\bar{b} + \ell^+\nu\ell'^-\bar{\nu}_{\ell'}$	+ 0 light parton	ALPGEN + PYTHIA	1516107	1.43×0.352
	+ 1 light parton		492647	1.43×0.143
	+ 2 light partons		288992	1.43×0.0713
$t\bar{t} \to b\bar{b} + 2j + \ell\nu$	+ 0 light parton	ALPGEN + PYTHIA	771271	1.43×1.414
	+ 1 light parton		492647	1.43×0.57
	+ 2 light partons		288992	1.43×0.283
$tb \to e\nu b\bar{b}$		CompHEP + PYTHIA	290262	0.99×0.112
$tb \to \mu\nu b\bar{b}$			287994	0.99×0.11
$tb \to \tau\nu b\bar{b}$			287991	0.99×0.117
$tqb \to e\nu bqb$		CompHEP + PYTHIA	290262	0.99×0.243
$tqb \to \mu\nu bqb$			287994	0.99×0.239
$tqb \to \tau\nu bqb$			289106	0.99×0.254

RunIIb MC		Generator	# events	k × (σ×BR)[pb]
$t\bar{t} \to b\bar{b} + \ell^+\nu\ell'^-\bar{\nu}_{\ell'}$	+ 0 light parton	ALPGEN + PYTHIA	749642	1.43×0.352
	+ 1 light parton		452177	1.43×0.142
	+ 2 light partons		281453	1.43×0.0676
$t\bar{t} \to b\bar{b} + 2j + \ell\nu$	+ 0 light parton	ALPGEN + PYTHIA	777068	1.43×1.40
	+ 1 light parton		457782	1.43×0.577
	+ 2 light partons		321166	1.43×0.267
$tb \to e\nu b\bar{b}$		CompHEP + PYTHIA	247517	0.99×0.112
$tb \to \mu\nu b\bar{b}$			225286	0.99×0.110
$tb \to \tau\nu b\bar{b}$			248722	0.99×0.117
$tqb \to e\nu bqb$		CompHEP + PYTHIA	272573	0.99×0.243
$tqb \to \mu\nu bqb$			273354	0.99×0.239
$tqb \to \tau\nu bqb$			246552	0.99×0.254

Table 7: List of simulated $t\bar{t}$ and single-top processes, along with the generator that was used for production, the number of events in the sample and the k factor times cross section times branching ratio, where $\ell = e, \tau$ or μ.

RunIIa MC Process		Generator	# events	$\sigma(\times BR)$[pb]
$Wjj \to \ell\nu$	+ 0 light parton	ALPGEN + PYTHIA	12.5M	4.513k
	+ 1 light parton		18.9M	1.278k
	+ 2 light partons		13.3M	299.4
	+ 3 light partons		3.5M	70.7
	+ 4 light partons		2.5M	16.2
	+ 5 light partons		781k	4.95
$Wb\bar{b} \to \ell\nu b\bar{b}$	+ 0 light parton	ALPGEN + PYTHIA	1.4M	9.37
	+ 1 light parton		667k	4.3
	+ 2 light partons		249k	1.55
	+ 3 light partons		377k	0.71
$Wc\bar{c} \to \ell\nu c\bar{c}$	+ 0 light parton	ALPGEN + PYTHIA	1.2M	24.5
	+ 1 light parton		740k	13.5
	+ 2 light partons		342k	5.5
	+ 3 light partons		446k	2.53

Table 8: List of simulated RunIIa W+jets processes, along with the generator that was used for production, the number of events in the sample and the cross section times branching ratio (the light partons are requested to have $p_T > 8$ GeV and $|\eta| < 5$). Samples generated with ALPGEN have been produced in bins of light parton multiplicity. These bins are exclusive, except for the last one, which is inclusive. ℓ denotes a lepton, i.e., either e, μ or τ.

RunIIa MC Process		Generator	# events	$\sigma(\times BR)$[pb]
	+ 0 light parton		577k	337
$Zjj \to ee$	+ 1 light parton		479k	40.3
15-75 GeV	+ 2 light partons	ALPGEN + PYTHIA	191k	10
	+ 3 light partons		96k	2.76
	+ 0 light parton		3.0M	132
$Zjj \to ee$	+ 1 light parton		1.9M	40.8
75-130 GeV	+ 2 light partons	ALPGEN + PYTHIA	982k	10
	+ 3 light partons		988k	3.15
	+ 0 light parton		295k	0.89
$Zjj \to ee$	+ 1 light parton		192k	0.37
130-250 GeV	+ 2 light partons	ALPGEN + PYTHIA	98k	0.09
	+ 3 light partons		98k	0.03
	+ 0 light parton		577k	336
$Zjj \to \mu\mu$	+ 1 light parton		483k	39.7
15-75 GeV	+ 2 light partons	ALPGEN + PYTHIA	192k	9.9
	+ 3 light partons		96k	2.8
	+ 0 light parton		3.0M	132
$Zjj \to \mu\mu$	+ 1 light parton		2.0M	40.6
75-130 GeV	+ 2 light partons	ALPGEN + PYTHIA	1.1M	9.8
	+ 3 light partons		1.1M	3.1
	+ 0 light parton		484k	0.88
$Zjj \to \mu\mu$	+ 1 light parton		391k	0.35
130-250 GeV	+ 2 light partons	ALPGEN + PYTHIA	298k	0.1
	+ 3 light partons		299k	0.03
	+ 0 light parton		2.9M	133
$Zjj \to \tau\tau$	+ 1 light parton		2.0M	40.6
75-130 GeV	+ 2 light partons	ALPGEN + PYTHIA	963k	10
	+ 3 light partons		978k	3.2
	+ 0 light parton		288k	0.88
$Zjj \to \tau\tau$	+ 1 light parton		194k	0.34
130-250 GeV	+ 2 light partons	ALPGEN + PYTHIA	97k	0.09
	+ 3 light partons		100k	0.03

Table 9: List of simulated RunIIa Z+ light jets processes, along with the generator that was used for production, the number of events in the sample and the cross section times branching ratio (the light partons are requested to have $p_T > 8$ GeV and $|\eta| < 5$). Samples generated with ALPGEN have been produced in bins of light parton multiplicity. These bins are exclusive, except for the last bin, which is inclusive. ℓ denotes a lepton, i.e., either e, μ or τ.

RunIIa MC Process		Generator	# events	$\sigma(\times BR)$[pb]
$Zb\bar{b} \to ee + b\bar{b}$	+ 0 light parton	ALPGEN + PYTHIA	201k	0.40
	+ 1 light parton		101k	0.19
	+ 2 light partons		50k	0.10
$Zc\bar{c} \to ee + c\bar{c}$	+ 0 light parton	ALPGEN + PYTHIA	202k	0.90
	+ 1 light parton		105k	0.48
	+ 2 light partons		49k	0.29
$Zb\bar{b} \to \mu\mu + b\bar{b}$	+ 0 light parton	ALPGEN + PYTHIA	194k	0.40
	+ 1 light parton		99k	0.19
	+ 2 light partons		50k	0.11
$Zc\bar{c} \to \mu\mu + c\bar{c}$	+ 0 light parton	ALPGEN + PYTHIA	194k	0.93
	+ 1 light parton		102k	0.50
	+ 2 light partons		51k	0.29
$Zb\bar{b} \to \tau\tau + b\bar{b}$	+ 0 light parton	ALPGEN + PYTHIA	202k	0.41
	+ 1 light parton		101k	0.19
	+ 2 light partons		50k	0.09
$Zc\bar{c} \to \tau\tau + c\bar{c}$	+ 0 light parton	ALPGEN + PYTHIA	196k	0.91
	+ 1 light parton		97k	0.51
	+ 2 light partons		48k	0.28

Table 10: List of simulated RunIIa Z+$b\bar{b}/c\bar{c}$ jets processes, along with the generator that was used for production, the number of events in the sample and the cross section times branching ratio (the light partons are requested to have $p_T > 8$ GeV and $|\eta| < 5$). Samples generated with ALPGEN have been produced in bins of light parton multiplicity. These bins are exclusive, except for the last bin, which is inclusive. ℓ denotes a lepton, i.e., either e, μ or τ.

RunIIb MC Process		Generator	# events	$\sigma(\times BR)$[pb]
$Wjj \to \ell\nu$	+ 0 light parton	ALPGEN + PYTHIA	46.4M	4.513k
	+ 1 light parton		19.9M	1.278k
	+ 2 light partons		18.1M	299.4
	+ 3 light partons		3.75M	70.7
	+ 4 light partons		2.6M	16.2
	+ 5 light partons		2.0M	4.95
$Wb\bar{b} \to \ell\nu b\bar{b}$	+ 0 light parton	ALPGEN + PYTHIA	1.1M	9.37
	+ 1 light parton		782k	4.3
	+ 2 light partons		524k	1.55
	+ 3 light partons		413k	0.71
$Wc\bar{c} \to \ell\nu c\bar{c}$	+ 0 light parton	ALPGEN + PYTHIA	934k	24.5
	+ 1 light parton		739k	13.5
	+ 2 light partons		554k	5.5
	+ 3 light partons		470k	2.53

Table 11: List of simulated RunIIb W+jets processes, along with the generator that was used for production, the number of events and the cross section times branching ratio (the light partons are requested to have $p_T > 8$ GeV and $|\eta| < 5$). Samples generated with ALPGEN have been produced in bins of light parton multiplicity. These bins are exclusive, except for the last bin, which is inclusive. ℓ denotes a lepton, i.e, either e, τ or μ.

RunIIb MC Process		Generator	# events	$\sigma(\times BR)$[pb]
	+ 0 light parton		1.9M	337
$Zjj \to ee$	+ 1 light parton		956k	40.0
15-75 GeV	+ 2 light partons	ALPGEN + PYTHIA	549k	9.74
	+ 3 light partons		536k	2.67
	+ 0 light parton		1.2M	133
$Zjj \to ee$	+ 1 light parton		567k	40.1
75-130 GeV	+ 2 light partons	ALPGEN + PYTHIA	268k	9.8
	+ 3 light partons		127k	3.2
	+ 0 light parton		352k	0.89
$Zjj \to ee$	+ 1 light parton		179k	0.38
130-250 GeV	+ 2 light partons	ALPGEN + PYTHIA	160k	0.10
	+ 3 light partons		300k	0.03
	+ 0 light parton		1.7M	344
$Zjj \to \mu\mu$	+ 1 light parton		570k	40.1
15-75 GeV	+ 2 light partons	ALPGEN + PYTHIA	275k	9.66
	+ 3 light partons		268k	2.74
	+ 0 light parton		1.5M	134
$Zjj \to \mu\mu$	+ 1 light parton		604k	41.4
75-130 GeV	+ 2 light partons	ALPGEN + PYTHIA	401k	9.71
	+ 3 light partons		146k	3.15
	+ 0 light parton		351k	0.89
$Zjj \to \mu\mu$	+ 1 light parton		170k	0.36
130-250 GeV	+ 2 light partons	ALPGEN + PYTHIA	160k	0.10
	+ 3 light partons		142k	0.03
	+ 0 light parton		1.5M	131
$Zjj \to \tau\tau$	+ 1 light parton		528k	40.3
75-130 GeV	+ 2 light partons	ALPGEN + PYTHIA	274k	9.81
	+ 3 light partons		174k	3.0
	+ 0 light parton		359k	0.92
$Zjj \to \tau\tau$	+ 1 light parton		171k	0.38
130-250 GeV	+ 2 light partons	ALPGEN + PYTHIA	162k	0.10
	+ 3 light partons		158k	0.03

Table 12: List of simulated RunIIb Z+light jets processes, along with the generator that was used for production, the number of events and the cross section times branching ratio (the light partons are requested to have $p_T > 8$ GeV and $|\eta| < 5$). Samples generated with ALPGEN have been produced in bins of light parton multiplicity. These bins are exclusive, except for the last bin, which is inclusive. ℓ denotes a lepton, i.e, either e, τ or μ.

RunIIb MC Process		Generator	# events	$\sigma(\times BR)$[pb]
$Zb\bar{b} \to ee + b\bar{b}$	+ 0 light parton	ALPGEN + PYTHIA	196k	0.40
	+ 1 light parton		93k	0.17
	+ 2 light partons		44k	0.11
$Zc\bar{c} \to ee + c\bar{c}$	+ 0 light parton	ALPGEN + PYTHIA	182k	0.90
	+ 1 light parton		89k	0.51
	+ 2 light partons		47k	0.29
$Zb\bar{b} \to \mu\mu + b\bar{b}$	+ 0 light parton	ALPGEN + PYTHIA	206k	0.42
	+ 1 light parton		96k	0.20
	+ 2 light partons		45k	0.10
$Zc\bar{c} \to \mu\mu + c\bar{c}$	+ 0 light parton	ALPGEN + PYTHIA	194k	0.93
	+ 1 light parton		93k	0.55
	+ 2 light partons		51k	0.28
$Zb\bar{b} \to \tau\tau + b\bar{b}$	+ 0 light parton	ALPGEN + PYTHIA	193k	0.42
	+ 1 light parton		98.2k	0.20
	+ 2 light partons		44k	0.10
$Zc\bar{c} \to \tau\tau + c\bar{c}$	+ 0 light parton	ALPGEN + PYTHIA	260k	0.90
	+ 1 light parton		101k	0.49
	+ 2 light partons		51k	0.30

Table 13: List of simulated RunIIb Z+$b\bar{b}$/$c\bar{c}$jets processes, along with the generator that was used for production, the number of events and the cross section times branching ratio (the light partons are requested to have $p_T > 8$ GeV and $|\eta| < 5$). Samples generated with ALPGEN have been produced in bins of light parton multiplicity. These bins are exclusive, except for the last bin, which is inclusive. ℓ denotes a lepton, i.e, either e, τ or μ.

6.3.3 *Experimental k factors and heavy flavor scale factors for W+jets and Z+jets samples*

As mentioned above, the simulated background processes are normalized to the SM prediction of their cross section. The W+jets ALPGEN samples, however, are normalized to data (before we apply b tagging). This normalization is set in conjunction with the scaling of the multijet background (see Sec. 6.6.1). The experimentally determined scale factor for the W+jets processes K_{LF}^{exp} is defined as

$$K_{LF}^{exp} = \frac{N_{data} - N_{SM} - N_{QCD}}{N_{W+jet}}. \tag{6.2}$$

where N_{SM} is the number of expected events in all background samples according to the Standard Model prediction but without the W+jets and multijet sample contributions, and N_{QCD} is the number of standard model events in the multijet background sample, estimated from data, as described in Sec. 6.6.1. The K_{LF}^{exp} for the electron and muon channel of the WH analysis (split by final states of the W decay) from each data set is summarized in Table 14.

	channel	2 jet	3 jet
RunIIa	Electron	1.07 ± 0.01	1.17 ± 0.03
	Muon	1.14 ± 0.01	1.31 ± 0.03
RunIIb	Electron	0.98 ± 0.01	1.05 ± 0.01
	Muon	1.04 ± 0.01	1.13 ± 0.01

Table 14: The experimental K_{LF}^{exp} factors for each sample, taking into account the theoretical next to leading order k factor of 1.3. The errors are statistical only. The total uncorrelated systematic uncertainty between the correction factors of the e and μ channel is approximately 7-8%, based on trigger (3-4% e, 5% μ) and lepton identification (3% e, 4% RunIIa μ, 2% RunIIb μ) uncertainties.

The average of these numbers in two jet events is 1.0 and within systematic uncertainties of the order of 10%, the numbers of all channels agree. The uncertainties come from lepton characteristics like the lepton trigger, the lepton efficiency, the estimation of the multijet background and other indirect constraints coming from the estimation of the missing transverse energy $\not\!\!E_T$, for example, that takes into account the lepton energy.

We correct the cross sections for heavy flavor processes by multiplying the Wbb, Wcc, Zbb and Zcc ALPGEN cross sections by K_{LF}^{exp} and by the heavy flavor factor s_{HF} which we derive from

data. Therefore, the full experimental correction factor for heavy flavor is given by

$$K_{HF}^{exp} = s_{HF} \times K_{LF}^{exp}. \tag{6.3}$$

The s_{HF} factor is determined on each orthogonal sample, the tagged sample (denoted by $'$) and the anti-tagged sample (denoted by $''$) by the following equation:

$$s_{HF} = \frac{(Data' - X') * W'' - (Data'' - X'') * W'}{(Data'' - X'') * B' - (Data' - X') * B''} \tag{6.4}$$

where W is the number of events in the full W+jets sample and B is the number of events in the W+heavy jets ($b\bar{b}$ and $c\bar{c}$) sample. X is the number of events in the MC background sample except for the W+jets sample (i.e. $t\bar{t}$, single top and diboson samples).

We determine this s_{HF} factor on a combination of all channels of this analysis (electron and muon, RunIIa and RunIIb samples). We obtain a value of 1.0 ± 0.1 that we apply to all the heavy flavor samples $W + b\bar{b}, W + c\bar{c}, Z + b\bar{b}$ and $Z + c\bar{c}$. In the limit setting procedure (see Sec. 7.4), we allow this factor to vary within its 20% uncertainty band.

6.4 EVENT CORRECTION

6.4.1 *Trigger Correction*

To simulate the effect of applying triggers to simulated events, we apply a scale factor equivalent to the efficiency of triggers in data to the simulated events. Trigger efficiencies in data are measured as probabilities of events passing all three trigger levels (described in Sec. 5.3.7). The overall efficiency of the trigger then equals the probability $P(L1, L2, L3)$ that the event consecutively passes L1, L2 and L3 triggers. This probability can be factorized as follows [74]:

$$P(L1, L2, L3) = P(L1) \cdot P(L2|L1) \cdot P(L3|L1, L2) \tag{6.5}$$

where $P(L1)$ is the probability that the event passes the L1 trigger requirements and $P(L2|L1)$ and $P(L3|L1, L2)$ are the conditional probabilities for an event to pass a set of criteria, given it has already passed the requirements of the preceding trigger level(s). We assume that the total probability of an event to pass a set of trigger requirements selecting a certain type of object is independent of other types of objects being present in the event.

Therefore, the total probability of the event to pass different kinds of triggers can be factorized as

$$P(obj_1, obj_2) = P(obj_1) \cdot P(obj_2) \tag{6.6}$$

where $obj_{1/2}$ are physics objects for which different sets of triggers are sensitive.

Trigger efficiencies in the electron and muon case are measured by the tag-and-probe method on $Z \to ee$ and $Z \to \mu\mu$ events where one of the leptons is randomly selected (tag) and required to pass the trigger requirements (done separately for L1, L2 and L3 and then combined as in Eq. 6.5). The other lepton is then used to measure the efficiency at which this lepton also passes the trigger requirement.

6.4.1.1 *Electron Trigger Correction*

Trigger efficiencies on the single EM and EM+JET trigger suites are measured as functions of the transverse momentum p_T of the lepton and η_{det}. The efficiency correction is applied to simulated events.

6.4.1.2 *Muon Trigger Correction*

We perform a whole run of the analysis up to the final event selection (without requiring b tagging), using the single muon trigger suite. We derive a correction factor for simulated events using the difference between the multijet-subtracted data requiring inclusive muon triggers and single muon triggers to take into account the non-single muon trigger contribution to data:

$$P_{corr} = \frac{(Data - multijet)_{incl} - (Data - multijet)_{single\mu}}{MC_{incl}} \tag{6.7}$$

where MC_{incl} refers to the Monte Carlo events with a trigger probability set to 1 (corresponding to the inclusive trigger requirement). We parameterize the correction in H_T (the sum of all transverse momenta in the event) and in muon η_{det} for $|\eta_{det}| < 1.6$.

For each simulated event, we set the trigger probability to be

$$P_{trig} = P_{corr}(H_T, \eta_{det}) + P_{single\mu} \tag{6.8}$$

where $P_{single\mu}$ is the probability for a given event to fire a single muon trigger (measured as in the electron case [74]). In each event, P_{trig} should be $\leqslant 1$. In case Eq. 6.8 returns a

value of $P_{trig} > 1$ for an event, it is set to 1 by requiring that $P_{corr} = 1 - P_{single\mu}$ so that $P_{corr} + P_{single\mu}$ never exceeds unity. Fig. 49 shows the muon trigger correction on simulated events as a function of H_T estimated on RunIIa and RunIIb data.

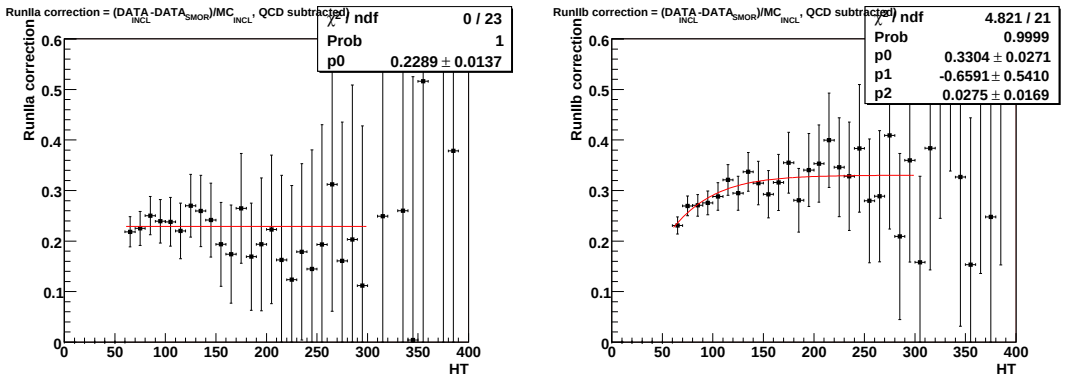

Figure 49: Muon trigger correction for simulated events, P_{corr} in Eq. 6.7, estimated on RunIIa (left) and RunIIb (right) data. In RunIIb we parameterize the RunIIb correction with a $\tanh$ function.

6.4.2 *Luminosity Profile*

The instantaneous luminosity delivered by the Tevatron decreases in a non monotonic way throughout a store. As we use minimum bias events to propagate detector inefficiencies and pile up effects to simulated events (see Sec. 6.2), it is necessary to reweight the simulated events to match the shape of the luminosity profile we measure in data. The luminosity profile in data is therefore compared to the one in MC separately for every simulated process in a bin by bin reweighting of the histograms.

6.4.3 *z Position of the Primary Vertex*

In simulated events, the distribution of the position of primary vertices along the z axis follows a Gaussian distribution around $z = 0$. In data, however, this distribution is slightly non Gaussian (see Fig. 50), showing a wider range than in simulated events and also having a greater loss in efficiency for $|z| > 40$ cm, we therefore apply a cut of $|z| < 40$ cm in the WH analysis. The shape of the luminous region at DØ depends on shapes of the proton and antiproton bunches and on the β parameter of the interaction point[3] [75]. The distribution has been measured in

3 β is a parameter generally used in describing beam shapes in particle accelerators.

data and it is used to correct the distribution in the simulation accordingly.

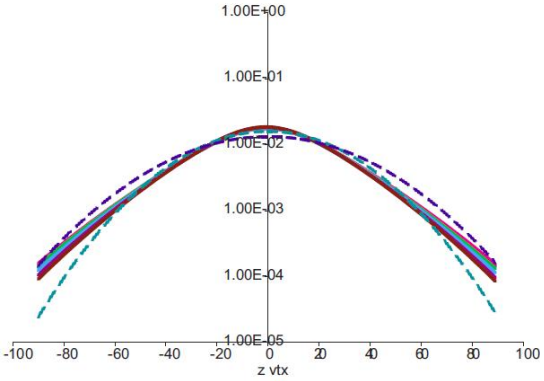

Figure 50: Beam shape distributions for different data subsamples (solid lines) compared to Gaussian functions of 25 and 30 cm (upper and lower dashed lines) on a log scale. The slight non-Gaussianity is an effect of the order of 3% that has to be corrected in simulation to match the data shape. [75]

6.5 ALPGEN REWEIGHTING

As mentioned before, we use ALPGEN and PYTHIA for the generation of our simulated events. MC samples generated with ALPGEN involved show some imperfections that we account for by correcting the corresponding samples manually to data. We reweight the W/Z+jets samples for all channels, electron and muon as well as RunIIa and RunIIb. We apply the same reweightings to the light and heavy jet samples. The way we derive the corrections is by building the ratio of the data sample subtracted by all MC samples but the ALPGEN MC samples (multijet, $t\bar{t}$, single top and diboson samples) divided by the ALPGEN MC samples. We then fit the obtained ratio with an appropriate correction function. In each reweighting figure shown below, the black curve represents the nominal correction function that we derive, while the red and blue dashed curves represent $\pm 1\sigma$ variations on the function. These variations are based on selecting the parameter that affects the shape of the function the most (the highest order polynomial term for most fits; the slope of the sigmoid turn-on for Wp_T), varying that by one full σ based on the uncertainty of the fit, and varying the other fit parameters by the appropriate amount based on the covariance matrix of the fit. In the following, all applied ALPGEN corrections are described.

6.5.1 Z *Boson Transverse Momentum*

Neither ALPGEN nor PYTHIA correctly model the distribution of the transverse momentum p_T of the Z boson, especially for events with $p_T > 100$ GeV. We compensate for this mismodeling by reweighting the simulated events [76]. The correction is derived from the measurement of the Z boson transverse momentum in $Z \to e\,e$ events in the RunIIa and RunIIb data samples [77]. The reweighting of the W p_T distribution is explained in 6.5.5.

6.5.2 *Jet* η_{det} *in the ICD region*

In the ICD region of the detector ($0.8 < |\eta_{det}| < 1.4$), the jet η_{det} distribution shows an excess of events in the simulated RunIIb samples. This is due to the zero bias event overlay which appears to shift more jets in simulated events into the ICD region. The applied jet correction is not perfectly modeled in this region because of the missing calorimeter information (the ICD region is the gap between the two spatial sections of the calorimeter, the CC and the EC region). We use constant factors in both ICD regions for the reweighting. The reweighting factors are shown in Fig. 51 and listed in Eq. 6.9.

$$\begin{aligned} F_{\eta_{j1ICD_{south}}} &= 0.928472 \\ F_{\eta_{j1ICD_{north}}} &= 0.992236 \\ F_{\eta_{j2ICD_{south}}} &= 0.862120 \\ F_{\eta_{j2ICD_{north}}} &= 0.899186 \end{aligned} \tag{6.9}$$

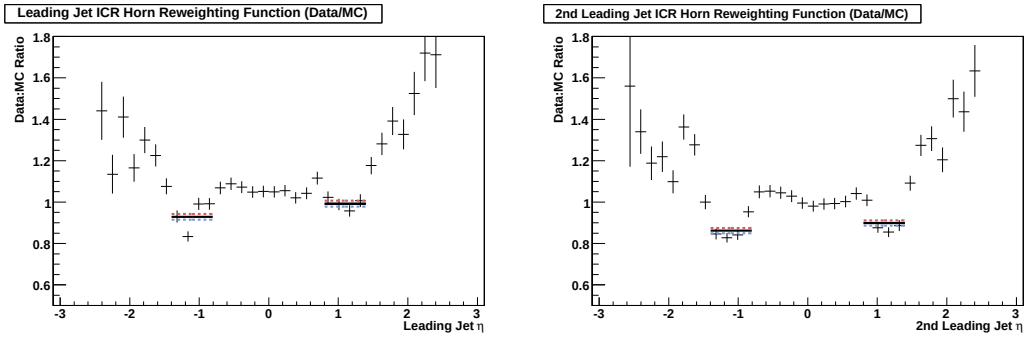

(a) ICD region reweighting parameters for the leading jet.

(b) ICD region reweighting parameters for the second leading jet.

Figure 51: Reweighting parameters on the leading and second leading jet as a function of η_{det} for the ICD region of the DØ detector. These parameters are applied to reweight simulated events in the RunIIb samples generated with ALPGEN.

6.5.3 *Jet* η

To better model the overall shape of the jet η distribution in simulated events (which is slightly mismodeled in ALPGEN when compared to data), we derive a correction function on the data to MC ratio of the jet η distribution of the leading and second leading jet in the event[4]. The fit functions are fourth order polynomials and are shown in Fig. 52 and listed in Eq. 6.10. The functions are symmetrical, so they only contain even order polynomial terms, because the DØ detector is symmetrical in η, therefore we expect the jet distribution to be symmetrical. Fig. 53 shows the effect of the reweighting exemplarily on the RunIIb electron sample distribution of the leading jet η in a comparison before and after the reweighting is applied.

$$F_{\eta_{j1}} = 0.976774 - 0.0262889\ \eta_{j1}^2 + 0.0191657\ \eta_{j1}^4 \tag{6.10}$$

$$F_{\eta_{j2}} = 0.942693 - 0.004809\ \eta_{j2}^2 + 0.018491\ \eta_{j2}^4 \tag{6.11}$$

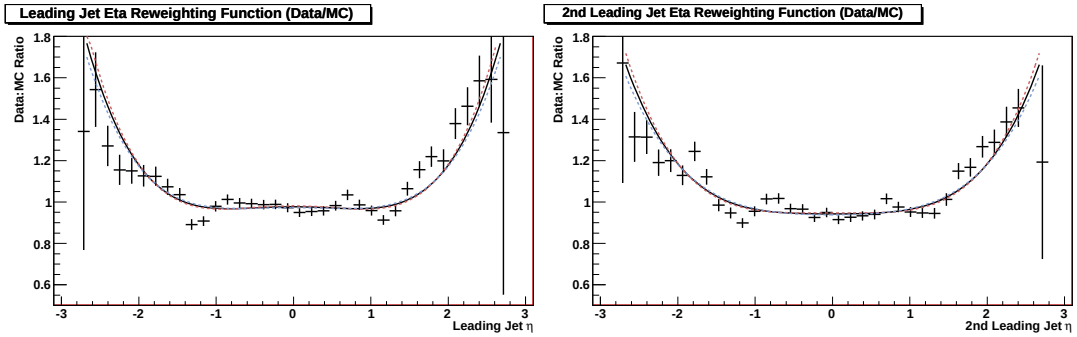

(a) Jet η reweighting function for the leading jet. (b) Jet η reweighting function for the second leading jet.

Figure 52: Reweighting functions on the leading and second leading jet as a function of jet η. These functions are used to reweight simulated events generated with ALPGEN.

6.5.4 *Lepton* η

For the η distribution of the lepton in simulated events of ALPGEN samples, we also see a slight generator mismodeling effect in comparison to the data distribution. Therefore, we fit a symmetrical second order polynomial function to the data to MC ratio that is then applied to the samples generated with ALPGEN. The function is listed in Eq. 6.12 and shown in Fig. 54. Fig. 55 shows

4 No reweighting is applied to the third jet in the three jet channel.

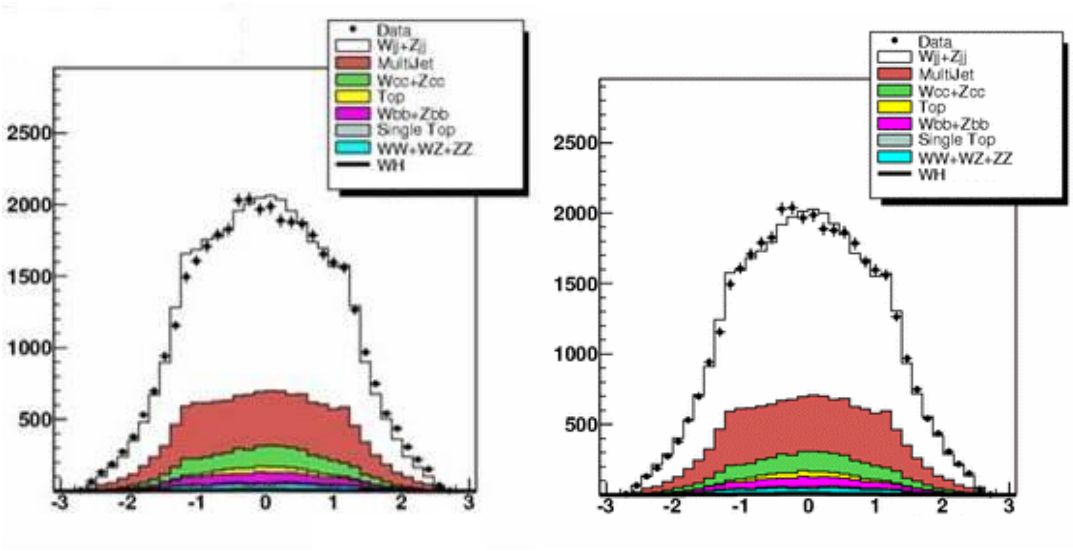

(a) Leading jet η before reweighting

(b) Leading jet η after reweighting

Figure 53: Distribution of the leading jet η (in the RunIIb electron sample) before and after the application of the derived fourth order polinomial reweighting function on the ALPGEN samples. A significant improvement especially in the high η regions is visible.

the effect of the reweighting exemplarily on the RunIIb electron η distribution in a comparison before and after the reweighting is applied.

$$F_{\eta_{lepton}} = 0.97426 + 0.0658797\ \eta^2_{lepton} \tag{6.12}$$

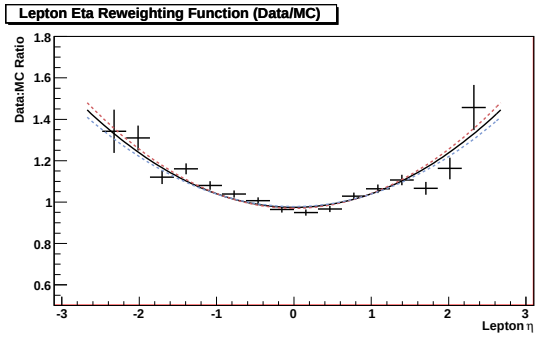

Figure 54: Reweighting function on the lepton in the event as a function of lepton η. This function is used to reweight simulated events generated with ALPGEN.

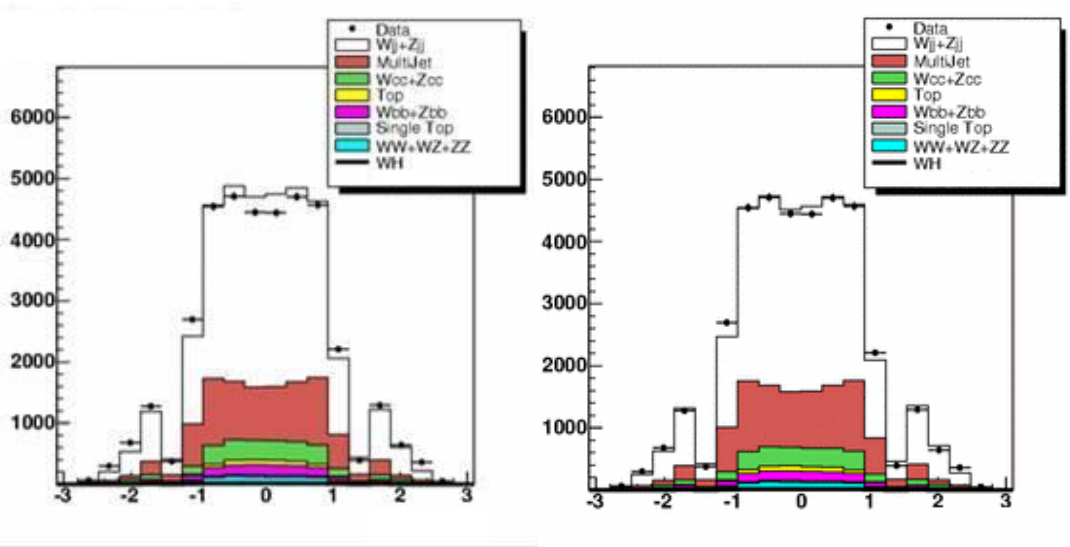

(a) Lepton η before reweighting

(b) Lepton η after reweighting

Figure 55: Distribution of lepton η (in the RunIIb electron sample) before and after the application of the derived second order polinomial reweighting function on the ALPGEN samples. A significant overall improvement of the distribution is visible.

6.5.5 $W\,p_T$ *and* ΔR

We also see a discrepancy between data and simulation in the shape of the distributions of ΔR between the two leading jets and the transverse momentum of the W boson Wp_T. These two variables show a certain correlation, therefore we derive a 2D reweighting function $W_{WpT} * W_{DeltaR}$ on the data to MC ratio in the ΔR – $W\,p_T$ plane (see Fig. 56 (a)–(c)). Both functions, as listed in Eq. 6.13 are then applied to the W+jets MC sample. The ΔR function is also applied to the Z+jets MC sample conserving the event yield for this sample. Figs. 57 and 58 show the effect of the reweighting exemplarily on the RunIIb electron distributions in a comparison before and after the reweighting for the ΔR and $W\,p_T$ distribution, respectively.

The functions are defined as

$$F_{DeltaR} = 4.3822 - 0.255443\ \Delta R + 0.085197\ \Delta R^2 - 0.00630133\ \Delta R^3 \tag{6.13}$$

$$F_{WpT} = 0.215941 + 0.0538577\ (1 + Erf[(p_T^W - 7.96332)/(\sqrt{2} * (-8.97439))])$$

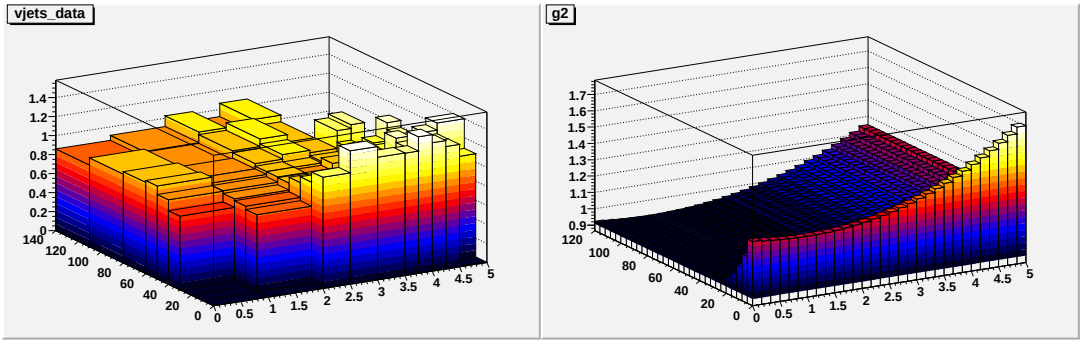

(a) Two-dimensional ratio of background subtracted W+jets data over W+jets MC in the $W\ p_T - \Delta R$ plane.

(b) Two-dimensional reweighting function for the data/MC ratio in the $W\ p_T - \Delta R$ plane.

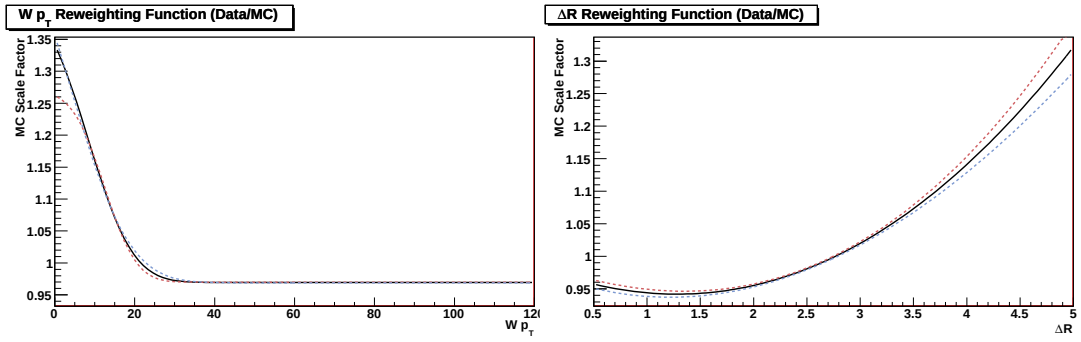

(c) One-dimensional reweighting function applied for ALPGEN MC parameterized in $W\ p_T$ obtained in the two-dimensional fit.

(d) One-dimensional reweighting function for ALPGEN MC parameterized in ΔR obtained in the two-dimensional fit.

Figure 56: Reweighting functions for $W\ p_T$ and ΔR obtained in a two-dimensional fit of the data/MC ratio of W+jets events. The one-dimensional functions are used to reweight simulated events generated with ALPGEN.

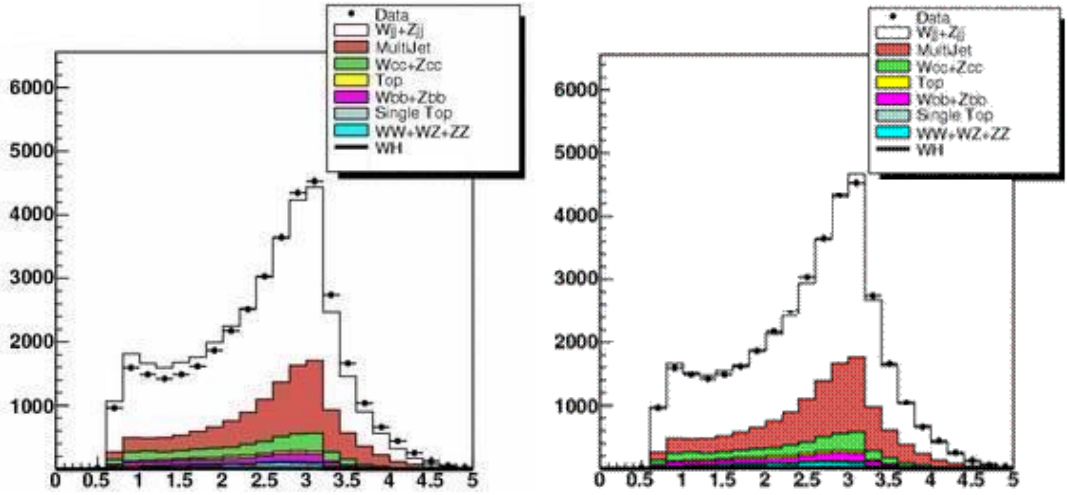

(a) ΔR before reweighting (b) ΔR after reweighting

Figure 57: Distribution of ΔR (in the RunIIb electron sample) before and after the application of the derived reweighting function on the ALPGEN samples. A significant overall improvement in the agreement is achieved.

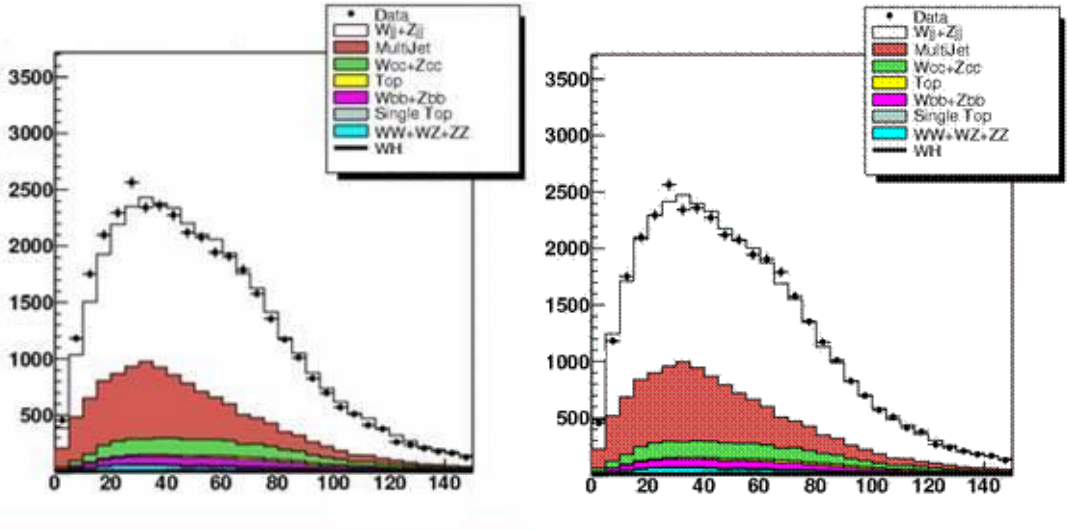

(a) W p_T before reweighting (b) W p_T after reweighting

Figure 58: Distribution of the W p_T (in the RunIIb electron sample) before and after the application of the derived reweighting function on the W + jets ALPGEN samples. A significant overall improvement in the agreement between data and simulation is visible.

6.6 MULTIJET BACKGROUND ESTIMATION

6.6.1 *Multijet background modeling*

Multijet events are events in which jets with rather low p_T are misidentified as leptons. In the electron case, most of these events come from γ + jets processes in which a jet passes the electron identification criteria. In the muon case, any multijet event could contain jets that contain muons that are then identified as isolated muons in the event.
The estimation of multijet background events (sometimes called QCD background) is a rather complicated procedure as we determine it from data. In the following, we will detail our process of deriving a proper estimate.

6.6.1.1 *Modeling strategy*

We build a modeling sample (short: template) that correctly models the kinematics of multijet events and is measured at low transverse momentum p_T. We have to make our estimate at low p_T to only identify non-signal-like events as our signal region for the WH analysis is at rather high p_T (> 50 GeV). Therefore, we scale up the template over the whole range as a way to account for the number of multijet events that pass our final selection. The way we make the estimation is by solving a system of two equations simultaneously:

$$N_L = N_\ell + N_{QCD}, \tag{6.14}$$
$$N_T = \varepsilon_\ell N_\ell + f_j N_{QCD}. \tag{6.15}$$

N_L denotes the number of data events in which a lepton passes the loose identification requirement (as described in Sec. 6.4). N_T accordingly describes the number of data events in which a lepton passes the tight identification criteria. N_ℓ represents the number of events in N_L with a real (correctly identified) lepton. N_{QCD} denotes the number of events in N_L with a misidentified lepton. ε_ℓ is the efficiency for a real lepton that passes the loose identification requirement to subsequently pass the tight identification requirement. f_j is the rate at which a jet that has been misidentified as a lepton passing the loose identification criteria to subsequently pass the tight identification requirement. Solving this system of equations for the number of multijet events in the tight sample yields:

$$N_{QCD}^T = \frac{f_j}{\varepsilon_\ell - f_j}(\varepsilon_\ell N_L - N_T) \tag{6.16}$$

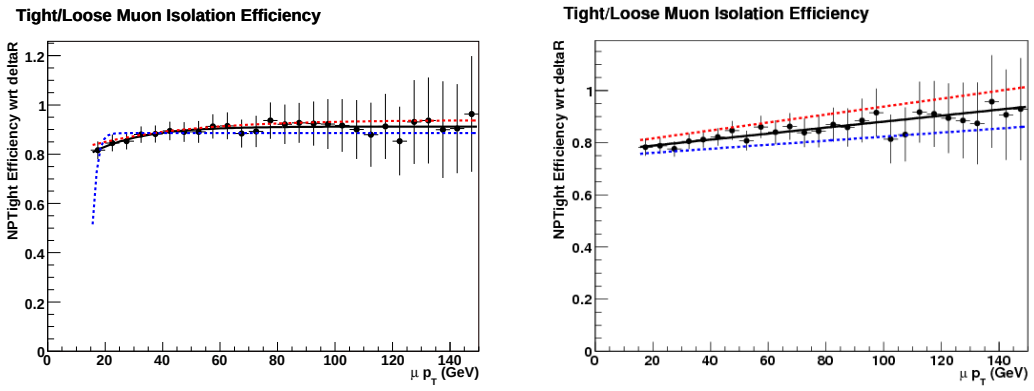

Figure 59: Muon efficiency parameterization for the multijet background, as a function of muon p_T, for the RunIIa (left) and RunIIb (right) sample.

This method is designed to work on a binned data sample, where N_L and N_T can be counted, and ε_ℓ and f_j are constants estimated on the sample as a whole. However, ε_ℓ and f_j may depend strongly on the kinematics of the events. The kinematic variations cannot be parameterized in each bin. Therefore, we estimate the multijet misidentification rate using an unbinned method, where each event in the loose identification sample contributes to the multijet estimation in the tight identification sample by assigning a weight w_i to each event. This weight can then depend on parameterized functions of ε_ℓ and f_j that depend on the kinematics $\vec{k}$ of a single event i:

$$w_i = \frac{f_j(\vec{k}_i)}{\varepsilon_\ell(\vec{k}_i) - f_j(\vec{k}_i)}(\varepsilon_\ell(\vec{k}_i) - \Theta_i^T), \tag{6.17}$$

where $\Theta^T = 1$ if the event satisfies the tight lepton identification criteria and 0 otherwise. The total multijet prediction in the tight sample is a sum over the weights in the inclusive loose sample:

$$N_{QCD}^T = \sum_{i=1}^{N^L} w_i \tag{6.18}$$

For electrons, the efficiency ε_e is parameterized in bins of transverse momentum of the electron p_T^e. For muons, the efficiency ε_μ is parameterized as a function of muon p_T^μ (see Fig. 59). The lepton efficiency rates are determined on data by studying a sample of $Z \to \ell\ell$ events.

6.6.1.2 *Misidentification rates*

The misidentification rate f_j for jets to be identified as electrons is determined as a function of electron p_T^e in events with $5 < \not{E}_T$

$<$ 15 GeV that otherwise match the signal preselection criteria, without the triangle cut (see Sec. 7.1.2). Separate parameterizations in p_T are determined for several two dimensional bins of $|\eta_{CAL}|$ and $\Delta\phi(\not\!\!E_T, e)$.

For electrons and muons, the misidentification rate for a given kinematic range is determined by the ratio of background subtracted data events in the loose and tight selection samples:

$$f_{QCD} = \frac{N_T - MC_T}{N_L - MC_L}, \tag{6.19}$$

where N_L (N_T) is the number of data events in the multijet estimation sample with a reconstructed loose (tight) lepton and MC_L (MC_T) is the total background estimation of the number of events with real loose (tight) leptons in them.

The electron misidentification rate is parameterized as:

$$f_{QCD}(p_T) = Exp[-a_0 p_T + a_1] + a_2 + a_3 p_T \qquad (|\eta| < 1.1) \tag{6.20}$$

$$f_{QCD}(p_T) = a_0 + a_1 p_T \qquad (1.5 < |\eta| < 2.5) \tag{6.21}$$

where a_N are the fit parameters. These parameters are determined separately in the EC and CC region of the calorimeter, using separate CC bins above and below $|\eta_{CAL}| = 0.7$. Each $|\eta_{CAL}|$ region is further divided into $\Delta\phi(\not\!\!E_T, e)$ bins between 0, 0.5, 1, 2 and π. In events with two jets, each of these individual $|\eta_{CAL}|$ and $\Delta\phi(\not\!\!E_T, e)$ bins is fitted separately. In events with three jets, parameterizations for each $|\eta_{CAL}|$ bin are determined, and these curves are scaled based on variations in $\Delta\phi(\not\!\!E_T, e)$ bins. Fig. 60 shows the fit obtained for each of these bins and each individual parameterized function overlaid with the corresponding data, with uncertainty bands.

The muon misidentification rate is determined separately for RunIIa and RunIIb data, with separate treatment above and below $\Delta\phi(\not\!\!E_T, \mu) = \pi/2$. Parameterization functions appear in Table 15 and are plotted in Fig. 61. These misidentification rates are applied to both two and three jet event samples.

	$\Delta\phi(\not\!\!E_T, \mu) < 1.5$	$\Delta\phi(\not\!\!E_T, \mu) > 1.5$
RunIIa	$a_0 + a_1 p_T$	Binned values used
RunIIb	$a_0 + a_1 p_T + a_2 p_T^2$	$a_0 + a_1 p_T$

Table 15: Muon misidentification rate (f_{QCD}) parameterization functions.

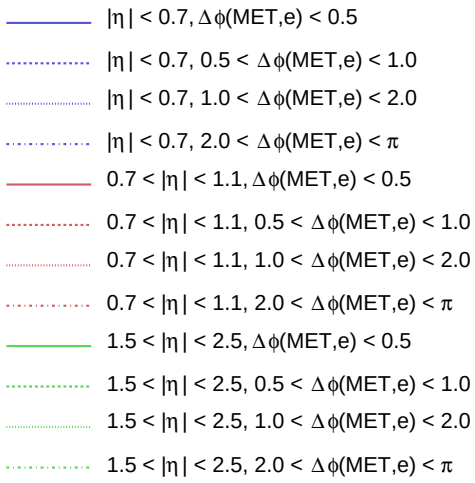

(a) Legend for the color code of the different regions in the misidentification plots.

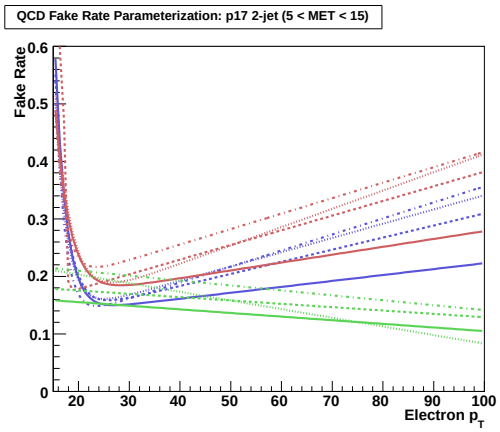

(b) RunIIa two jet sample.

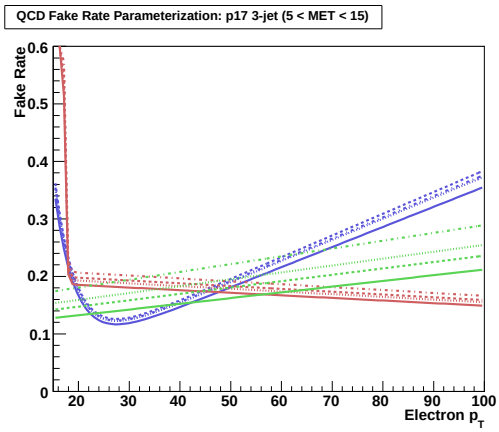

(c) RunIIa three jet sample.

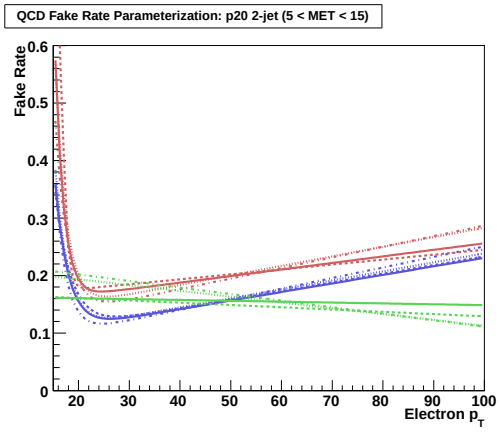

(d) RunIIb two jet sample.

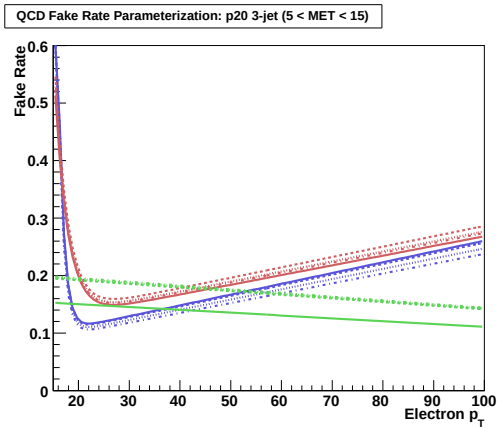

(e) RunIIb three jet sample.

Figure 60: Multijet misidentification rate in two jet and three jet electron channel as a function of electron p_T for each bin in $|\eta_{CAL}|$ vs. $\Delta\phi(\not\!\!E_T, e)$.

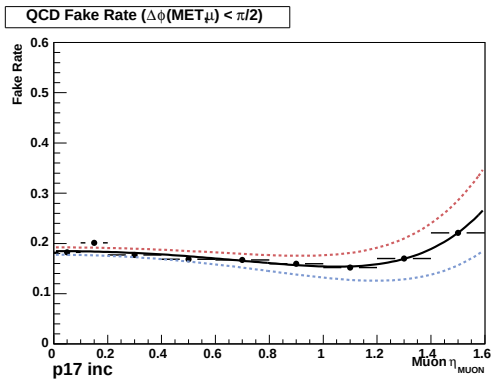

(a) RunIIa sample for $\Delta\phi(\not\!\!E_T, \mu) < \pi/2$.

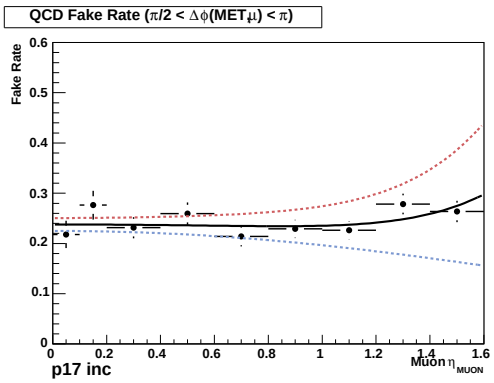

(b) RunIIa sample for $\Delta\phi(\not\!\!E_T, \mu) > \pi/2$.

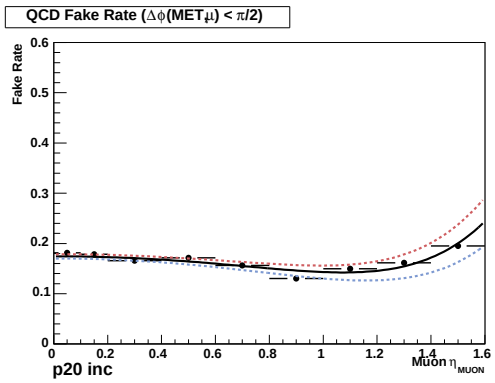

(c) RunIIb sample for $\Delta\phi(\not\!\!E_T, \mu) < \pi/2$.

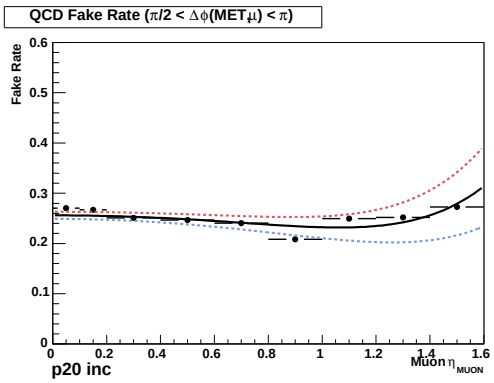

(d) RunIIb sample for $\Delta\phi(\not\!\!E_T, \mu) > \pi/2$.

Figure 61: Multijet misidentification rate ratios in the muon channel in data as a function of muon $|\eta_{det}|$, including parameterized fit functions, when applicable.

6.6.1.3 *Template normalization*

After applying the unbinned method of estimating the multijet background in order to build a multijet template, we normalize the template by performing a χ^2 minimization fit to the W boson transverse mass (m_T^W) distribution before applying b tagging. We thereby optimize agreement on the pretag level (before applying b tagging to our events). While determining the multijet template normalization factor, we vary the W+jet normalization so that the total number of estimated events matches the number of data events observed before applying b tagging. Separate multijet normalization factors are determined for both the loose and tight lepton identification criteria. These normalization factors remain fixed for the remainder of the analysis.

6.7 JET CORRECTIONS IN SIMULATED EVENTS

The jet energy scale correction applied to reconstructed jets in data (Sec. 5.5.3) is also applied to jets in simulated events. But as detector effects in simulated events can only be modeled to a certain level of accuracy, it is necessary to apply an additional correction on the energy resolution of jets. The energy resolution of jets in both data and simulated events is measured and a correction factor is applied to the simulated events. This correction is a Gaussian shaped smearing function σ_{smear} that is calculated as

$$\sigma_{\text{smear}} = \sqrt{\sigma^2_{\text{Data}} - \sigma^2_{\text{MC}}}. \tag{6.22}$$

σ_{Data} and σ_{MC} denote the width of the transverse momentum distribution of the jet. By applying σ_{smear} to the simulated events, we correct for the difference in width and therefore energy resolution. If the transverse momentum after applying the jet energy scale correction drops below a threshold of $p_T < 15$ GeV the jet is removed from the event.
As described in Sec. 5.5.4, vertex confirmation is also applied on jets in simulated events. Additionally, we correct for differences in efficiency between data and simulation by applying a random removal of jets. This random removal takes into account a certain probability calculated from the ratio of efficiencies between data and simulation to remove jets from the event. This probability is parameterized in p_T and η of the jet.

6.8 TAGGING CORRECTION FACTORS

Due to differences in efficiency between data and simulation, we apply correction factors for both the taggability criterion and the b jet identification.

6.8.1 *Taggability Correction Factors*

Before we apply b tagging to the jets in our analysis, we ask for jets to be taggable (as described earlier in Sec. 5.6). For simulated events, we apply taggability scale factors to account for tracking mismodeling in the simulation compared to data. The scale factors will make the taggability efficiency of simulated events match the one measured in data. We measure this efficiency in the two jet samples in both data and simulation. To determine the efficiency, we take the ratio of taggable jets to all jets in the sample. We then take the ratio of the efficiencies in data to simulation to estimate the scale factors. They determined in four different regions of distance to the primary vertex along the z axis, z_{vtx}. We measure them as a function of jet p_T (which is applied to the RunIIa sample only, as the RunIIb sample does not show any p_T dependence in taggability efficiency) and jet η. Figs. 62-63 (RunIIa), and Figs. 64-65 (RunIIb), show in plots (a) and (b) the parameterizations for $-40 < z_{vtx} < -30$ cm and $-30 < z_{vtx} < 0$ cm and in plots (c) and (d) the parameterizations for $0 < z_{vtx} < 30$ cm and $30 < z_{vtx} < 40$ cm.

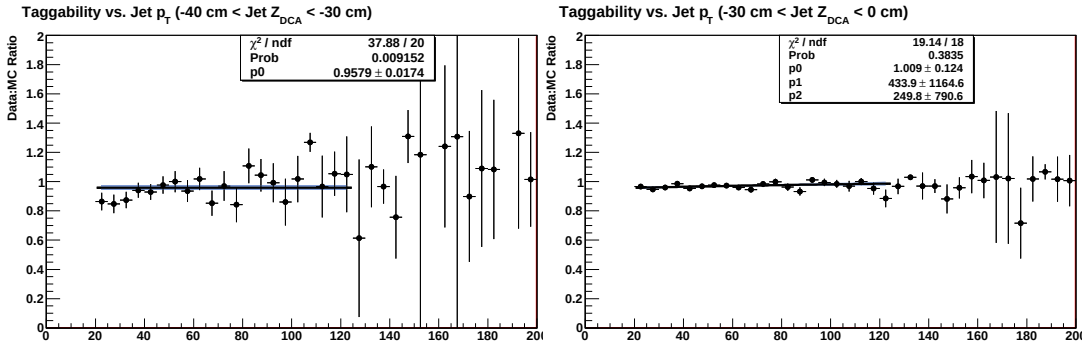

(a) Jet taggability scale factor measured in the $-40 < z_{vtx} < -30$ cm bin as a function of p_T^{jet}

(b) Jet taggability scale factor measured in the $-30 < z_{vtx} < 0$ cm bin as a function of p_T^{jet}

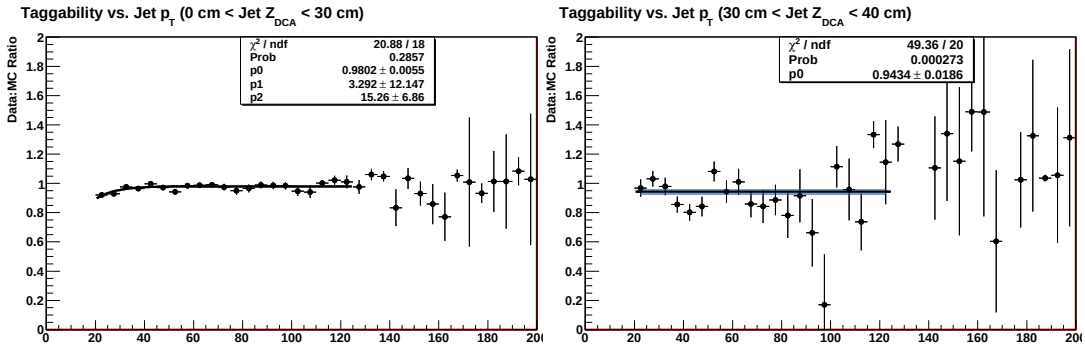

(c) Jet taggability scale factor measured in the $0 < z_{vtx} < 30$ cm bin as a function of p_T^{jet}

(d) Jet taggability scale factor measured in the $30 < z_{vtx} < 40$ cm bin as a function of p_T^{jet}

Figure 62: Jet taggability scale factors measured in the muon channel versus transverse momentum p_T of the jet measured from the data and simulated samples of the RunIIa analysis. The black line represents the nominal fit and the blue band represents the $\pm 1\sigma$ uncertainty band on the fit.

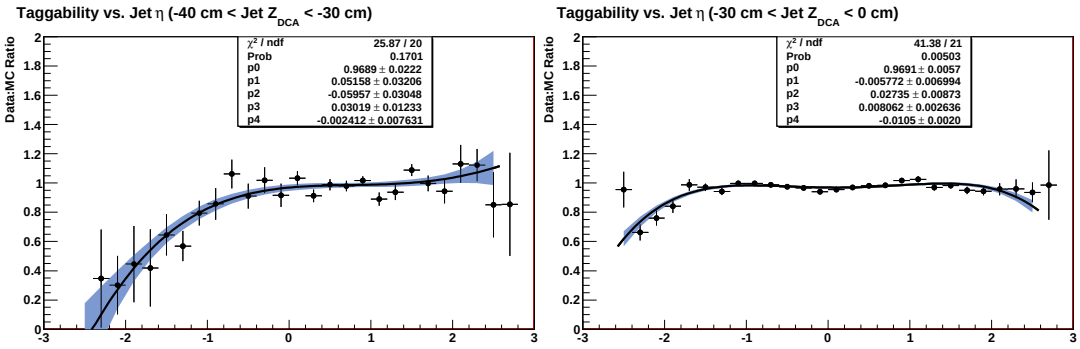

(a) Jet taggability scale factor measured in the $-40 < z_{vtx} < -30$ cm bin as a function of η^{jet}

(b) Jet taggability scale factor measured in the $-30 < z_{vtx} < 0$ cm bin as a function of η^{jet}

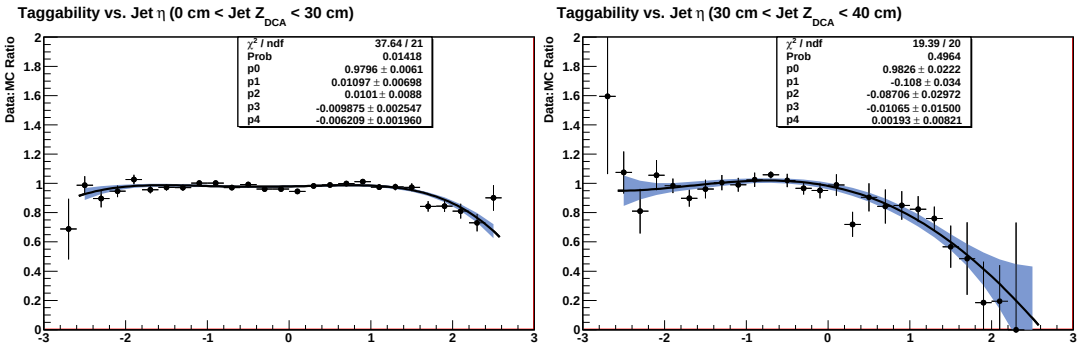

(c) Jet taggability scale factor measured in the $0 < z_{vtx} < 30$ cm bin as a function of η^{jet}

(d) Jet taggability scale factor measured in the $30 < z_{vtx} < 40$ cm bin as a function of η^{jet}

Figure 63: Jet taggability scale factors measured in the muon channel versus jet η measured from the data and simulated samples of the RunIIa analysis. The black line represents the nominal fit and the blue band represents the $\pm 1\sigma$ uncertainty band on the fit.

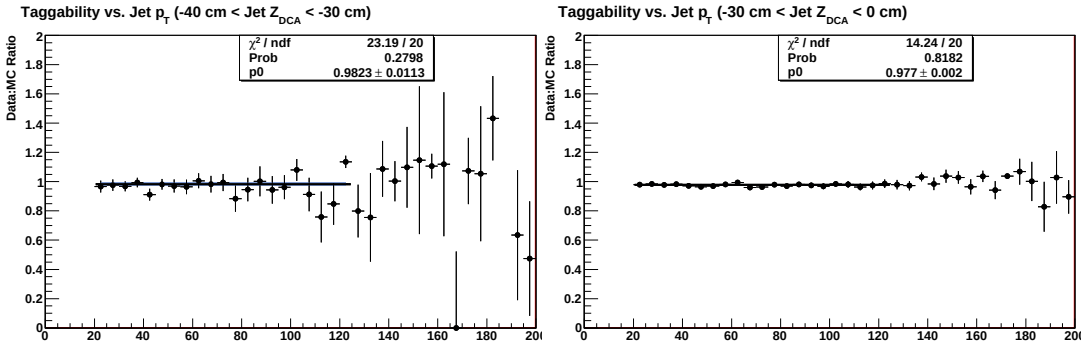

(a) Jet taggability scale factor measured in the $-40 < z_{vtx} < -30$ cm bin as a function of p_T^{jet}

(b) Jet taggability scale factor measured in the $-30 < z_{vtx} < 0$ cm bin as a function of p_T^{jet}

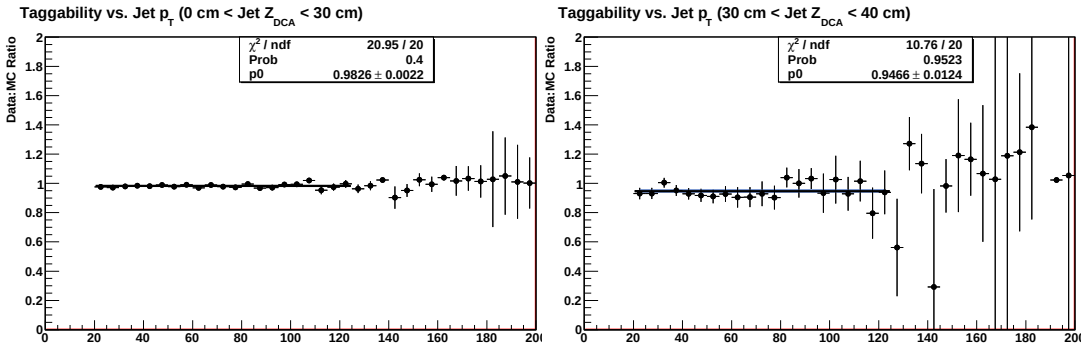

(c) Jet taggability scale factor measured in the $0 < z_{vtx} < 30$ cm bin as a function of p_T^{jet}

(d) Jet taggability scale factor measured in the $30 < z_{vtx} < 40$ cm bin as a function of p_T^{jet}

Figure 64: Jet taggability scale factors measured in the muon channel versus transverse momentum p_T of the jet measured from the data and simulated samples of the RunIIb analysis. The black line represents the nominal fit and the blue band represents the $\pm 1\sigma$ uncertainty band on the fit.

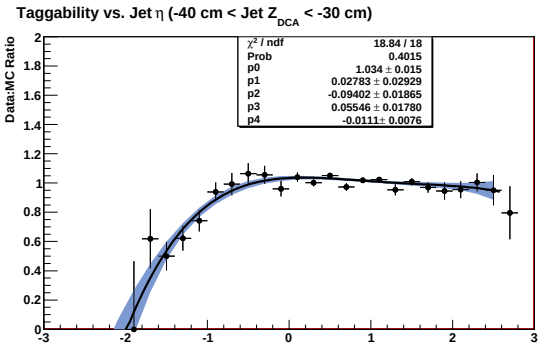

(a) Jet taggability scale factor measured in the $-40 < z_{vtx} < -30$ cm bin as a function of η^{jet}

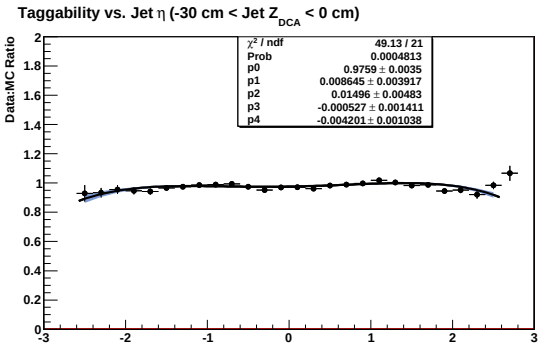

(b) Jet taggability scale factor measured in the $-30 < z_{vtx} < 0$ cm bin as a function of η^{jet}

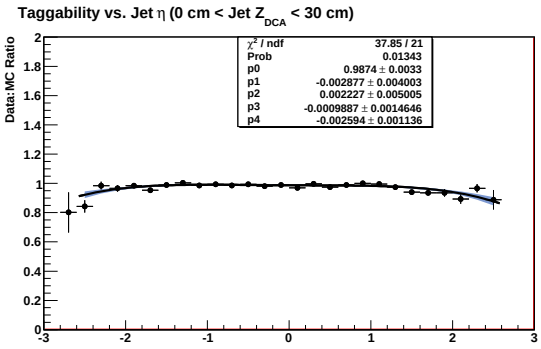

(c) Jet taggability scale factor measured in the $0 < z_{vtx} < 30$ cm bin as a function of η^{jet}

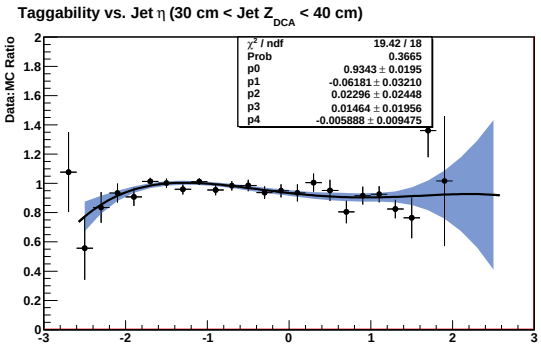

(d) Jet taggability scale factor measured in the $30 < z_{vtx} < 40$ cm bin as a function of η^{jet}

Figure 65: Jet taggability scale factors measured in the muon channel versus jet η measured from the data and simulated samples of the RunIIb analysis. The black line represents the nominal fit and the blue band represents the $\pm 1\sigma$ uncertainty band on the fit.

6.8.2 *b Tagging Correction Factors*

The efficiency of correctly identifying (tagging) a b jet with the NN b tagging algorithm in simulated events is higher than in data. Therefore, e correct this discrepancy by applying additional b jet identification scale factors. These factors depend on the kinematics of the jets.

We apply the scale factors on tagged events as follows:
The scale factor weight for double tagged events, DT_{weight} is defined as

$$DT_{weight} = SF_{j1} \times SF_{j2} \tag{6.23}$$

where SF_{j1} and SF_{j2} are the scale factors for the leading and second leading jet, respectively. They are derived as functions of the ratio of data to simulation of the jet p_T and jet η. Fig. 66 shows the corresponding functions for the two different tagging points, the loose point (called L2 in the plot) and the tight point.

The scale factor weight (ST_{weight}) on the single tagged events is determined by:

$$ST_{weight} = ST_{weight}^{STevent} + ST_{weight}^{DTevent} \tag{6.24}$$

where $ST_{weight}^{STevent}$ is the event weight calculated for the single exclusively tagged event, and $ST_{weight}^{DTevent}$ is the contribution from double tagged events that can migrate (due to the scale factor) into the single tagged sample. The single tagged event weights are calculated as

$$ST_{weight}^{STevent} = SF_j \tag{6.25}$$

where SF_j is the scale factor for the tagged jet in the single tagged event.

The scale factor for the other jet in the event is calculated as the product of the single tag scale factor SF_j and the complementary factor of the tagging scale factor in the double tagged sample (1-SF^{DT}). The latter represents events from the simulated DT event sample that migrate to the ST sample due to the application of the efficiency scale factor on simulated events that causes less jets to be double tagged. Therefore, the weight applied to the second jet in ST events reads:

$$ST_{weight}^{DTevent} = (1 - SF_{\bar{j}}^{DT}) * SF_j. \tag{6.26}$$

This parameterization is valid only in the case where the DT selection cut is looser than the ST selection cut, which is of course

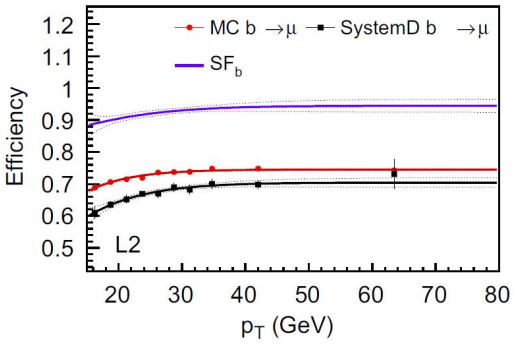

(a) Loose tagging criterion, as a function of p_T.

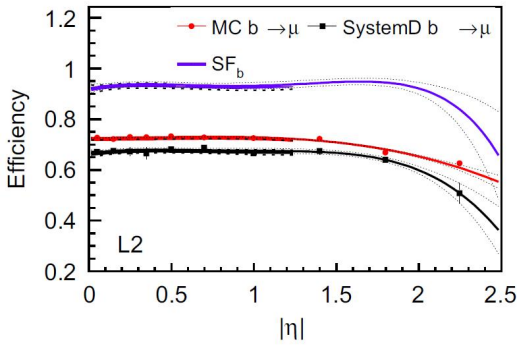

(b) Loose tagging criterion, as a function of jet η.

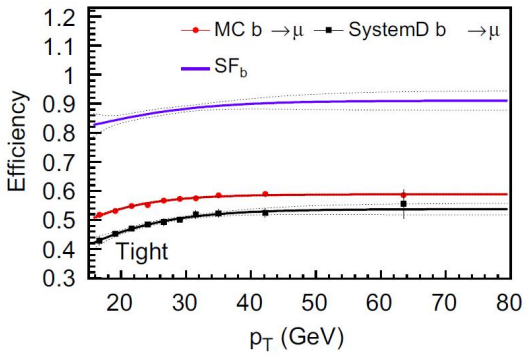

(c) Tight tagging criterion, as a function of p_T.

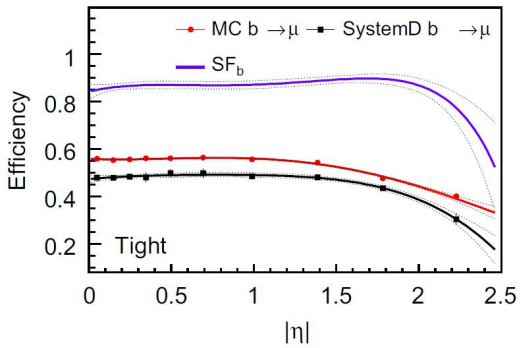

(d) Tight tagging criterion, as a function of jet η.

Figure 66: b identification scale factors for the loose (L2, upper row) and tight (lower row) tagging criterion, parameterized in p_T (left column) and jet η (right column). The black line shows the data efficiency on a $b\bar{b}$ enriched data sample, the red line shows the efficiency in simulated events. The blue line shows the derived scale factor to compensate for the difference in efficiencies. [65]

the case in this analysis.

7

ANALYSIS

We are looking for events in which a W boson is produced together with a Higgs boson, so our desired event topology in the final state is a lepton and missing transverse energy to account for the ν coming from the W boson decay and two b quark jets coming from the decaying Higgs boson. More precisely, this analysis is based on the selection of events with exactly one electron (muon) with transverse momentum $p_T > 15\,\text{GeV}$ within a pseudorapidity range of $|\eta| < 2.5(1.6)$, and a minimum of missing transverse energy $\not\!\!E_T > 20\,\text{GeV}$. Events are selected based on the number of jets in the pseudorapidity range of $|\eta| < 2.5$. We require the event to have exactly two or three jets with a $p_T > 20\,\text{GeV}$ for the leading jet (after corrections to the jet energy scale are applied, as described in Sec. 5.4.5). A 2-dimensional 'triangular' cut $M_W^T > 40 - 0.5 \cdot \not\!\!E_T$ (where M_W^T is the reconstructed transverse mass of the W boson) is applied to reduce the background coming from low energy multijet events (commonly called QCD background in this analysis). We also require that the sum (H_T) of the p_T of the jets exceeds 60 GeV (80 GeV in the 3-jet case). For a cleaner electron reconstruction, we exclude part of the ICD region of the detector ($1.1 < \eta_{det} < 1.5$).

We reject events with an additional lepton (a muon within $|\eta| < 2.0$ or an electron within $|\eta| < 2.5$ for the respective channel) isolated from jets and having a transverse momentum above $p_T > 15\,\text{GeV}$ to decrease backgrounds coming from events in which Z bosons or a $t\bar{t}$ pair are produced which then decay into two leptons. Only events are selected in which the production vertex of the event has a maximal distance of 40 cm from the nominal interaction point of the detector (measured on the z axis). We also require events to have at least three attached tracks.

In total, we split our analysis in 8 channels, electron and muon, RunIIa and RunIIb sample, two and three jets[1]. We perform separate analyses for these channels and combine their results in the final calculation of our result to optimize sensitivity.

7.1 *W* BOSON RECONSTRUCTION

The *W* boson plays an important role in this analysis. Without a proper reconstruction of the *W* boson, we would not be able to conduct a search for a Higgs boson in the *WH* production

1 For improved readability of the text, plots of the three jet channel are only shown in Appendix A.

channel which is superior to a direct search at low mass due to background composition as mentioned before. In this analysis, we are considering only leptonic W decays because of their distinct signature to decay into a lepton and a neutrino. To properly reconstruct the W boson signature in its leptonic decay channel, we therefore have to identify an electron or a muon in the final state as well as missing transverse energy $\not\!\!E_T$ to account for the ν. At this level, no b tagging is applied.

7.1.1 *Lepton Reconstruction*

We use the tight selection criteria for electrons and muons detailed in Sec. **??**. Additionally, we require the transverse momentum of the lepton in the event to be $p_T > 15$ GeV and reject a second lepton in the event as described in Sec. **??**. The distributions we obtain for the kinetic variables of the lepton in our final event sample are shown in Fig. 67 for the RunIIa sample in the electron channel, Fig. 68 for the RunIIa muon sample, Fig. 69 for the RunIIb electron sample and Fig. 70 for the RunIIb muon sample. All figures show event samples with exactly two jets in the final state. They show the transverse momentum of the lepton, the lepton energy, the pseudorapidity η and the azimuthal angle ϕ of the reconstructed lepton in the event. The figures in all channels, electron and muon, as well as RunIIa and RunIIb event samples show good agreement between data and simulated events. The event samples with three jets in the events also show good agreement in all kinematic lepton variables, but are not explicitly shown here.

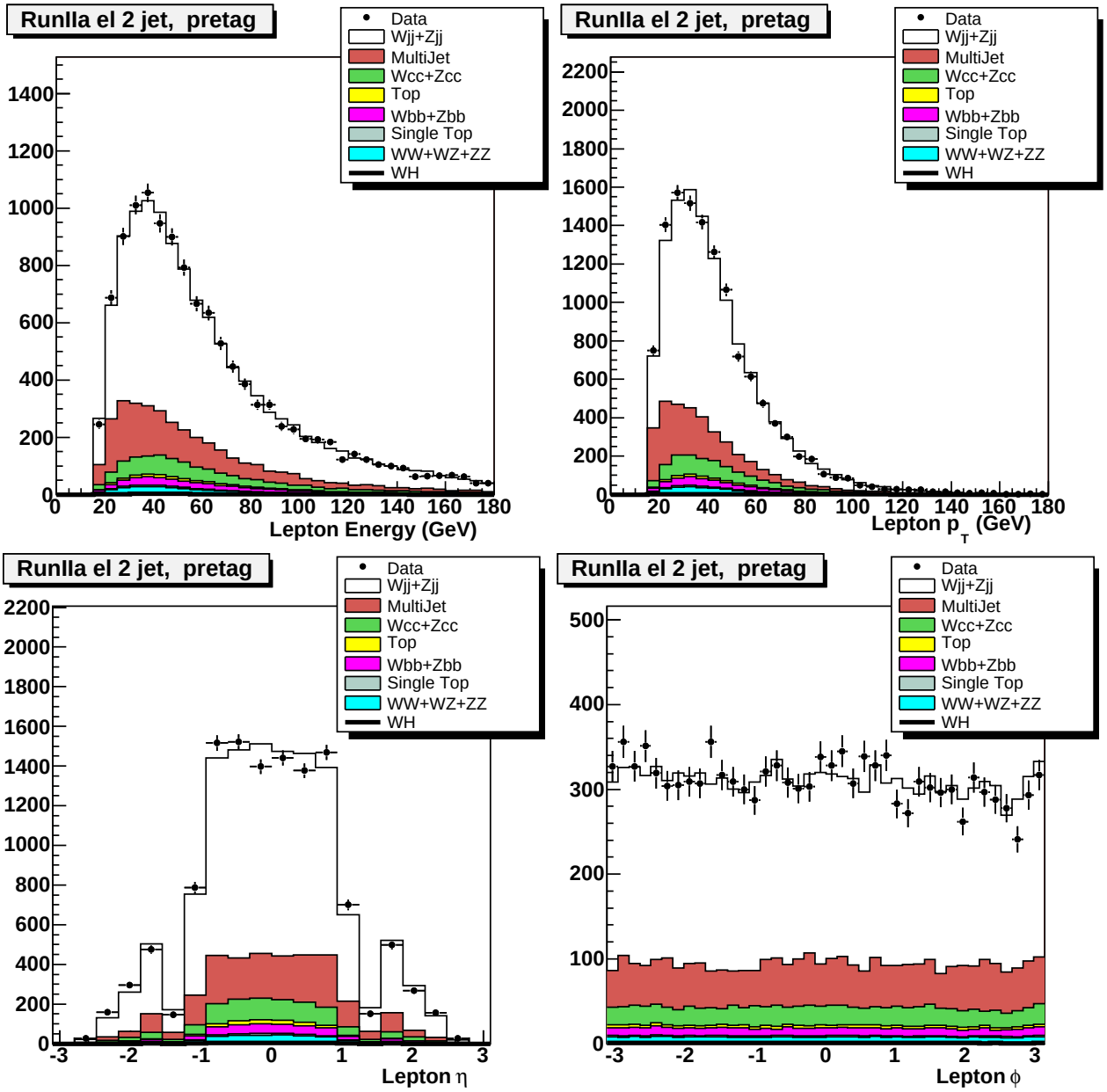

Figure 67: Kinematic distributions of the lepton in *RunIIa* events in the *electron* channel with exactly two jets. No b tagging has been applied.

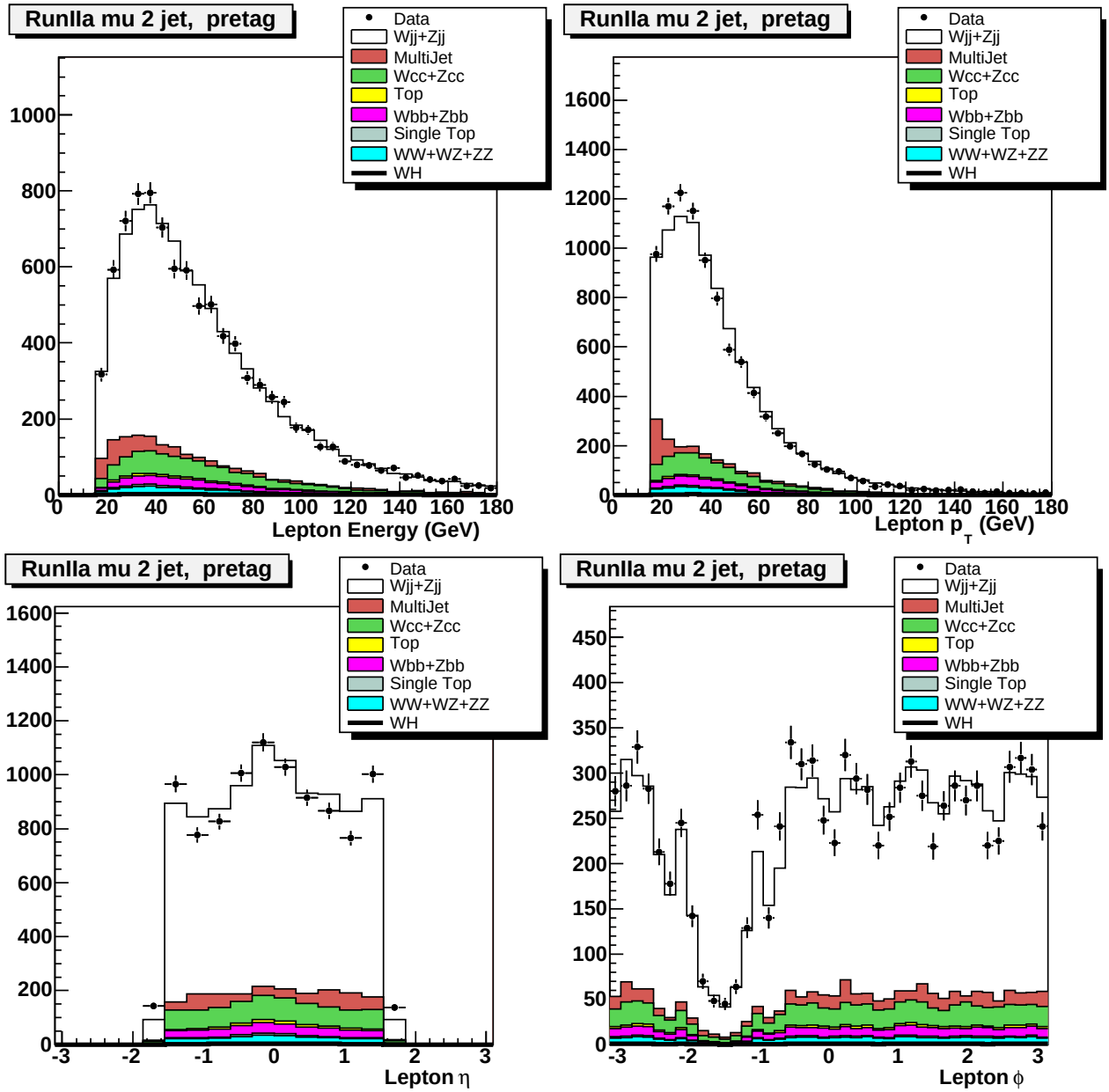

Figure 68: Kinematic distributions of the lepton in *RunIIa* events in the *muon* channel with exactly two jets. No b tagging has been applied.

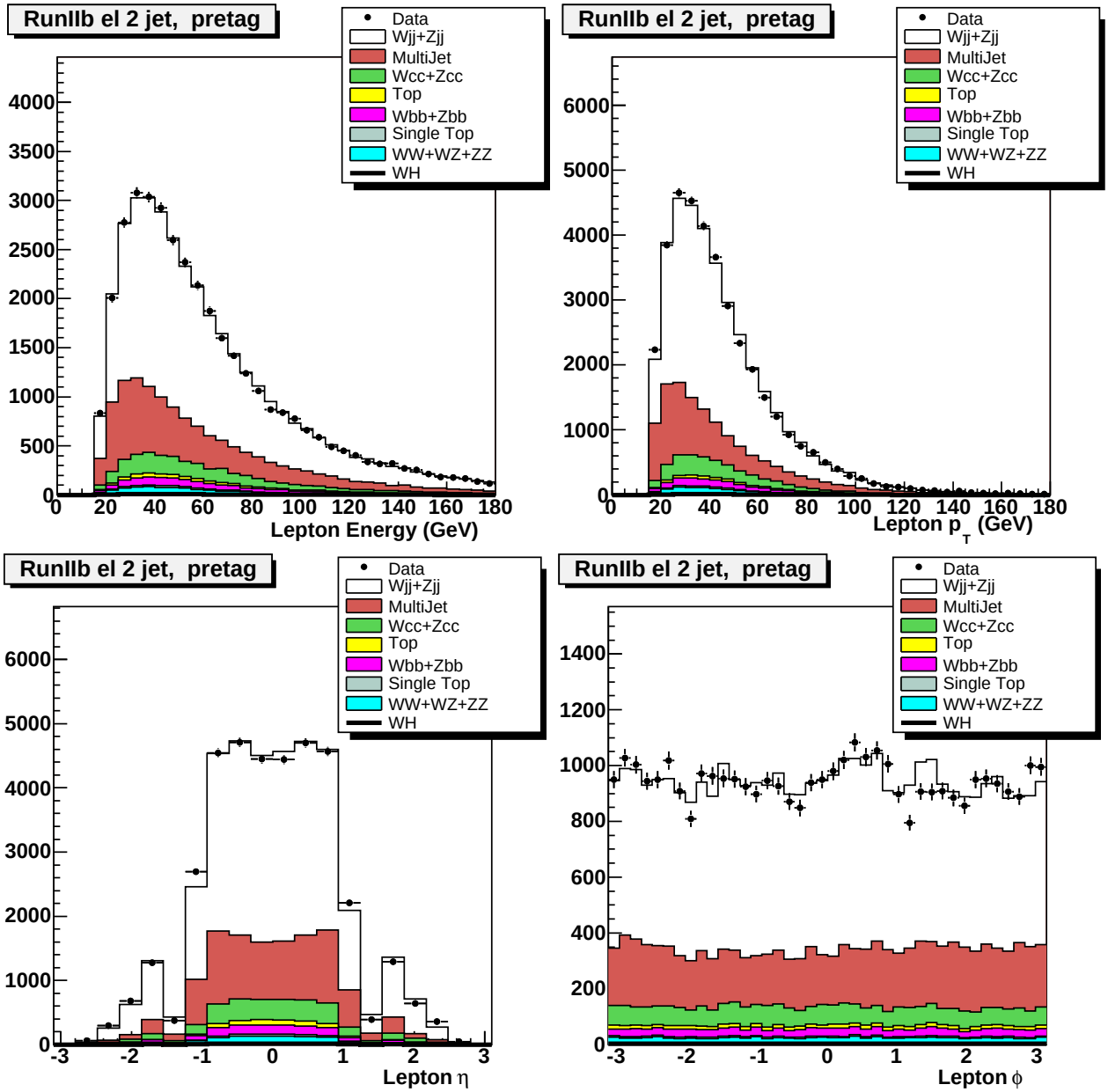

Figure 69: Kinematic distributions of the lepton in *RunIIb* events in the *electron* channel with exactly two jets. No b tagging has been applied.

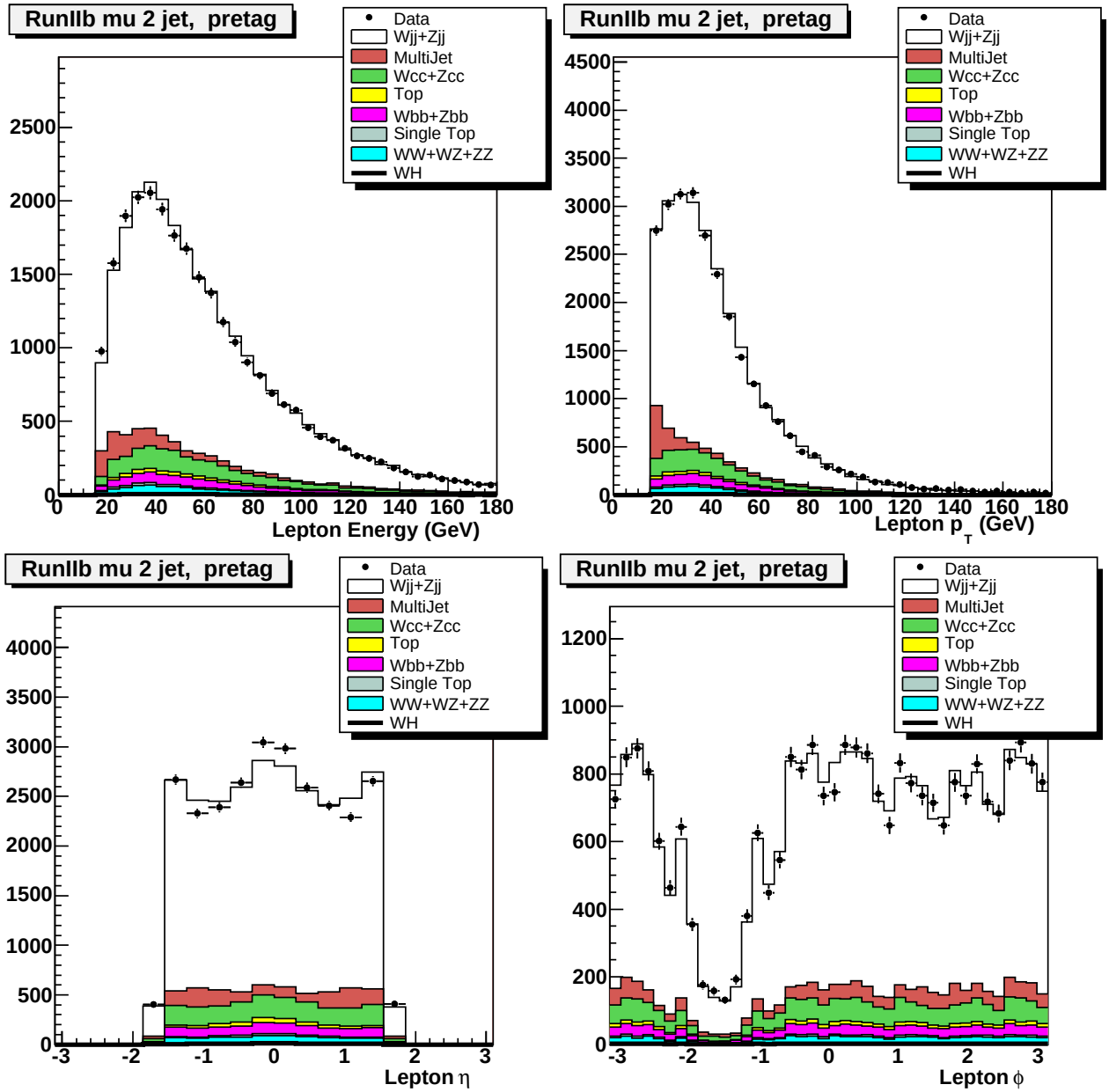

Figure 70: Kinematic distributions of the lepton in *RunIIb* events in the *muon* channel with exactly two jets. No b tagging has been applied.

7.1.2 $\not{E}_T$ *Reconstruction*

To account for the neutrino from the decaying W boson, we require a minimum of 20 GeV of missing transverse energy in the final state. The transverse momentum and transverse mass M_T^W of the W boson can be reconstructed from the kinematics of the lepton and the missing transverse energy:

$$M_T^W = \sqrt{(\not{E}_T + p_T^\ell)^2 - (\not{E}_T{}^x + p_x^\ell)^2 - (\not{E}_T{}^y + p_y^\ell)^2} \qquad (7.1)$$

The reconstructed missing transverse energy $\not{E}_T$ is shown in Fig. 71 separately for all channels.

Before looking how the data compares to the full background simulation including the multijet background estimation from data for the properties of the W boson, we will have a closer look at the multijet background events.

The multijet background becomes more important in the transverse mass distribution for values above about 35 GeV. This is due to the requirements of 15 GeV on the transverse momentum of the muon candidate and 20 GeV on the $\not{E}_T$.

Even though we apply a multi-dimensional misidentification rate in the multijet background estimation (as described in Sec. 6.6.1), it is difficult to get a good description in the region of low $\not{E}_T$ and low M_T^W because of mismeasurements on $\not{E}_T$. In this region the lepton and the $\not{E}_T$ have the same direction.

To significantly reduce the multijet background, we exclude this region by applying a triangle cut of $M_T^W > 40 - 0.5\ \not{E}_T$. Fig. 72 shows the two-dimensional ratio of (data / WH mc) for the electron sample in the M_T^W–$\not{E}_T$ plane, the triangle cut we apply is shown as a black line.

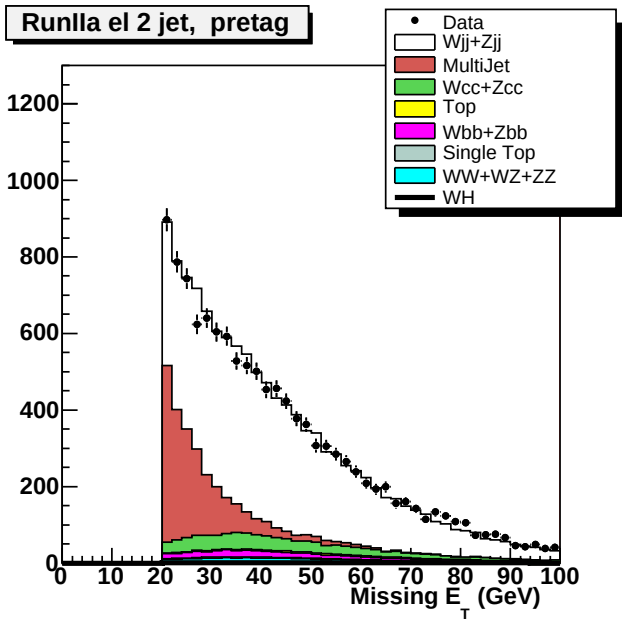

(a) $\not\!\!E_T$ for the RunIIa electron sample.

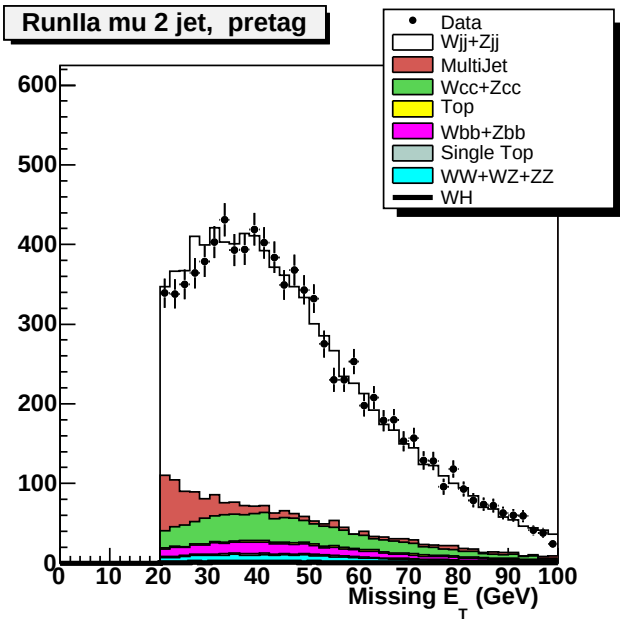

(b) $\not\!\!E_T$ for the RunIIa muon sample.

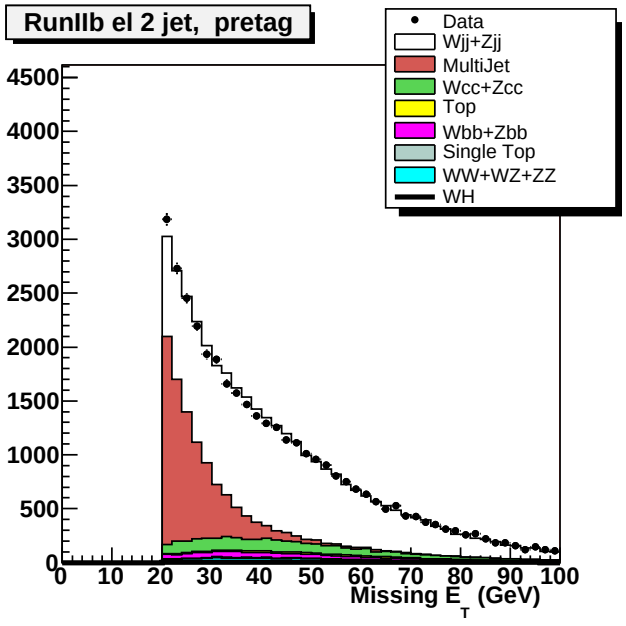

(c) $\not\!\!E_T$ for the RunIIb electron sample.

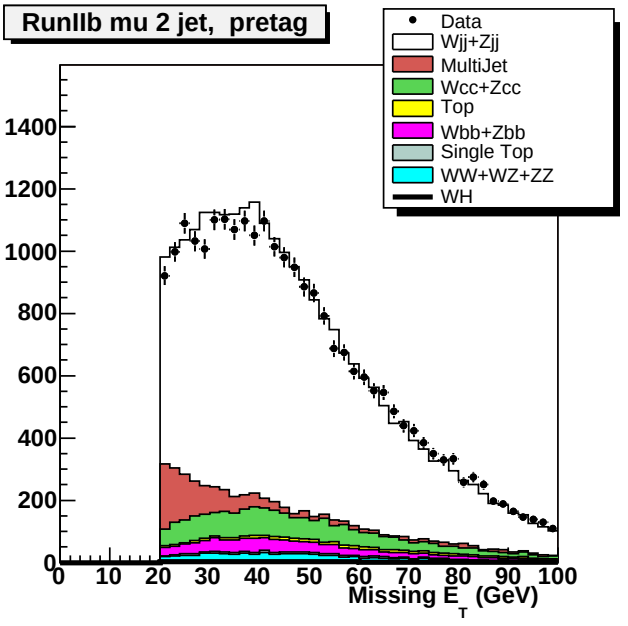

(d) $\not\!\!E_T$ for the RunIIb muon sample.

Figure 71: Missing transverse energy distributions for all four analysis channels in events with two jets in the final state. No b tagging has been applied.

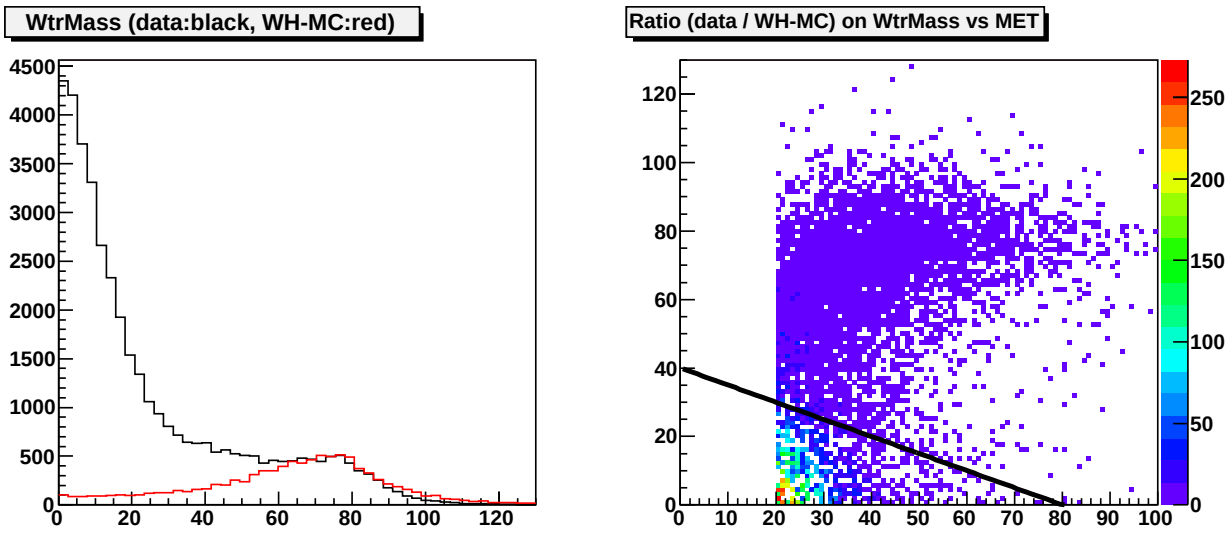

(a) W transverse mass in data events (black) and in the simulated WH signal sample (red).

(b) Two-dimensional ratio plot of data to WH MC of the $\not\!\!E_T$ (x-axis) vs. the W transverse mass (y-axis). The black line represents the cut we apply to reduce the multijet background.

Figure 72: Triangle Cut to reduce the multijet background. Comparing the two distributions in the left plot with the applied cut in the right plot shows that we cut on events in a region where the expected signal is low.

7.1.3 *W Boson Reconstruction*

We now take a look at the reconstructed quantities of the *W* boson, namely its transverse mass and transverse momentum p_T. The results of their reconstruction in the electron (muon) channels are shown in Fig. 73 (74) for the RunIIa sample and in Fig. 75 (76) for the RunIIb sample. The shape and amplitude of these distributions agree well between data and simulation. In the *W* transverse mass distribution we can see the Jacobian peak as the sign of *W* boson production in our data sample.

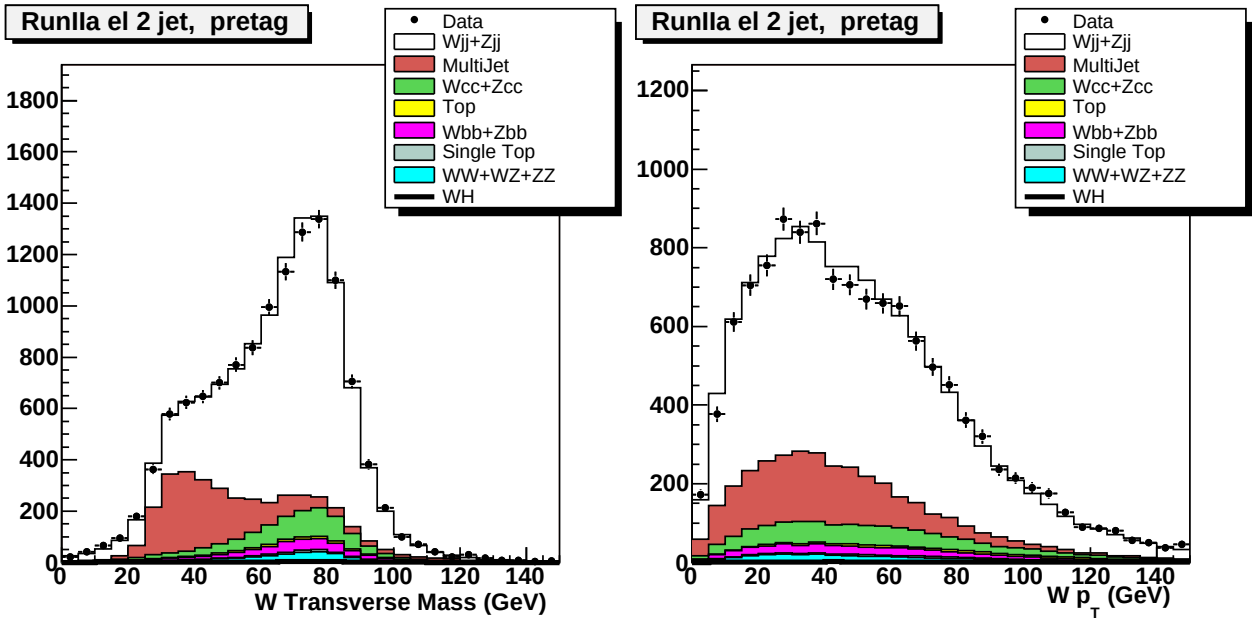

Figure 73: W transverse mass and transverse momentum in *RunIIa* events in the *electron* channel with exactly two jets. No b tagging has been applied.

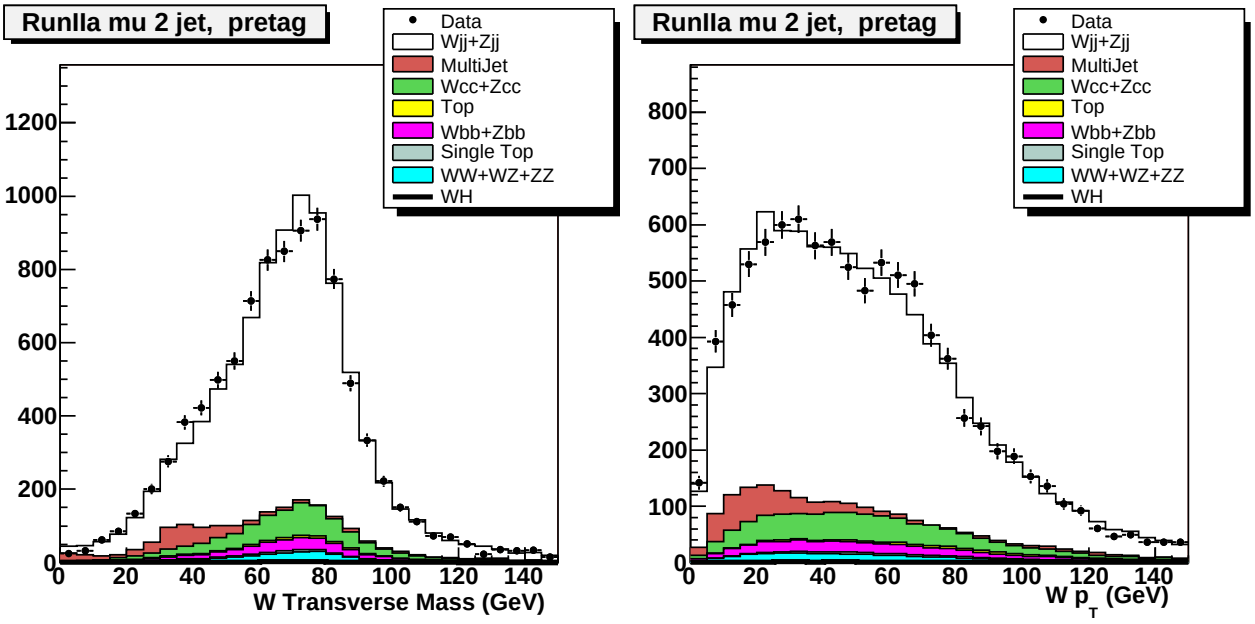

Figure 74: W transverse mass and transverse momentum in *RunIIa* events in the *muon* channel with exactly two jets. No b tagging has been applied.

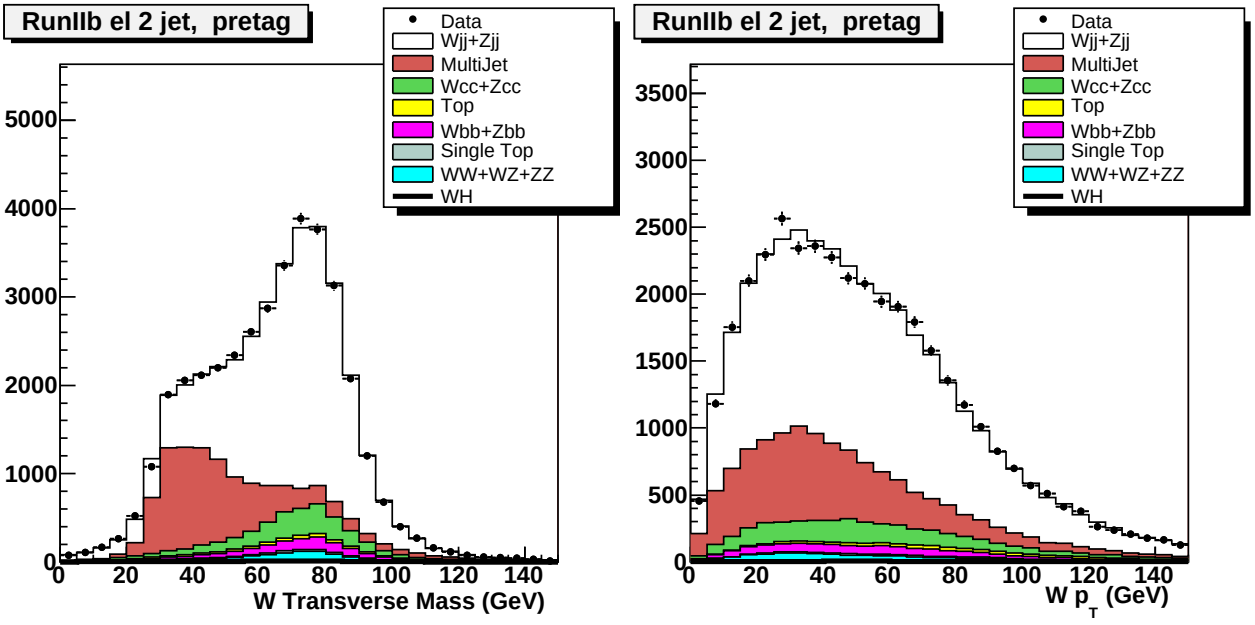

Figure 75: W transverse mass and transverse momentum in *RunIIb* events in the *electron* channel with exactly two jets. No b tagging has been applied.

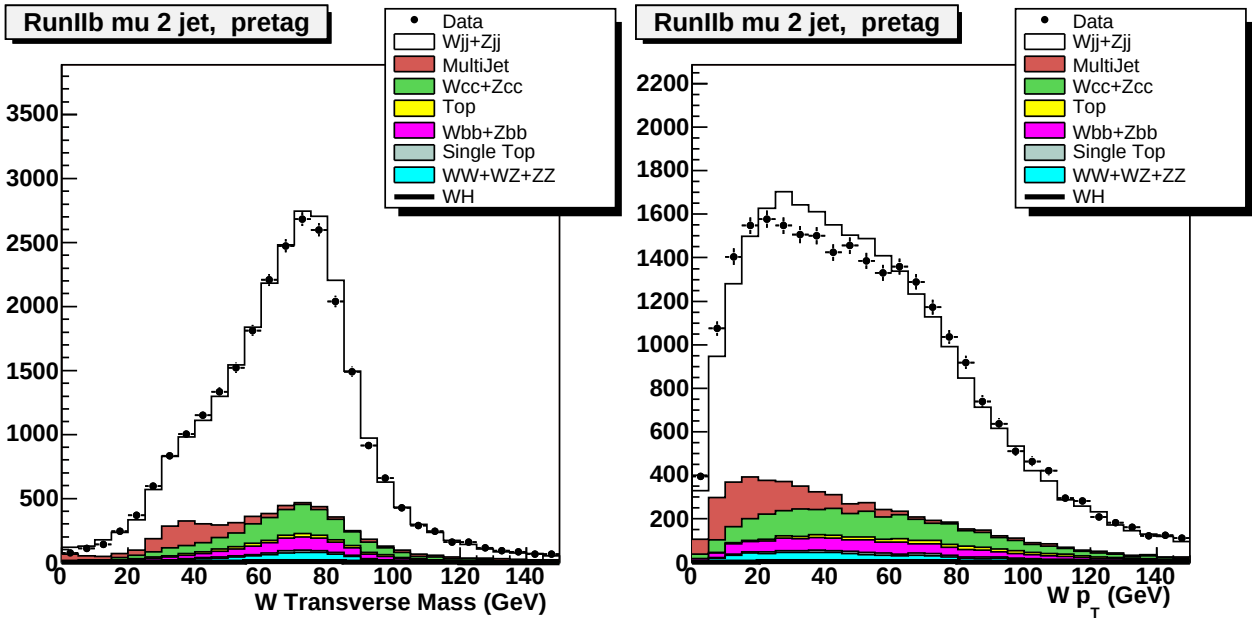

Figure 76: W transverse mass and transverse momentum in *RunIIb* events in the *muon* channel with exactly two jets. No b tagging has been applied.

Fig. 77 shows the combination of all events across channels with exactly two jets in the final state for the lepton p_T, $\not\!\!E_T$ and the transverse mass and momentum of the W boson. Also the combination, having a much higher statistics than the single channels, shows good agreement between data and simulation.

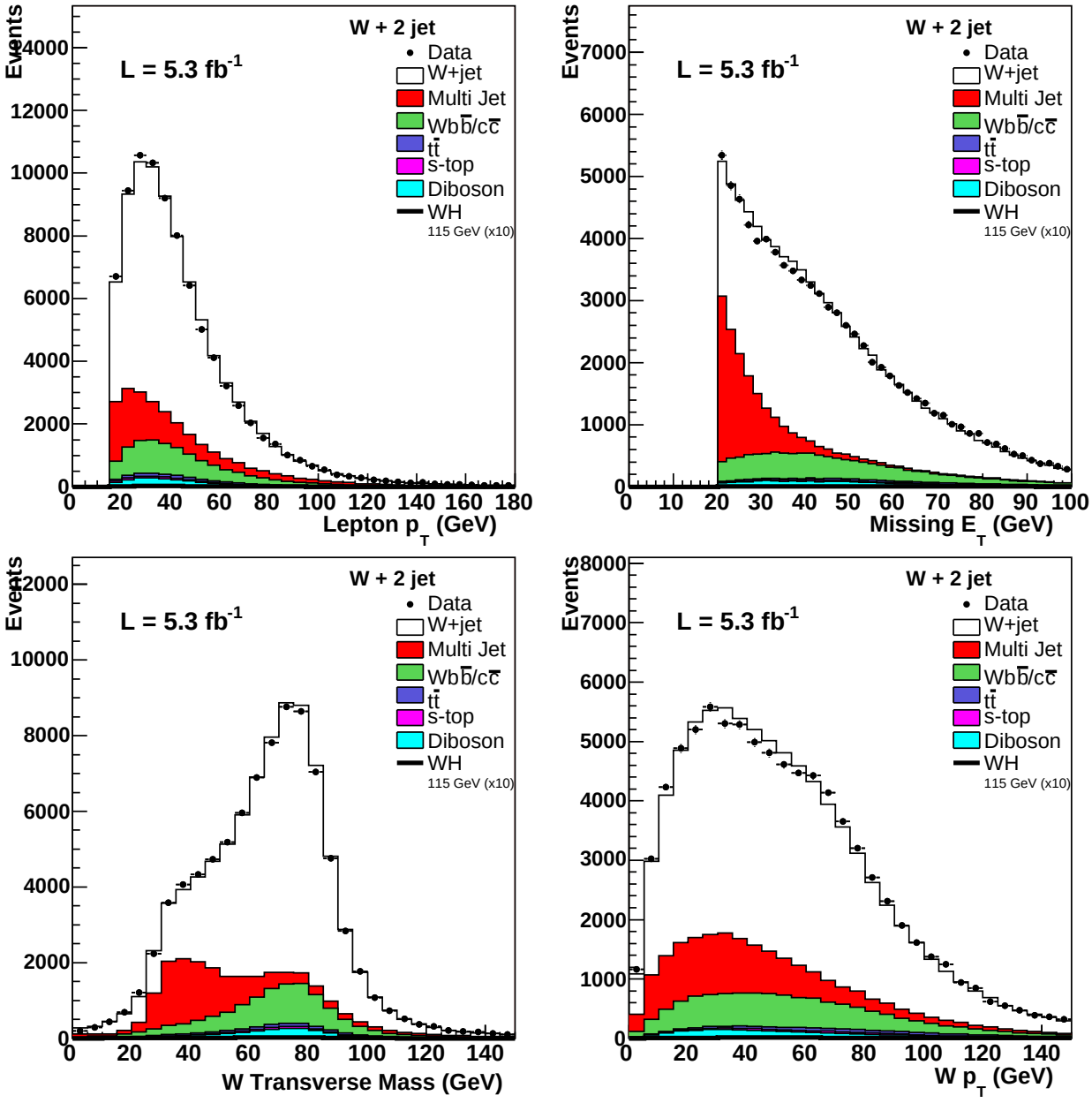

Figure 77: Kinematic distributions of the lepton p_T and $\not{E}_T$ (top row) and transverse mass and momentum of the W boson (bottom row) for the combination of all subsets for exactly two jets.

7.2 HIGGS BOSON RECONSTRUCTION

7.2.1 *Pretag Level*

For the identification of a Higgs boson at low mass, we want to identify two jets originating from b quarks in the final state. We require the jets in the final state to have at least 20 GeV of transverse momentum. We use the jet selection criteria described in Sec. 5.4.5 to select samples with either exactly two jets or exactly three jets in the final state. The three jet sample accounts for cases in which gluon radiation adds a third jet to the final state. Including this channel adds about 5% in terms of sensitivity to the analysis. Additionally to the jet p_T requirements, we require the sum of all transverse jet momenta in the event to be $H_T > 60$ GeV (> 80 GeV in the three jet case). This effectively lifts the p_T requirement on the leading jet[2] up to 30 GeV in the case of the two jet sample. The distributions of the data to simulation comparisons of the leading and second leading jet p_T, η and ϕ, as well as the sum of the transverse momenta H_T and the angular separation ΔR between the jets are shown in Fig. 78 (79) for the RunIIa electron (muon) sample and Fig. 80 (81) for the RunIIb electron (muon) sample. Fig. 82 shows the combination of all events across channels with exactly two jets in the final state for the jet η, H_T and ΔR distributions. All distributions show good agreement between data and simulation.

2 We order the jets in terms of transverse momentum p_T. So the leading jet denotes the jet with the highest p_T in the event.

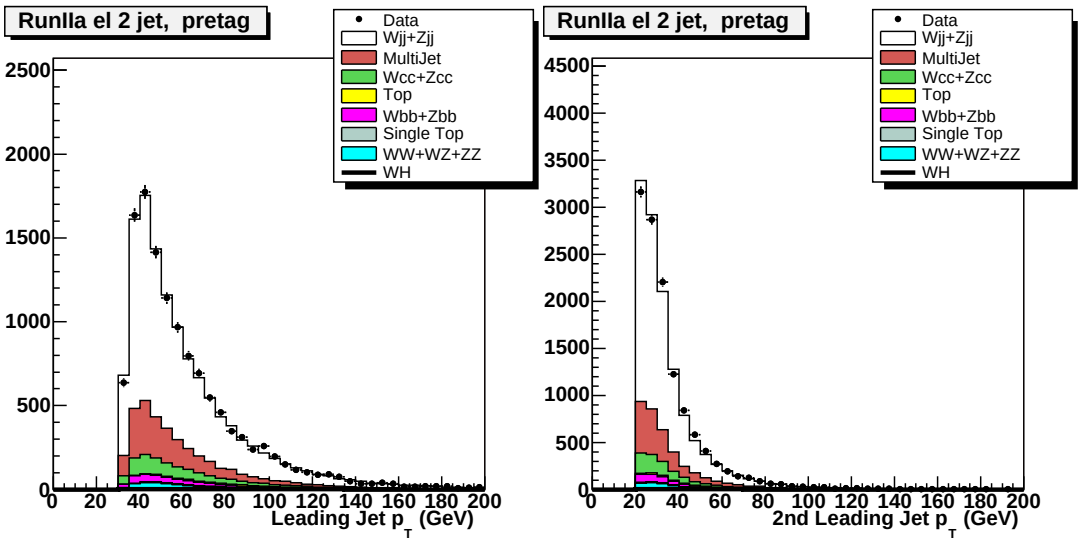

(a) Transverse momentum of the leading jet. (b) Transverse momentum of the second leading jet.

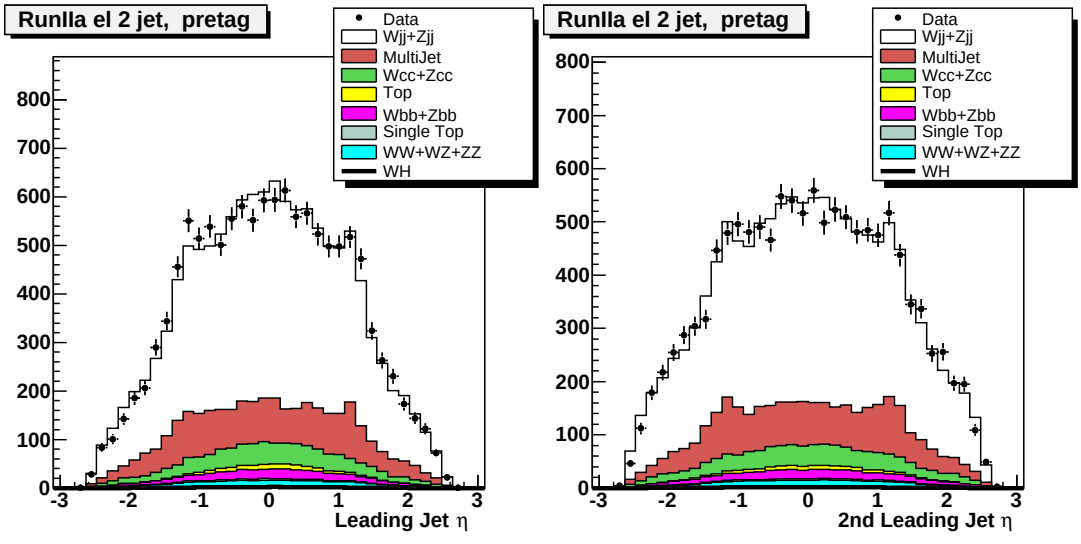

(c) η of the leading jet. (d) η of the second leading jet.

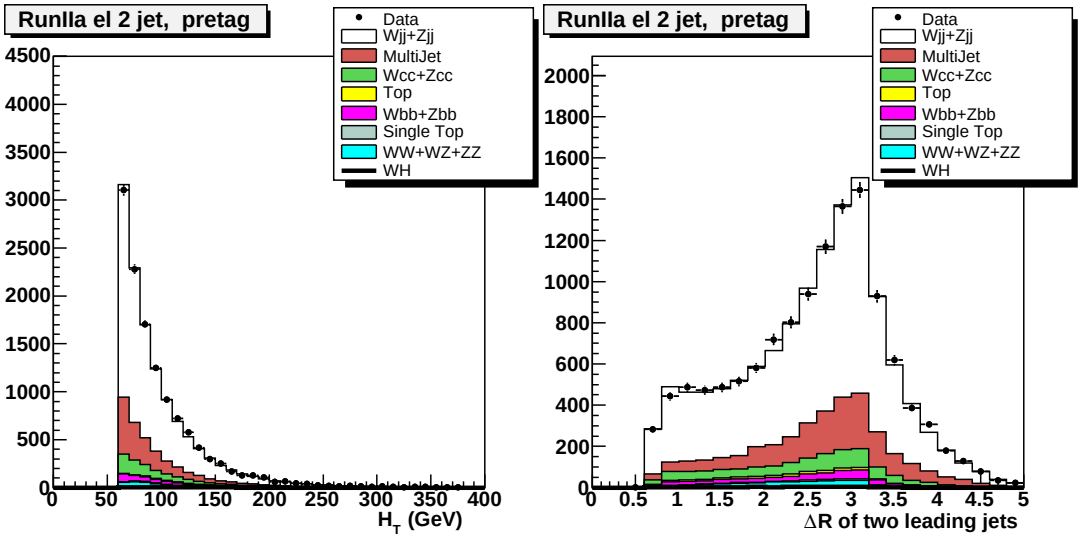

(e) Sum of the transverse jet momenta H_T. (f) ΔR between the two jets.

Figure 78: Kinematic distribution of RunIIa events in the electron channel with exactly two jets. No b tagging is applied.

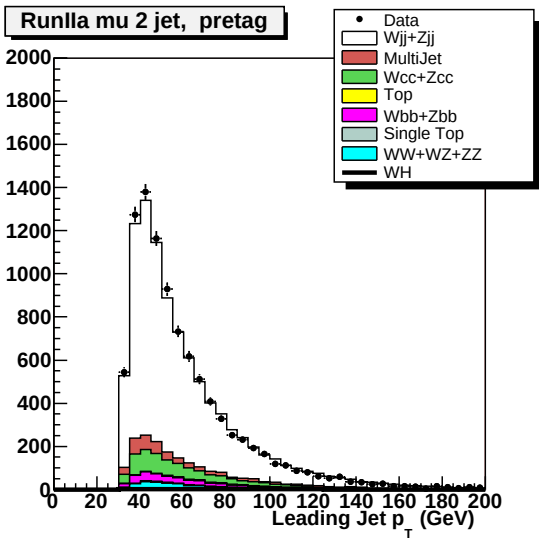

(a) Transverse momentum of the leading jet.

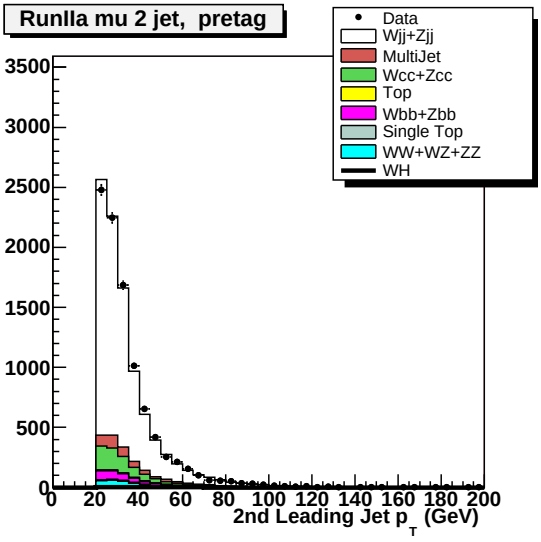

(b) Transverse momentum of the second leading jet.

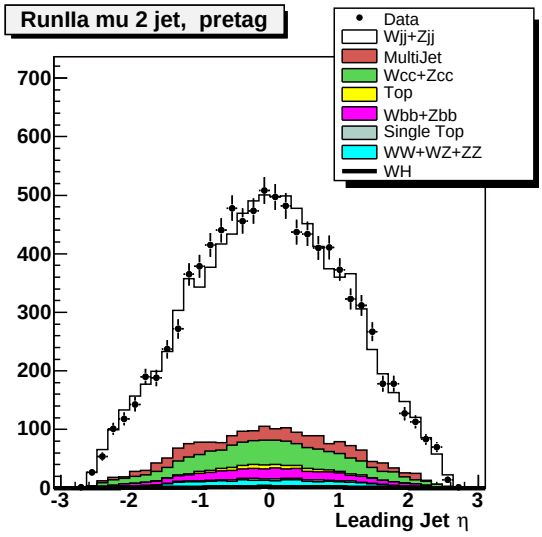

(c) η of the leading jet.

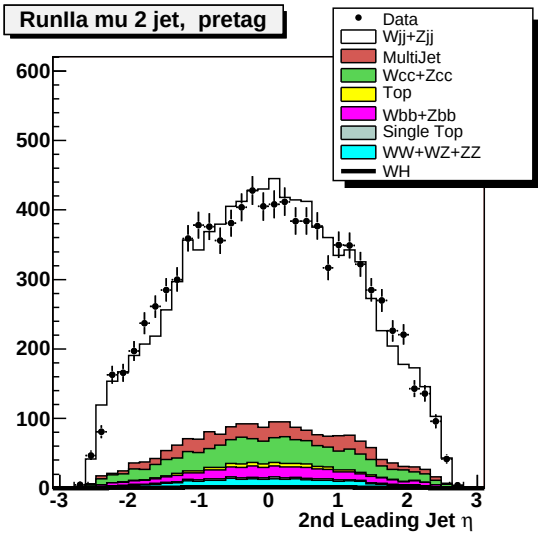

(d) η of the second leading jet.

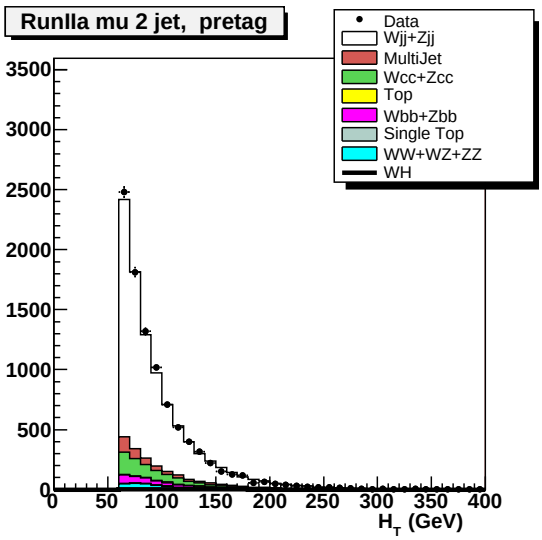

(e) Sum of the transverse jet momenta H_T.

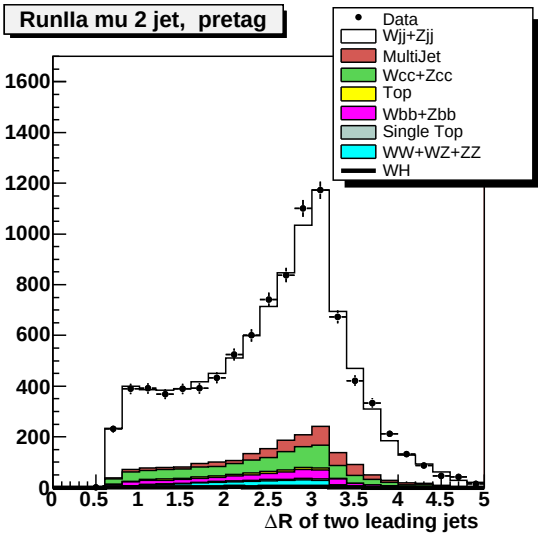

(f) ΔR between the two jets.

Figure 79: Kinematic distribution of RunIIa events in the muon channel with exactly two jets. No b tagging is applied.

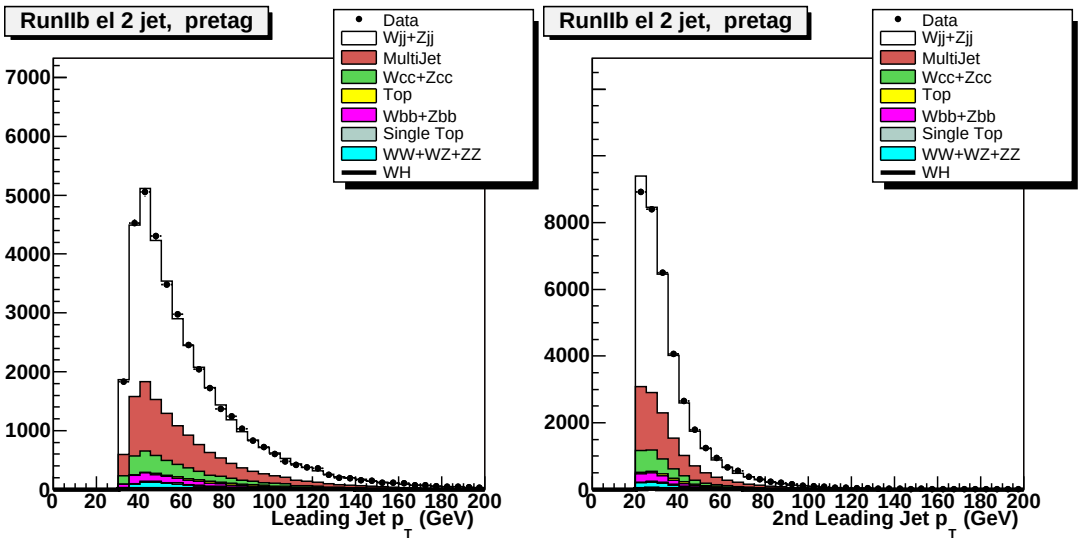

(a) Transverse momentum of the leading jet. (b) Transverse momentum of the second leading jet.

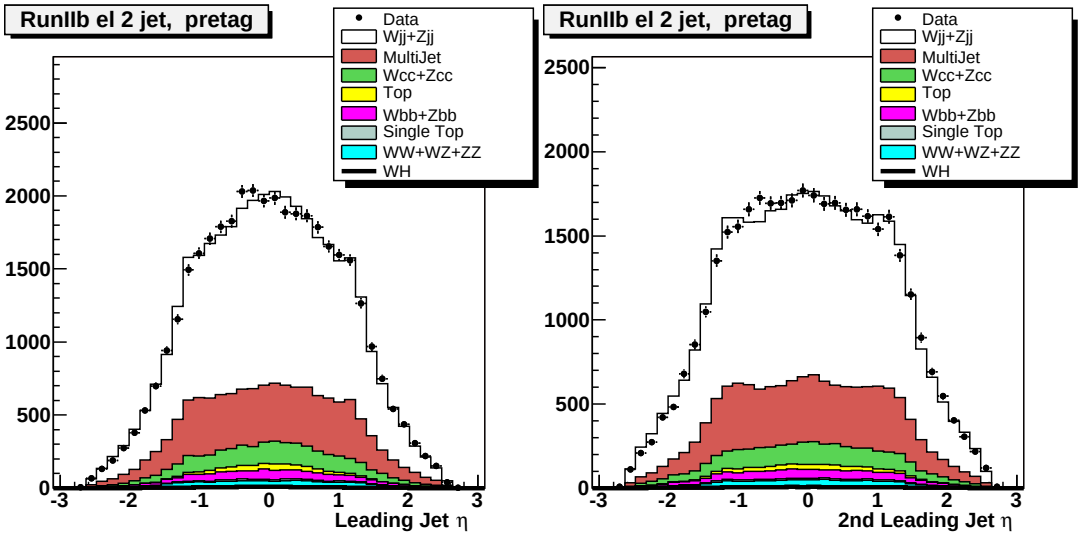

(c) η of the leading jet. (d) η of the second leading jet.

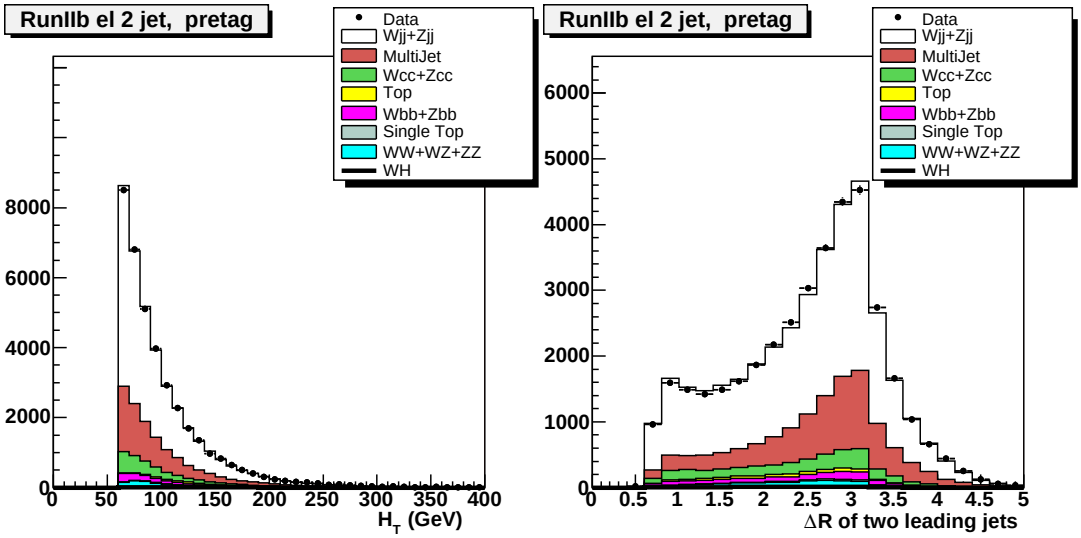

(e) Sum of the transverse jet momenta H_T. (f) ΔR between the two jets.

Figure 80: Kinematic distribution of RunIIb events in the electron channel with exactly two jets. No b tagging is applied.

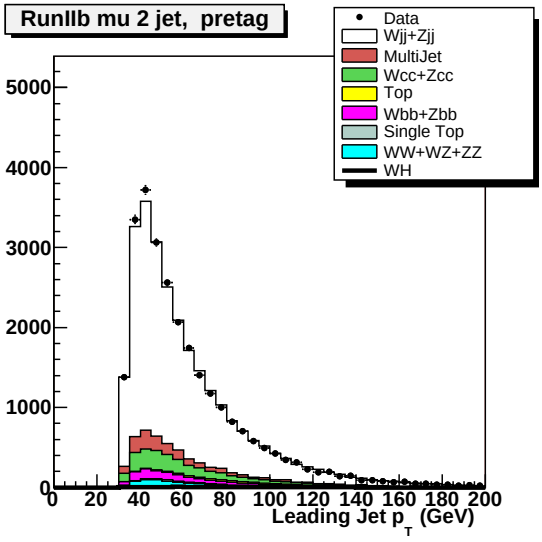

(a) Transverse momentum of the leading jet.

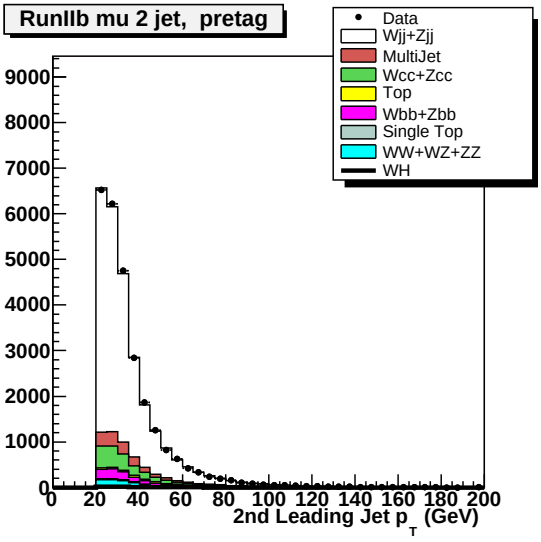

(b) Transverse momentum of the second leading jet.

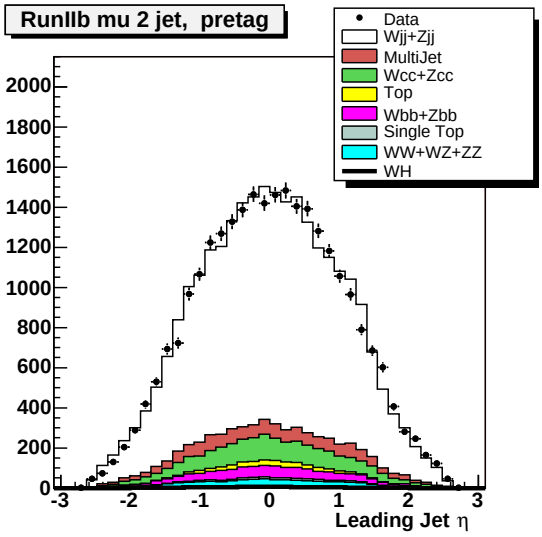

(c) η of the leading jet.

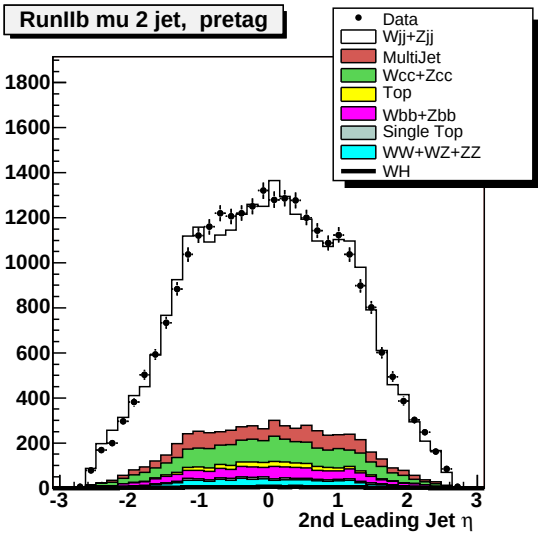

(d) η of the second leading jet.

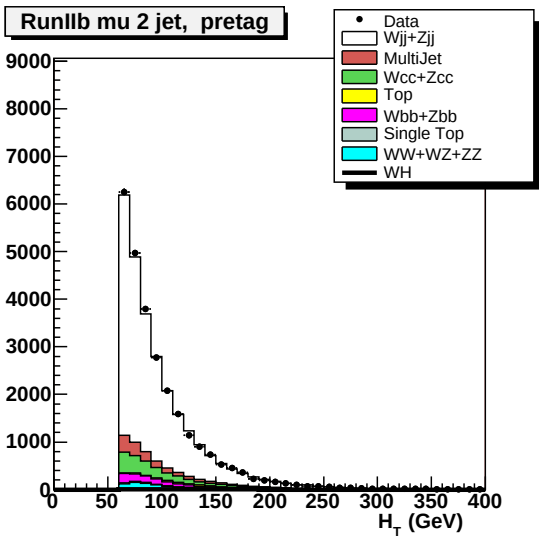

(e) Sum of the transverse jet momenta H_T.

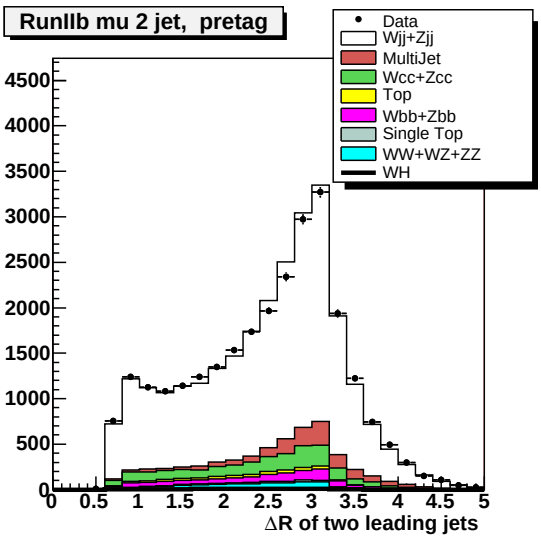

(f) ΔR between the two jets.

Figure 81: Kinematic distribution of RunIIb events in the muon channel with exactly two jets. No b tagging is applied.

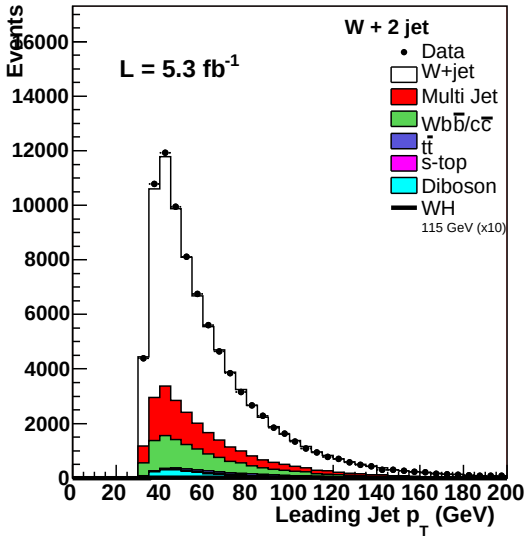

(a) Transverse momentum of the leading jet.

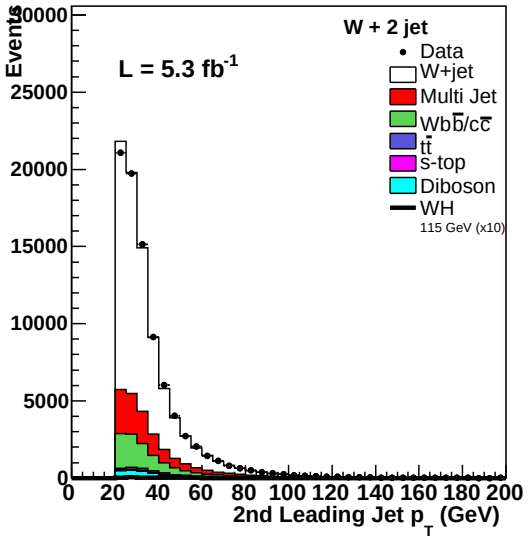

(b) Transverse momentum of the second leading jet.

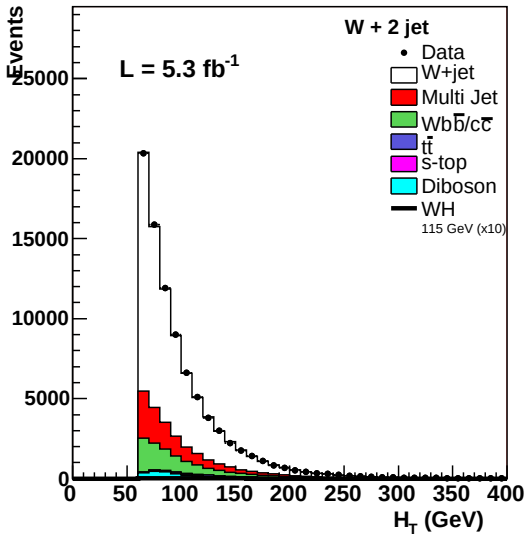

(c) Sum of the transverse jet momenta H_T.

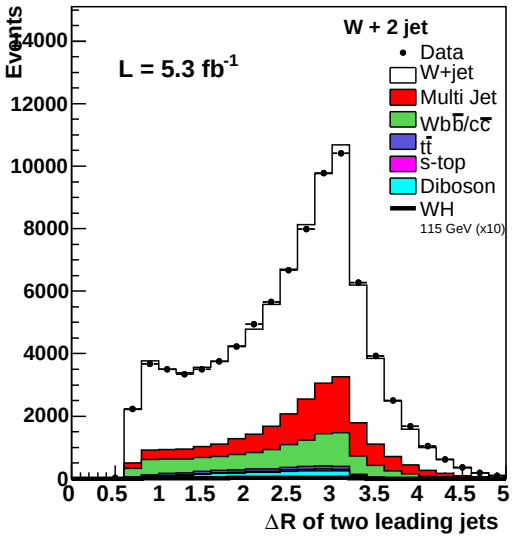

(d) ΔR between the two jets.

Figure 82: Kinematic distribution of all events combined across channels with exactly two jets in the final state. No b tagging is applied.

Once good agreement is with the data is achieved, we can apply more advanced techniques to extract the signal from the background. Before doing that, however, we can still build a variable that gives more sensitivity in separating signal from background than any other variable in this analysis. Corresponding to the potential Higgs mass coming from the decay of the two b jets, we calculate the mass of the two leading jets in the final state (short: dijet mass).

$$M(j_1, j_2) = \sqrt{(E^{j1} + E^{j2})^2 - (p_x^{j1} + p_x^{j2})^2 - (p_y^{j1} + p_y^{j2})^2 - (p_z^{j1} + p_z^{j2})^2} \tag{7.2}$$

where j_1 and j_2 stand for the leading and second leading jet in the event. Fig. 83a (83b) shows the dijet mass distribution for the electron (muon) channel for the RunIIa sample, Fig. 83c (83d) shows the electron (muon) channel distribution for the RunIIb sample. Fig. 84 shows the dijet mass distribution for the combination across channels for all events with exactly two jets in the final state. Data and simulation agree very well in all distributions, a sign that we understand the data in this analysis well.

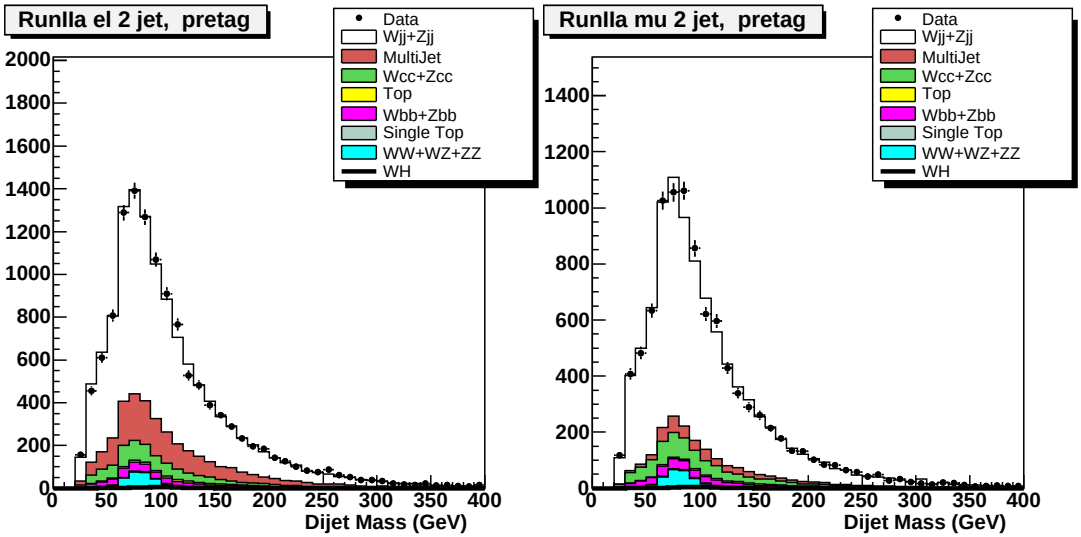

(a) Dijet mass distribution in the electron RunIIa channel.

(b) Dijet mass distribution in the muon RunIIa channel.

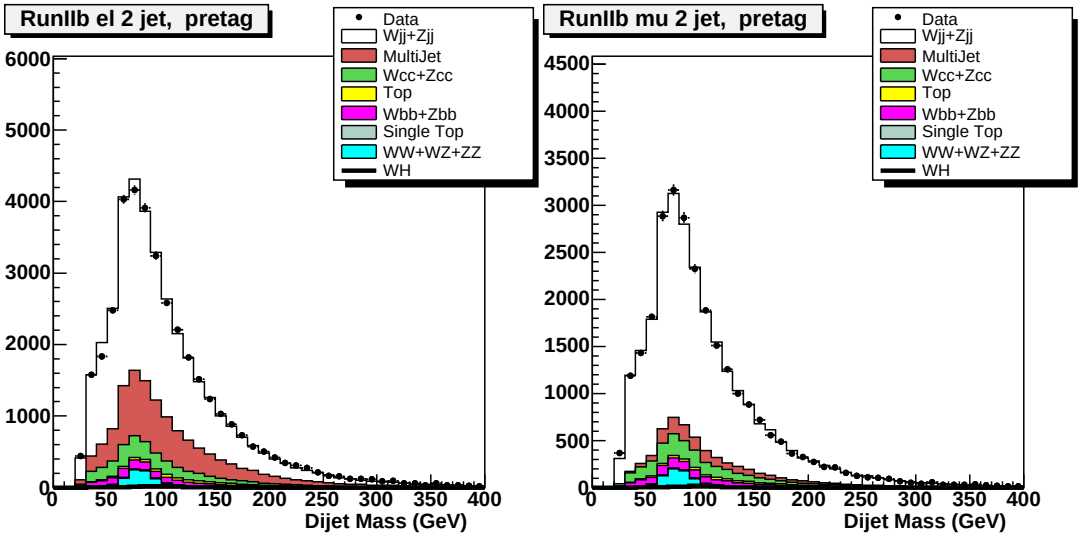

(c) Dijet mass distribution in the electron RunIIb channel.

(d) Dijet mass distribution in the muon RunIIb channel.

Figure 83: Distributions of the dijet mass in all analysis channels containing two jets in the final state. Good agreement is achieved between data and simulation, including all MC backgrounds and the multijet background modeled from data. No b tagging has been applied.

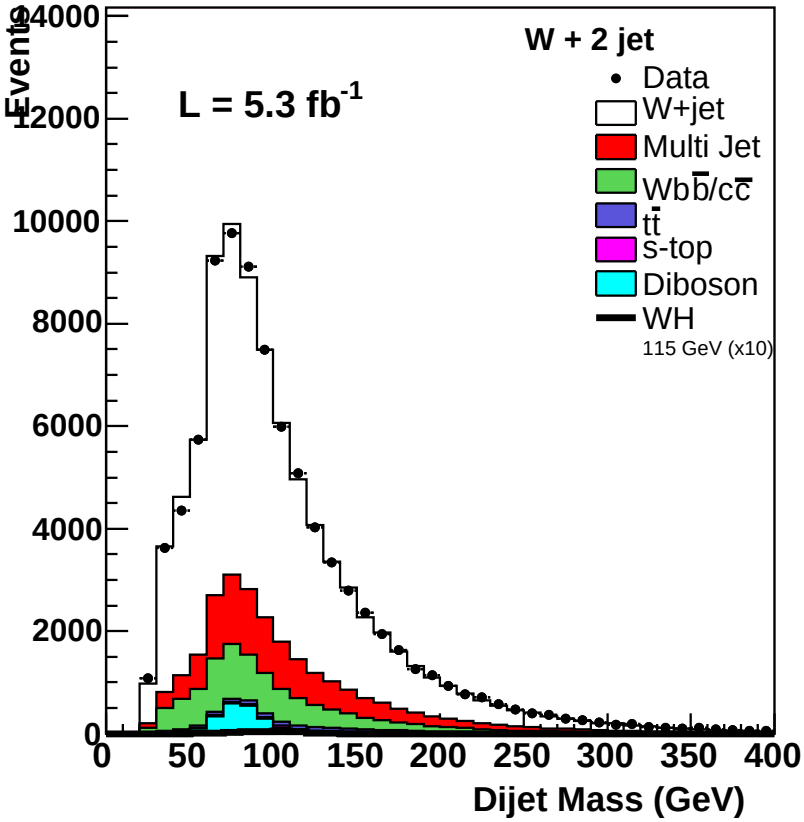

Figure 84: Distribution of the dijet mass for the combination across channels of all events with exactly two jets in the final state. No b tagging has been applied.

7.2.2 *b Tagging in the WH Analysis*

To further reduce the background, mostly from W and Z + jets events, we apply a b tagging procedure that has been described in a more general way in Sec. 5.6. We will now go into the details of b tagging applied in our analysis.
We feed the events passing all our preselection requirements into the NN b tagger (see Sec. 5.6.2.2) after requiring taggability for all jets (see Sec. 5.6.1). We also apply all jet and tagging corrections previously mentioned.

Fig. 85 (86) shows a series of kinematic variable plots of the data and simulation overlay for the RunIIa sample of the electron (muon) channel for events with exactly two jets of which exactly one is tagged with the tight tagging criterion[3]. Fig. 87 (88) shows the same set of plots for the RunIIb electron (muon) sample. The transverse momenta p_T of the leading and second leading jet, the jet η of the leading and second leading jet as well as the sum of the transverse momentum of the two jets H_T and the ΔR

3 A cut on the NN b tagging output of > 0.775, see Sec. 5.6.2.2 for details

between the two jets show reasonable agreement between data and simulation. Fig. 89 shows the combination of events across channels with exactly two jets in the final state of which exactly one is b tagged for the jet η, H_T and ΔR distributions.
In all plots which require one jet to be tagged, we see that the fractions of the background contribution change. Was the W/Z+ light jet sample the dominant background on the pretag level, so is now the $W/Z + b\bar{b}$ sample the main contribution to the background. Also, the fraction of $W/Z + c\bar{c}$ events grows significantly, as well as other backgrounds that are more likely to contain jets that pass the b tagging in the final state. The multijet background that we determine from data is now significantly reduced, as it mostly only contains light jets at low p_T.

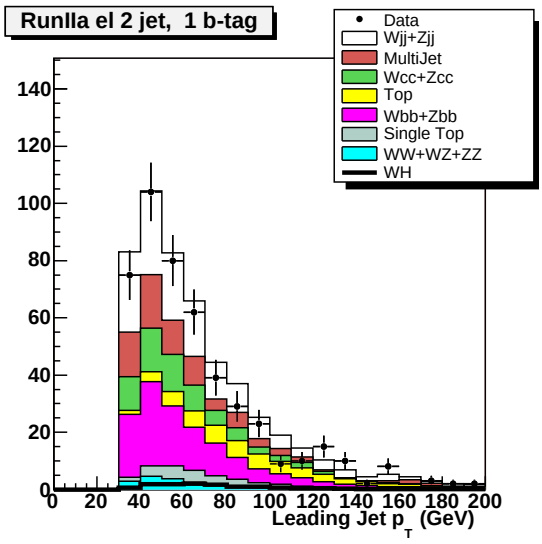

(a) Transverse momentum of the leading jet.

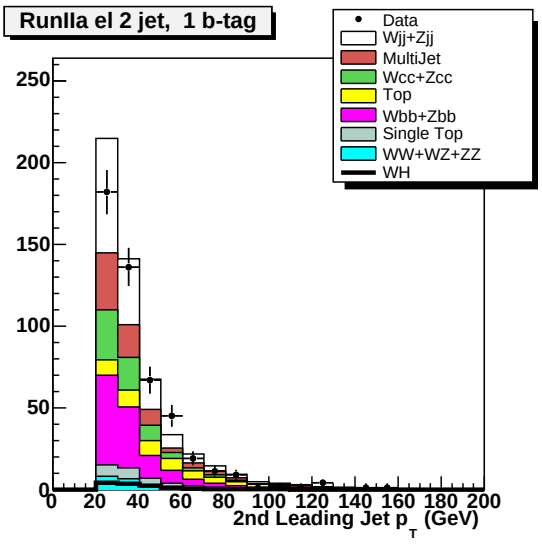

(b) Transverse momentum of the second leading jet.

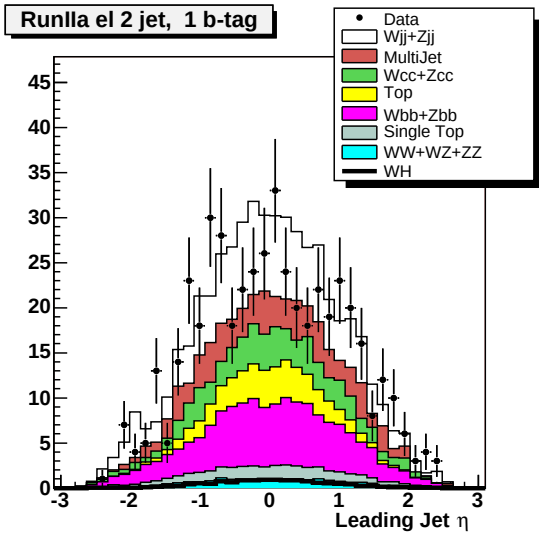

(c) η of the leading jet.

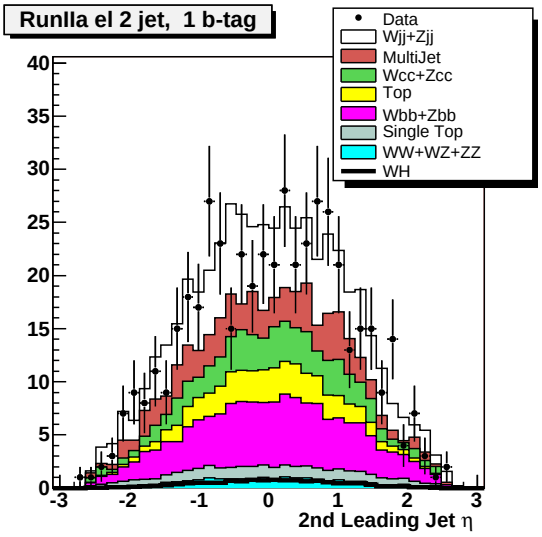

(d) η of the second leading jet.

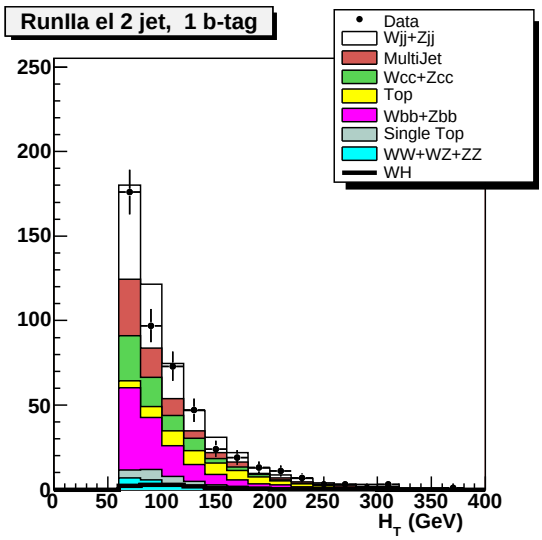

(e) Sum of the transverse jet momenta H_T.

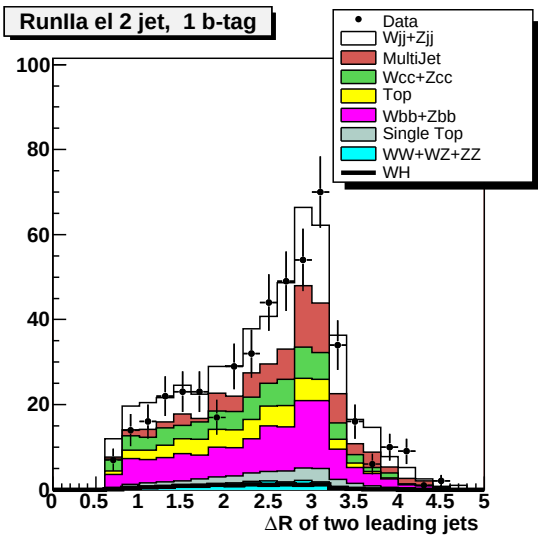

(f) ΔR between the two jets.

Figure 85: Kinematic distribution of RunIIa events in the electron channel with exactly two jets of which exactly one is tagged with the tight b tagging criterion.

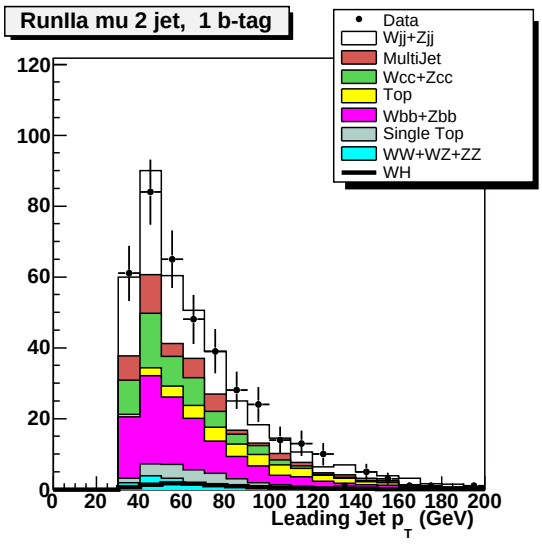

(a) Transverse momentum of the leading jet.

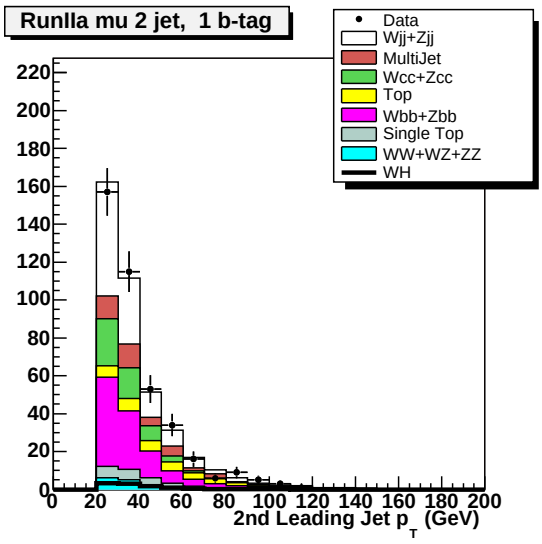

(b) Transverse momentum of the second leading jet.

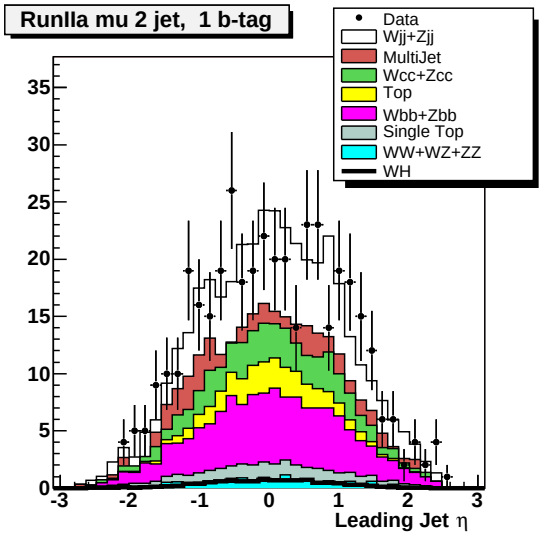

(c) η of the leading jet.

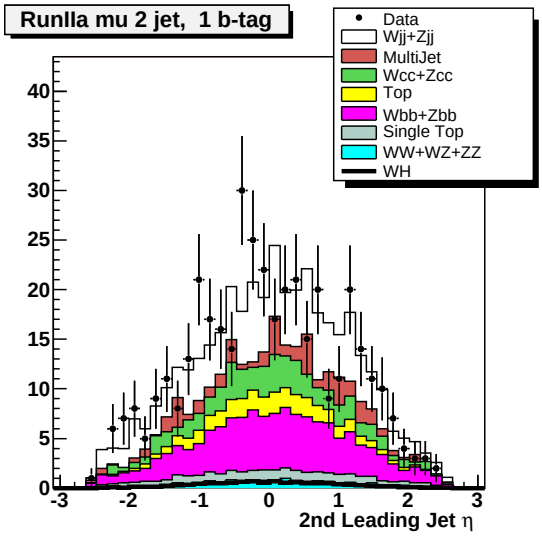

(d) η of the second leading jet.

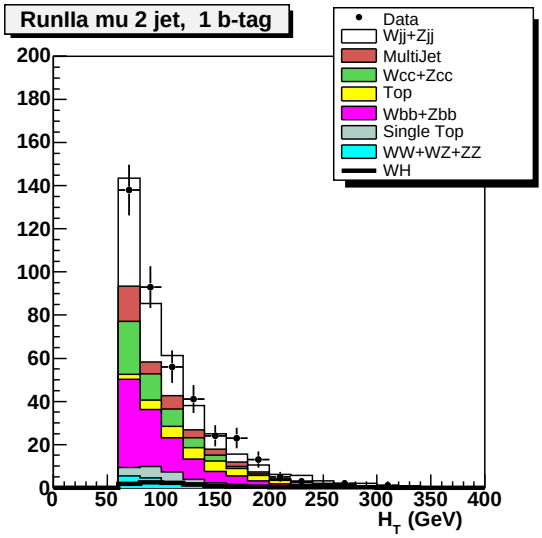

(e) Sum of the transverse jet momenta H_T.

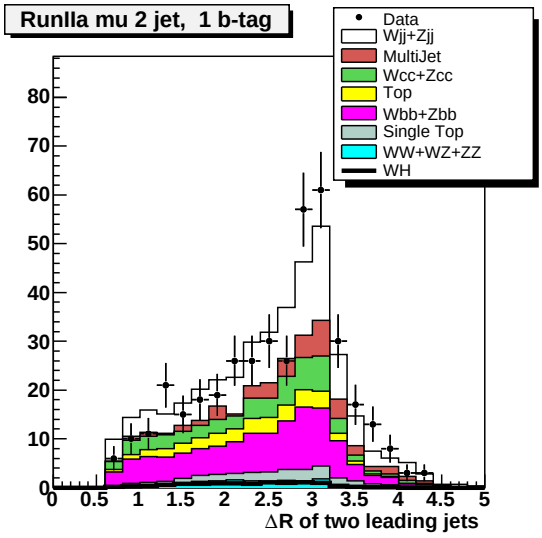

(f) ΔR between the two jets.

Figure 86: Kinematic distribution of RunIIa events in the muon channel with exactly two jets of which exactly one is tagged with the tight b tagging criterion.

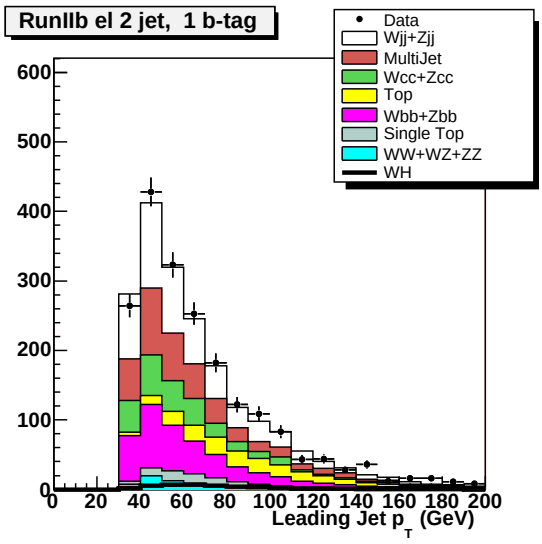

(a) Transverse momentum of the leading jet.

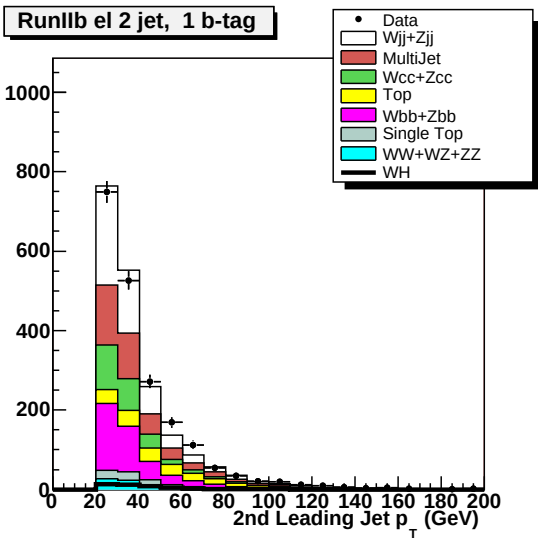

(b) Transverse momentum of the second leading jet.

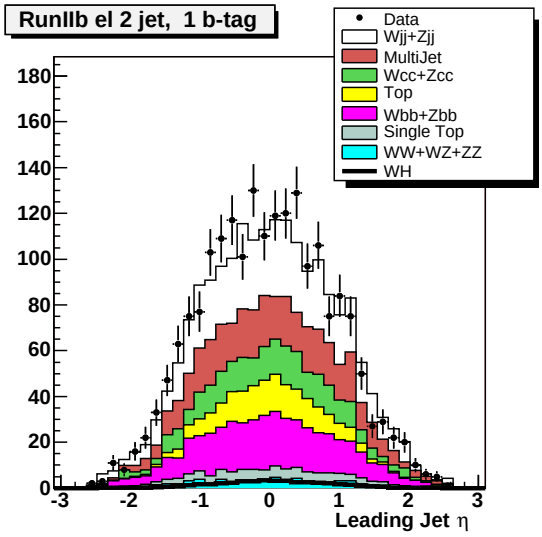

(c) η of the leading jet.

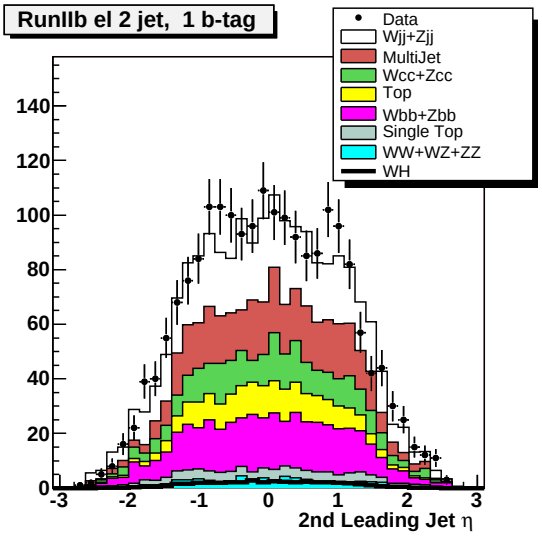

(d) η of the second leading jet.

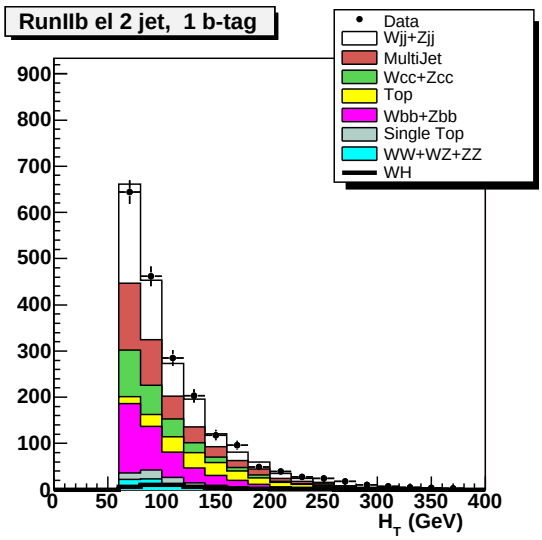

(e) Sum of the transverse jet momenta H_T.

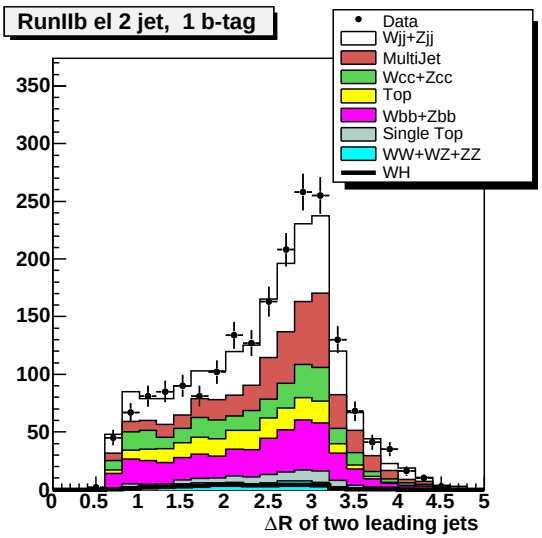

(f) ΔR between the two jets.

Figure 87: Kinematic distribution of RunIIb events in the electron channel with exactly two jets of which exactly one is tagged with the tight b tagging criterion.

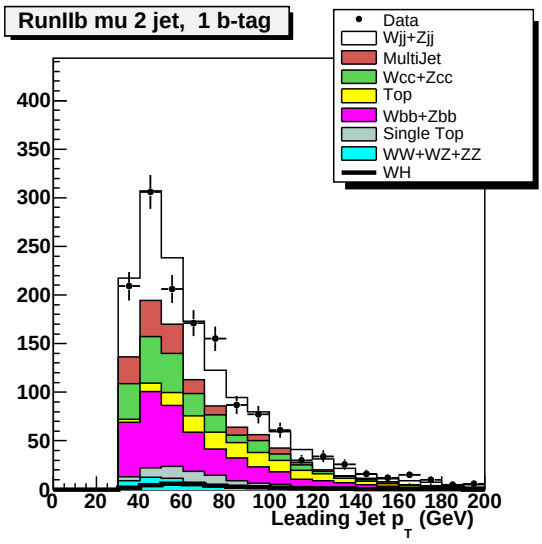

(a) Transverse momentum of the leading jet.

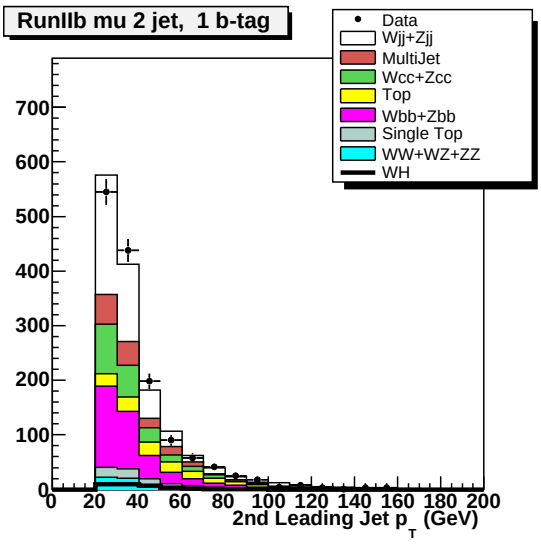

(b) Transverse momentum of the second leading jet.

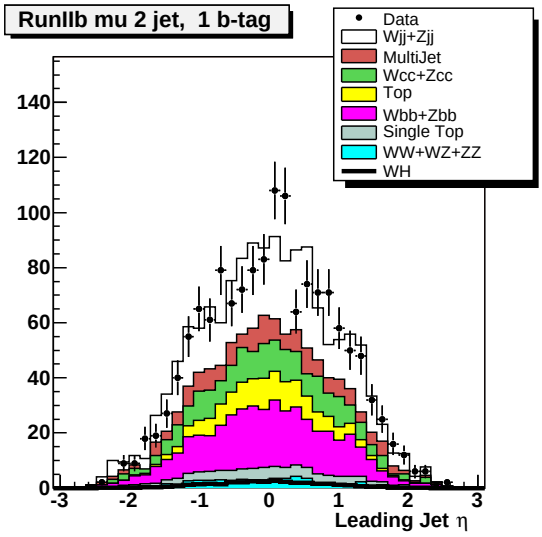

(c) η of the leading jet.

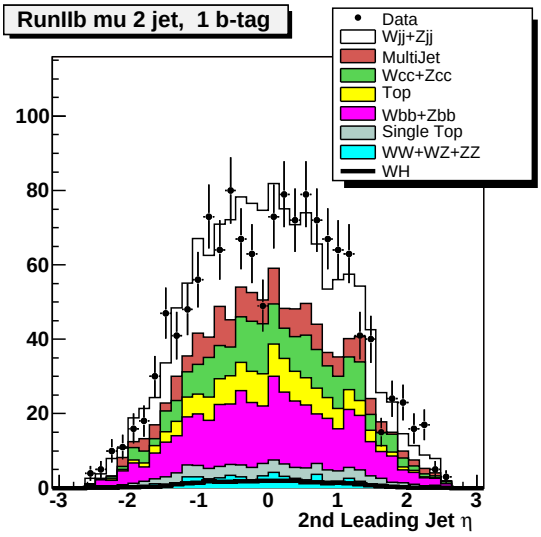

(d) η of the second leading jet.

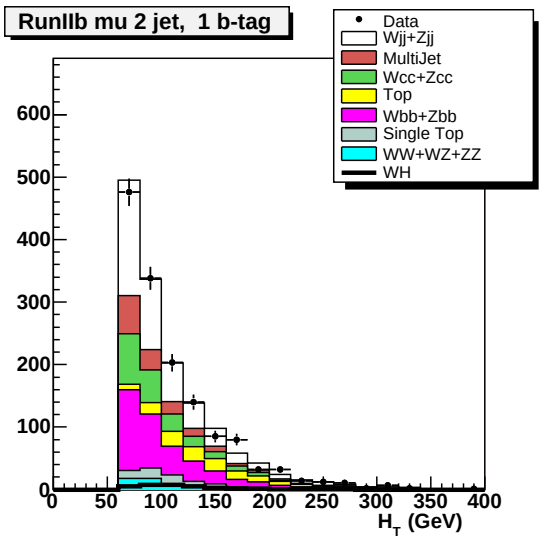

(e) Sum of the transverse jet momenta H_T.

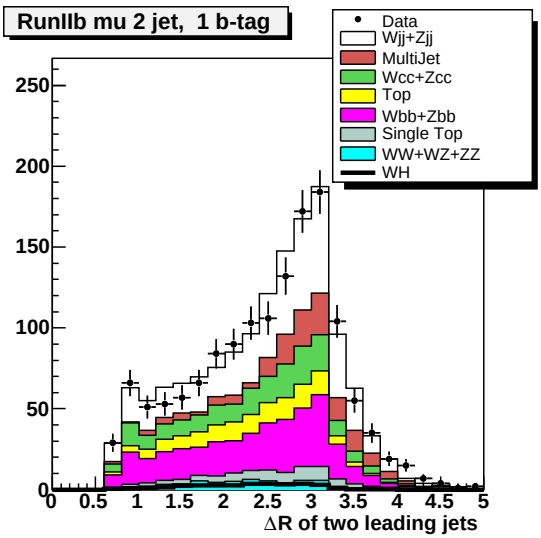

(f) ΔR between the two jets.

Figure 88: Kinematic distribution of RunIIb events in the muon channel with exactly two jets of which exactly one is tagged with the tight b tagging criterion.

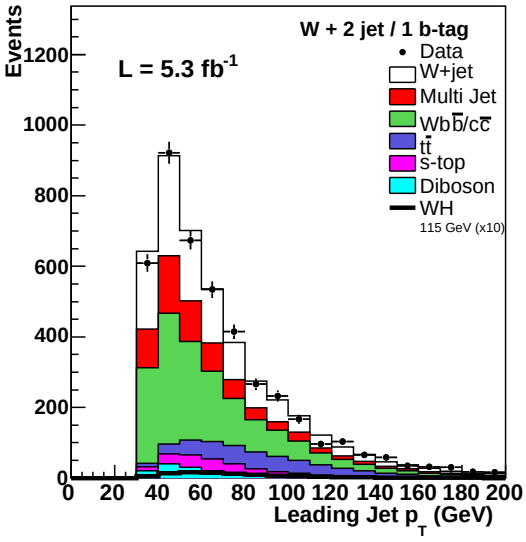

(a) Transverse momentum of the leading jet.

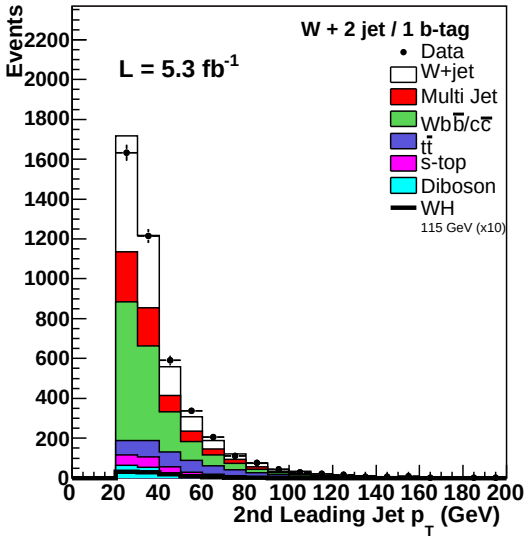

(b) Transverse momentum of the second leading jet.

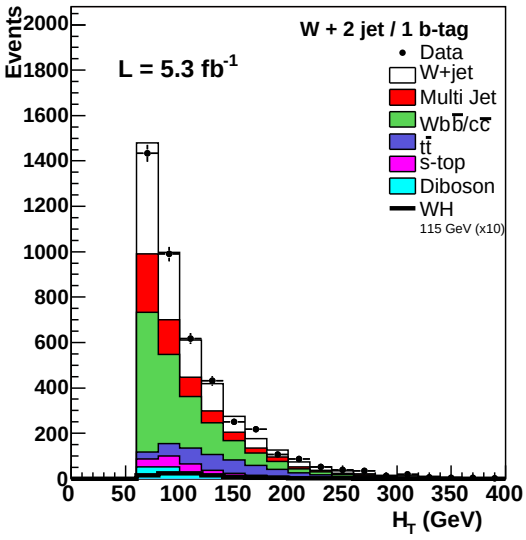

(c) Sum of the transverse jet momenta H_T.

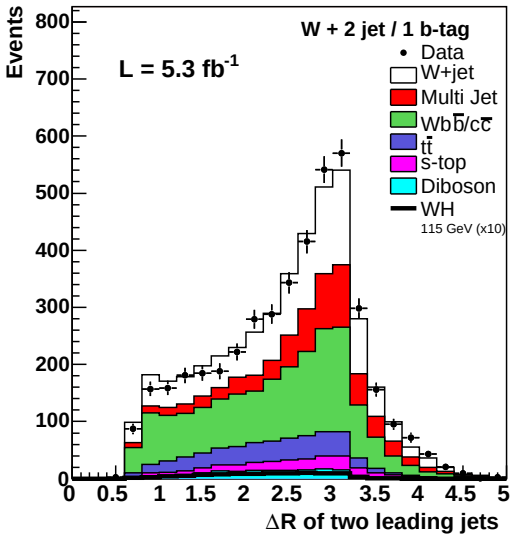

(d) ΔR between the two jets.

Figure 89: Kinematic distribution of all events combined across channels with exactly two jets in the final state of which exactly one is tagged with the tight b tagging criterion.

Again, we take a closer look at the most sensitive variable for our signal, the dijet mass. Fig. 90a (90b) shows the dijet mass distribution for the electron (muon) RunIIa sample, Fig. 90c (90d) shows the electron (muon) distribution for the RunIIb sample. Fig. 91 shows the dijet mass distribution for the combination across channels for all events with exactly two jets in the final state. In these plots, we require exactly one of the two jets in the final state to pass the tight tagging criterion. We see the same behavior in the shifting of background fractions as in the other variables. The dijet mass, however, shows a visible signal shape prediction (solid black line).

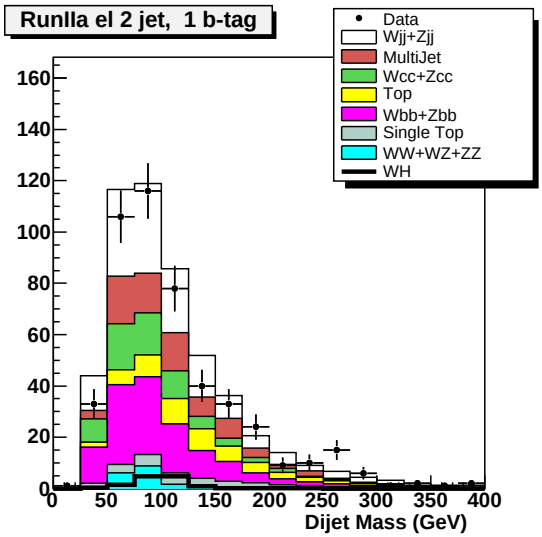

(a) Dijet mass distribution in the electron RunIIa channel.

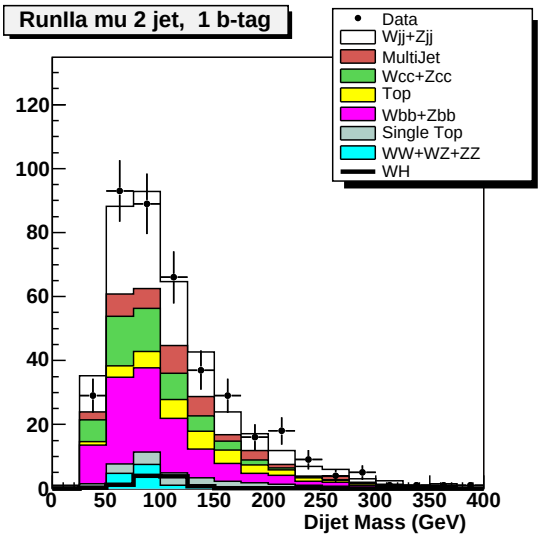

(b) Dijet mass distribution in the muon RunIIa channel.

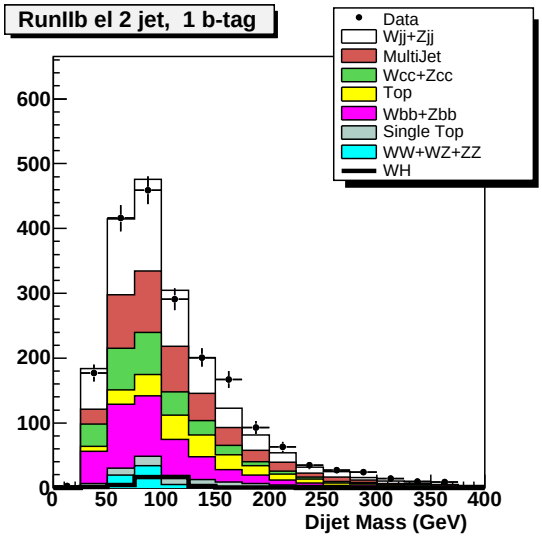

(c) Dijet mass distribution in the electron RunIIb channel.

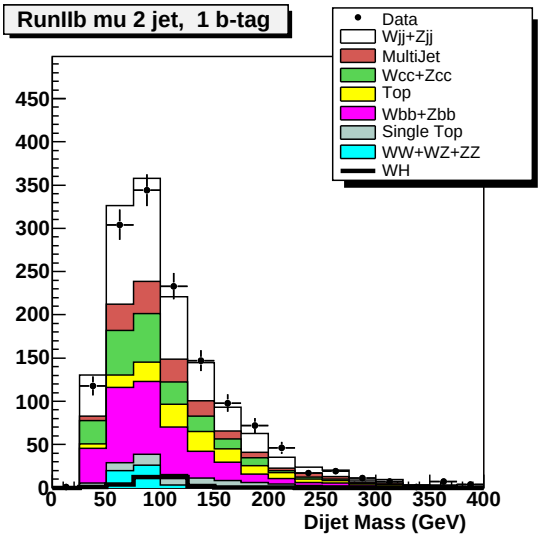

(d) Dijet mass distribution in the muon RunIIb channel.

Figure 90: Distributions of the dijet mass in all analysis channels containing two jets in the final state of which exactly one is required to pass the tight b tagging criterion. Good agreement is achieved between data and simulation, including all simulated backgrounds and the multijet background modeled from data.

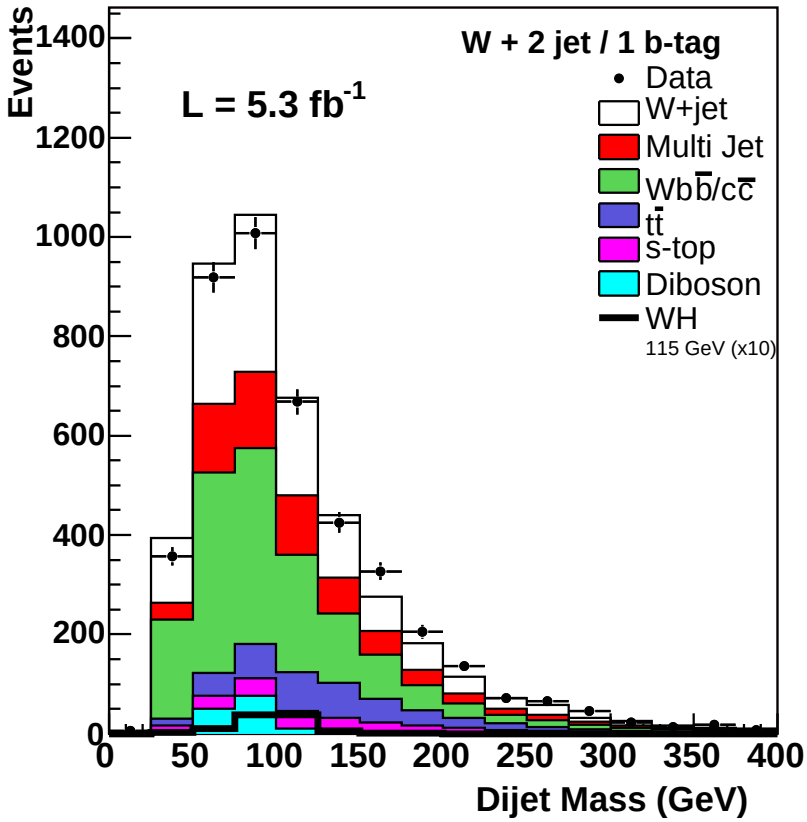

Figure 91: Distribution of the dijet mass for the combination across channels of all events with exactly two jets in the final state of which exactly one is b tagged with the tight tagging criterion.

To further move the signal/background ratio in our favor, we now ask for two b-tagged jets in the final state, both fulfilling the loose tagging criterion[4].. Fig. 92 (93) shows the same kinematic distributions as before now for the double tagged sample in electron (muon) RunIIa events, Fig. 94 (95) shows the distributions for the double tagged electron (muon) RunIIb events. Fig. 96 shows the combination of events across channels with exactly two jets in the final state of which exactly two are b tagged for the jet η, H_T and ΔR distributions. Background from the W/Z+ light jets samples disappears almost completely from the double b tagged distributions and backgrounds that likely have two heavy flavor jets in the final state grow in their relative background contribution.

4 A cut on the NN b tagging output of > 0.5, see Sec. 5.6.2.2 for details

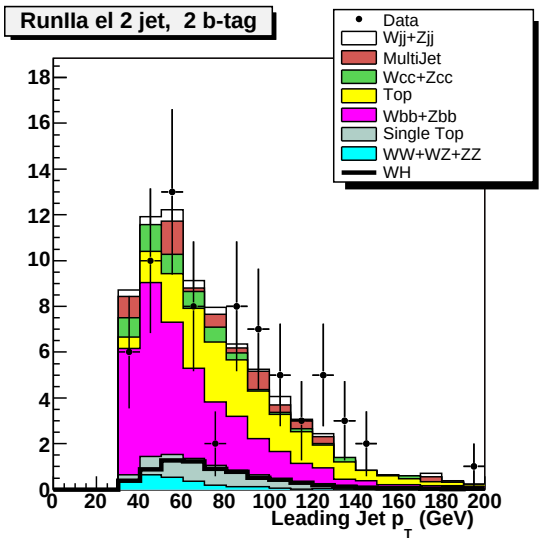

(a) Transverse momentum of the leading jet.

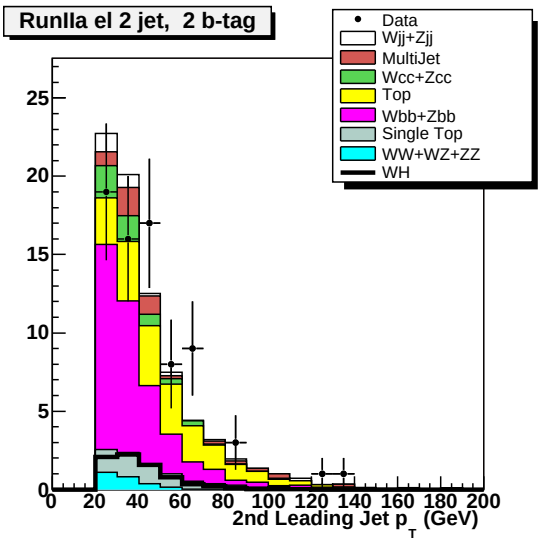

(b) Transverse momentum of the second leading jet.

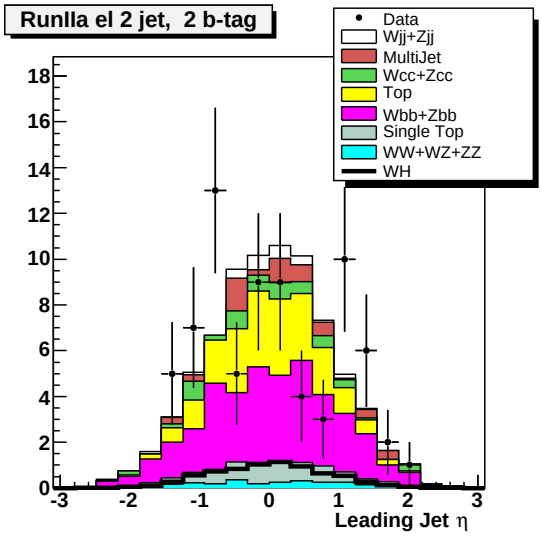

(c) η of the leading jet.

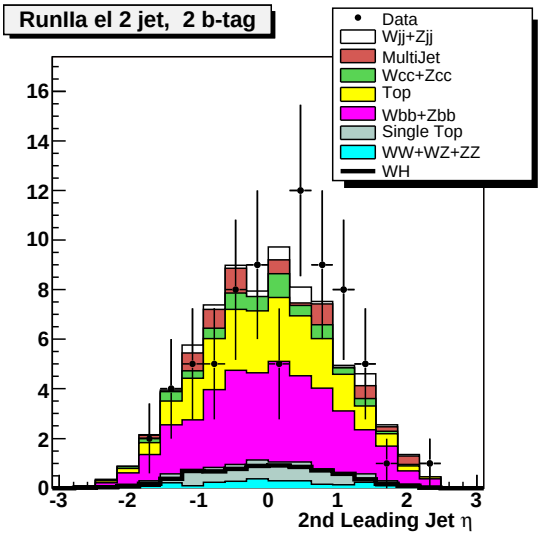

(d) η of the second leading jet.

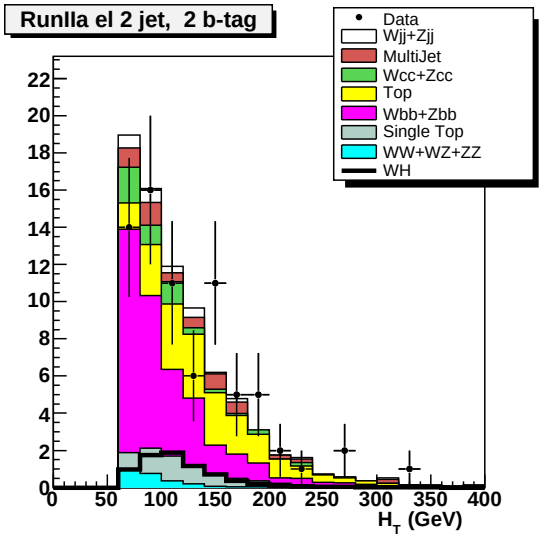

(e) Sum of the transverse jet momenta H_T.

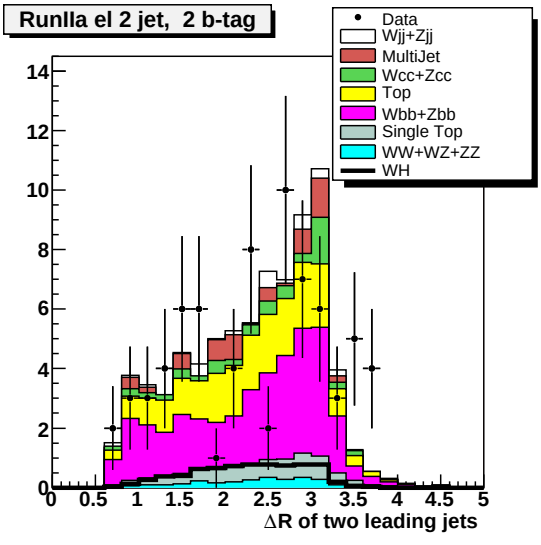

(f) ΔR between the two jets.

Figure 92: Kinematic distribution of RunIIa events in the electron channel with exactly two jets of which exactly two are tagged with the loose b-tagging criterion.

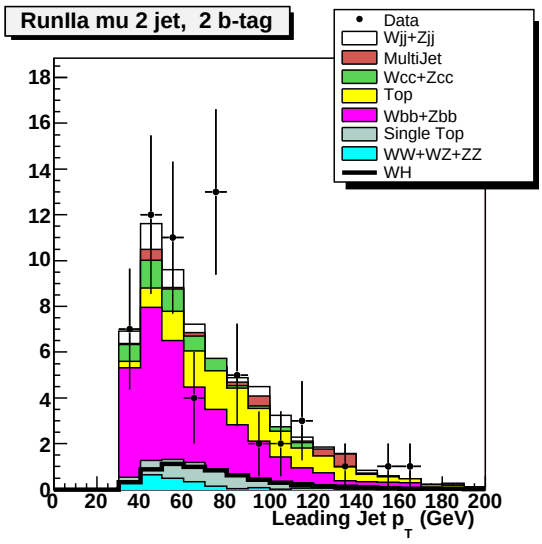

(a) Transverse momentum of the leading jet.

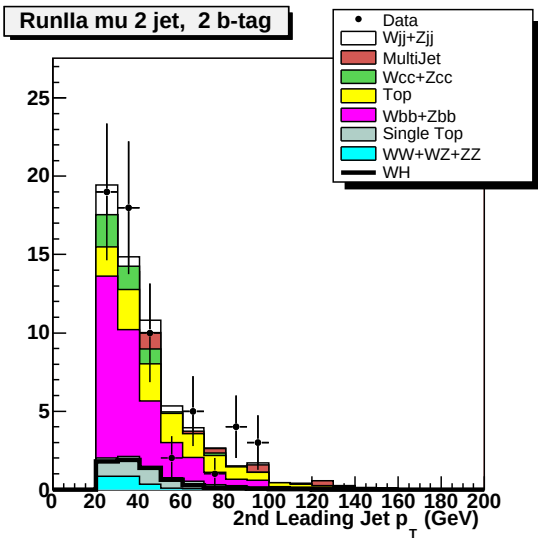

(b) Transverse momentum of the second leading jet.

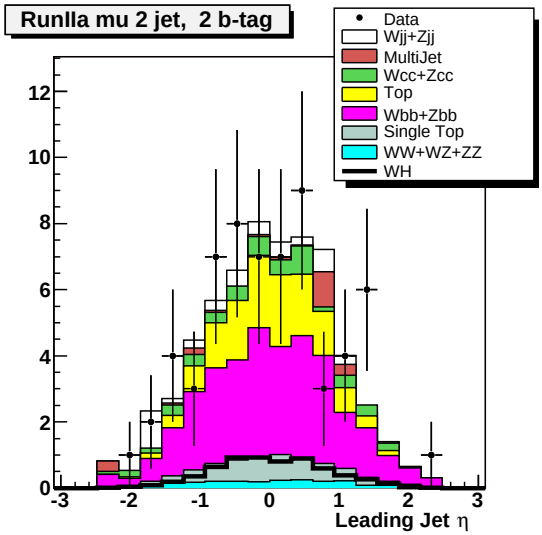

(c) η of the leading jet.

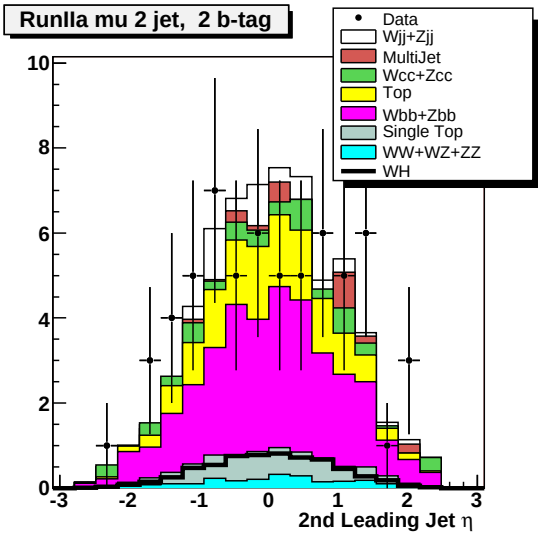

(d) η of the second leading jet.

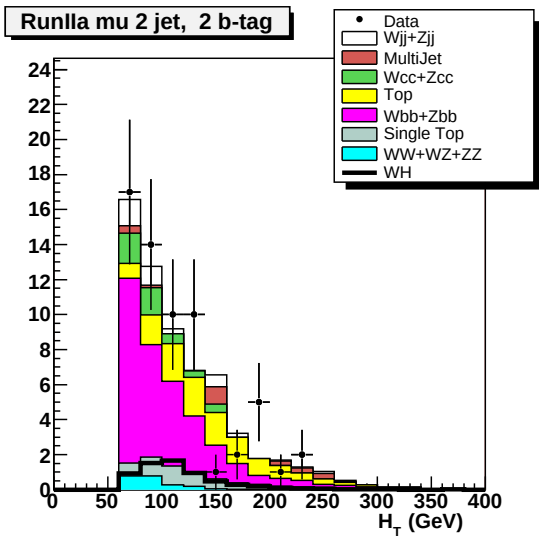

(e) Sum of the transverse jet momenta H_T.

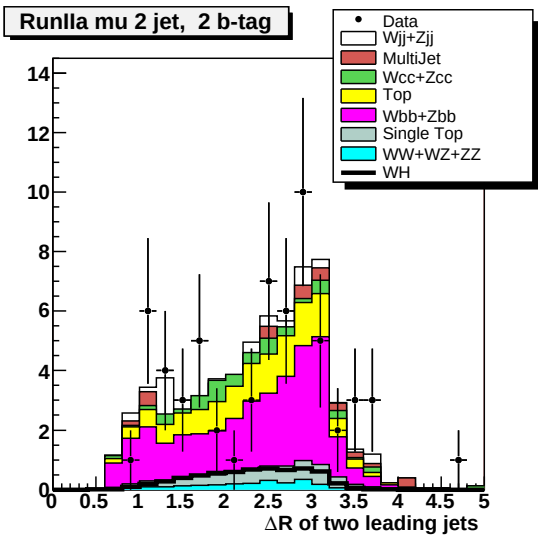

(f) ΔR between the two jets.

Figure 93: Kinematic distribution of RunIIa events in the muon channel with exactly two jets of which exactly two are tagged with the loose b-tagging criterion.

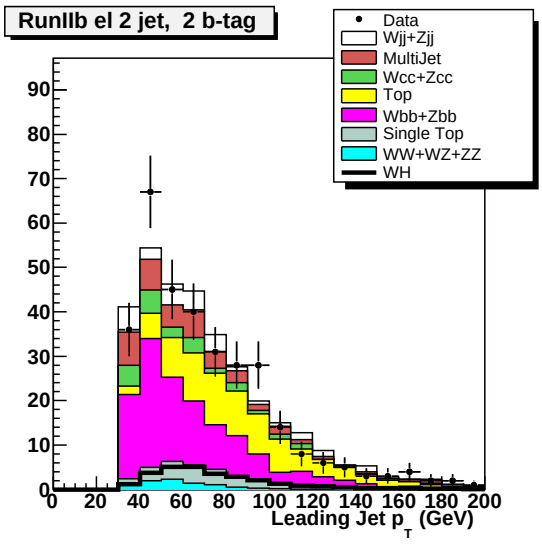

(a) Transverse momentum of the leading jet.

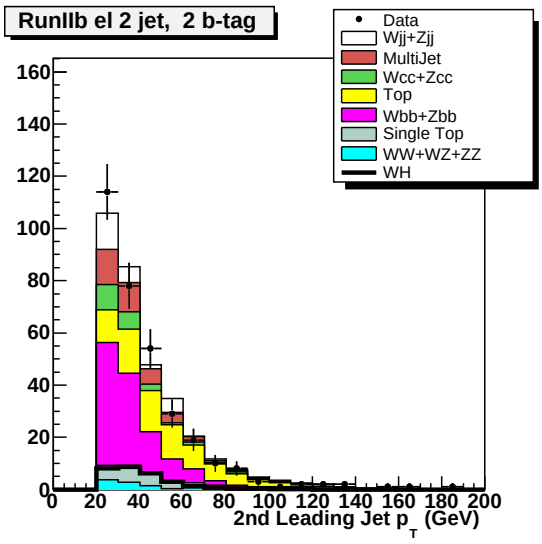

(b) Transverse momentum of the second leading jet.

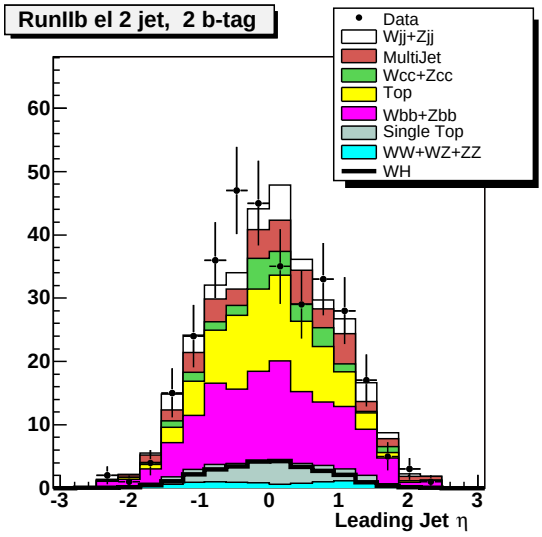

(c) η of the leading jet.

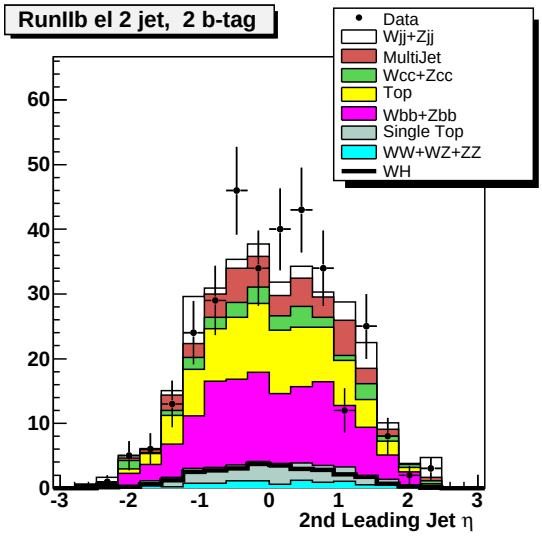

(d) η of the second leading jet.

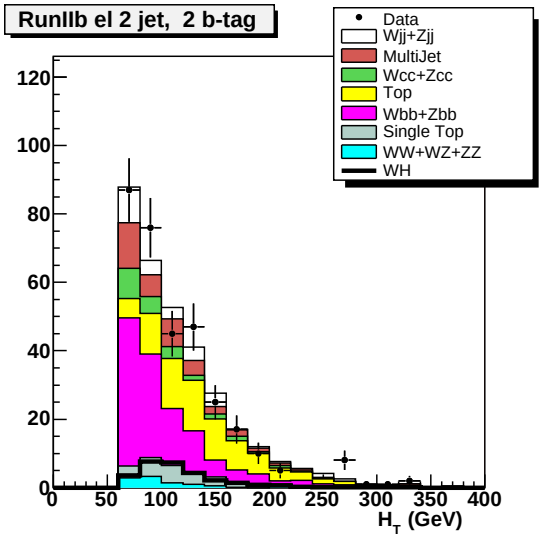

(e) Sum of the transverse jet momenta H_T.

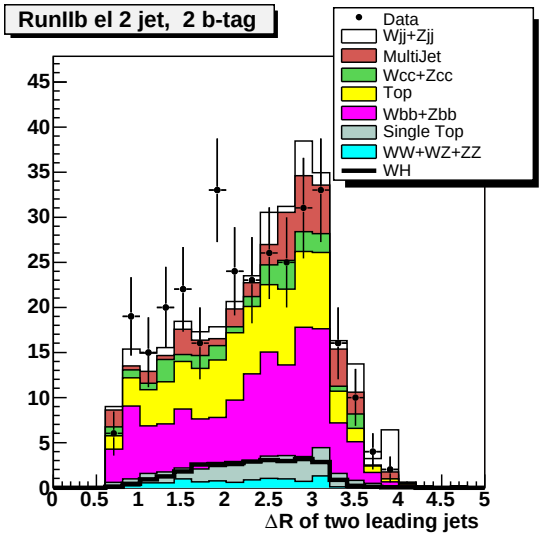

(f) ΔR between the two jets.

Figure 94: Kinematic distribution of RunIIb events in the electron channel with exactly two jets of which exactly two are tagged with the loose b tagging criterion.

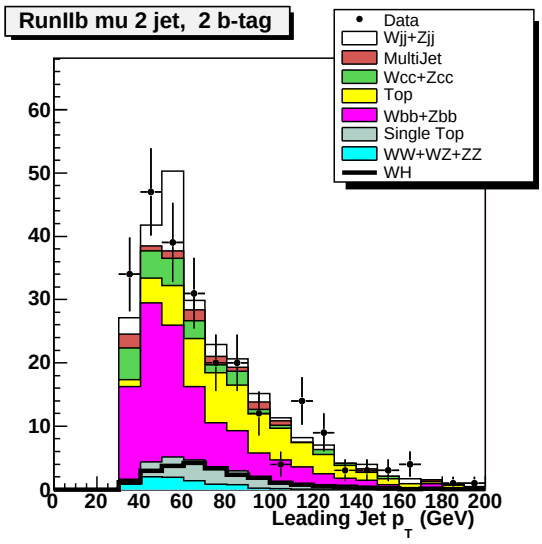

(a) Transverse momentum of the leading jet.

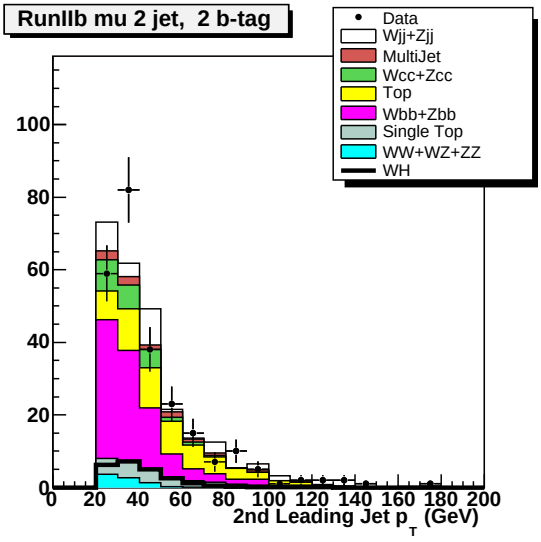

(b) Transverse momentum of the second leading jet.

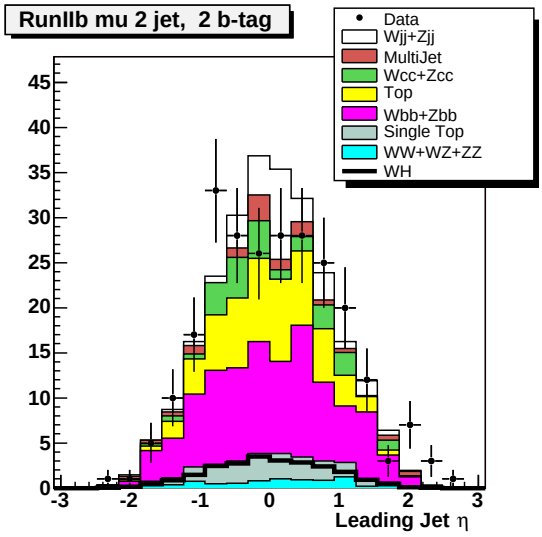

(c) η of the leading jet.

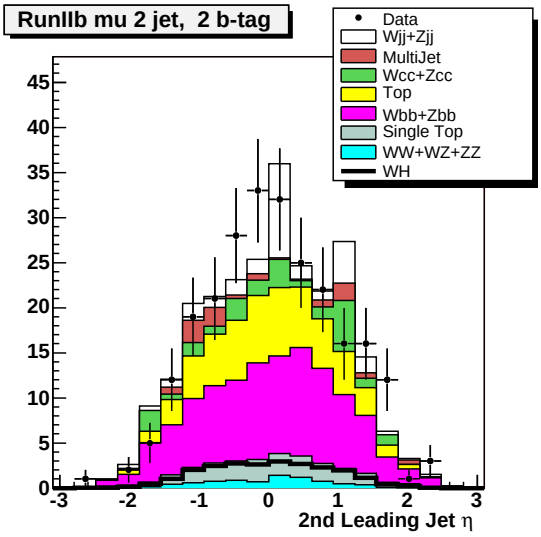

(d) η of the second leading jet.

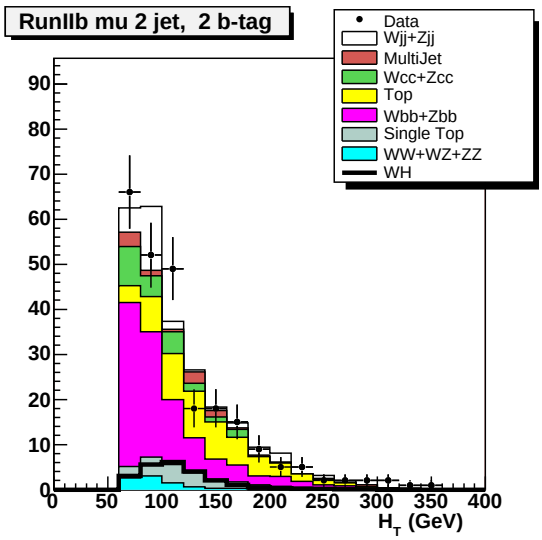

(e) Sum of the transverse jet momenta H_T.

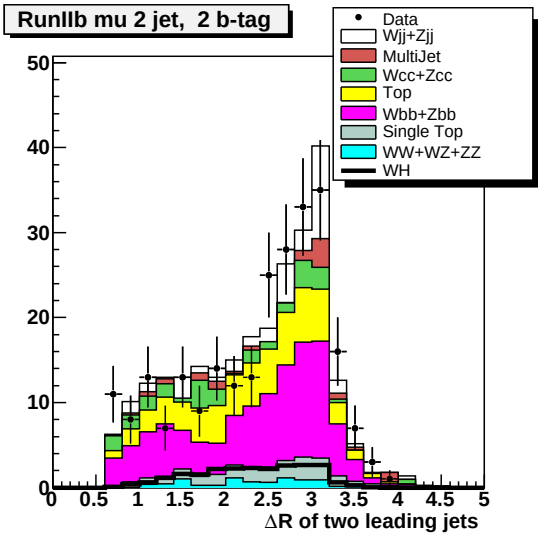

(f) ΔR between the two jets.

Figure 95: Kinematic distribution of RunIIb events in the muon channel with exactly two jets of which exactly two are tagged with the loose b tagging criterion.

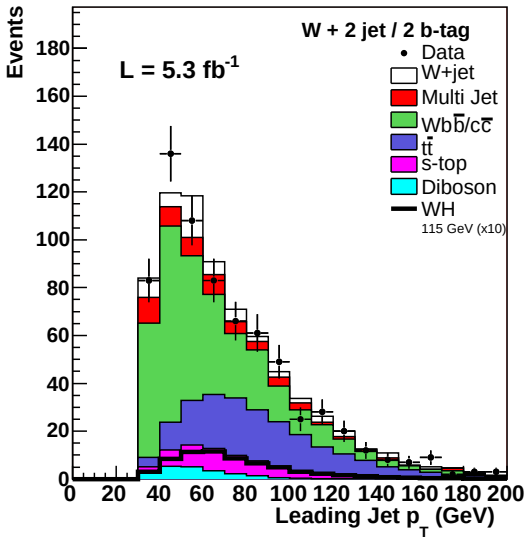

(a) Transverse momentum of the leading jet.

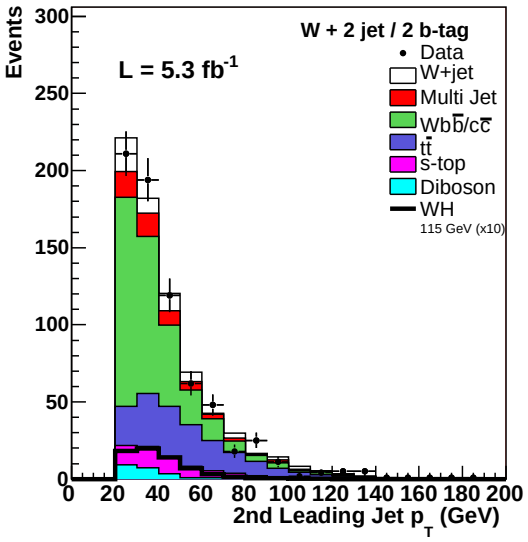

(b) Transverse momentum of the second leading jet.

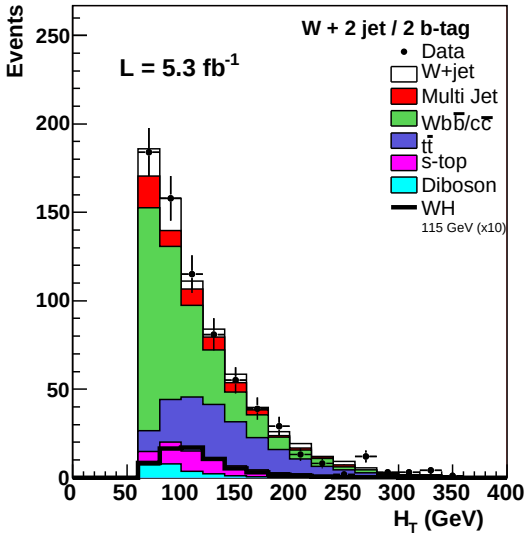

(c) Sum of the transverse jet momenta H_T.

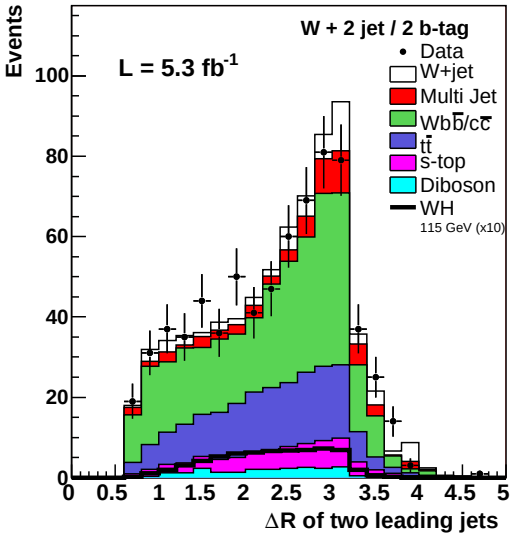

(d) ΔR between the two jets.

Figure 96: Kinematic distribution of all events combined across channels with exactly two jets in the final state of which exactly two are tagged with the loose b tagging criterion.

In the double tagged selection sample, the dijet mass distribution now starts to show a well visible shape prediction for the simulated WH sample. Fig. 97a (97b) shows the dijet mass distribution for the electron (muon) RunIIa sample, Fig. 97c (97d) shows the electron (muon) distribution on the RunIIb sample. Fig. 98 shows the dijet mass distribution for the combination across channels for all events with exactly two b tagged jets in the final state.

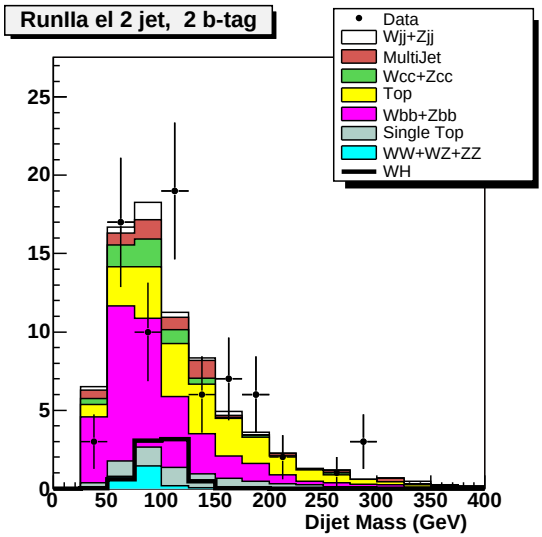

(a) Dijet mass distribution in the electron RunIIa channel.

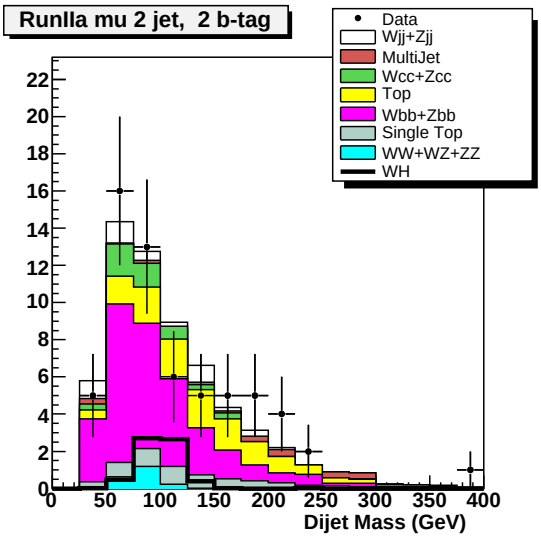

(b) Dijet mass distribution in the muon RunIIa channel.

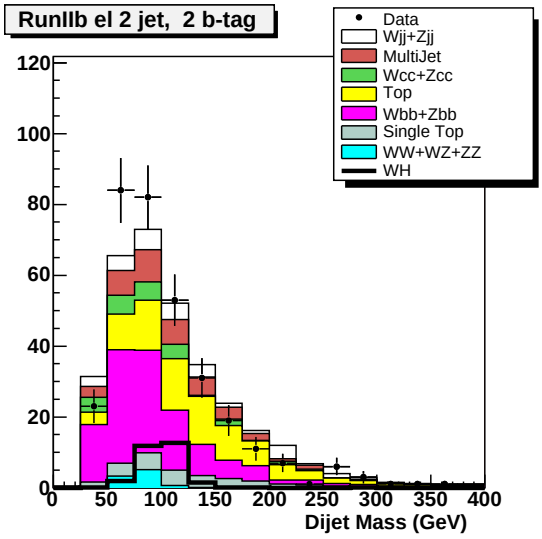

(c) Dijet mass distribution in the electron RunIIb channel.

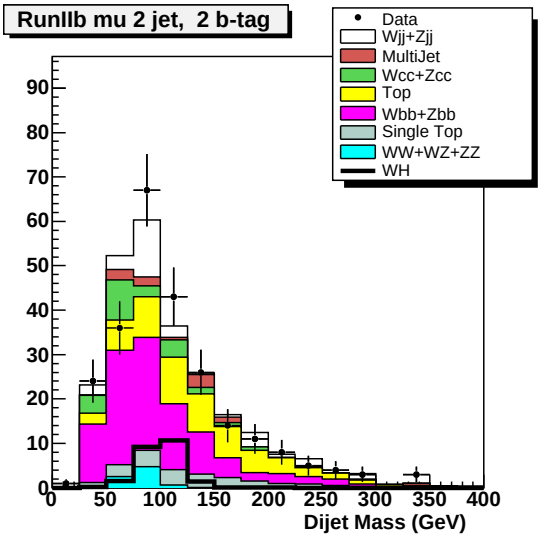

(d) Dijet mass distribution in the muon RunIIb channel.

Figure 97: Distributions of the dijet mass in all analysis channels containing two jets in the final state of which exactly two are required to pass the loose b tagging criterion. Good agreement is achieved between data and simulation, including all MC backgrounds and the multijet background modeled from data.

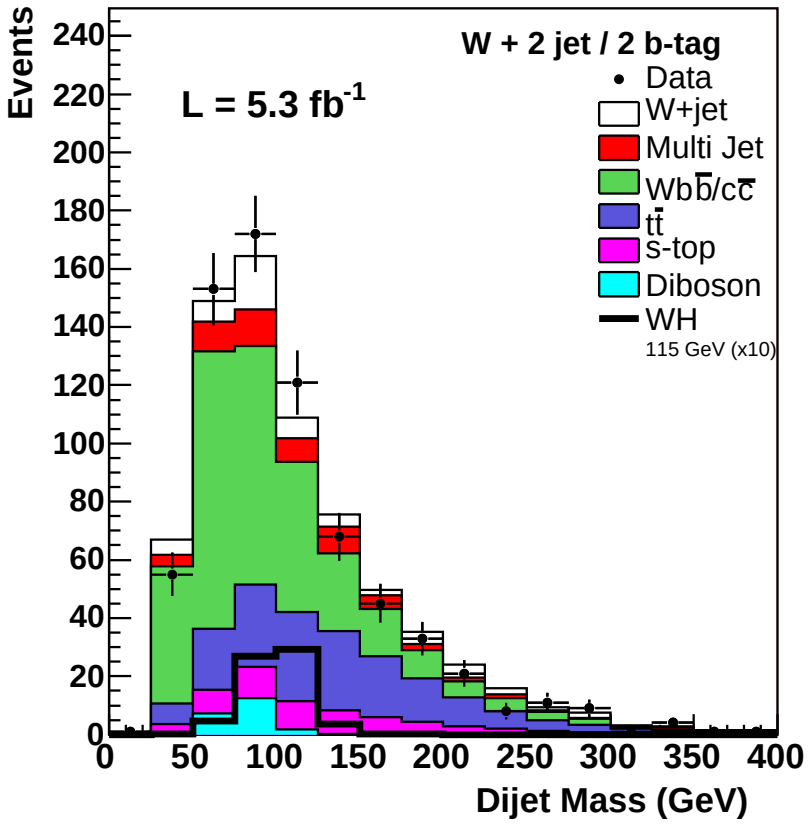

Figure 98: Distribution of the dijet mass for the combination across channels of all events with exactly two jets in the final state of which exactly two are b tagged with the loose tagging criterion.

7.3 BACKGROUND REDUCTION

7.3.1 *Improvement using a Random Forest*

As we have seen in the sections above, the dijet invariant mass is a very powerful variable in our analysis. However, its sensitivity alone will not allow us to set stringent limits on the production cross section of the Higgs boson in associated production with a W boson. We strive therefore for ways of further improving our sensitivity. This leads to the application of multivariate techniques that allow to combine the separation power of several kinematic variables. We have already explained the working principle of one of these techniques, the neural network, earlier in Sec. 5.6.2.2 in the context of b tagging. Now we want to introduce another multivariate technique called *Decision Tree*. It has been successfully applied in high energy physics in recent years. The Decision Tree is an event classifier that separates an event sample in two subsamples, in our case signal- and background-like events, using an ensemble of variables x. It works in several steps in which one specific requirement at a time on a certain variable is used to separate the whole event sample in two samples in the next layer. These samples are then labeled signal- background-like. In every sample there is a certain number of misclassified events, background-like in the signal sample and vice-versa. To increase the purity of the samples, another variable with its specific requirements is used to separate the events in the subsamples again in signal- and background-like sub-subsamples. This procedure is repeated until either a certain minimal threshold on the number of events in a subsample is reached or certain criteria on the signal- or background-purity of the subsample is reached. The subsamples are typically called leaves.
In our case, we use a quantity called CROSS ENTROPY as the figure of merit, defined as

$$\text{CROSS ENTROPY} = -p \ln p - (1-p)\ln(1-p) \tag{7.3}$$

where p is the purity of the leaf. p is defined as $\frac{\text{signal events in the leaf}}{\text{all events in the leaf}}$. The requirements on the variables at each bifurcation of the Decision Tree are optimized to maximize this quantity. Fig. 99 illustrates this fact of classifying events in a Decision Tree.

The Decision Tree by itself has the disadvantage that the event subsamples at deeper leaf levels become more and more statistically limited and information from events in different paths of the tree is lost. Furthermore, too stringent requirements on the variables that separate events at each bifurcation can cause the algorithm to fail in finding the optimal event separation in the

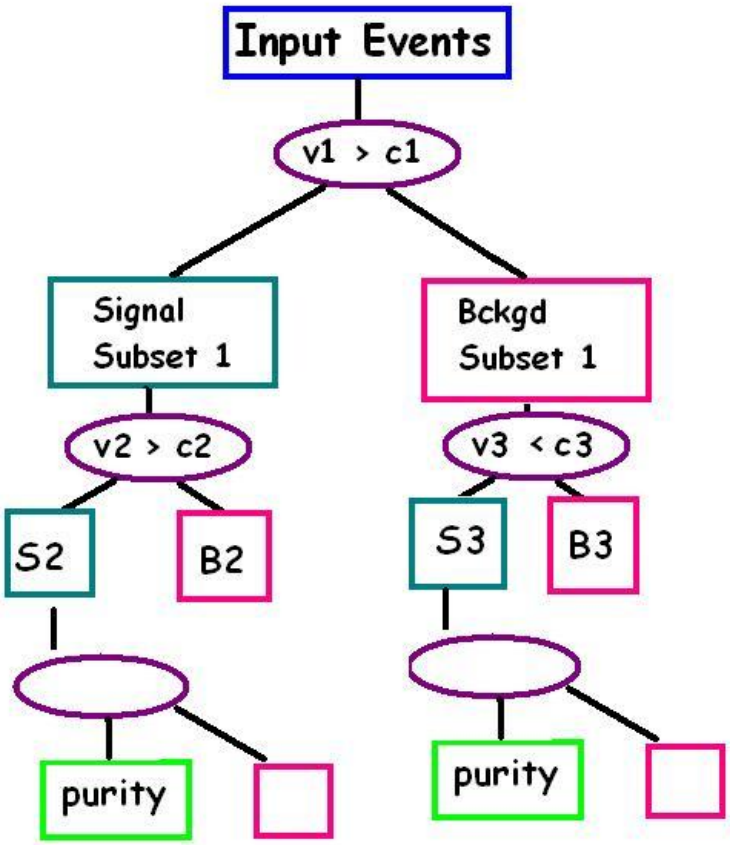

Figure 99: Schematic of a Decision Tree. At every separation node, also called leaf, the input events are separated into background-like or signal-like events, according to a selection criterion on one of the input variables. The separation process continues throughout the tree, using different a different variable and selection criterion in every leaf, until a certain minimal event threshold or signal purity is reached in the subsample.

final leaves.

To avoid these problems, we train a large number N of Decision Trees, called a *Random Forest* (RF). The trees in the RF all use a different subset of input events and variables for the separation. While a single tree is still prone to the above mentioned problems and training instabilities, the ensemble now becomes robust against these effects by two specific properties of the RF:

- The random choice of separation variables leads to different optimized separated event subsets and thereby reduces the effect of correlations between the variables.
- The random choice of input events, also called bootstrap aggregating (*bagging*), leads to the possibility to randomly select an event several times which is the key feature of this technique. By averaging over the output of the ensemble of trees, the final result becomes better in terms of signal and background separation power and becomes less susceptible to training instabilities.

In comparison to neural networks[5], Decision Trees have some advantages: Their sensitivity to poorly discriminating input variables and to correlations between variables is smaller. Technical details on the Random Forest algorithm we use, the C++ StatPatternRecognition package, can be found in Ref. [78], further details on Random Forests can be found in Ref. [79].

7.3.1.1 *Selection of Input Variables and Training*

VARIABLE SELECTION A preliminary result of the *WH* analysis on 5.0 fb^{-1} of data used neural networks to improve sensitivity [1]. The neural networks used seven kinematic variables to distinguish signal from background. They were trained to separate the *W*+b jets background from signal. In the Random Forest implemented in this analysis, we now use twenty variables, including all seven neural network training variables.
We use the following variables in the training of our Random Forest:

- p_T(leading jet), p_T(second leading jet)
- ΔR(jets), $\Delta\phi$(jets), p_T(dijet system), dijet invariant mass
- p_T(ℓ-$\not{E}_T$ system)
- $\Delta\phi$(ℓ, leading jet)
- $\not{E}_T$

5 previously used in earlier iterations of the *WH* analysis on smaller data sets

- Aplanarity (total p_T-component transverse to the dijet-(ℓ-ν) plane),
- $\sqrt{s}$, invariant mass of the neutrino-lepton-dijet system
- ΔR(dijet system,ℓ-ν system)
- lepton-$\not\!\!E_T$ invariant mass
- H_T, H_Z,sum of the transverse and z-momenta of all jets in the event, respectively
- $\cos\theta*, \cos\chi$, spin correlation variables described in [80]

For both $\sqrt{s}$ and $\Delta R(\ell - \not\!\!E_T)$ there are two inputs for each event, corresponding to the two solutions for the neutrino z-momentum $p_{z\nu}$. We obtain the two solutions from solving the following equation:

$$p_{T,\ell}^2 p_{z,\nu}^2 - p_{z,\ell}(M_W^2 + 2\left(p_{x,\ell}p_{x,\nu} + p_{y,\ell}p_{y,\nu}\right) + p_{T,\ell}^2 p_{T,\nu}^2 + p_{z,\ell}^2 p_{T,\nu}^2 - \frac{1}{4}(M_W^2 + 2\left(p_{x,\ell}p_{x,\nu} + p_{x,\ell}p_{y,\nu}\right)^2 = 0. \quad (7.4)$$

As a test of further improvement, we evaluated the final expected limit of the analysis using the Random Forest output in the case where we use the output of the neural network (the one used as a multivariate technique on a previous iteration of the analysis of a subset of the now used data sample) as an additional input variable. We, however, found no further improvement and therefore did not pursue this approach.

TRAINING We train the Random Forest separately for each Higgs mass point (100 - 150 GeV in steps of 5 GeV). We train against all backgrounds except for the multijet background as it is derived from data. We assign consecutive event numbers to all our simulated events and then use odd numbered events for training the Random Forest and even numbered events for testing.
For further sensitivity improvement, we also train the Random Forest separately on the sample of events from the electron and muon channel as well as the single and double tag samples. In events with 2 jets, we train RunIIa and RunIIb events separately, but we combine them for events with 3 jets due to lower statistics.

The three parameters that the training of a Random Forest depends on, are:

- S, the maximum number of input variables per tree,
- n, the number of trees in the forest,

Sample	Single tag		Double tag	
	N	l	N	l
RunIIa ele 2-jet	70	1000	100	300
RunIIa mu 2-jet	70	500	200	300
RunIIb ele 2-jet	50	400	50	150
RunIIb mu 2-jet	50	300	50	150
RunIIa+RunIIb ele 3-jet	70	1500	70	850
RunIIa+RunIIb mu 3-jet	70	1500	70	750

Table 16: Number of trees N and minimum leaf size l for the Random Forest training for each analysis subchannel.

- l, the minimum number of events at a leaf.

Typically, l is the most important variable in a Random Forest.

We use a technique called CROSS VALIDATION to determine the optimal training parameters for n and l in our analysis. Cross validation splits the training sample into N pieces with an equal number of events. The first piece is then used for validation while the others are used to train the Random Forest. The process repeats by using the second piece for validation and the others for training. This procedure is repeated N times for the total of the N pieces of the split up event sample. The final output is then taken as the average over all iterations. We choose the optimal parameter by optimizing the figure of merit.

For events with two jets in double tag events, l is typically around 150, in single tag events it is between 300 and 400 for events with 2 jets.
To determine the optimal number of trees n we follow a procedure described in Ref. [81], using 60% of our events for training and 40% for testing. We find that the final result is relatively insensitive to the choice of S. We choose $S = 13$ for our analysis. Table 16 lists the values of N and l for each sample.

7.3.1.2 *Performance*

We obtain Random Forest output distributions for each analysis subchannel (i.e. electron, muon, RunIIa and RunIIb sample), Fig. 100 (101) shows the distributions for the Random Forest trained on the ST and DT samples for the RunIIa (RunIIb) sample without requiring b tagging in the final state. Fig. 102 (103) shows the RF output for the RunIIa (RunIIb) sample requiring either exactly one tagged jet fulfilling the tight tagging criterion for usage with the RF trained on the ST sample or exactly two tagged jets fulfilling the loose tagging criterion for usage with the RF trained on

the DT sample .
Compared to the previous 5.0 fb^{-1} WH analysis using neural networks, we find an improvement between 7 and 13% on the expected limit when using a Random Forest on the same data sample. Fig. 105 shows the improvement in the expected sensitivity of the final output variable (NN or RF distribution) along the different Higgs mass points.

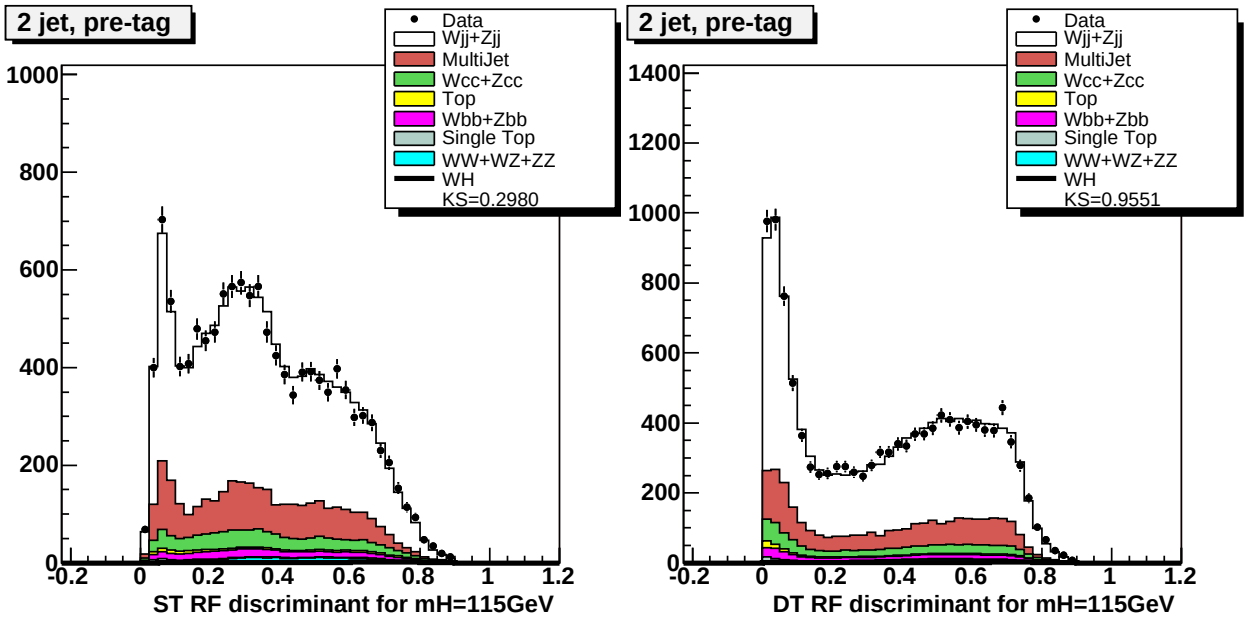

(a) Random Forest (pretag) trained on the Single Tag Electron Channel Sample, tested on the pretag sample

(b) Random Forest trained on the Double Tag Electron Channel Sample, tested on the pretag sample

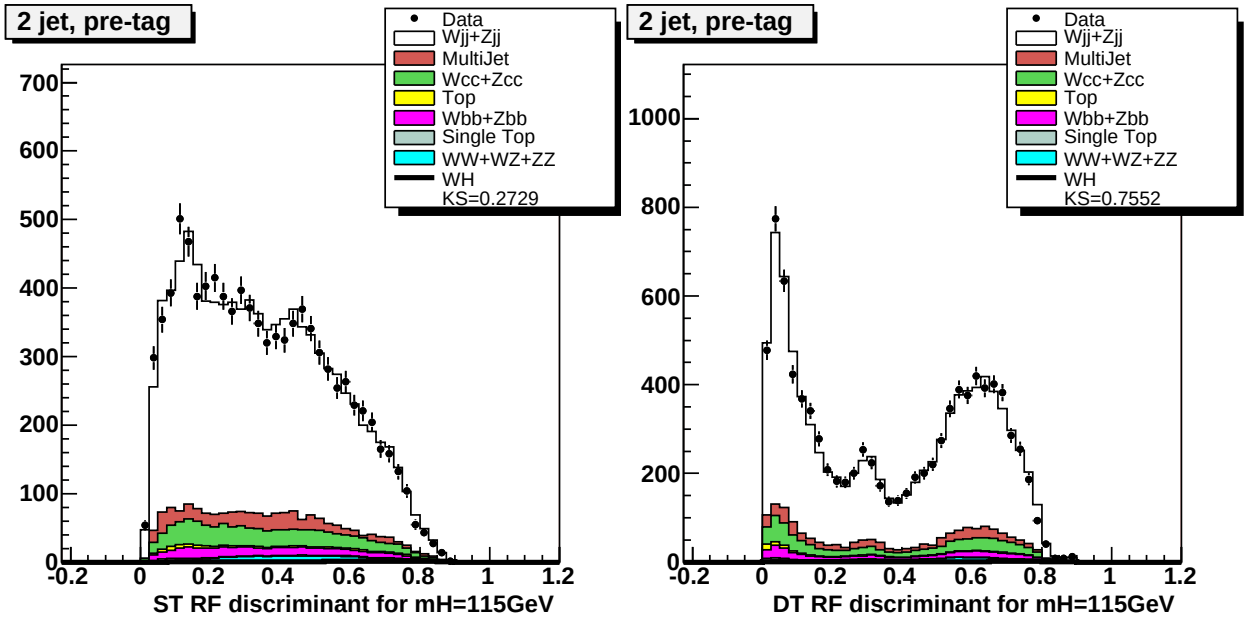

(c) Random Forest (pretag) trained on the Single Tag Muon Channel Sample, tested on the pretag sample

(d) Random Forest (pretag) trained on the Double Tag Muon Channel Sample, tested on the pretag sample

Figure 100: Random forest output distributions for two jet events (top: e-channel, bottom: μ-channel, RunIIa data) pretag level. The data are compared to $Wb\bar{b}$, $t\bar{t}$, W+jets and other smaller expectations. The simulated processes are normalized to the integrated luminosity of the data sample using the expected cross sections (absolute normalization) except for the W+jets sample which is normalized to data on the pretag sample, taking into account all the other backgrounds. b tagging was not required in the events in these plots.

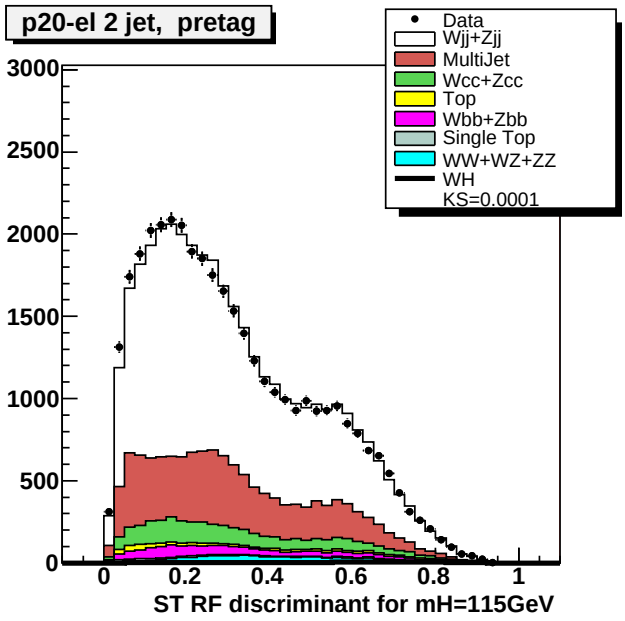

(a) Random Forest (pretag) trained on the Single Tag Electron Channel Sample, tested on the pretag sample

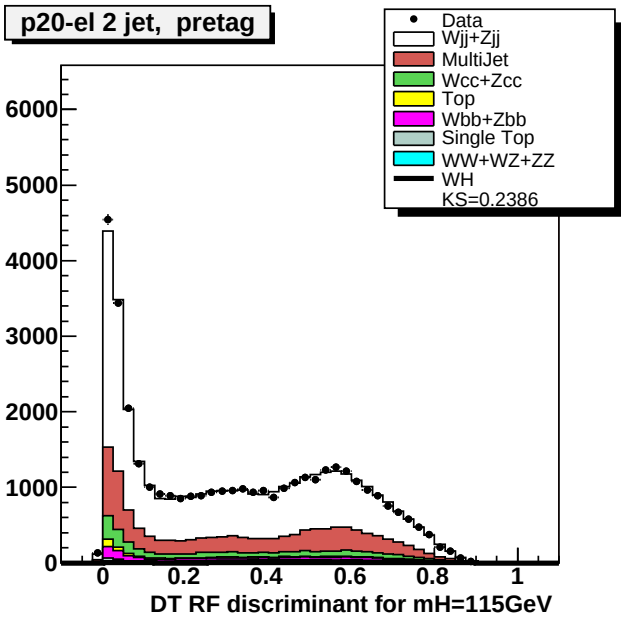

(b) Random Forest (pretag) trained on the Double Tag Electron Channel Sample, tested on the pretag sample

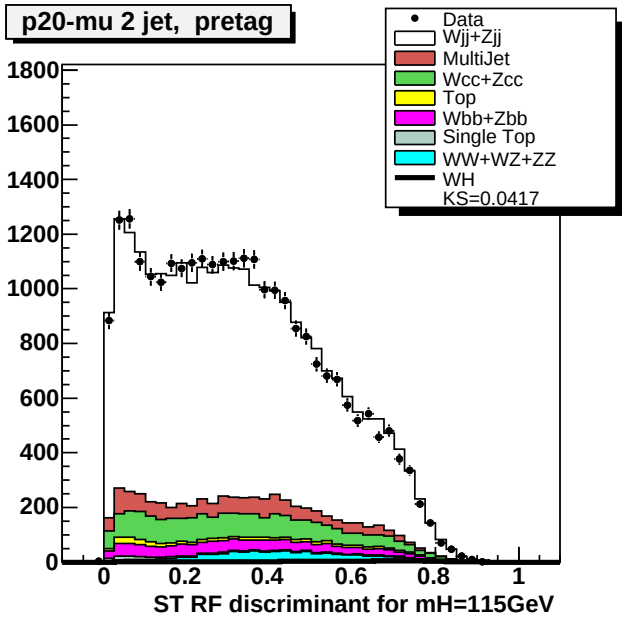

(c) Random Forest (pretag) trained on the Single Tag Muon Channel Sample, tested on the pretag sample

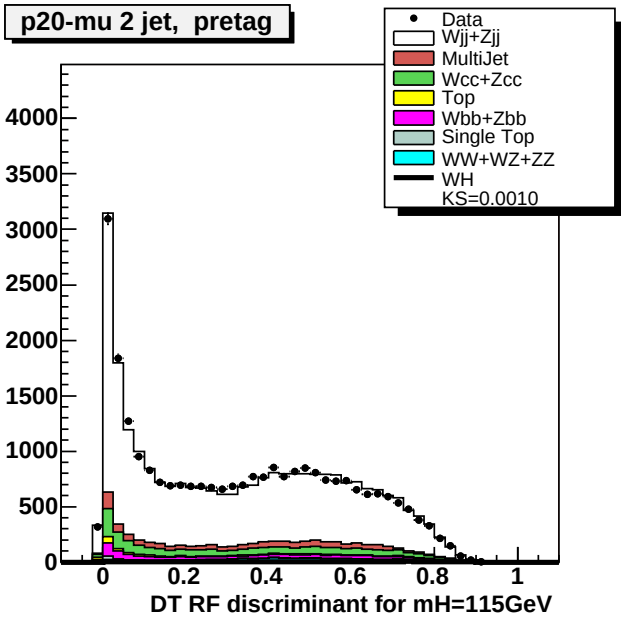

(d) Random Forest (pretag) trained on the Double Tag Muon Channel Sample, tested on the pretag sample

Figure 101: Random forest output distributions for two jet events (top: e-channel, bottom: μ-channel, RunIIb data) pretag level. The data are compared to $Wb\bar{b}$, $t\bar{t}$, W+jets and other smaller expectations. The simulated processes are normalized to the integrated luminosity of the data sample using the expected cross sections (absolute normalization) except for the W+jets sample which is normalized to data on the pretag sample, taking into account all the other backgrounds. b tagging was not required in the events in these plots.

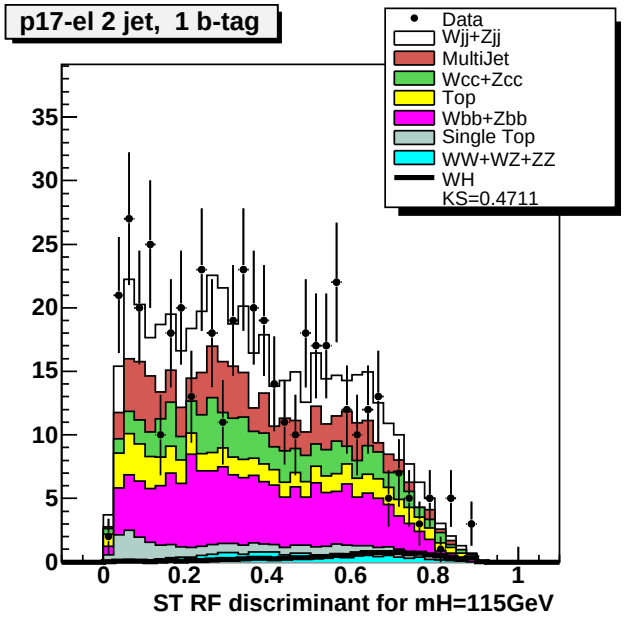

(a) Random Forest (single tag) trained and tested on the Single Tag Electron Channel Sample

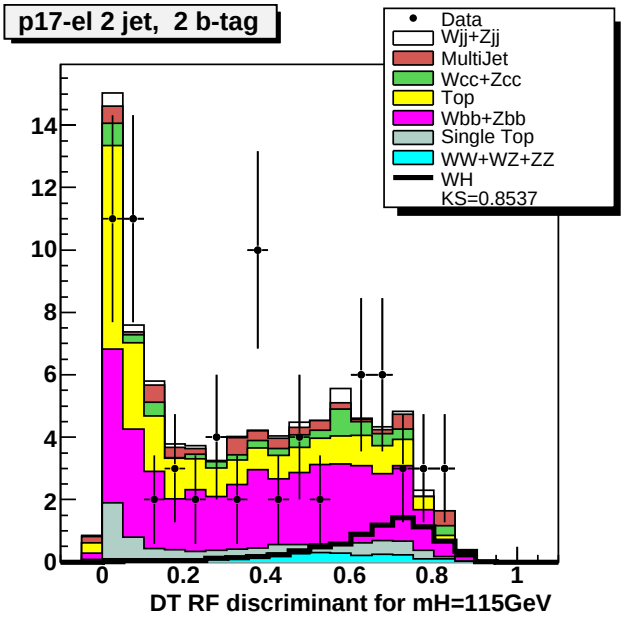

(b) Random Forest (double tag) trained on the Double Tag Electron Channel Sample

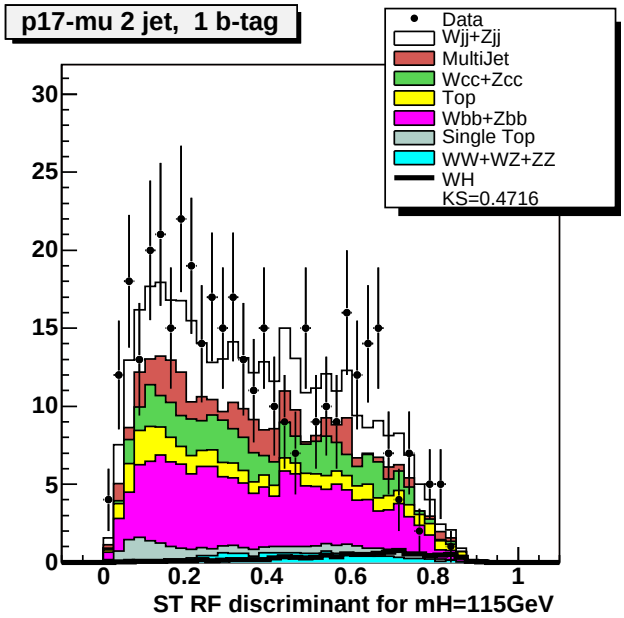

(c) Random Forest (single tag) trained and tested on the Single Tag Muon Channel Sample

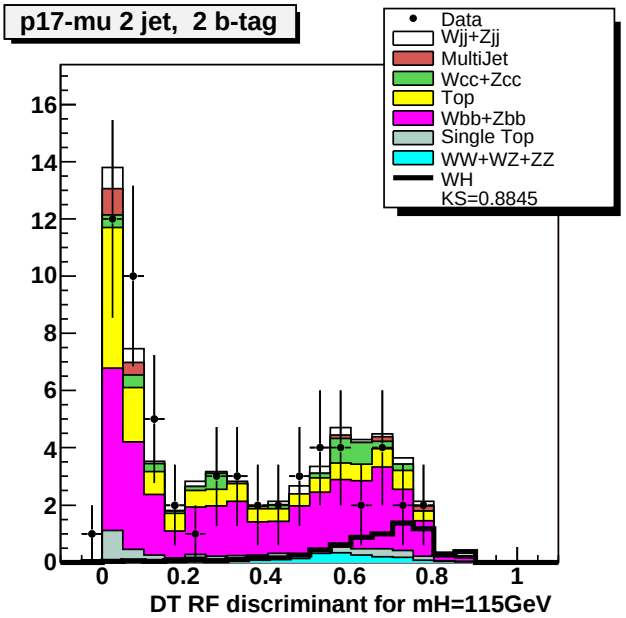

(d) Random Forest (double tag) trained and tested on the Double Tag Muon Channel Sample

Figure 102: Random forest output distributions for two jet events (top: e-channel, bottom: μ-channel, RunIIa data) when one or two jets are b tagged. The data are compared to $Wb\bar{b}$, $t\bar{t}$, W+jets and other smaller expectations. The simulated processes are normalized to the integrated luminosity of the data sample using the expected cross sections (absolute normalization) except for the W+jets sample which is normalized to data on the pretag sample, taking into account all the other backgrounds. We ask for one or two jets to be b tagged in the events in these plots.

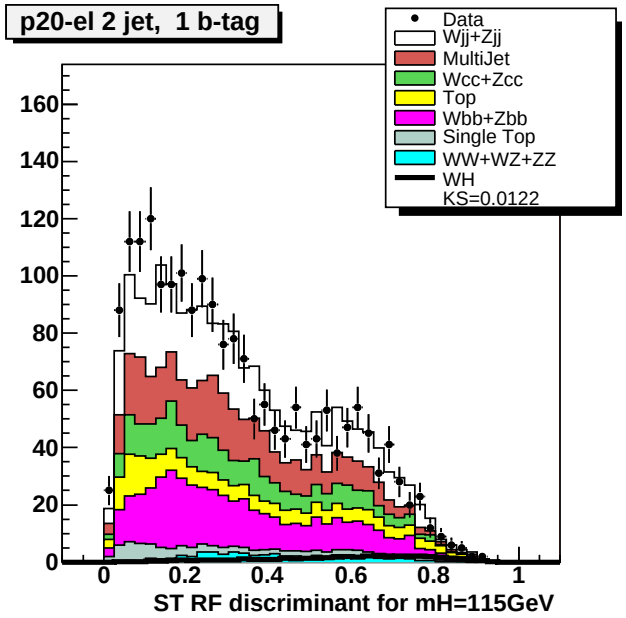

(a) Random Forest (single tag) trained and tested on the Single Tag Electron Channel Sample

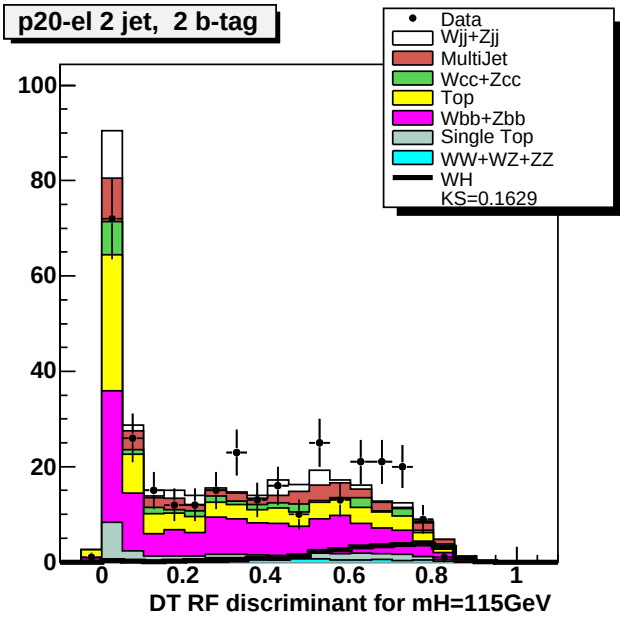

(b) Random Forest (double tag) trained and tested on the Double Tag Electron Channel Sample

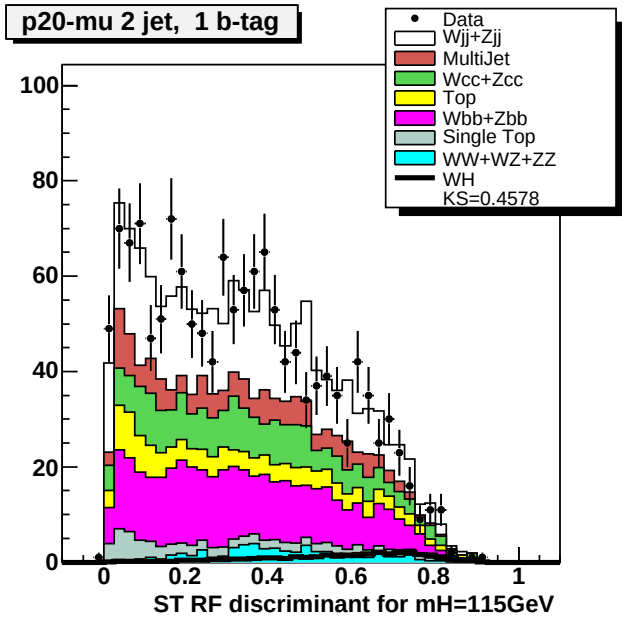

(c) Random Forest (single tag) trained and tested on the Single Tag Muon Channel Sample

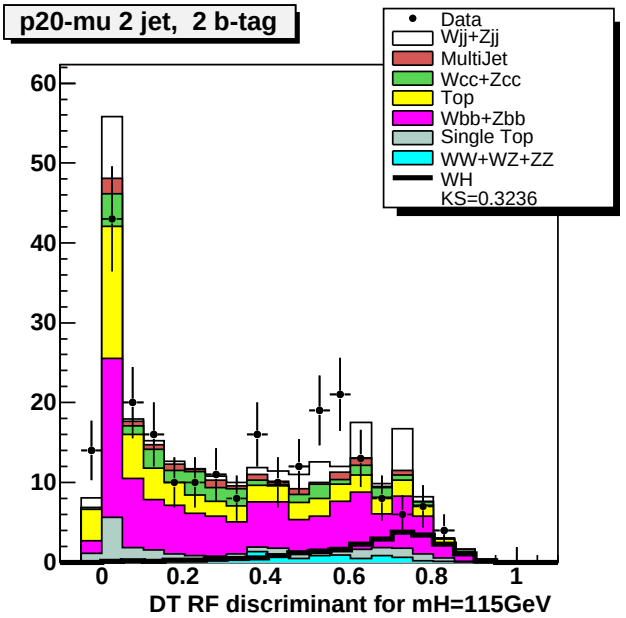

(d) Random Forest (double tag) trained and tested on the Double Tag Muon Channel Sample

Figure 103: Random forest output distributions for two jet events (top: e-channel, bottom: μ-channel, RunIIb data) when one or two jets are b tagged. The data are compared to $Wb\bar{b}$, $t\bar{t}$, W+jets and other smaller expectations. The simulated processes are normalized to the integrated luminosity of the data sample using the expected cross sections (absolute normalization) except for the W+jets sample which is normalized to data on the pretag sample, taking into account all the other backgrounds. We ask for one or two jets to be b tagged in the events in these plots.

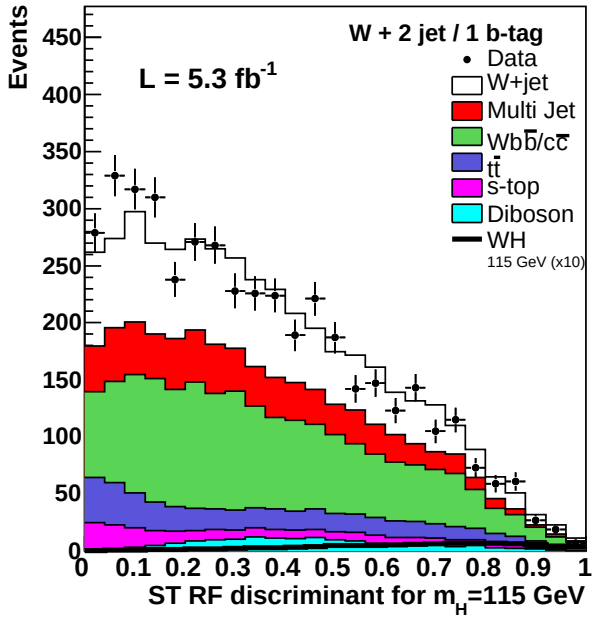

(a) Random Forest (single tag) trained and tested on the Single Tag

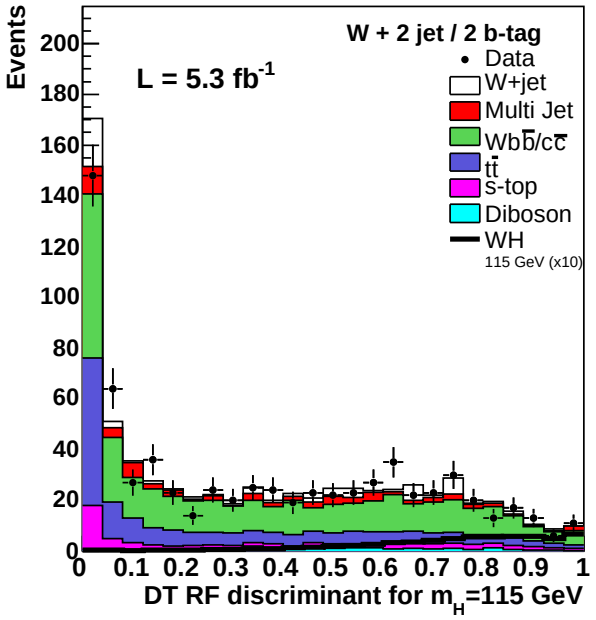

(b) Random Forest (double tag) trained and tested on the Double Tag

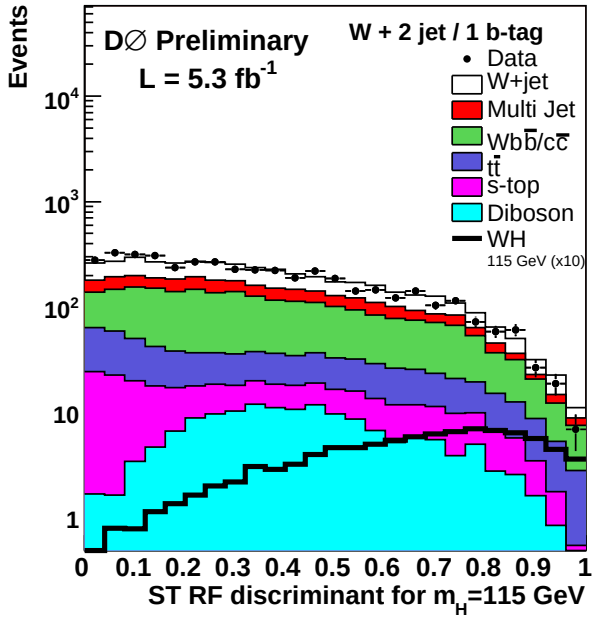

(c) Log Scale

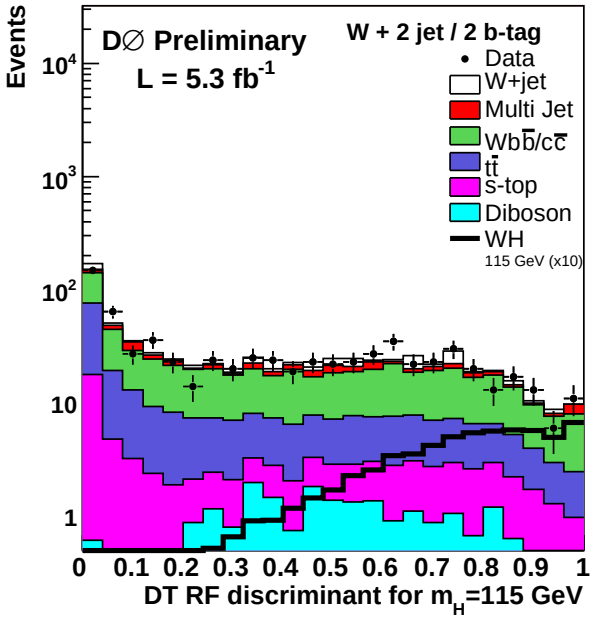

(d) Log Scale

Figure 104: Random forest output distributions for the combined two jet events (electron and muon, RunIIa and RunIIb). Left: RF trained and tested on the single tag sample. Right: RF tested and trained on the double tag sample. Top: Linear scale. Bottom: Log scale.

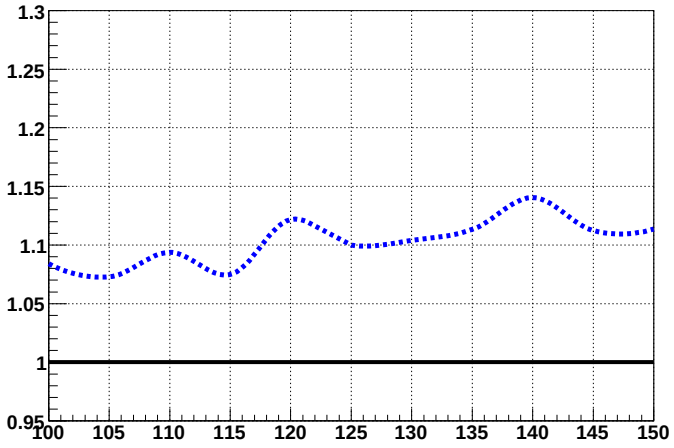

Figure 105: Expected sensitivity improvement using a Random Forest relative to the NN based analysis.

7.4 SIGNAL EXTRACTION

7.4.1 *Procedure*

In Secs. 7.1 - 7.3 we have shown how a dataset of 5.3fb^{-1} has been analyzed to find a hint on the associated production of a W and a Higgs boson. With the current dataset, we are unfortunately not yet sensitive enough to see a signal of a Higgs boson at low mass. Therefore, in the absence of a signal, we will calculate a limit on the production cross section in the WH channel.
Interpreting the final distribution of an analysis in terms of limit setting is a common procedure in high energy physics. There are two main statistical approaches to this.
The first one is called the *Frequentist approach*. The analysis is evaluated in terms of the likelihood that the observed result would occur at a certain frequency if the analysis was repeated many times. A background-only or signal+background hypothesis is tested to be true within a certain confidence interval.
The second approach is called the *Bayesian probability*. It interprets the outcome of the analysis as a measure of the knowledge of the experimenter. A certain probability is assigned to a background-only hypothesis and the level of agreement of the result with this hypothesis is then evaluated.

In the WH analysis we use a modified version of the Frequentist approach to evaluate our result [82, 83]. Therefore, we will detail this method in the following. We will go over techniques to reduce the impact of systematic errors on the final limit and detail the systematic errors relevant for the WH analysis. We will then present the final limit compared to the Standard Model expectation and the limit on the production cross section of the WH channel.

7.4.1.1 *Statistical Method*

For a particle search, we are interested in two possible different outcomes. Either the data-MC agreement in our final variable (in our case the RF output) is compatible with a background-only hypothesis (b) or with a signal+background hypothesis (s+b). This means that we are able to describe our data with background MC only or with MC including also a signal simulation, respectively. To quantify the quality of these hypotheses, we use a method commonly know as the "CL_s method" which was first used in the LEP experiment at CERN in Higgs searches. CL stands for confidence level, as we will be able to determine at which frequency it is likely for the result that we find in the analysis to occur. For example a 95% confidence level (CL) denotes that this particular outcome will occur in at least 95 out of 100 cases.

An important part of the method we use is the estimation of a log-likelihood ratio (LLR) test statistics. The test statistics Q is defined as the ratio of the two likelihoods L for the signal+background and the background-only hypothesis:

$$Q = \frac{L(s+b)}{L(b)} \tag{7.5}$$

If we interpret this statistics as a Poisson-like counting experiment in which s represents the number of expected signal events and b represents the number of expected background events with an observed number of data d, we can explicitly write Q in the following form:

$$Q = \frac{e^{-(s+b)}(s+b)^d}{d!} / \frac{e^{-b}(b)^d}{d!} \tag{7.6}$$

The advantage of this equation is that when we combine several statistics, the final statistics is just the product of the single statistics: $Q_\Pi = \prod_k Q_k$. Although we obtain continuous distributions for our final variables in the analysis, we can interpret them in the form of histograms with a finite binning. For the evaluation of the statistical tests we then interpret them as a sequence of Poisson distributions. We can also easily combine different channels of the analysis or even different analyses (like the Tevatron Higgs combination between DØ and CDF) using this method.
By taking the logarithm of the above expression, we can make it more easily computable. We define the LLR χ as

$$\chi = -2 \ln Q \tag{7.7}$$

which becomes, in the case of a particular observation m of either s or b events (for either one of the hypotheses),

$$\chi = 2\left(s - m \ln\left(1 + \frac{s}{b}\right)\right) \tag{7.8}$$

or in the case of a series of statistics,

$$\chi_\Pi = 2\left(\sum_k s_k - \sum_k m_k \ln\left(1 + \frac{s_k}{b_k}\right)\right). \tag{7.9}$$

Now we get back to the Frequentist interpretation of this test statistics in terms of a confidence level for a certain hypothesis. The confidence level for a hypothesis, e.g. signal+background (s+b) is defined as

$$CL_{s+b} = P_{s+b}(\chi \leqslant \chi_d) = \int_{-\infty}^{\chi_d} \frac{dP_{s+b}}{d\chi} d\chi \tag{7.10}$$

and analogous for the background-only hypothesis

$$CL_b = P_b(\chi \leqslant \chi_d) = \int_{-\infty}^{\chi_d} \frac{dP_b}{d\chi} d\chi. \tag{7.11}$$

The differential probability is defined by a distribution of the LLR χ of many pseudo-experiments n where n is the expected number $s + b$ of signal+background events in the signal+background hypothesis or b in the background-only hypothesis, respectively. Now that we have ways to calculate the CL_{s+b} and CL_b confidence levels, we can easily calculate the confidence level CL_s by building the ratio [84]:

$$CL_s = \frac{CL_{s+b}}{CL_b} \tag{7.12}$$

If we directly used CL_{s+b}, we would risk to be biased on our model for the simulation in the case where the MC does not describe the data well. By taking the ratio of CL_{s+b} and CL_b, we avoid this risk.
In practice, CL_s has two distinct values. CL_{exp} is the expected and CL_{obs} is the observed confidence level. We obtain the value of CL_{exp} by replacing the number of data d with the number of expected background events b in Eqs. 7.10 and 7.11. The smaller this value the more sensitive is the analysis. One remarkable point on this value is that it does not depend on observation and therefore provides an unbiased measure on the outcome of the analysis, in particular in comparison to the observed limit CL_{obs}. The calculation of the final limits is implemented in a statistical algorithm package called *Confidence Level Limit Evaluator* (COLLIE).

7.4.1.2 *Treatment of Systematic Uncertainties*

Making a valuable prediction on the upper limits of the signal model search parameter (such as the production cross section in the WH analysis) requires including systematic uncertainties. Now, the estimation of these uncertainties is rarely completely accurate as most of them depend on a large number of parameters. Typically, systematic uncertainties are therefore approximated by upper boundaries that might in some cases overestimate the real uncertainty. Such an overestimation leads naturally to a degradation of the final limits [85]. To compensate for this effect, we will describe a method to set constraints on systematic uncertainties

and reduce the impact of their effect on the final limits [86].
A measure for the quality of agreement on the final variable between data and MC is the χ^2 per number of degrees of freedom (NDF):

$$\frac{\chi^2}{\text{NDF}} = \sum_i \left(\frac{p_i - d_i}{\sigma_i} \right)^2 / \text{NDF} \tag{7.13}$$

where p_i is the predicted value, σ_i its uncertainty and d_i is the observation in data. An indicator for well understood uncertainties and a good MC modeling of the observed data is a value of $\chi^2/\text{NDF} \approx 1$, values above would indicate an underestimation of systematic uncertainties, values below would indicate an overestimation. Assuming Gaussian statistics for the likelihood $\mathcal{L}$, we can take a look at a very general form of χ^2 [85]:

$$\chi^2 = \sum_i \frac{(p_i - d_i)^2}{\sigma_i^2} \cong -2 \ln \left(\frac{\mathcal{L}}{\mathcal{L}_0} \right) \tag{7.14}$$

where $\mathcal{L}_0$ represents the likelihood in case of a perfect estimation of $p_i = d_i$. Going from Gaussian statistics to Poisson statistics for the likelihood functions, we can rewrite Eq. 7.14 to:

$$\chi^2 = 2 \sum_i \left[(p_i - d_i) - d_i \ln \left(\frac{p_i}{d_i} \right) \right] \tag{7.15}$$

To account for the impact of the systematic uncertainties, we insert them via their nuisance parameters into the predicted values:

$$p_i' = p_i \prod_{k=1}^{K} (1 - f_k^i S_k) \tag{7.16}$$

where p_i' is now the systematically varied prediction and the value f_k^i described the size of each of the K nuisance parameters. S_k represents a Gaussian constraint with a mean value of 0 and a width of 1.
To now minimize the impact of the systematic uncertainties, we apply a method called *profile likelihood* [85]. It relies on minimizing χ^2 by means of including the best estimates for each background and signal sample. We modify Eq. 7.15:

$$\chi^2 = 2 \sum_i \left[(p_i' - d_i) - d_i \ln \left(\frac{p_i'}{d_i} \right) \right] + \sum_k S_k^2 \tag{7.17}$$

where S_k and p'_i are defined as in Eq. 7.16. Fitting the S_k will now minimize χ^2. When the profile likelihood method is applied in our limit setting procedure, we recalculate it for every pseudo-experiment for the background and signal+background hypotheses separately which is then equivalent to estimating a best fit for each outcome of the experiment. Therefore, this is also called the best fit model and is implemented in the way the COLLIE package treats systematic uncertainties. The result of this best fit will be shown later in Fig. 107 for all systematic uncertainties discussed in the following.

For the final limit calculation on the production cross section, COLLIE uses the signal cross section as an unconstrained parameter in the fit of MC templates (including all systematic errors) to data. The resulting fit yields in a signal cross section estimation most compatible with the data provided, given in units of the nominal input cross section from the SM expectation. The results of this fit are listed later in Sec. 7.4.3.

7.4.2 *Systematic Uncertainties in the WH Analysis*

To estimate the systematic uncertainties in our analysis, we look at the effect of each source of uncertainty along the analysis chain on our final variable, the RF output distribution. The way we estimate the uncertainty is by individually varying each source of systematic uncertainty by $\pm 1\sigma$ (where σ is the size of the source of uncertainty, e.g. the jet energy scale correction). We re-perform a full analysis with the change in quantity of each source of uncertainty and then take the ratio of the obtained final distribution to our nominal distribution (where no additional systematic variation has been applied). This ratio is then a measure of the systematic uncertainty of the varied quantity.

We study each source of systematic uncertainty separately for each lepton type (e and μ) and for each jet multiplicity (2-jet and 3-jet) sample. We treat the multijet background separately since we derive it from data. We derive the systematic uncertainties in our analysis on the RunIIb samples only and then apply the same uncertainty to both the RunIIb and RunIIa samples[6].

In the following, we will further detail how we determine the systematic uncertainties (e.g. arising from the uncertainty in the efficiency ratios between data and simulation, the uncertainties on the propagation of trigger effects, energy calibration, jet energy scale correction). Appendix B exemplarily shows figures of the $\pm 1\sigma$ variation of all sources of systematic uncertainties in the RunIIb two jet electron channel on the RF output distribution. For

6 Unless stated differently in the following detailed descriptions

the calculation of the final limits we take into account the systematic errors on all analysis channels on the RF output. We estimate the errors separately on all simulated background contributions as well as on the simulated signal sample. Table 17 lists the systematic uncertainties in the single and double tagged samples which are used for the final limit calculation. Fig. 107 shows the results of the best fit to data for the different systematic uncertainties in units of Nσ deviations from the nominal uncertainty value of the systematic uncertainty for both the background-only and signal+background hypothesis.

7.4.2.1 *Jet Energy Scale Correction*

We evaluate the JES systematic uncertainty by scaling the energy correction of the reconstructed jet by $\pm 1\sigma$ instead of using the nominal jet energy.

7.4.2.2 *Jet Resolution and Jet Identification Efficiency*

This systematic uncertainty is evaluated in the same way as the JES correction. The energy correction applied to the jet is scaled up or down by 1σ instead of using the nominal jet energy.
To evaluate the systematic error on the jet identification efficiency, the shifted value of the applied efficiency factor is taken to obtain the -1σ variation. For the $+1\sigma$ variation, we symmetrize the -1σ distribution.

7.4.2.3 *Vertex Confirmation Scale Factor*

The scale factor for vertex confirmation defined as the probability of randomly removing a jet is shifted down by 1σ to evaluate its systematic error. For the $+1\sigma$ variation, we symmetrize the -1σ distribution, because the probability of removing a jet could already reach its maximum at 1 without being shifted in which case it could not be shifted up further.

7.4.2.4 *Lepton Identification*

ELECTRON IDENTIFICATION The systematic uncertainty on electron identification, reconstruction, efficiency and energy smearing is obtained by varying the correction factor by $\pm 1\sigma$.

MUON IDENTIFICATION The systematic uncertainty on muon identification has three components: the uncertainty on the muon identification efficiency, the uncertainty on the track reconstruction efficiency and the uncertainty on the muon isolation efficiency. We apply separate uncertainties on the RunIIa and RunIIb samples.

- *Identification Efficiency uncertainty:* We apply a 0.8% uncertainty on the RunIIa sample and a 1.2% uncertainty on the RunIIb sample. For the RunIIb sample we also apply an additional 2% systematic uncertainty in events with a transverse momentum of the muon $p_T < 20$ GeV.
- *Track Reconstruction Efficiency Uncertainty:* We apply a 2.3% uncertainty on the RunIIa sample and a 1.4% uncertainty on the RunIIb sample.
- *Isolation Efficiency Uncertainty:* We apply a 3.8% uncertainty on the RunIIa sample and a 0.9% uncertainty on the RunIIb sample.

7.4.2.5 *ALPGEN Reweightings*

- The systematic uncertainty of the ALPGEN reweighting is estimated by comparing the nominal (i.e. reweighted) version to a version in which reweighting functions are applied that generate a reweighting effect increased or decreased by 1 σ. The η reweightings of the leading and second leading jets as well as the reweighting of the ΔR between the two leading jets (for details on reweighting see Sec. 6.5) are each varied in this way.
- Additionally, the ALPGEN MLM parton matching is reweighted on the dijet mass. The evaluation is done in the same way as for the other ALPGEN reweightings, with reweighting functions shifted by $\pm 1\sigma$. This reweighting is applied to W/Z+light jets MC background samples only.
- The systematic uncertainty related to the ALPGEN event scale (k_T and Q^2) and the underlying event modeling are also evaluated.

7.4.2.6 *Z-vertex Position Reweighting*

A reweighting of the z vertex position is applied in this analysis. We determine an uncertainty on this reweighting by shifting its correction by $\pm 1\sigma$.

7.4.2.7 *Taggability Scale Factor*

The systematic uncertainty for taggability is evaluated by shifting the parameterizations of the Taggability Scale Factor functions up and down by 1σ.

7.4.2.8 *b Jet Identification*

The systematic uncertainty on b jet identification is evaluated by using the $\pm 1\sigma$ deviation from the Tagging Scale Factor (TSF).

In this analysis, we are applying direct tagging to the MC, and apply a scale factor which is the ratio of the data TRF and the MC TRF. This systematic uncertainty is evaluated separately for light and for heavy flavor jets. On average, 3% uncertainty for the b tagging efficiency per b quark jet (2.5% per c quark jet and 1~4% per light jet) are observed in single tag events (twice as much for double tag events).

7.4.2.9 *Parton Density Functions (PDF)*

In total 40 PDF variations are considered (20 pairs of positive and negative variations). While each PDF variation can change both the cross section and the kinematic acceptance of a MC process, only the changes due to kinematic acceptance are retained as part of the PDF systematic. To do this, we determine the cross section of each process under each PDF variation and then renormalize each of these variations to match the nominal cross section for that process. This method retains the effect that each PDF variation has on the kinematic acceptance of a process, while avoiding double counting the cross section uncertainties (described in Sec. 7.4.2.12).

7.4.2.10 *Electron and Muon trigger*

In the electron channel a 2% uncertainty from the trigger efficiency derived from the data sample used in this analysis is taken, whereas in the muon channel where all triggers are used (inclusive muon trigger selection) a larger systematic for the normalization change from the applied correction is used. To confirm that the muon trigger efficiency is 100%, we compare this result with a result triggered with the Single Muon triggers. The change in surface normalization is 2% between the inclusive MU trigger and the Single Muon trigger result. In order to check for a shape uncertainty, we build ratios for Data/MC (inclusive trigger - single mu trigger) over Data/MC (single mu trigger) and also separately the ratios Data/Data and MC/MC (inclusive)/(single mu) that show the trigger effect. We then develop a fit function (sigmoid + exponential decay) parameterized in p_T of the in dijet system for the double ratio of Data/MC (inclusive trigger - single mu trigger) over Data/MC (single mu trigger). We derive the function in the pretag sample and apply it to the ST and DT samples (on signal and all MC backgrounds) as well. Fig. 106 shows the derived function. We apply the value of the function as a multiplicative factor on P_{corr} (Sec. 6.4.1) and take the difference to the nominal version as the systematic on the muon trigger (normalization included.). The muon systematic is of the order of 3% .

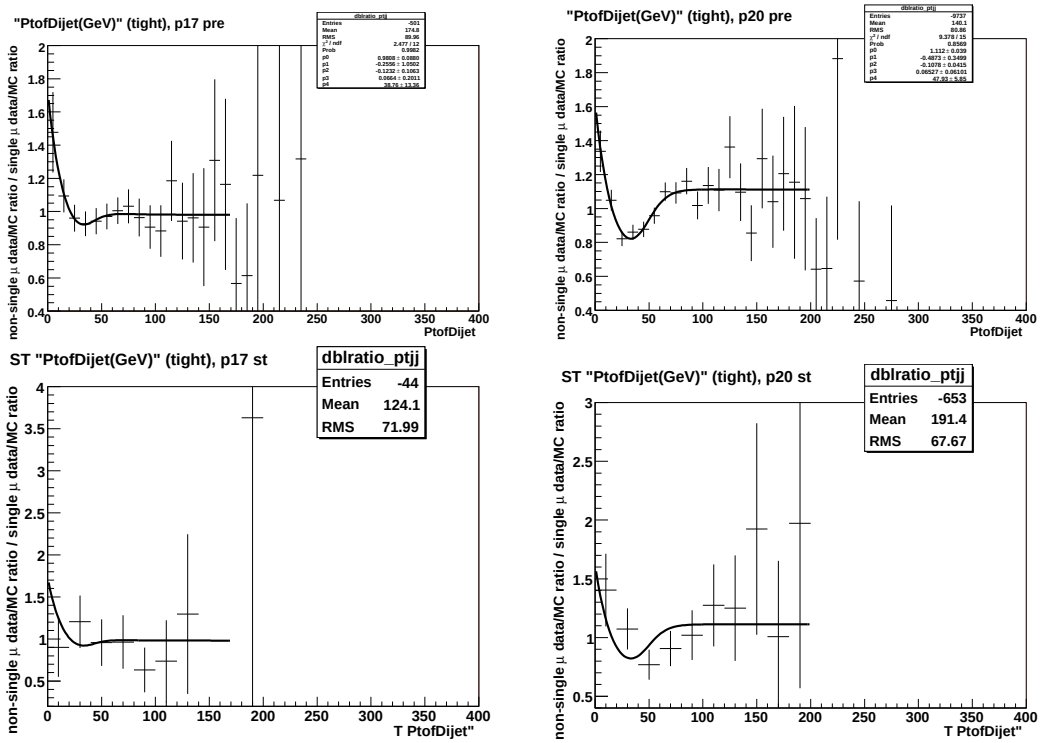

Figure 106: Fit function (sigmoid + exponential) parameterized in p_T of the dijet system for the double ratio of Data/MC (inclusive trigger - single mu trigger) over Data/MC (single mu trigger) used as the systematic uncertainty on the muon trigger. We derive the function in the pretag sample and apply it to both the ST and DT samples. Upper left: RunIIa pretag. Upper right: RunIIb pretag. Lower left: RunIIa single tag. Lower right: RunIIb single tag.

7.4.2.11 *Multijet Background*

The systematic uncertainty on the multijet background is estimated by varying separately the lepton efficiency and the jet misidentification rate by $\pm 1\sigma$ which are described in Sec. 6.6.1. The normalization of the multijet sample is anti-correlated with the normalization of the W+jets (light and heavy flavor) sample, which it taken into account during the limit setting procedure.

7.4.2.12 *Cross Section Uncertainties*

Overall, the total experimental systematic uncertainty for WH production is approximately 6%. The luminosity uncertainty is treated separately and amounts to 6.1%. The uncertainties on the cross sections of the background processes are 10% for $t\bar{t}$ production, 10% for single top production and 6% for WW, WZ and ZZ inclusive production [87].

We also apply uncertainties to the k factors applied to the W+jets samples, which directly affect the apparent cross section. We apply a 20% uncertainty on the W/Z+heavy flavor jets k factor, and a 6% uncertainty on the W/Z+light jets k factor. We will allow the s_{HF} factor to float during the limit setting and thus do not assign an uncertainty here.

Systematic Uncertainties [%] in the Single Tag channel

Contribution	WZ/WW	Wbb/Wcc	Wjj/Wcj	$t\bar{t}$	single top	Multijet	WH
Luminosity	6	6	6	6	6	0	6
Trigger eff.	2-3	2-3	2-3	2-3	2-3	0	2-3
EM ID/Reco eff./resol.	3	3	3	3	3	0	3
Muon ID/Reco eff./resol.	4.1	4.1	4.1	4.1	4.1	0	4.1
Jet ID/Reco eff.	1	1	2	1	1	0	1
Jet Energy Scale	2-5	2-5	2-5	2-4	2-5	0	2-5
b-tagging/taggability	5-6	3-4	8-9	2-4	2-4	0	2-4
Cross Section	6	9	9	10	10	0	6
Heavy-Flavor factor s_{HF}	0	20	0	0	0	0	0
Instrumental	0	0	0	0	0	1	0
PDF, reweighting	0-1	0-2	2-3	2-3	0-4	0	0-1

Systematic Uncertainties [%] in the Double Tag channel

Contribution	WZ/WW	Wbb/Wcc	Wjj/Wcj	$t\bar{t}$	single top	Multijet	WH
Luminosity	6	6	6	6	6	0	6
Trigger eff.	2-3	2-3	2-3	2-3	2-3	0	2-3
EM ID/Reco eff./resol.	3	3	3	3	3	0	3
Muon ID/Reco eff./resol.	4.1	4.1	4.1	4.1	4.1	0	4.1
Jet ID/Reco eff.	1	1	2	2	1	0	1-2
Jet Energy Scale	2-5	2-5	2-5	2-3	1-2	0	2-5
b-tagging/taggability	9-11	9-11	7	11-14	11-14	0	11-14
Cross Section	6	9	9	10	10	0	6
Heavy-Flavor factor s_{HF}	0	20	0	0	0	0	0
Instrumental	0	0	0	0	0	1	0
PDF, reweighting	0-1	0-1	1-2	2-3	0-1	0	0-1

Table 17: Systematic uncertainties (in percent) from all different sources important for the WH analysis.

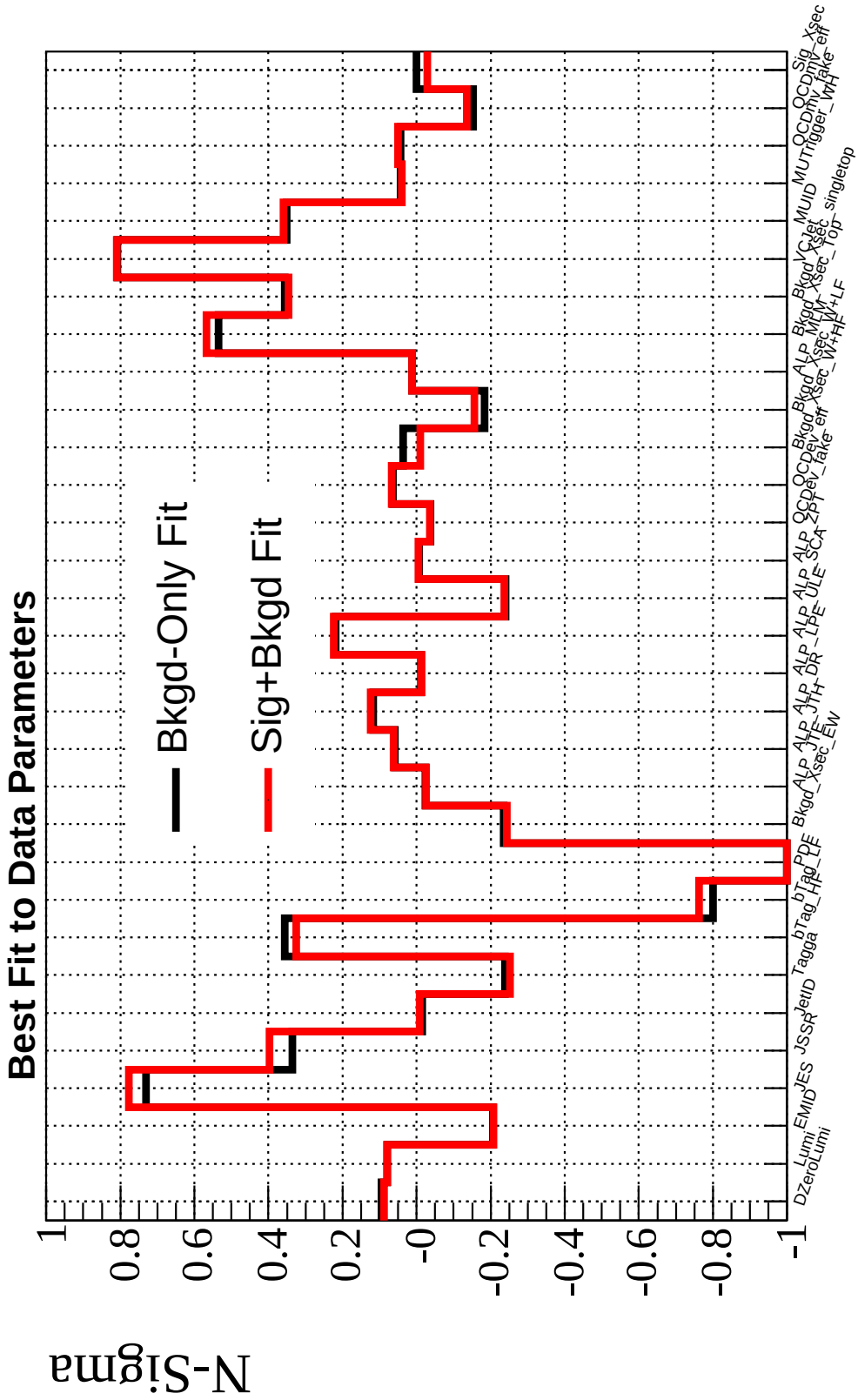

Figure 107: Values of systematic uncertainties after the best fit to data given in units of Nσ deviations of the nominal value of the input systematic uncertainty listed in Tab. 17. The black line denotes the fit result for the background-only hypothesis and the red line denotes the fit result assuming the signal+background hypothesis. For most systematic uncertainties a significant reduction in size is visible.

7.4.3 *Final Result on WH Production*

The final variables of our analysis, the dijet mass and the output of the random forest, do not show a significant signal excess compared to the background expectation. Tables 18–21 summarize the event yields in the different background and signal samples compared to data for the untagged, single tagged and double tagged selection in two and three jet events, separately for the electron and muon channel.

	$W(e)+2$ jets	$W(e)+2$ jets (1 b jet)	$W(e)+$ 2 jets (2 b jets)	$W(\mu)+2$ jets	$W(\mu)+$ 2 jets (1 b jet)	$W(\mu)+$ 2 jets (2 b jets)
WH	3.01 ± 0.33	1.25 ± 0.14	0.73 ± 0.08	2.45 ± 0.27	1.02 ± 0.11	0.62 ± 0.07
WW	266.45 ± 29.31	13.35 ± 1.47	0.36 ± 0.12	222.96 ± 24.53	10.50 ± 1.16	0.21 ± 0.22
WZ	43.96 ± 4.84	4.79 ± 0.53	2.17 ± 0.24	37.14 ± 4.09	3.86 ± 0.43	1.89 ± 0.21
ZZ	2.43 ± 0.27	0.29 ± 0.07	0.07 ± 0.14	2.14 ± 0.24	0.23 ± 0.06	0.11 ± 0.10
$Wb\bar{b}$	358.68 ± 71.74	124.26 ± 24.85	33.59 ± 6.72	316.62 ± 63.32	107.56 ± 21.51	29.93 ± 5.99
$Zb\bar{b}$	16.84 ± 3.37	5.38 ± 1.08	0.63 ± 0.14	8.93 ± 1.79	3.26 ± 0.65	0.58 ± 0.13
$Wc\bar{c}$	856.02 ± 171.20	68.07 ± 13.61	5.31 ± 1.06	771.01 ± 154.20	54.81 ± 10.96	4.76 ± 0.95
$Zc\bar{c}$	30.84 ± 6.17	2.07 ± 0.42	0.04 ± 0.25	21.37 ± 4.27	1.38 ± 0.28	0.06 ± 0.32
$t\bar{t}$	126.57 ± 17.72	51.97 ± 7.28	20.53 ± 2.87	80.29 ± 11.24	32.97 ± 4.62	13.37 ± 1.87
Single top	62.13 ± 8.08	26.39 ± 3.43	6.65 ± 0.86	52.35 ± 6.81	22.54 ± 2.93	5.50 ± 0.72
QCD Multijet	2048.58 ± 184.37	76.76 ± 6.91	5.07 ± 0.47	457.19 ± 41.15	38.55 ± 3.47	1.74 ± 0.20
$W+$ jets (light)	8225.6 ± 740.30	141.73 ± 12.76	2.11 ± 0.19	7406.36 ± 666.57	122.56 ± 11.03	4.04 ± 0.38
$Z+$ jets (light)	373.89 ± 33.65	4.58 ± 0.42	0.19 ± 0.28	178.64 ± 16.08	2.83 ± 0.26	0.00 ± 0.00
Total expectation	12412.00 (n.t.d.)	519.62 ± 32.90	76.73 ± 7.46	9555.00 (n.t.d.)	401.05 ± 27.37	62.19 ± 6.41
Observed Events	12412	479	74	9555	400	62

Table 18: Summary table for the event yields in the electron and muon **two jet** final state in the **RunIIa** sample. Observed events in data are compared to the expected number of events before tagging, after one tight b tag and after two loose b tags in simulated events, split up for all different background contributions (for WH a Higgs mass of $m_H = 115$ GeV was assumed). "n.t.d." stands for "normalized to data".

	$W(e)+3$ jets	$W(e)+3$ jets (1 b jet)	$W(e)+$ 3 jets (2 b jets)	$W(\mu)+3$ jets	$W(\mu)+$ 3 jets (1 b jet)	$W(\mu)+$ 3 jets (2 b jets)
WH	0.68 ± 0.08	0.29 ± 0.03	0.09 ± 0.03	0.58 ± 0.07	0.24 ± 0.03	0.09 ± 0.04
WW	60.13 ± 6.61	2.91 ± 0.32	0.11 ± 0.21	52.53 ± 5.78	3.16 ± 0.35	0.07 ± 0.41
WZ	10.95 ± 1.20	1.18 ± 0.14	0.37 ± 0.11	9.13 ± 1.00	0.98 ± 0.12	0.26 ± 0.10
ZZ	1.55 ± 0.17	0.13 ± 0.10	0.02 ± 0.32	0.60 ± 0.08	0.06 ± 0.11	0.02 ± 0.23
$Wb\bar{b}$	94.5 ± 18.90	28.47 ± 5.69	4.69 ± 0.94	89.63 ± 17.93	26.55 ± 5.31	3.58 ± 0.72
$Zb\bar{b}$	6.53 ± 1.31	1.90 ± 0.38	0.26 ± 0.10	3.01 ± 0.60	1.00 ± 0.20	0.21 ± 0.10
$Wc\bar{c}$	243.43 ± 48.69	17.65 ± 3.53	1.42 ± 0.28	237.63 ± 47.53	15.62 ± 3.12	1.07 ± 0.23
$Zc\bar{c}$	13.62 ± 2.72	0.84 ± 0.18	0.01 ± 0.44	6.84 ± 1.37	0.68 ± 0.17	0.00 ± 0.00
$t\bar{t}$	201.56 ± 28.22	82.52 ± 11.55	22.07 ± 3.09	151.45 ± 21.20	63.09 ± 8.83	16.97 ± 2.38
Single top	18.01 ± 2.34	7.27 ± 0.95	1.60 ± 0.21	15.48 ± 2.01	6.34 ± 0.82	1.40 ± 0.18
QCD Multijet	662.18 ± 59.60	30.13 ± 2.71	1.70 ± 0.22	132.01 ± 11.88	11.28 ± 1.02	0.63 ± 0.23
$W+$ jets (light)	1360.77 ± 122.47	22.29 ± 2.01	0.33 ± 0.03	1365.48 ± 122.89	21.32 ± 1.92	0.95 ± 0.09
$Z+$ jets (light)	83.77 ± 7.54	1.14 ± 0.13	0.03 ± 0.44	36.20 ± 3.26	0.78 ± 0.12	0.01 ± 0.63
Total expectation	2757.00 (n.t.d.)	196.43 ± 13.81	32.60 ± 3.26	2100.00 (n.t.d.)	150.85 ± 11.02	25.17 ± 2.52
Observed Events	2757	178	32	2100	137	25

Table 19: Summary table for the event yields in the electron and muon **three jet** final state in the **RunIIa** sample. Observed events in data are compared to the expected number of events before tagging, after one tight b tag and after two loose b tags in simulated events, split up for all different background contributions (for WH a Higgs mass of $m_H = 115$ GeV was assumed). "n.t.d." stands for "normalized to data".

	$W(e)+2$ jets	$W(e)+2$ jets (1 b jet)	$W(e)+$ 2 jets (2 b jets)	$W(\mu)+2$ jets	$W(\mu)+$ 2 jets (1 b jet)	$W(\mu)+$ 2 jets (2 b jets)
WH	10.66 ± 1.17	4.21 ± 0.46	2.83 ± 0.31	8.18 ± 0.90	3.23 ± 0.36	2.32 ± 0.26
WW	819.06 ± 90.10	48.56 ± 5.34	1.77 ± 0.26	628.50 ± 69.14	41.76 ± 4.59	1.73 ± 0.29
WZ	134.36 ± 14.78	15.30 ± 1.68	7.47 ± 0.82	107.17 ± 11.79	12.67 ± 1.39	6.24 ± 0.69
ZZ	5.03 ± 0.55	0.56 ± 0.11	0.25 ± 0.17	7.95 ± 0.88	0.72 ± 0.11	0.22 ± 0.14
$Wb\bar{b}$	1099.18 ± 219.84	385.74 ± 77.15	117.8 ± 23.56	963.55 ± 192.71	348.44 ± 69.69	101.54 ± 20.31
$Zb\bar{b}$	31.25 ± 6.25	10.09 ± 2.02	2.13 ± 0.43	33.75 ± 6.75	11.89 ± 2.38	3.05 ± 0.61
$Wc\bar{c}$	2637.17 ± 527.43	258.79 ± 51.76	22.59 ± 4.52	2035.37 ± 407.07	207 ± 41.40	22.68 ± 4.54
$Zc\bar{c}$	60.86 ± 12.17	5.33 ± 1.07	0.83 ± 0.23	73.94 ± 14.79	7.11 ± 1.42	0.65 ± 0.22
$t\bar{t}$	496.90 ± 69.57	196.71 ± 27.54	84.47 ± 11.83	336.94 ± 47.17	135.36 ± 18.95	58.69 ± 8.22
Single top	196.40 ± 25.53	82.81 ± 10.77	25.35 ± 3.30	165.66 ± 21.54	71.32 ± 9.27	20.76 ± 2.70
QCD Multijet	8319.60 ± 748.76	397.26 ± 35.75	39.65 ± 3.57	1477.89 ± 133.01	149.89 ± 13.49	10.00 ± 0.90
$W+$ jets (light)	23416.9 ± 2107.52	535.17 ± 48.17	25.36 ± 2.28	20357.1 ± 1832.14	457.24 ± 41.15	24.67 ± 2.22
$Z+$ jets (light)	496.15 ± 44.65	15.50 ± 1.40	0.65 ± 0.44	615.15 ± 55.36	10.42 ± 0.94	0.45 ± 0.62
Total expectation	37712.90 (n.t.d.)	1951.82 ± 114.69	328.31 ± 27.30	26803.00 (n.t.d.)	1453.81 ± 94.49	250.68 ± 22.68
Observed Events	37713	2002	325	26803	1435	248

Table 20: Summary table for the event yields in the electron and muon **two jet** final state in the **RunIIb** sample. Observed events in data are compared to the expected number of events before tagging, after one tight b tag and after two loose b tags in simulated events, split up for all different background contributions (for WH a Higgs mass of $m_H = 115$ GeV was assumed). "n.t.d." stands for "normalized to data".

	$W(e)+3$ jets	$W(e)+3$ jets (1 b jet)	$W(e)+$ 3 jets (2 b jets)	$W(\mu)+3$ jets	$W(\mu)+$ 3 jets (1 b jet)	$W(\mu)+$ 3 jets (2 b jets)
WH	2.14 ± 0.24	0.86 ± 0.10	0.37 ± 0.05	1.68 ± 0.19	0.69 ± 0.08	0.30 ± 0.05
WW	176.06 ± 19.37	10.82 ± 1.19	0.00 ± 0.00	118.03 ± 12.98	7.19 ± 0.80	0.05 ± 0.51
WZ	32.84 ± 3.61	4.25 ± 0.47	0.95 ± 0.16	20.33 ± 2.24	2.84 ± 0.32	0.67 ± 0.16
ZZ	1.86 ± 0.22	0.19 ± 0.17	0.05 ± 0.35	1.90 ± 0.22	0.18 ± 0.17	0.05 ± 0.37
$Wb\bar{b}$	256.11 ± 51.22	78.68 ± 15.74	14.32 ± 2.86	224.08 ± 44.82	72.93 ± 14.59	11.72 ± 2.34
$Zb\bar{b}$	9.51 ± 1.90	2.81 ± 0.56	0.37 ± 0.15	9.64 ± 1.93	2.74 ± 0.55	0.47 ± 0.15
$Wc\bar{c}$	710.24 ± 142.05	64.89 ± 12.98	4.38 ± 0.88	489.05 ± 97.81	39.68 ± 7.94	4.89 ± 0.98
$Zc\bar{c}$	22.09 ± 4.42	1.80 ± 0.37	0.01 ± 0.50	19.38 ± 3.88	1.79 ± 0.37	0.35 ± 0.31
$t\bar{t}$	681.66 ± 95.43	274.84 ± 38.48	77.33 ± 10.83	518.42 ± 72.58	212.20 ± 29.71	59.69 ± 8.36
Single top	53.03 ± 6.89	20.93 ± 2.72	5.45 ± 0.71	46.48 ± 6.04	19.04 ± 2.48	4.57 ± 0.59
QCD Multijet	2084.97 ± 187.65	109.62 ± 9.87	7.36 ± 0.67	353.38 ± 31.80	34.52 ± 3.11	2.99 ± 0.28
$W+$ jets (light)	3458.06 ± 311.23	88.56 ± 7.97	7.18 ± 0.66	3112.87 ± 280.16	74.49 ± 6.70	3.55 ± 0.35
$Z+$ jets (light)	93.57 ± 8.42	0.29 ± 0.36	0.00 ± 0.00	96.44 ± 8.68	1.46 ± 0.29	0.00 ± 0.00
Total expectation	7580.00 (n.t.d.)	657.70 ± 45.48	117.41 ± 11.30	5010.00 (n.t.d.)	469.05 ± 34.94	89.01 ± 8.77
Observed Events	7580	671	125	5010	477	119

Table 21: Summary table for the event yields in the electron and muon **three jet** final state in the **RunIIb** sample. Observed events in data are compared to the expected number of events before tagging, after one tight b tag and after two loose b tags in simulated events, split up for all different background contributions (for WH a Higgs mass of $m_H = 115$ GeV was assumed). "n.t.d." stands for "normalized to data".

With no signal excess in the $WH \to \ell\nu b\bar{b}$ analysis being observed, we proceed to set limits on the production cross section times branching ratio of the SM Higgs boson for all analyzed mass points. For the limit setting, we only use the final RF discriminant.

We calculate the limits at a 95% confidence level using the modified frequentist CL_s approach with a Poisson log-likelihood ratio test statistics as described in Sec. 7.4. We set upper expected and observed limits. Expected limits rely on a background-only hypothesis that assumes a hypothetical experimental outcome matching the expected background events. We present the limits in terms of ratios of the absolute cross section limit divided by the expected Standard Model Higgs boson production cross section. Table 22 and Fig. 110 show the final expected and observed limits.

Electron channel Results (RunIIa+IIb combined)											
Mass (GeV)	100	105	110	115	120	125	130	135	140	145	150
Expected Limit $/\sigma_{SM}$	4.39	4.78	5.57	6.13	7.53	9.09	11.46	14.99	21.44	31.09	66.91
Observed Limit $/\sigma_{SM}$	4.40	4.89	5.09	6.11	9.28	8.55	9.19	12.35	17.77	24.42	64.18
Muon channel Results (RunIIa+IIb combined)											
Mass (GeV)	100	105	110	115	120	125	130	135	140	145	150
Expected Limit $/\sigma_{SM}$	4.68	5.03	5.98	6.86	7.90	9.64	12.46	16.57	23.11	33.20	75.10
Observed Limit $/\sigma_{SM}$	4.12	5.65	5.60	5.78	6.29	12.31	10.46	13.86	21.23	25.69	75.10
Electron + Muon channel in Single tag (RunIIa+IIb combined)											
Mass (GeV)	100	105	110	115	120	125	130	135	140	145	150
Expected Limit $/\sigma_{SM}$	6.58	6.92	8.30	9.01	10.47	12.21	15.09	20.30	28.16	58.23	88.83
Observed Limit $/\sigma_{SM}$	4.12	4.89	4.27	5.44	8.56	12.27	11.30	14.37	27.74	49.52	108.31
Electron + Muon channel in Double tag (RunIIa+IIb combined)											
Mass (GeV)	100	105	110	115	120	125	130	135	140	145	150
Expected Limit $/\sigma_{SM}$	3.83	4.14	4.87	5.50	6.54	8.14	10.15	13.44	19.05	27.16	59.58
Observed Limit $/\sigma_{SM}$	4.49	5.78	5.98	6.89	7.37	11.17	8.76	12.25	15.32	20.56	49.40
Full Combined Results											
Mass (GeV)	100	105	110	115	120	125	130	135	140	145	150
Expected Limit $/\sigma_{SM}$	3.4	3.6	4.4	4.8	5.7	6.8	8.7	11.8	17.0	23.4	36.2
Observed Limit $/\sigma_{SM}$	2.0	4.3	3.4	4.1	5.7	7.8	6.8	7.3	12.6	12.2	32.7

Table 22: Expected and observed limits for all considered Higgs masses at 95% C.L. (taking into account all systematic errors in the limit setting procedure). The limits are presented as a ratio to the standard model prediction for the production cross section times branching ratio for all Higgs masses between 100 and 150 GeV (in steps of 5 GeV).

The obtained ratio translates into an observed limit on the production cross section times branching ratio $\sigma(p\bar{p} \to WH) \times B(H \to b\bar{b})$ of 0.533 pb or a factor of 4.1 at a 95% C.L. compared to the SM expectation of 0.13 pb, with a corresponding expected upper limit of 0.624 pb or a factor of 4.8, for a Higgs boson mass of 115 GeV.

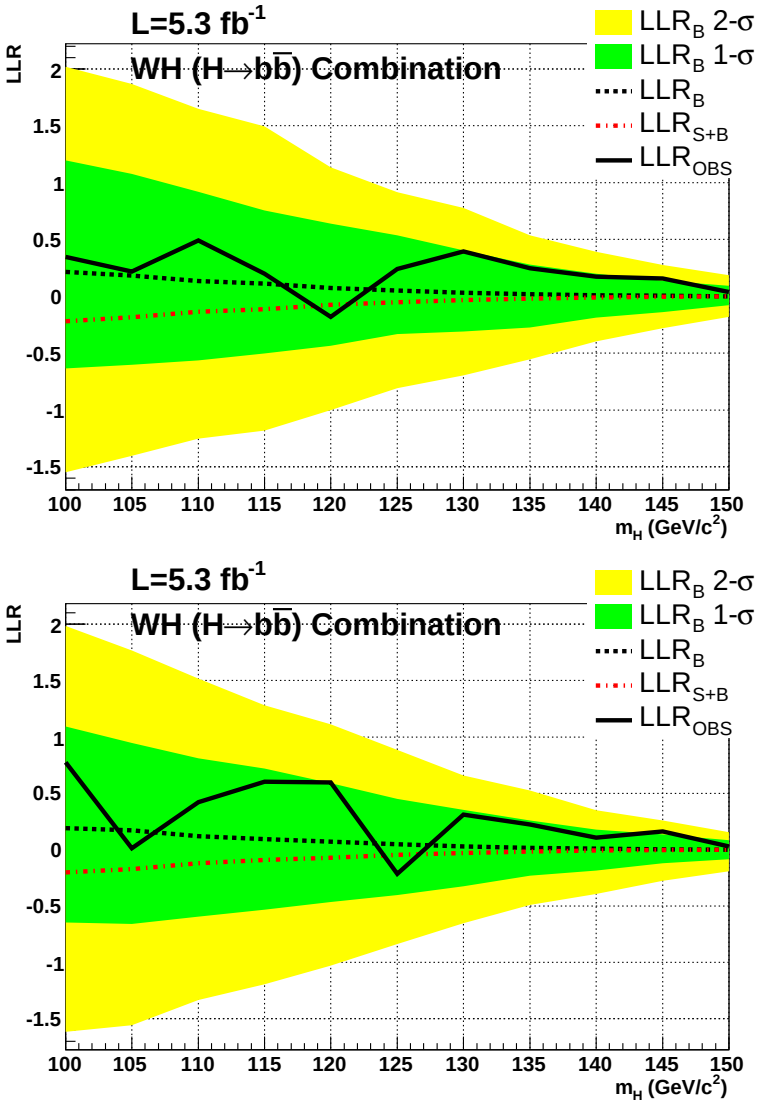

Figure 108: Log-likelihood ratio (LLR) distribution as a function of Higgs boson mass (taking into account all systematic errors) for the electron channel (top) and the muon channel (bottom), combining the output from RunIIa and RunIIb as well as two and three jet samples. The black (red) dashed line is the LLR for the background-only (signal+background) hypothesis, the solid black line is the result obtained from data. The green (yellow) band is the 1σ (2σ) uncertainty on the background-only LLR. The distance between the background-only and signal+background lines is a measure of sensitivity to a potential signal. In this case, the signal+background line lies within the 1σ uncertainty band, therefore, this analysis is not yet sensitive to a potential signal by itself.

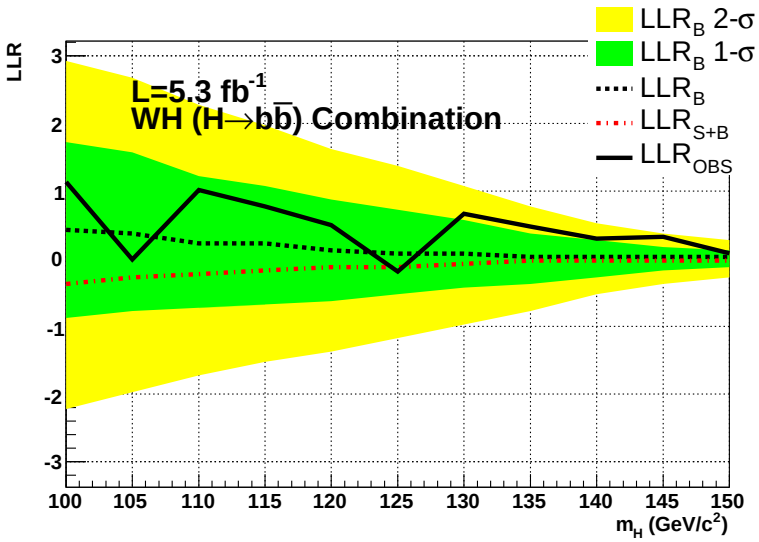

Figure 109: Log-likelihood ratio (LLR) distribution as a function of Higgs mass (taking into account all systematic errors) for the combination of all analysis channels. The black (red) dashed line is the LLR for the background-only (signal+background) hypothesis, the solid black line is the result obtained from data. The green (yellow) band is the 1σ (2σ) uncertainty on the background-only LLR. The distance between the background-only and signal+background lines is a measure of sensitivity to a potential signal. In this case, the signal+background line lies within the 1σ uncertainty band, therefore, this analysis is not yet sensitive to a potential signal by itself.

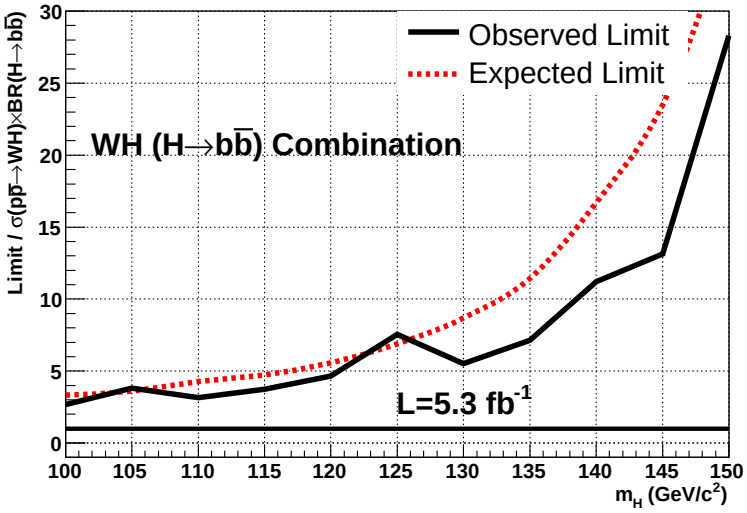

Figure 110: Limit on the cross section times branching ratio of the Higgs boson in the WH channel in units of the Standard Model prediction as a function of Higgs mass (taking into account all systematic errors) for the combination of all analysis channels. The dashed black line represents the expectation from simulated events only (CL_b), the solid black line represents the observation from data only (CL_s), both at 95% C.L.

Part III

CONCLUSION AND OUTLOOK

8

CONCLUSION AND OUTLOOK

We have presented results in two different yet strongly linked aspects of Higgs boson physics.
We have learned about the importance of the Higgs boson for the fate of the Standard Model, being either only a theory limited to explaining phenomena at the electroweak scale or, if the Higgs boson lies within a mass range of $130 < m_H < 160$ GeV the SM would remain a self consistent theory up to highest energy scales $\mathcal{O}(m_{Pl})$. This could have direct implications on theories of cosmological inflation using the Higgs boson as the particle giving rise to inflation in the very early Universe, if it couples non-minimally to gravity, an effect that would only become significant at very high energies.
After understanding the immense meaning of proving whether the Higgs boson exists and if so, at which mass, we have presented a direct search for a Higgs boson in associated production with a W boson in a mass range $100 < m_H < 150$ GeV. A light Higgs boson is favored regarding constraints from electroweak precision measurements. As a single analysis is not yet sensitive for an observation of the Higgs boson using 5.3 fb^{-1} of Tevatron data, we set limits on the production cross section times branching ratio.
At the Tevatron, however, we are able to combine the sensitivity of our analyses not only across channels or analyses at a single experiment but also across both experiments, namely CDF and DØ. This yields to the so-called Tevatron Higgs combination which, in total, combines 129 analyses from both experiments with luminosities of up to 6.7 fb^{-1}. The results of a previous Tevatron combination led to the first exclusion of possible Higgs boson masses since the LEP exclusion in 2001. The latest Tevatron combination from July 2010 can be seen in Fig. 111 and limits compared to the Standard Model expectation are listed in Table 23. It excludes a SM Higgs boson in the regions of $100 < m_H < 109$ GeV as well as $158 < m_H < 175$ GeV based on the observed final limits at 95% C.L.

In the most interesting low mass region between 115 and 135 GeV, even the full Tevatron combination is not yet sensitive enough to exclude a Higgs boson, or to even prove its existence with a meaningful significance. Fig. 112 shows a projection plot for sensitivity to the SM Higgs boson at the Tevatron as a measure of increasing luminosity.

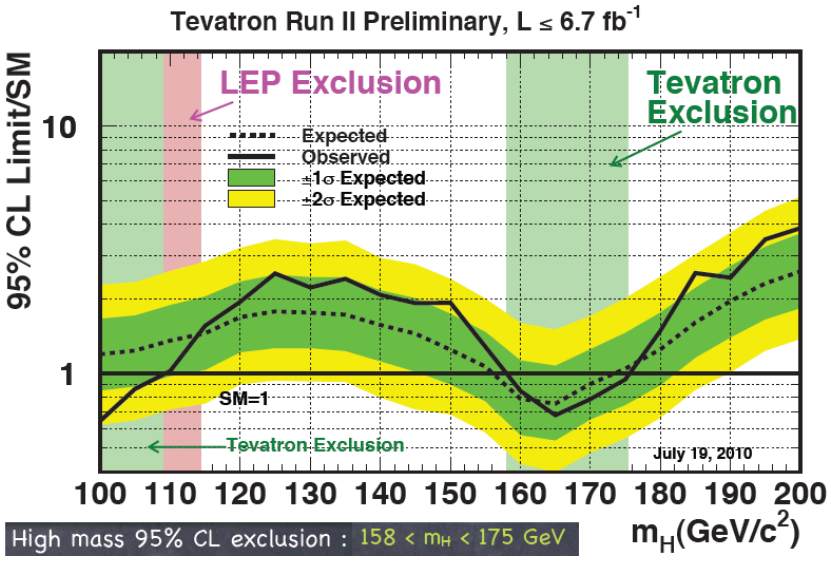

Figure 111: Observed (solid black line) and expected (dashed black line) limits on the production cross section times branching ratio for the SM Higgs boson as a factor of the Standard Model expectation. The green (yellow) shaded band represents the $\pm1\sigma$ ($\pm2\sigma$) uncertainty on the expected limit. The observed limit is the one measured from data, the expected limit represents the background-only prediction at 95% confidence level. The pink shaded band on the left is the mass region excluded by the LEP experiment ($m_H < 114.4$ GeV). The dark shaded band on the left represents the most recent (July 2010) exclusion from the Tevatron combination excluding Higgs masses in the region $100 < m_H < 109$ GeV, as well as the dark shaded band on the right excluding Higgs masses in the region $158 < m_H < 175$ GeV at 95% C.L. based on the observed values. [3]

Full Combined Results											
Mass (GeV)	100	105	110	115	120	125	130	135	140	145	150
Expected Limit $/\sigma_{SM}$	1.16	1.22	1.34	1.47	1.67	1.77	1.74	1.67	1.59	1.40	1.27
Observed Limit $/\sigma_{SM}$	0.66	0.87	1.07	1.64	2.12	2.85	2.44	2.48	2.09	1.90	1.80
Mass (GeV)	155	160	165	170	175	180	185	190	195	200	
Expected Limit $/\sigma_{SM}$	1.04	0.76	0.72	0.86	1.00	1.24	1.56	1.93	2.28	2.60	
Observed Limit $/\sigma_{SM}$	1.26	0.84	0.68	0.76	0.96	1.43	2.51	2.39	3.47	3.88	

Table 23: Expected and observed limits at 95% C.L. for the full Tevatron combination of xx analyses between the CDF and DØ experiment. Systematic errors are taken into account in the limit setting procedure. The limits are presented as a ratio to the standard model prediction for the production cross section times branching ratio for all Higgs masses between 100 and 200 GeV (in steps of 5 GeV).

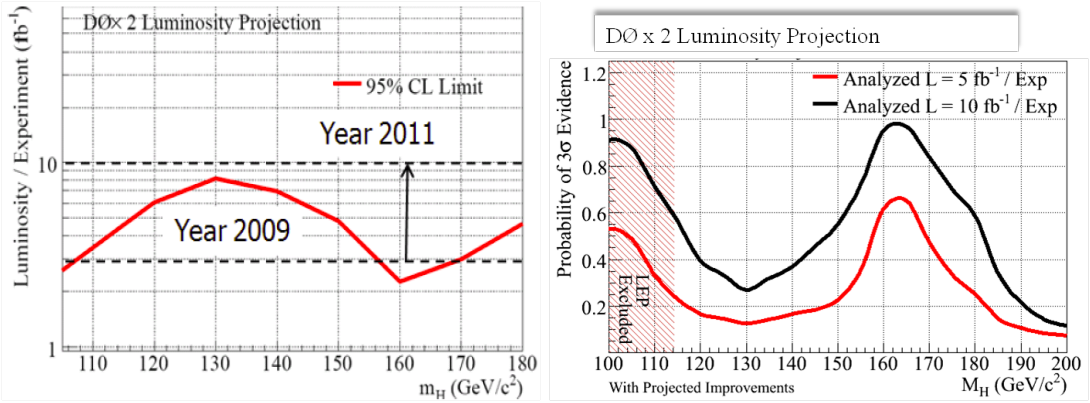

Figure 112: *Left*: The red line denotes the expected limit of the SM Higgs boson production cross section times branching ratio as a factor of the Standard Model expectation at 95% C.L. The dashed lines mark a factor of 1 compared to the SM expectation and therefore the boundary at which an exclusion at 95% C.L. is possible. In regions where the red line lies below the dashed line, a SM Higgs boson can be excluded. Therefore, in 2009 a first exclusion was possible in the high mass range and with the luminosity accumulated in 2011 an exclusion should be possible over the whole mass range according to this projection. *Right*: The red (black) line shows the probability of a 3σ evidence with 5 fb^{-1} (10 fb^{-1}) including some analysis improvements analogous to the progress made over the last years. Both figures assume the same integrated luminosity in both Tevatron experiments and a combination of sensitivities of analyses across the CDF and DØ experiment for these projections.

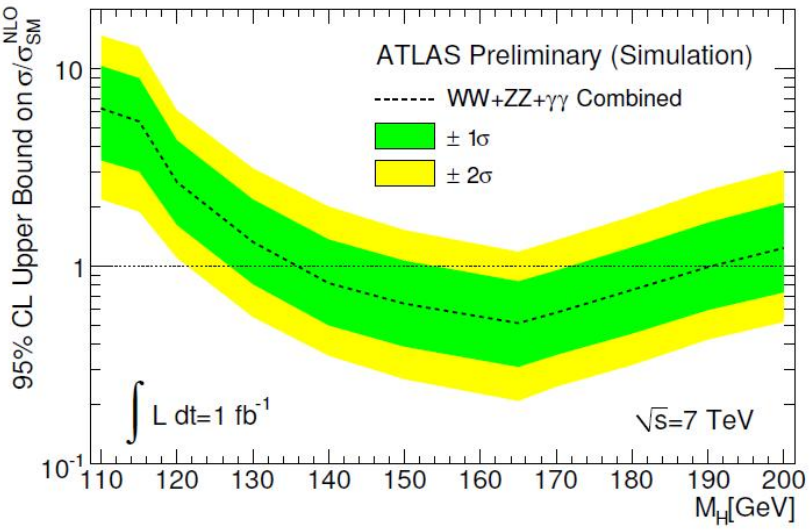

Figure 113: Expected limit of the SM Higgs boson production cross section times branching ratio as a factor of the Standard Model expectation at the LHC ATLAS experiment. The projection was made a dataset of 1 fb^{-1} of LHC data at a center of mass energy of 7 TeV. According to the projection, the SM Higgs boson would be excluded for a mass range of 135-188 GeV. [88]

The 10 fb^{-1} projection is a rather conservative outlook for the coming year of data taking as the Tevatron runs smoothly and the run till the end of 2011 is assured. By now, already 9 fb^{-1} have been recorded by the two experiments. As the extrapolation plot shows, this amount of luminosity will allow to exclude the Higgs boson over a wide mass range at a 95% C.L.

With the LHC at CERN now running and successfully collecting first data, it is worth looking at projections of Higgs boson sensitivity at the current center of mass energy of 7 TeV of the LHC accelerator. Fig. 113 shows a projection of a possible SM Higgs boson exclusion using 1 fb^{-1} of LHC data collected by the ATLAS experiment. An exclusion is expected between 135 and 188 GeV at 95% C.L., combining the three decay channels $H \to WW$, $H \to ZZ$ and $H \to \gamma\gamma$. A combination between LHC experiments would possibly yield an even broader range of excluded Higgs boson mass points. Therefore, whether at the Tevatron or the LHC, exciting times in the exclusion or possible discovery of the SM Higgs boson lie ahead.

BIBLIOGRAPHY

[1] *DØ Collaboration, Search for WH associated production using Neural Networks with 5.0 fb^{-1} of Tevatron data* DØ Note 5972-CONF, http://www-do.fnal.gov/Run2Physics/WWW/results/prelim/HIGGS/H78/H78.pdf. (Cited on pages 2, 57, and 191.)

[2] *DØ Collaboration, Search for WH associated production with 5.3 fb^{-1} of Tevatron data* To be submitted to PLB. (Cited on page 2.)

[3] *DØ Collaboration* Combined CDF and DØ Upper Limits on Standard Model Higgs-Boson Production with up to 6.7 fb^{-1} of Data, FERMILAB-CONF-10-xxx-E. (Cited on pages 2 and 224.)

[4] Gangopadhyaya, M. *Indian atomism: History and sources*. Humanities Press, Atlantic Highlands, NJ, USA, 1st edition, (1981). (Cited on page 17.)

[5] Ponomarev, L. *The Quantum Dice*. Institute of Physics Pub., Bristol, PA, USA, 2nd edition, (1993). (Cited on page 17.)

[6] Karagiorgi, G., Aguilar-Arevalo, A., Conrad, J. M., and Shaevitz, M. H. *Phys. Rev. D* **75**, 013011 (2007). (Cited on page 18.)

[7] Christenson, J. H., Cronin, J. W., Fitch, V. L., and Turlay, R. *Phys. Rev. Lett.* **13**, 138–140 Evidence for the 2 pi Decay of the k(2)0 Meson (1964). (Cited on page 19.)

[8] Pich, A. *FTUV/95-19, IFIC/95-19, arXiv:hep-ph/9505231v1* QUANTUM CHROMODYNAMICS, Lectures. (Cited on page 20.)

[9] Amsler, C. et al. *Phys. Lett. B* **667**(1), 1–298 January (2008). (Cited on pages 21 and 39.)

[10] Kobayashi, M. and Maskawa, T. *Prog. Theor. Phys. 49* 652 (1973). (Cited on page 21.)

[11] *http://nobelprize.org/nobel_prizes/physics/laureates/1979/* . (Cited on page 22.)

[12] Mosel, U. *Fields, Symmetries, and Quarks*. Springer-Verlag, Berlin, Germany, 2nd edition, (1999). (Cited on page 24.)

[13] Narison, S. *QCD as a theory of hadrons*. Cambridge University Press, Cambridge, UK, 1st edition, (2004). (Cited on page 25.)

[14] Langacker, P. *Lectures presented at TASI2008* , arXiv:0901.0241v1 (2009). (Cited on page 26.)

[15] Abbiendi, G. et al. *Search for the Standard Model Higgs Boson at LEP* CERN-EP/2003-011. (Cited on page 28.)

[16] *LEP-Tevatron Electroweak Working Group* http://lepewwg.web.cern.ch/LEPEWWG/. (Cited on pages 29, 30, and 31.)

[17] Flaecher, H., Goebel, M., Haller, J., Hoecker, A., Moenig, K., and Stelzer, J. *Revisiting the Global Electroweak Fit of the Standard Model and Beyond with Gfitter* CERN-OPEN-2008-024, DESY-08-160. (Cited on page 30.)

[18] *GSM - A Gfitter Package for the Global Electroweak Fit* http://gfitter.desy.de/GSM/. (Cited on pages 30 and 32.)

[19] working group, T. H. *Standard Model Higgs cross sections at hadron colliders* http://maltoni.web.cern.ch/maltoni/TeV4LHC/SM.html. (Cited on page 34.)

[20] Kalinowski, J., Djouadi, A., and Spira, M. *HDECAY: a Program for Higgs Boson Decays in theStandard Model and its Supersymmetric Extension*. Comput. Phys. Commun., 108, 1998. (Cited on page 35.)

[21] Fernández, F. *Introduction to perturbation theory in quantum mechanics*. CRC Press, Boca Raton, FL, USA, 1st edition, (2001). (Cited on page 37.)

[22] Burgess, C. and Moore, G. *The Standard Model: A Primer*. Cambridge University Press, Cambridge, UK, 1st edition, (2007). (Cited on page 38.)

[23] Ma, E. and Pakvas, S. *Phys. Rev. D* **20**(11), 2899–2902 December (1979). (Cited on page 38.)

[24] Arkani-Hamed, N., Dubovsky, S., Senatore, L., and Villadoro, G. *JHEP* **0803**(3), 075 March (2008). (Cited on pages 40 and 46.)

[25] Press, W., Flannery, B., Teukolsky, S., and Vetterling, W. *Numerical Recipes, Vol. I*. Cambridge University Press, Cambridge, UK, 1st edition, (1986). (Cited on page 41.)

[26] Amsler, C. et al. *Phys. Lett. B* **667**(1) January (2008 and 2009 partial update for the 2010 edition). (Cited on page 42.)

[27] Schrempp, B. and Wimmer, M. *Progress in Particle and Nuclear Physics* **37** (1996). (Cited on page 42.)

[28] Amelino-Camelia, G. *QUANTUM-GRAVITY PHENOMENOLOGY: STATUS AND PROSPECTS* Mod. Phys. Lett. A. (Cited on page 42.)

[29] Ellis, J., Espinosa, J., Guidice, G., Hoecker, A., and Riotto, A. *Phys. Lett. B* **679**(4), 369–375 August (2009). (Cited on pages 45, 46, and 47.)

[30] Casas, J., Espinosa, J., and Quiros, M. *Phys. Lett. B* (342), 171–179 (1995). (Cited on page 45.)

[31] Hambye, T. and Riesselmann, K. *Phys. Rev. D* **7255**(55) (1997). (Cited on page 46.)

[32] Abbiendi, G. et al. *Phys. Lett. B* **565**, 61–75 (2003). (Cited on page 47.)

[33] Tevatron New Phenomena, H. w. g. *FERMILAB-PUB-09-060-E* (2009). (Cited on page 47.)

[34] Dodelson, S. *Modern Cosmology*. Academic Press, New York City, NY, USA, 1st edition, (2003). (Cited on page 50.)

[35] *WMAP collaboration, 7 years data release* . (Cited on pages 50 and 52.)

[36] Starobinsky, A. A. *JETP Lett.* **30**, 682 (1979). (Cited on page 51.)

[37] Starobinsky, A. A. *Phys, Lett. B* **91**, 99 (1980). (Cited on page 51.)

[38] Mukhanov, V. F. and Chibisov, G. V. *JETP Lett.* **33**, 532 (1981). (Cited on page 51.)

[39] Guth, A. H. *Phys. Rev. D* **23**, 347 (1981). (Cited on page 51.)

[40] Linde, A. D. *Phys. Lett. B* **108**, 389 (1982). (Cited on page 51.)

[41] Albrecht, A. and Steinhardt, P. J. *Phys. Rev. Lett.* **48**, 1220 (1982). (Cited on page 51.)

[42] Schwarz, D. J. and Terrero-Escalante, C. A. *Primordial fluctuations and cosmological inflation after WMAP 1.0* JCAP 0408 (2004) 003. (Cited on page 53.)

[43] Fakir, R. and Unruh, W. *Improvement on cosmological chaotic inflation through nonminimal coupling* Phys. Rev. D. (Cited on page 53.)

[44] Bezrukov, F. and Shaposhnikov, M. *The Standard Model Higgs boson as the inflaton* Phys. Lett. B659, 2008. (Cited on page 53.)

[45] *DØ Collaboration, Luminosity ID group* Improved Determination of theDØ Luminosity, DØ Note 5140 (2006). (Cited on page 59.)

[46] *Fermilab Accelerator Division: Fermilab's Tevatron* http://www.fnal.gov/pub/science/accelerator/. (Cited on page 60.)

[47] *Fermilab Accelerator Details Website* http://www-bd.fnal.gov/public/multiturn.html. (Cited on page 61.)

[48] Abazov, V. et al. *The Upgraded DØ Detector, Nucl. Instrum. Meth.* (2005). (Cited on pages 63, 66, 69, 70, 72, 73, 74, 75, 76, 77, 78, 80, 81, 83, and 84.)

[49] *Fermilab Accelerator Details Website* http://www-bd.fnal.gov/public/antiproton.html. (Cited on pages 64 and 65.)

[50] *Fermilab Accelerator Division Pbar Rookie Book* http://www-bdnew.fnal.gov/pbar/documents/rookiebook.htm. (Cited on page 64.)

[51] Abachi, S. et al. *The DØ Detector, Nucl. Instrum. Meth.* **A338**, 185–253 (1994). (Cited on page 66.)

[52] *Fermilab: Explaining the DØ detector* http://www.fnal.gov/pub/now/live_events/explain_det_dzero.html. (Cited on page 67.)

[53] *Inter Cryostat Detector Group Web Page* http://www-do.fnal.gov/icd/icd_main.html. (Cited on page 68.)

[54] Greenlee, H. *The DØ Kalman Track Fit* DØ Note 4303. (Cited on page 87.)

[55] Khanov, A. *HTF: histogramming method for finding tracks. The algorithm description* DØ Note 3778. (Cited on page 87.)

[56] Borissov, G. *Ordering a Chaos or...Technical Details of AA Tracking* www-do.fnal.gov/global_tracking/talks/20030228/talk-adm-030228.ps. (Cited on page 88.)

[57] Schwartzman, A. and Tully, C. *Primary Vertex Reconstruction by Means of Adaptive Vertex Fitting* DØ Note 4918. (Cited on page 88.)

[58] Schwartzman, A. and Narain, M. *Probabilistic Primary Vertex Selection* DØ Note 4042. (Cited on page 89.)

[59] Group, M. *Muon ID Certification for p20 data* DØ Note 5824. (Cited on pages 93 and 94.)

[60] Blazey, G. C. et al. *Run II Jet Physics: Proceedings of the Run II QCD and Weak Boson Physics Workshop* hep-ex/0005012v2 (2000). (Cited on page 96.)

[61] Collaboration, T. B. *A Measurement of the Neutral B Meson Lifetime using Partially Reconstructed* $B^0 \to D^{*-}\pi^+$ *Decays* (2002). (Cited on page 100.)

[62] Scanlon, T. *A Neural Network b-tagging Tool* DØ Note 4889. (Cited on page 102.)

[63] Hornik, K. et al. *Multilayer Feedforward Networks are Universal Approximators* Neural Networks, Vol. 2, p359-366 (1989). (Cited on page 103.)

[64] Ruck, D. et al. *The Multilayer Perceptron as an Approximation to a Bayes Optimal Discriminant Function* IEEE Transactions on Neural Networks, Vol. 1, p296-298 (1990). (Cited on page 103.)

[65] Collaboration, D. *b-Jet identification in the Do experiment, Nuclear Instruments and Methods in Physics Research A* (2010). (Cited on pages 108 and 148.)

[66] Mangano, M. L. et al. *ALPGEN, a generator for hard multiparton processes in hadronic collisions* JHEP, 001, 2003, hep-ph/0206293. (Cited on page 109.)

[67] Sjostrand, T., Lonnblad, L., and Mrenna, S. *PYTHIA 6.2: Physics and manual* 2001, hep-ph/0108264. (Cited on page 109.)

[68] Boos, E. E., Bunichev, V. E., Dudko, L. V., Savrin, V. I., and Sherstnev, A. V. *Method for simulating electroweak top-quark production events in the NLO approximation: Single-Top event generator* Phys. Atom. Nucl., 69, 2006. (Cited on page 110.)

[69] Pumplin, J. et al. *New generation of parton distributions with uncertainties from global QCD analysis* JHEP, 07, 2002, hep-ph/0201195. (Cited on page 110.)

[70] Hoeche, S., Krauss, F., Lavesson, N., Lonnblad, L., Mangano, M., Schaelicke, A., and Schumann, S. *Matching Parton Showers and Matrix Elements* Proceedings of the "HERA and the LHC" workshop, CERN/DESY 2004/2005. (Cited on page 111.)

[71] *dogstar website* http://www-do.fnal.gov/computing/MonteCarlo/simulation/dogstar.html. (Cited on page 111.)

[72] Asai, M. *GEANT4 - A Simulation Toolkit* **95**, 757 Trans. Amer. Nucl. Soc. (2006). (Cited on page 111.)

[73] *dosim website* http://www-do.fnal.gov/computing/MonteCarlo/simulation/dosim.html. (Cited on page 111.)

[74] Agelou, M. et al. *Top Trigger Efficiency Measurements and the top trigger package* DØ Note 4512. (Cited on pages 125 and 126.)

[75] Schellman, H. *The longitudinal shape of the luminous region at DØ* DØ Note 5142. (Cited on pages 127 and 128.)

[76] Shamim, M. and Bolton, T. *Generator Level Reweighting of Z boson* p_T DØ Note 5565. (Cited on page 129.)

[77] Wang, L., Eno, S., Sanders, M., and Zhu, J. *Measurement of Z boson transverse momentum at* $\sqrt{s} = 1.96$ *TeV* DØ Note 5187. (Cited on page 129.)

[78] Narsky, I. *StatPatternRecognition: A C++ Package for Statistical Analysis of High Energy Physics Data* arXiv:physics/0507143v1. (Cited on page 191.)

[79] Narsky, I. *Optimization of Signal Significance by Bagging Decision Trees* arXiv:physics/0507157v1. (Cited on page 191.)

[80] Parke, S. and Veseli, S. *Distinguishing WH and* $Wb\bar{b}$ *production at the Fermilab Tevatron* Phys. Rev. D 60, 093003 (1999). (Cited on page 192.)

[81] *DØ Collaboration, First Evidence for Diboson Production in Lepton Plus Jets Decays* Phys. Rev. Lett.102, 161801 (2009). (Cited on page 193.)

[82] Fisher, W. *Calculating Limits for Combined Analyses* DØ Note 4975. (Cited on page 201.)

[83] Junk, T. *Nucl. Instrum. Meth. A 434, 435* (1999). (Cited on page 201.)

[84] Read, A. *First workshop on confidence limits, 2000, CERN, Geneva* . (Cited on page 203.)

[85] Fisher, W. *Systematics and Limit Calculations* DØ Note 5309. (Cited on pages 203 and 204.)

[86] Junk, T. *Building a More General* χ^2 CDF/DOC/STATISTICS/PUBLIC/7904. (Cited on page 204.)

[87] Bernardi, G., Choi, S., and Hanagaki, K. *Cross Section Errors Used in the Higgs Searches* DØ Note 5043. (Cited on page 210.)

[88] ATLAS-Collaboration. Technical Report ATL-PHYS-PUB-2010-009. ATL-COM-PHYS-2010-373, CERN, Geneva, Jul (2010). (Cited on page 226.)

[89] Weinberg, S. *The Quantum Theory of Fields, Vol. I*. Cambridge University Press, Cambridge, UK, 1st edition, (1995). (Not cited.)

[90] Weinberg, S. *The Quantum Theory of Fields, Vol. II*. Cambridge University Press, Cambridge, UK, 1st edition, (1996). (Not cited.)

[91] Muta, T. *Foundations of Quantum Chromodynamics*. World Scientific Publishing Co., River Edge, NY, USA, 1st edition, (1998). (Not cited.)

[92] de Wit, B. and Smith, J. *Field Theory in Particle Physics, Vol. I*. North-Holland Physics Publishing, Amsterdam, The Netherlands, 1st edition, (1986). (Not cited.)

[93] Griffiths, D. *Introduction to Elementary Particles*. WILEY-VCH, Weinheim, Germany, 2nd edition, (2008). (Not cited.)

[94] Auyang, S. *How is Quantum Field Theory Possible?* Oxford University Press, New York, NY, USA, 1st edition, (1995). (Not cited.)

[95] Amit, D. *Field Theory, the Renormalization Group, and Critical Phenomena*. World Scientific Publishing Co., River Edge, NY, USA, 2nd edition, (1984). (Not cited.)

[96] Peskin, M. and Schroeder, D. *An Introduction to Quantum Field Theory*. Westview Press, Boulder, CO, USA, 1st edition, (1995). (Not cited.)

[97] McCabe, G. *Philosophy and Foundations of Physics, Vol. 2. The Structure and Interpretation of the Standard Model*. Elsevier, Oxford, UK, 1st edition, (2007). (Not cited.)

[98] Kane, G. *Modern Elementary Particle Physics*. Addison-Wesley, Redwood City, CA, USA, 1st edition, (1999). (Not cited.)

[99] Linde, A. *Particle Physics and Inflationary Cosmology*. Harwood academic publishers, Amsterdam, The Netherlands, 1st edition, (1990). (Not cited.)

[100] Birrell, N. D. and Davies, P. C. W. *Quantum Fields in Curved Space*. Cambridge University Press, Cambridge, UK, 1st edition, (1982). (Not cited.)

Part IV

APPENDIX

A

FIGURES FOR THE THREE JET FINAL STATE

In the following the figures for exactly three jets in the final state are shown. Good agreement between data and simulation is achieved in all distributions.

A.1 LEPTON RECONSTRUCTION

The kinematic properties of the lepton (cf Sec. 7.1.1) in the event sample containing exactly three jets in the final state are shown. Fig. 114 (115) shows the energy, transverse momentum η and ϕ of the lepton in the electron (muon) channel for the RunIIa sample, Fig. 116 (117) shows the same set of figures for the RunIIb sample.

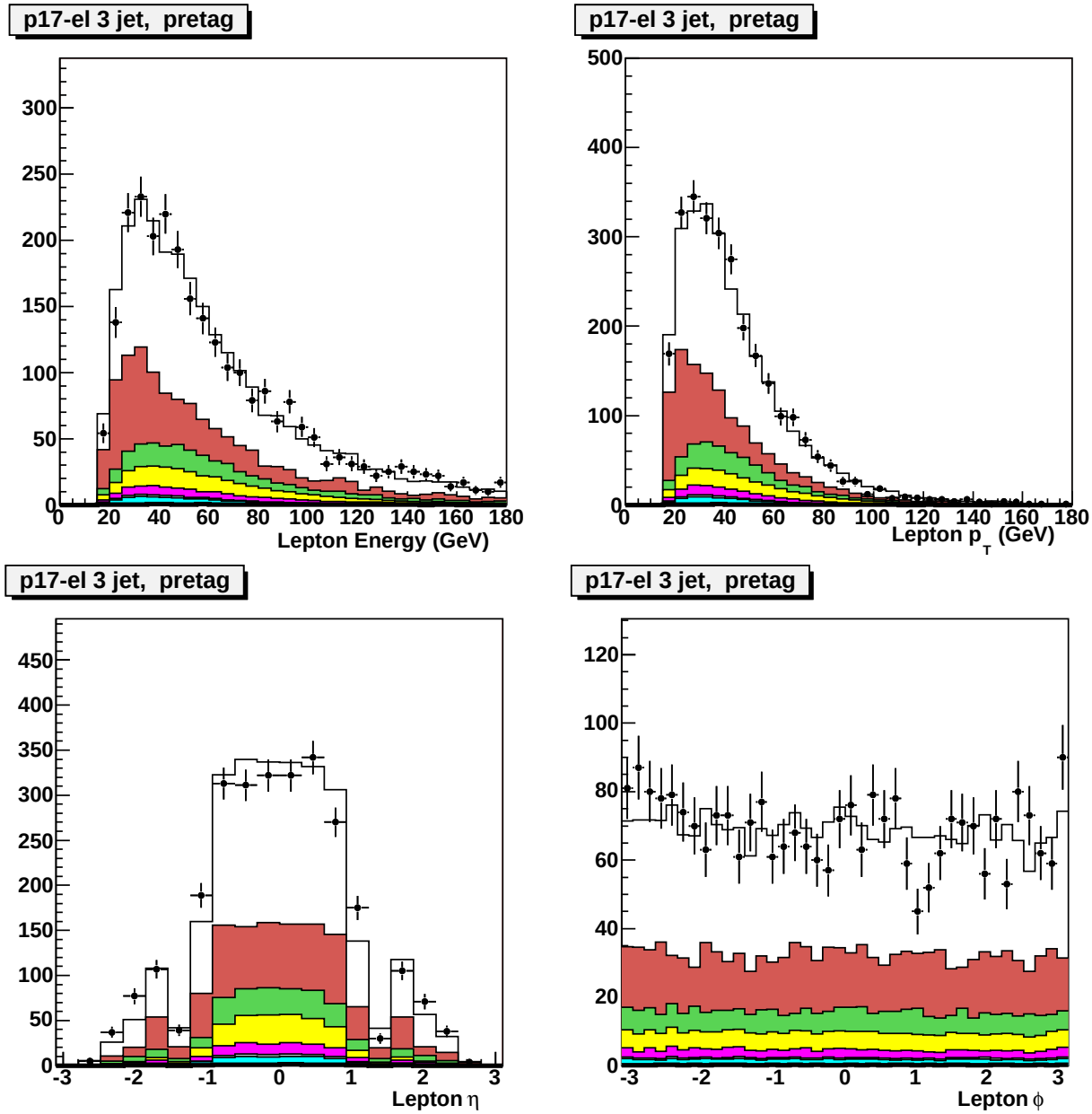

Figure 114: Kinematic distributions of the lepton in *RunIIa* events in the *electron* channel with exactly three jets. No b tagging has been applied.

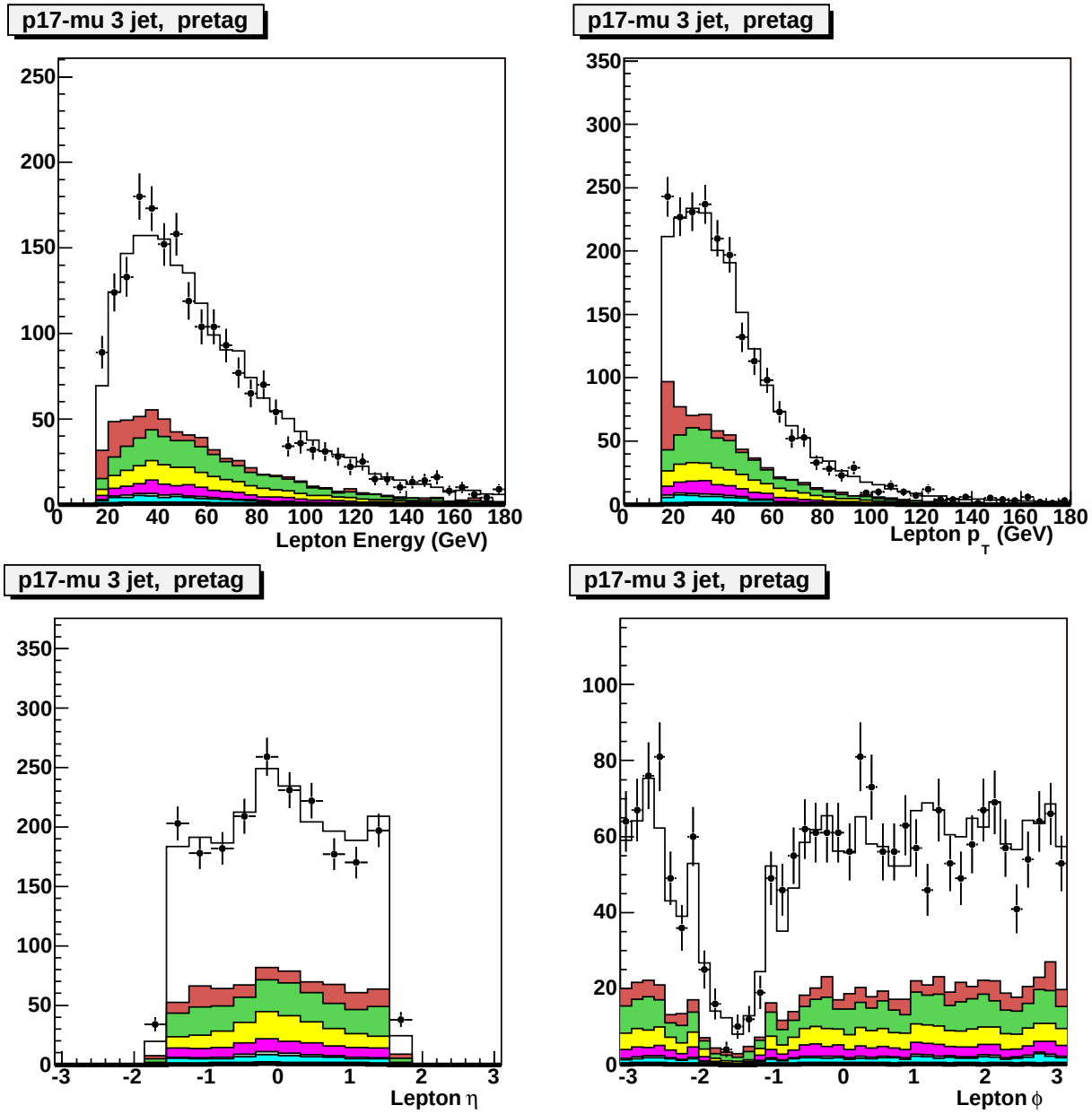

Figure 115: Kinematic distributions of the lepton in *RunIIa* events in the *muon* channel with exactly three jets. No b tagging has been applied.

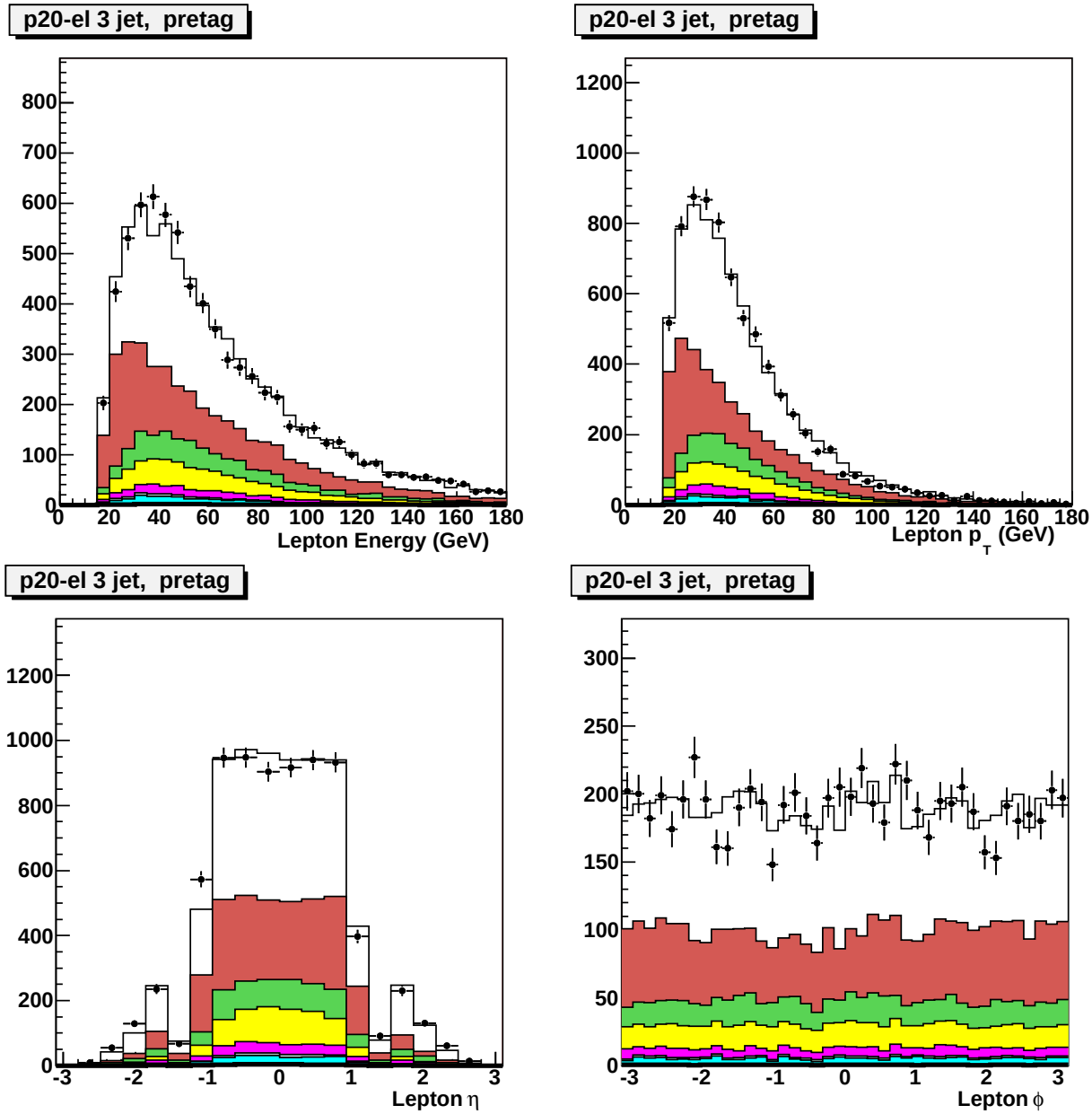

Figure 116: Kinematic distributions of the lepton in *RunIIb* events in the *electron* channel with exactly three jets. No b tagging has been applied.

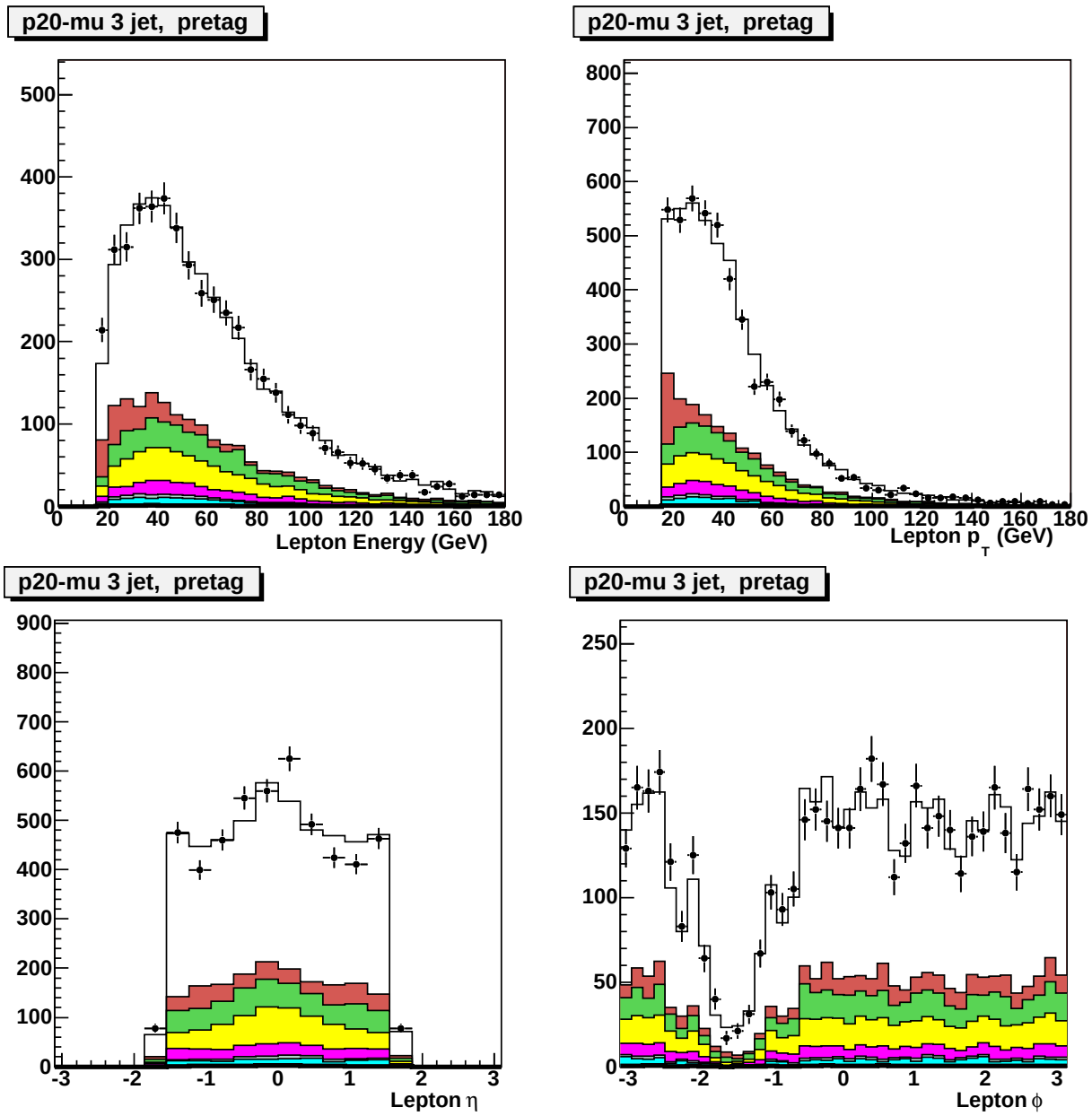

Figure 117: Kinematic distributions of the lepton in *RunIIb* events in the *muon* channel with exactly three jets. No b tagging has been applied.

A.2 MISSING TRANSVERSE ENERGY RECONSTRUCTION

Fig. 118 shows the missing transverse energy (cf Sec. 7.1.2) for all analysis channels containing three jets in the final state.

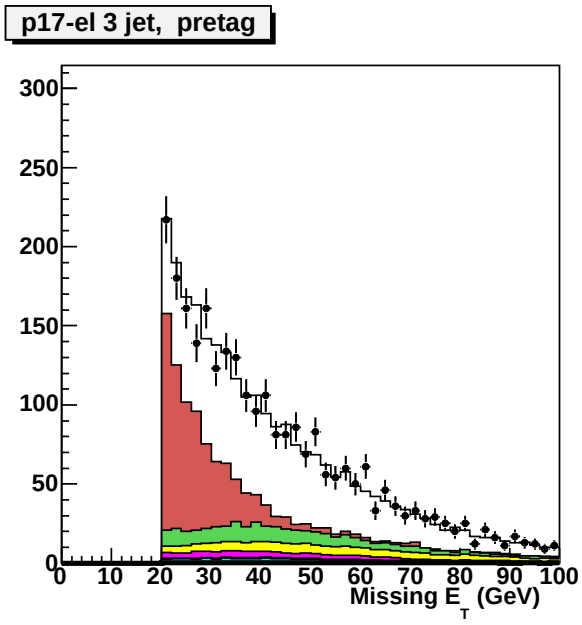

(a) $\not\!\!E_T$ for the RunIIa electron sample.

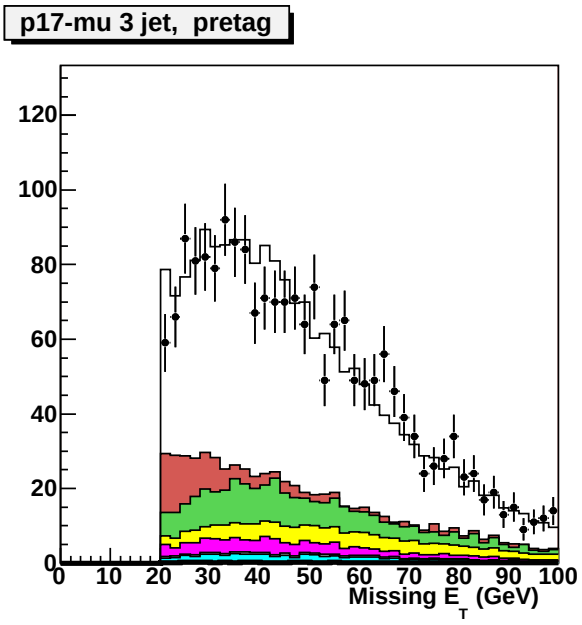

(b) $\not\!\!E_T$ for the RunIIa muon sample.

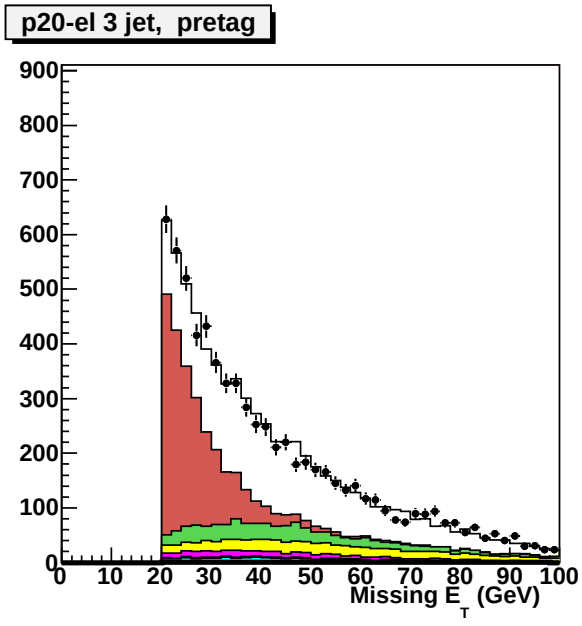

(c) $\not\!\!E_T$ for the RunIIb electron sample.

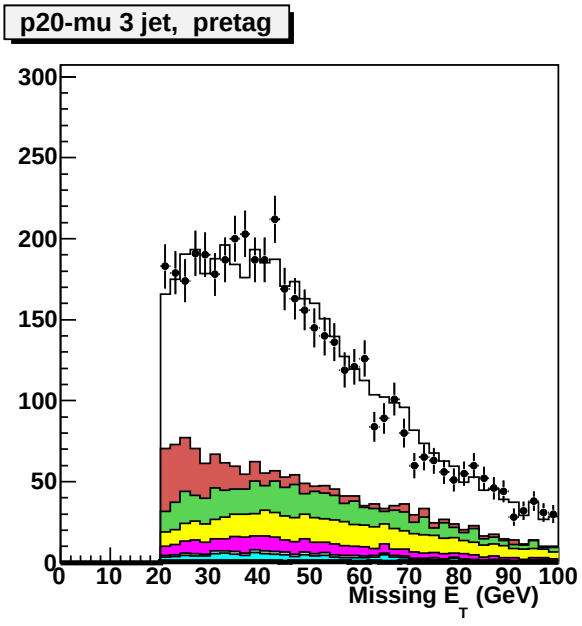

(d) $\not\!\!E_T$ for the RunIIb muon sample.

Figure 118: Missing transverse energy distributions for all four analysis channels in events with three jets in the final state. No b tagging has been applied.

A.3 *W* BOSON RECONSTRUCTION

The kinematic properties of the reconstructed *W* boson (cf Sec. 7.1.3) in the event sample containing exactly three jets in the final state are shown. Fig. 119 (120) shows the transverse mass and the transverse momentum of the reconstructed *W* boson in the electron (muon) channel for the RunIIa sample, Fig. 121 (122) shows the same set of figures for the RunIIb sample.

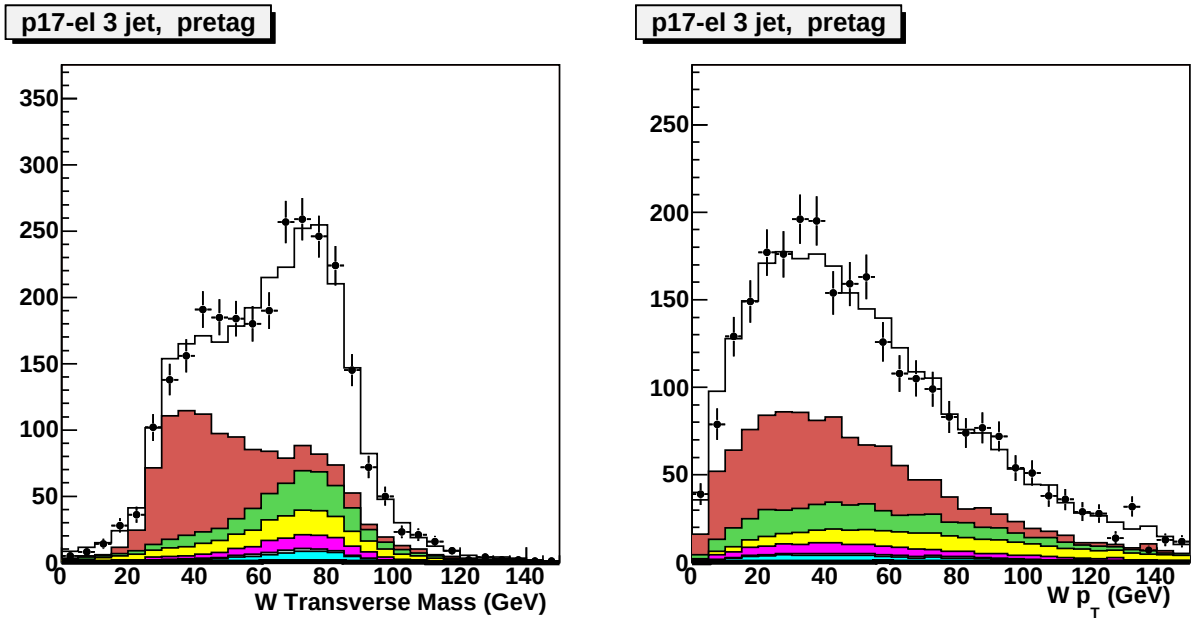

Figure 119: W transverse mass and transverse momentum in *RunIIa* events in the *electron* channel with exactly three jets. No b tagging has been applied.

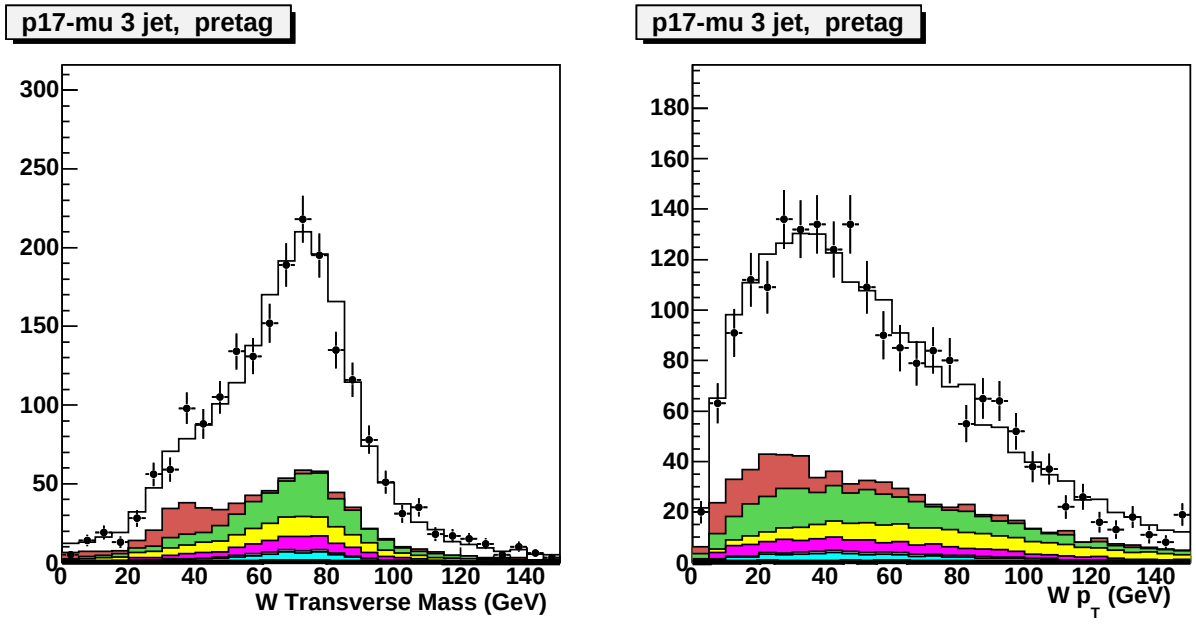

Figure 120: W transverse mass and transverse momentum in *RunIIa* events in the *muon* channel with exactly three jets. No b tagging has been applied.

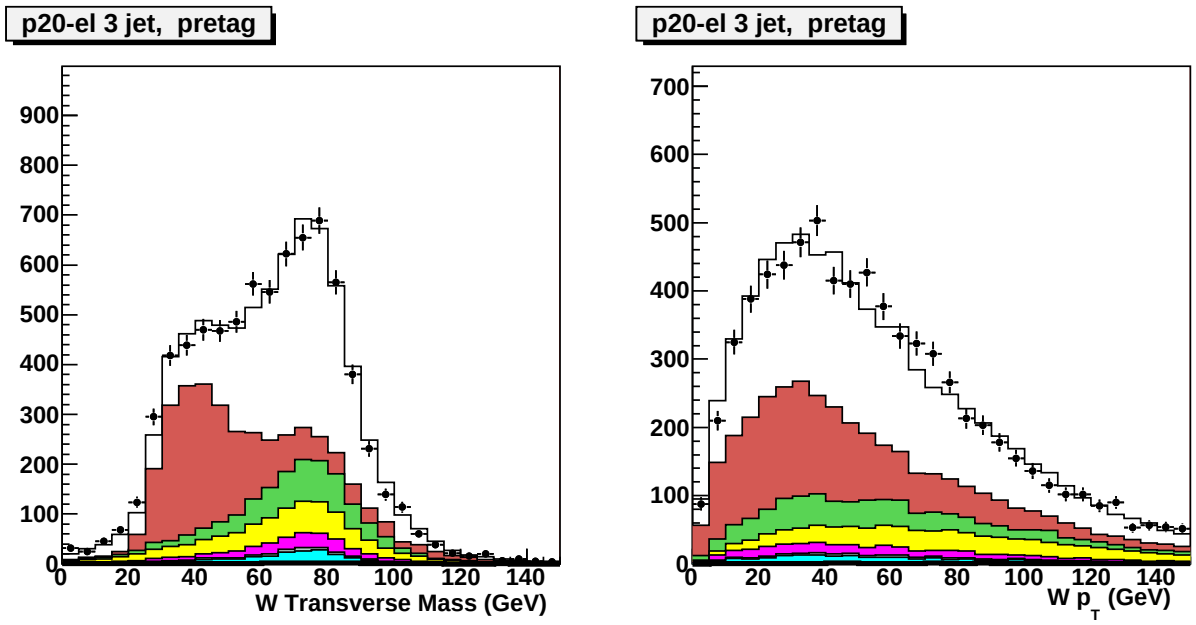

Figure 121: W transverse mass and transverse momentum in *RunIIb* events in the *electron* channel with exactly three jets. No b tagging has been applied.

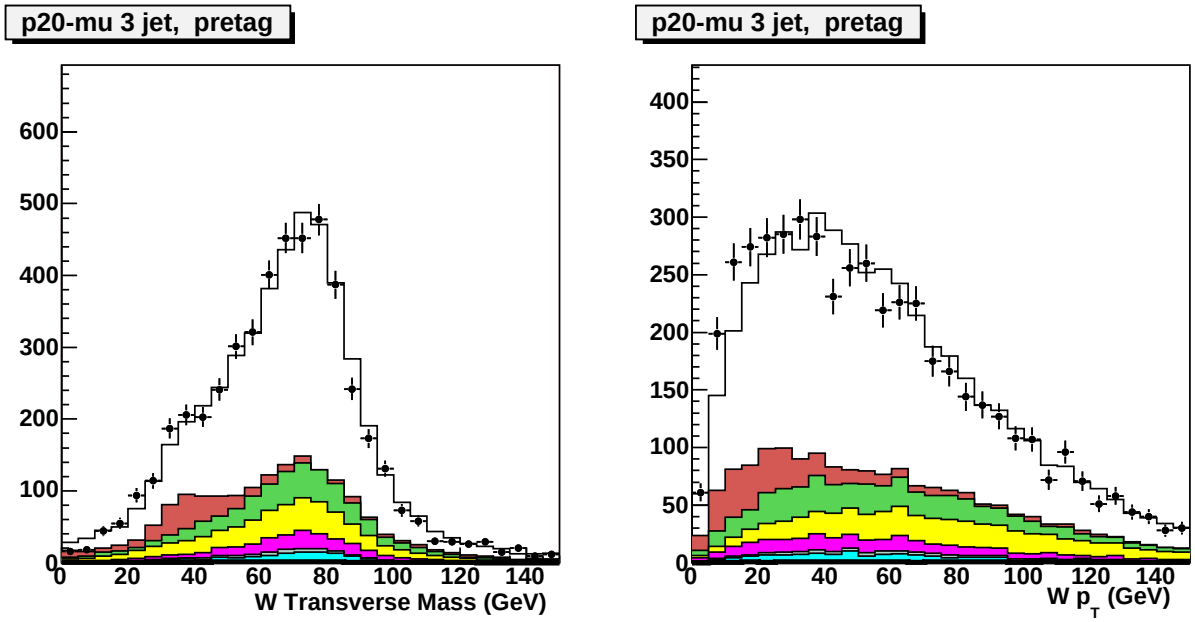

Figure 122: W transverse mass and transverse momentum in *RunIIb* events in the *muon* channel with exactly three jets. No b tagging has been applied.

A.4 HIGGS BOSON RECONSTRUCTION

For the identification of a possible Higgs boson signal (cf Sec. 7.2), a good understanding of jet identification is necessary. Figs. 123 - 126 show the transverse momentum and η of the leading and second leading jet, the sum of the transverse momenta of all jets in the event and the angular separation between the two leading jets in all three jet events on the pretag level separately in all analysis channels.
Figs. 128 - 131 show the same set of plots for the single tag sample, Figs. 133 - 136 show these plots for the double tag sample.
Fig. 127 shows the dijet mass distributions calculated from the two leading jets in the event for the pretag sample, Fig. 132 for the single tag sample and Fig. 137 for the double tag sample.

A.4.1 *Pretag Level*

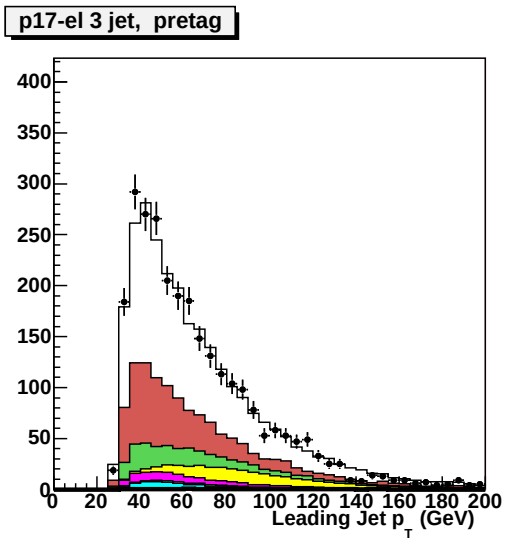

(a) Transverse momentum p_T of the leading jet.

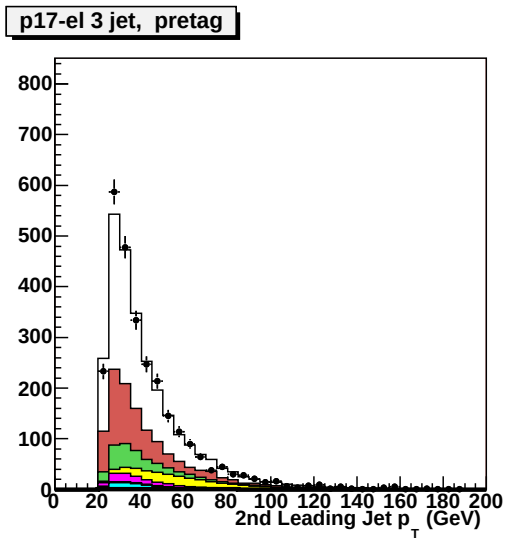

(b) Transverse momentum p_T of the second leading jet.

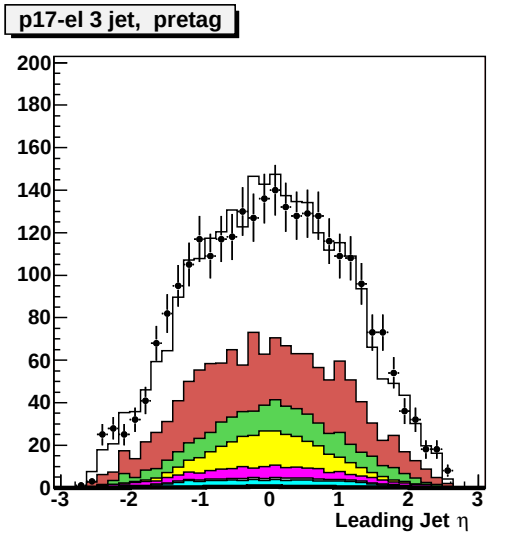

(c) Jet η of the leading jet.

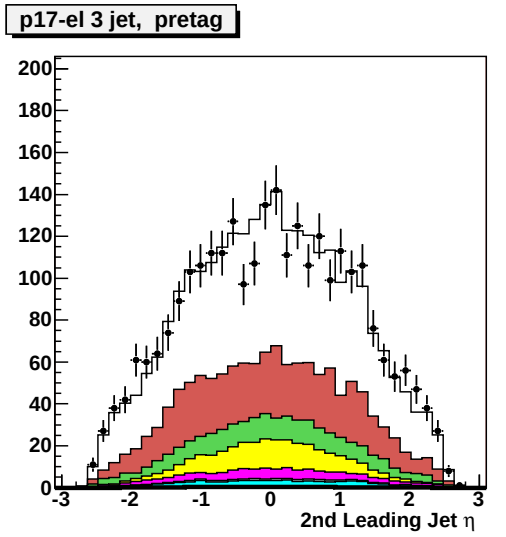

(d) Jet η of the second leading jet.

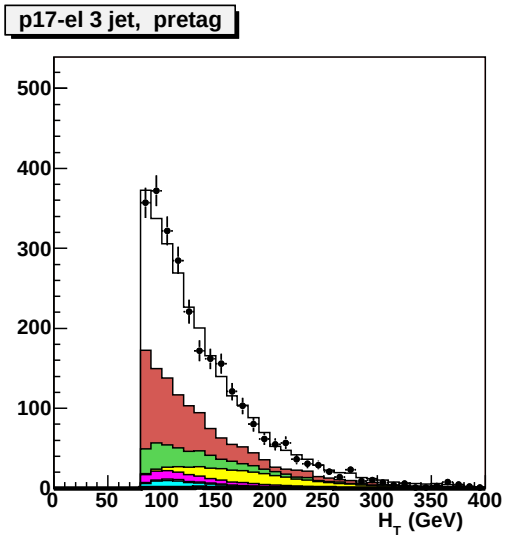

(e) Sum of the transverse jet momenta H_T.

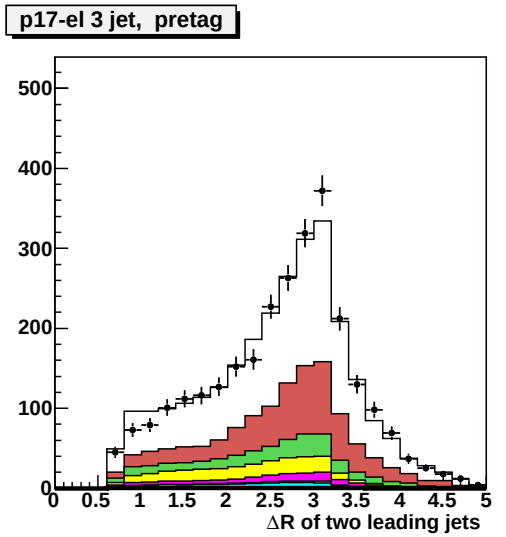

(f) Δ R between the two leading jets.

Figure 123: Kinematic distribution of RunIIa events in the electron channel with exactly three jets. No b tagging is applied.

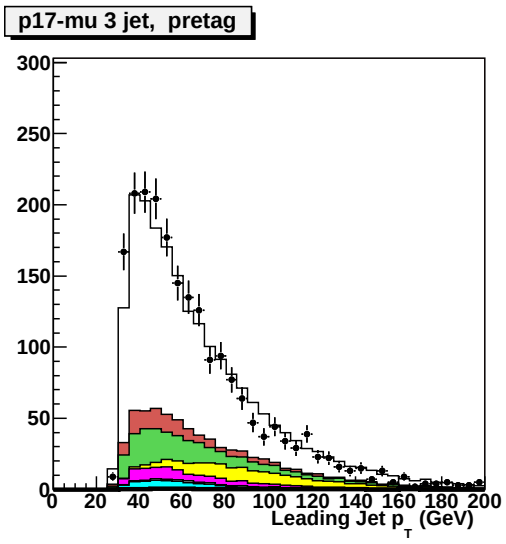

(a) Transverse momentum p_T of the leading jet.

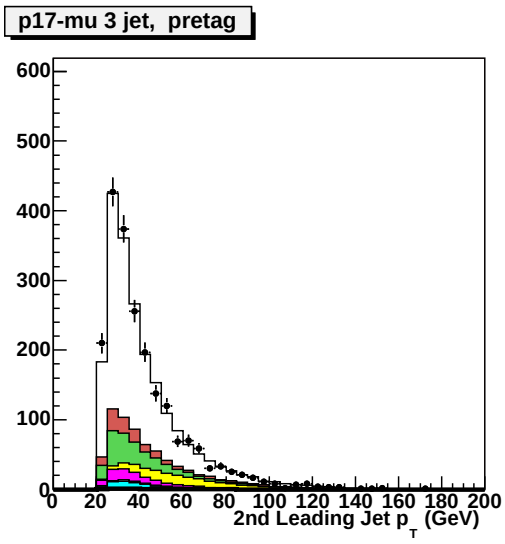

(b) Transverse momentum p_T of the second leading jet.

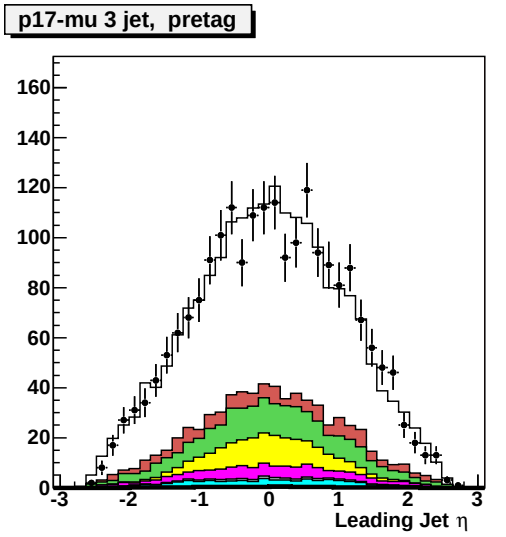

(c) Jet η of the leading jet.

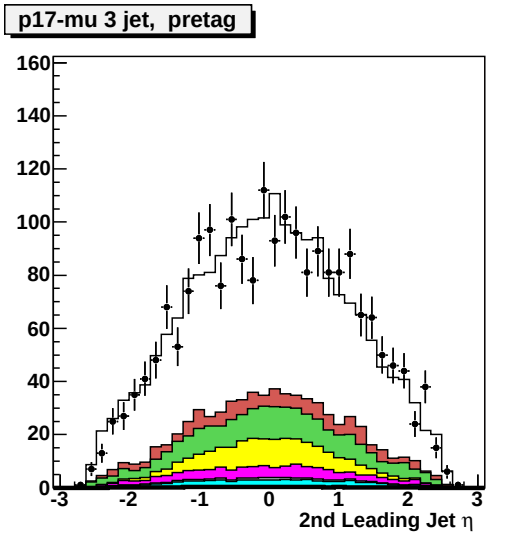

(d) Jet η of the second leading jet.

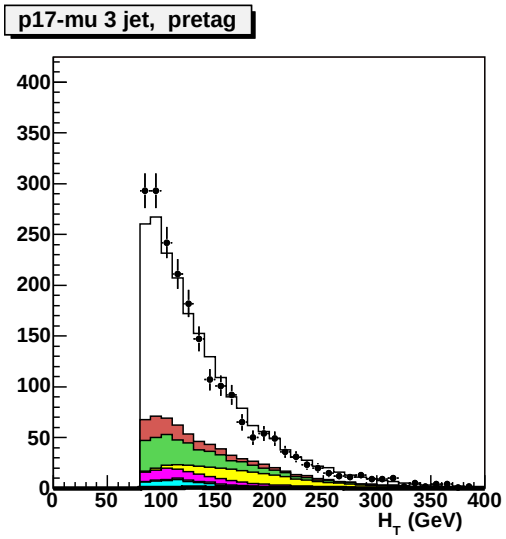

(e) Sum of the transverse jet momenta H_T.

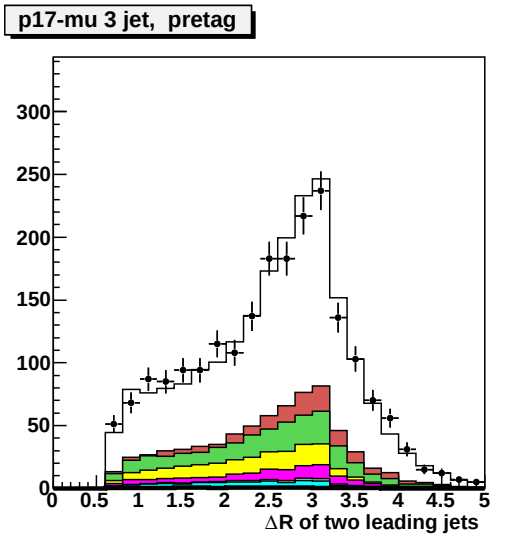

(f) Δ R between the two leading jets.

Figure 124: Kinematic distribution of RunIIa events in the muon channel with exactly three jets. No b tagging is applied.

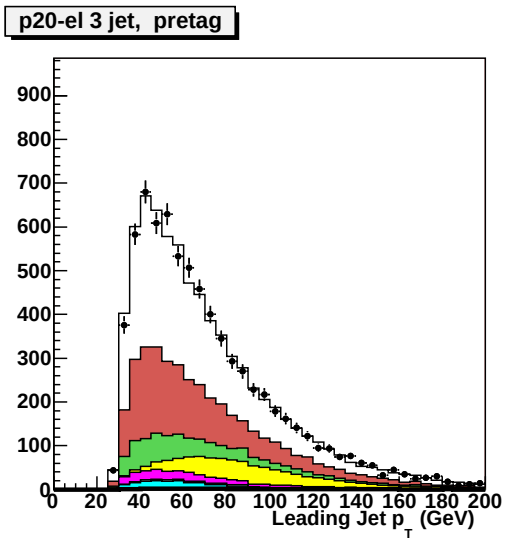

(a) Transverse momentum p_T of the leading jet.

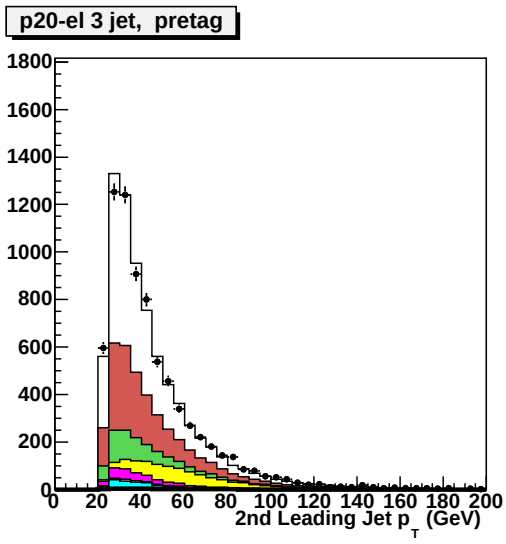

(b) Transverse momentum p_T of the second leading jet.

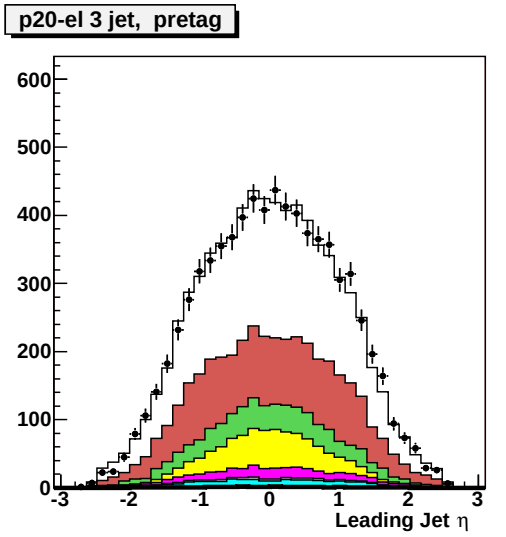

(c) Jet η of the leading jet.

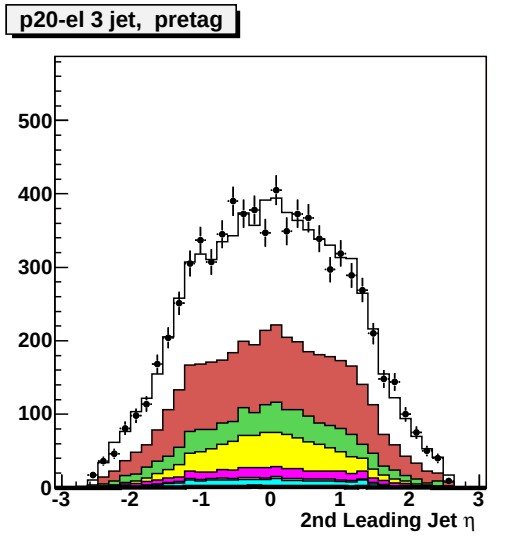

(d) Jet η of the second leading jet.

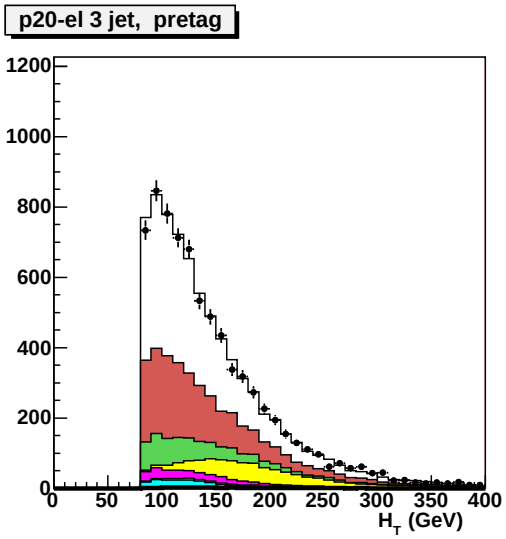

(e) Sum of the transverse jet momenta H_T.

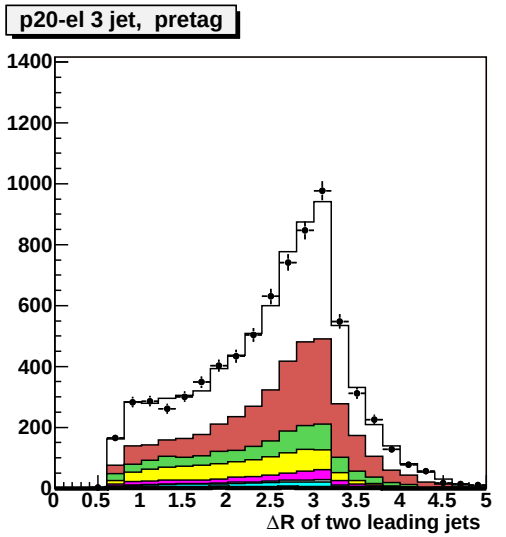

(f) Δ R between the two leading jets.

Figure 125: Kinematic distribution of RunIIb events in the electron channel with exactly three jets. No b tagging is applied.

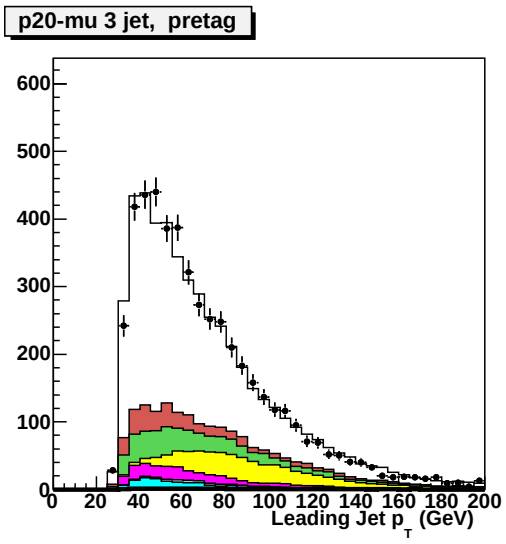

(a) Transverse momentum p_T of the leading jet.

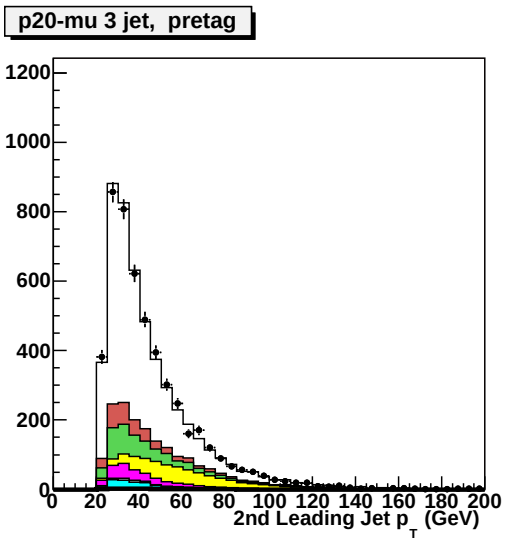

(b) Transverse momentum p_T of the second leading jet.

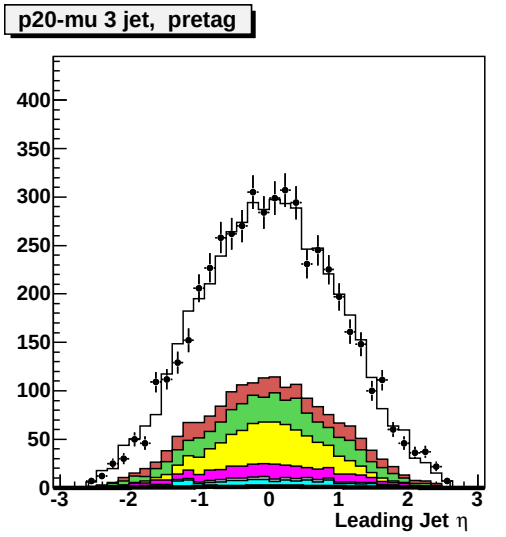

(c) Jet η of the leading jet.

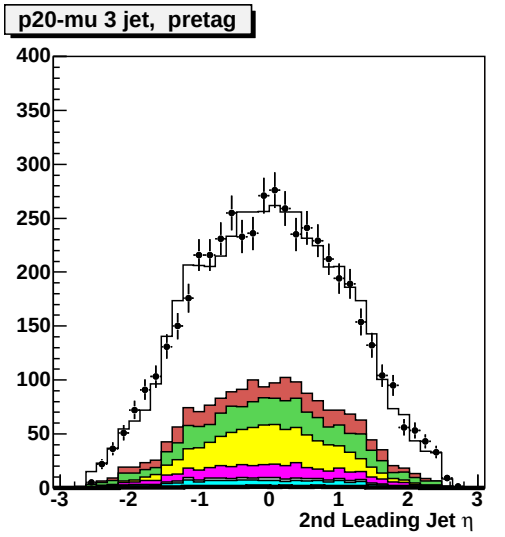

(d) Jet η of the second leading jet.

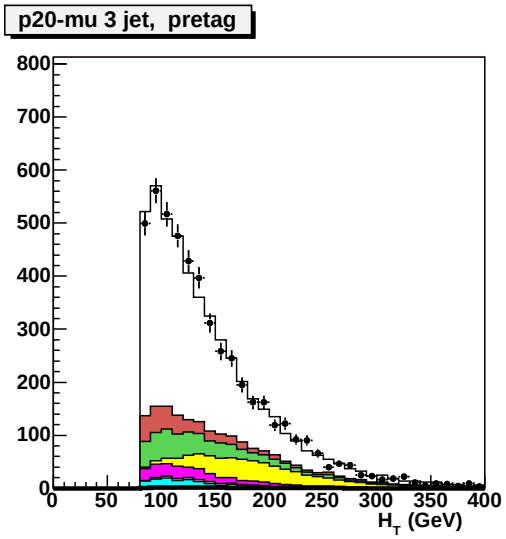

(e) Sum of the transverse jet momenta H_T.

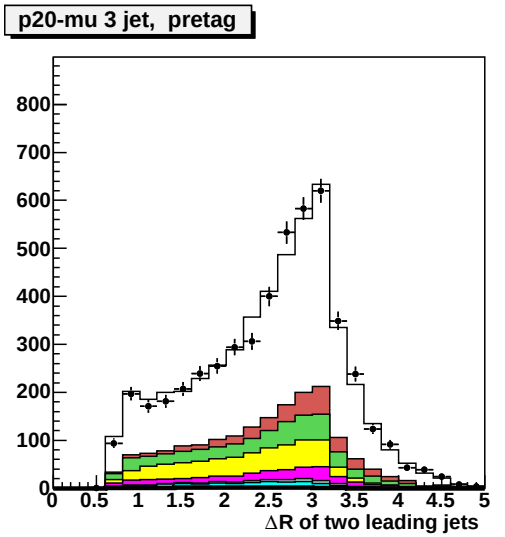

(f) Δ R between the two leading jets.

Figure 126: Kinematic distribution of RunIIb events in the muon channel with exactly three jets. No b tagging is applied.

A.4.2 *Single Tag*

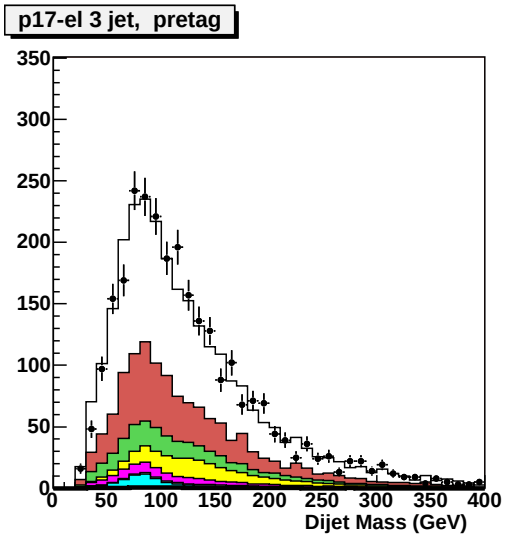

(a) Dijet mass distribution in the electron RunIIa channel.

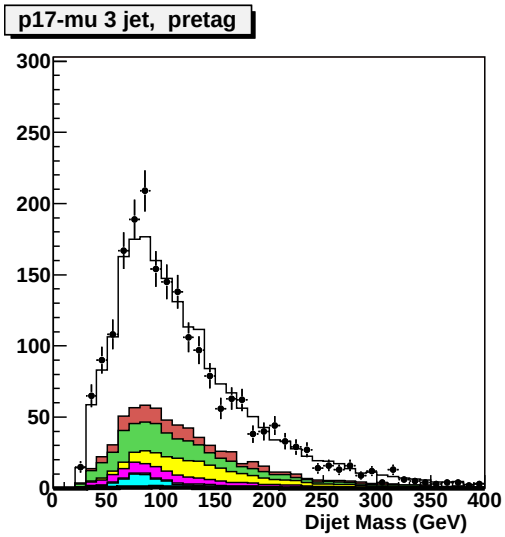

(b) Dijet mass distribution in the muon RunIIa channel.

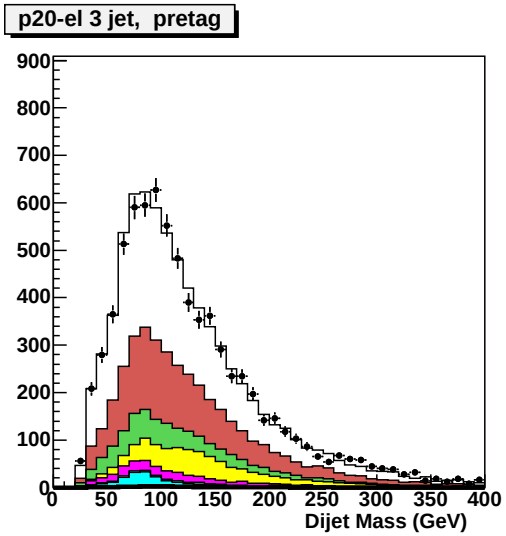

(c) Dijet mass distribution in the electron RunIIb channel.

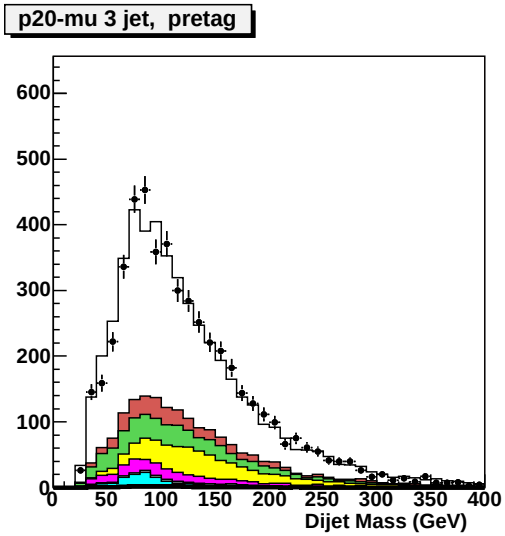

(d) Dijet mass distribution in the muon RunIIb channel.

Figure 127: Distributions of the dijet mass in all analysis channels containig three jets in the final state. Good agreement is achieved between data and simulation, including all MC backgrounds and the multijet background modeled from data. No b tagging has been applied.

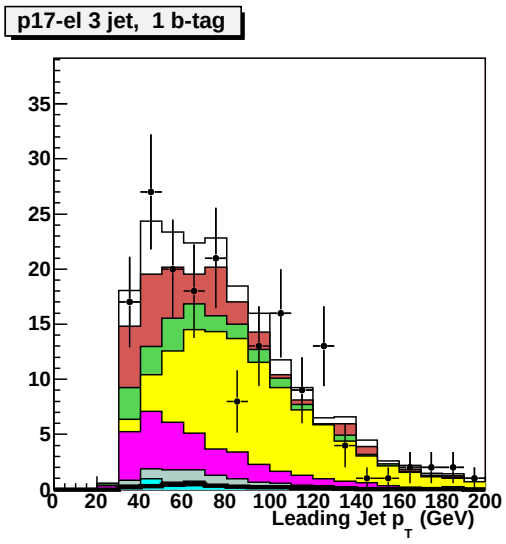

(a) Transverse momentum p_T of the leading jet.

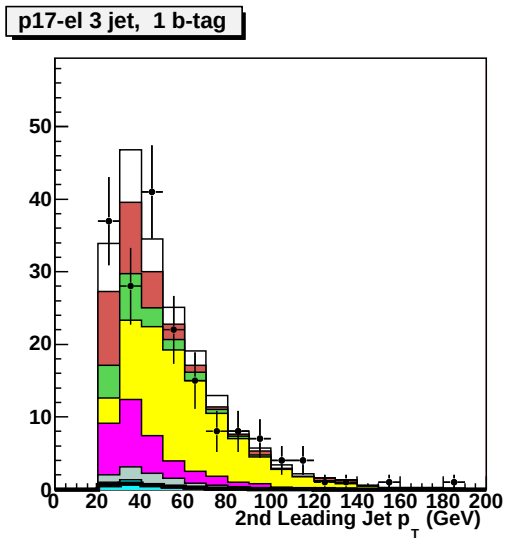

(b) Transverse momentum p_T of the second leading jet.

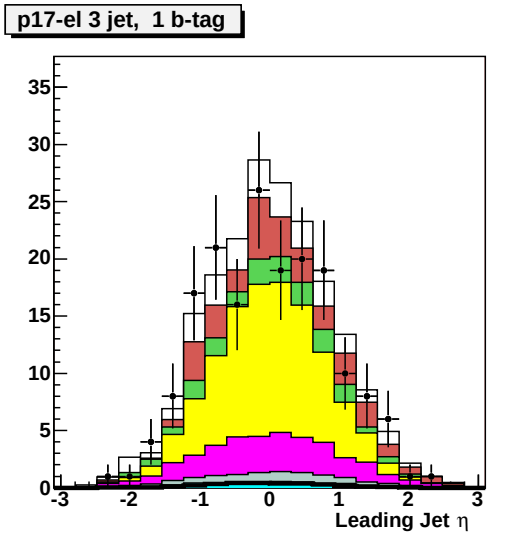

(c) Jet η of the leading jet.

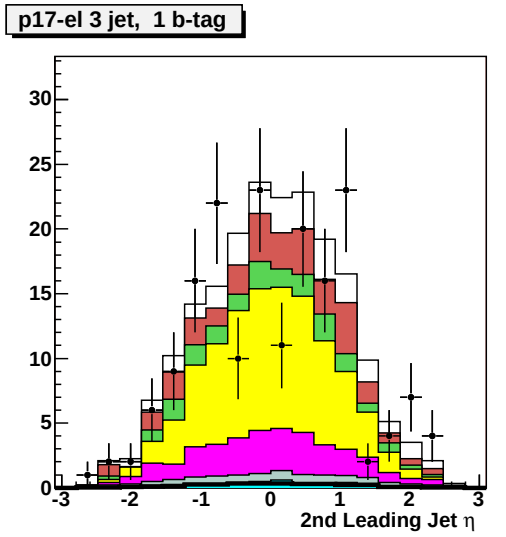

(d) Jet η of the second leading jet.

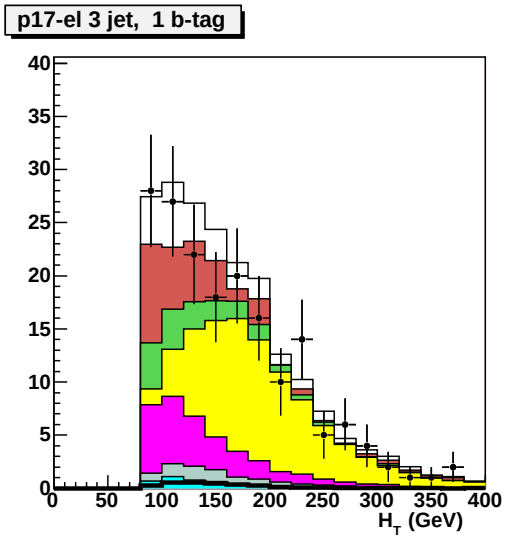

(e) Sum of the transverse jet momenta H_T.

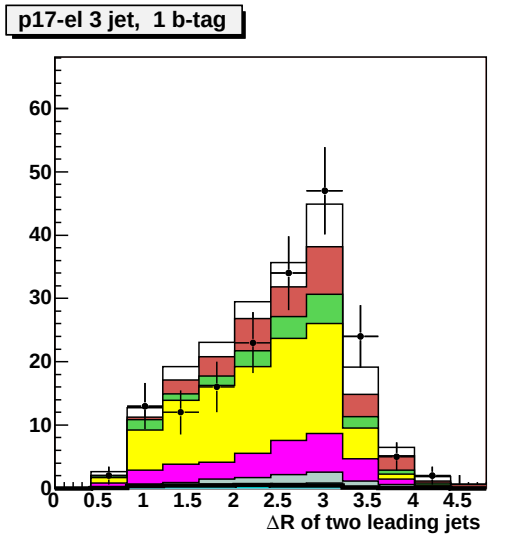

(f) ΔR between the two leading jets.

Figure 128: Kinematic distribution of RunIIa events in the electron channel with exactly three jets of which exactly one is tagged with the tight b tagging criterion.

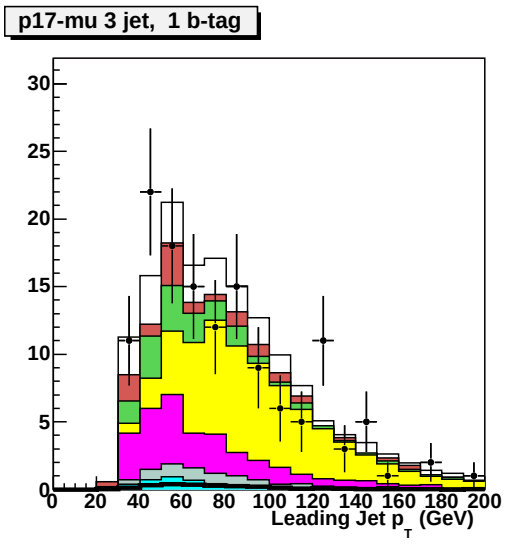

(a) Transverse momentum p_T of the leading jet.

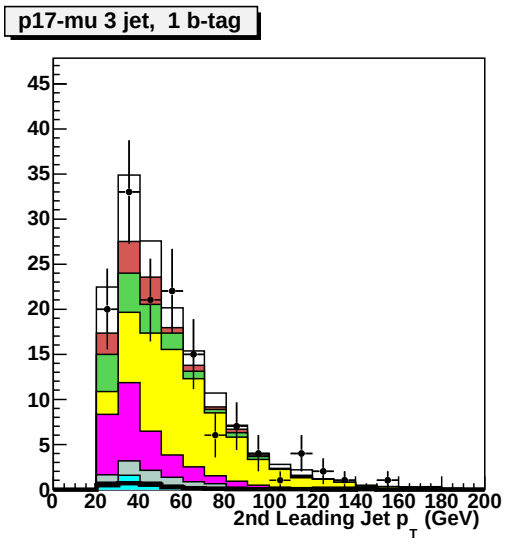

(b) Transverse momentum p_T of the second leading jet.

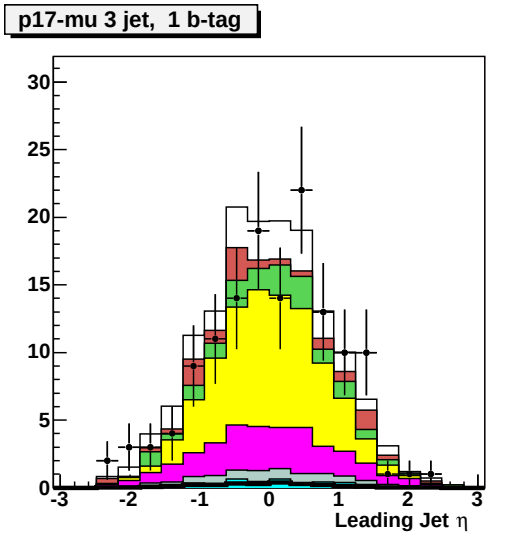

(c) Jet η of the leading jet.

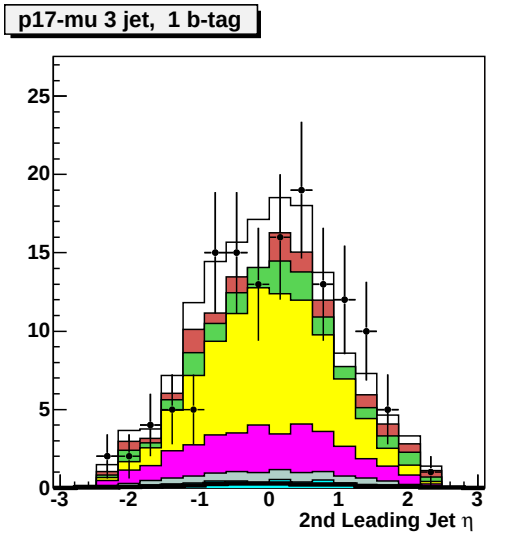

(d) Jet η of the second leading jet.

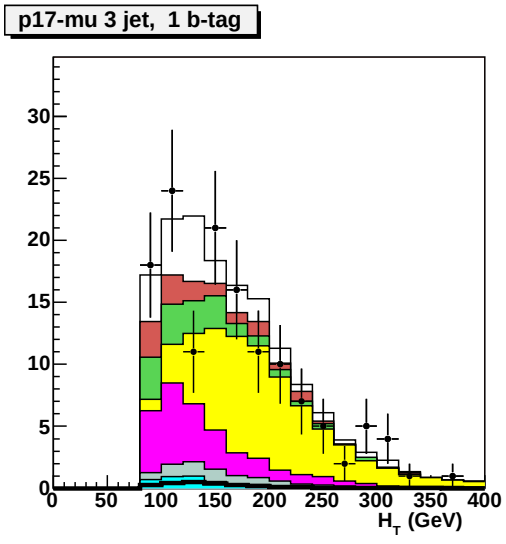

(e) Sum of the transverse jet momenta H_T.

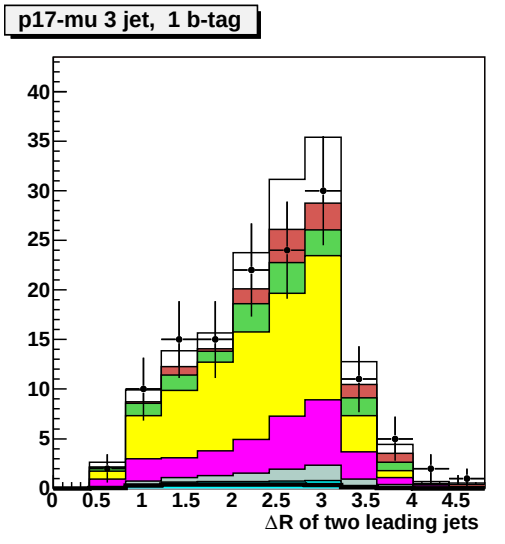

(f) ΔR between the two leading jets.

Figure 129: Kinematic distribution of RunIIa events in the muon channel with exactly three jets of which exactly one is tagged with the tight b tagging criterion.

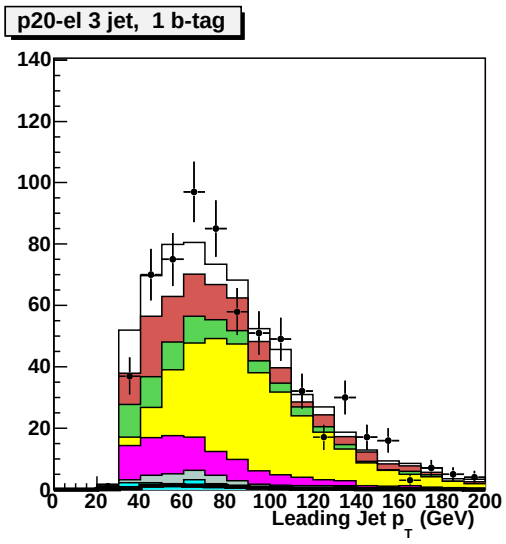

(a) Transverse momentum p_T of the leading jet.

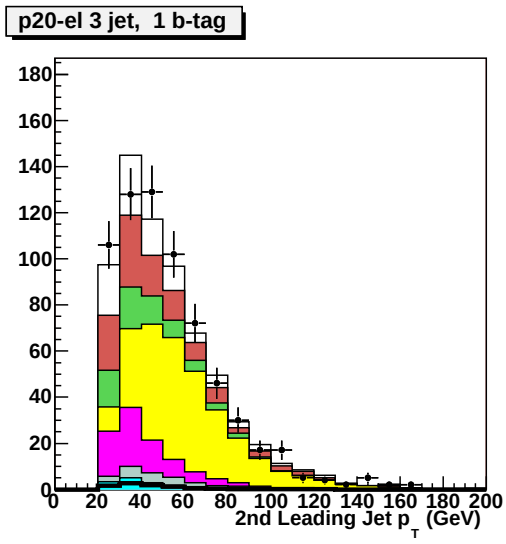

(b) Transverse momentum p_T of the second leading jet.

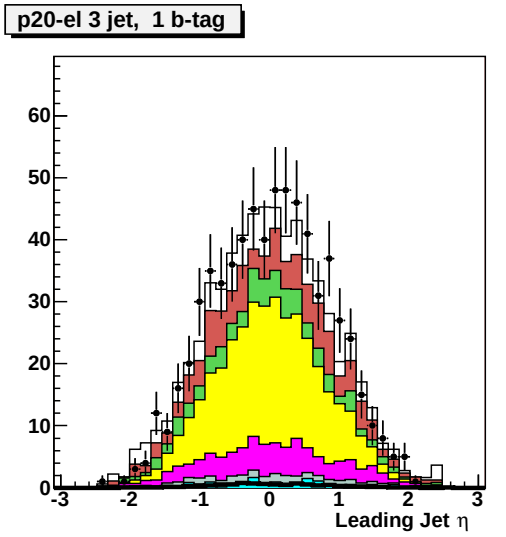

(c) Jet η of the leading jet.

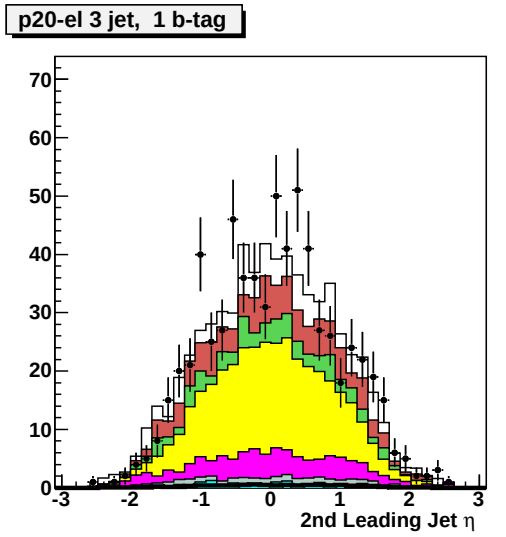

(d) Jet η of the second leading jet.

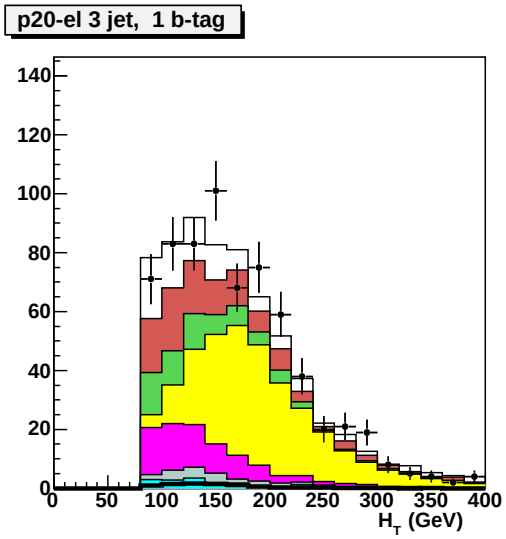

(e) Sum of the transverse jet momenta H_T.

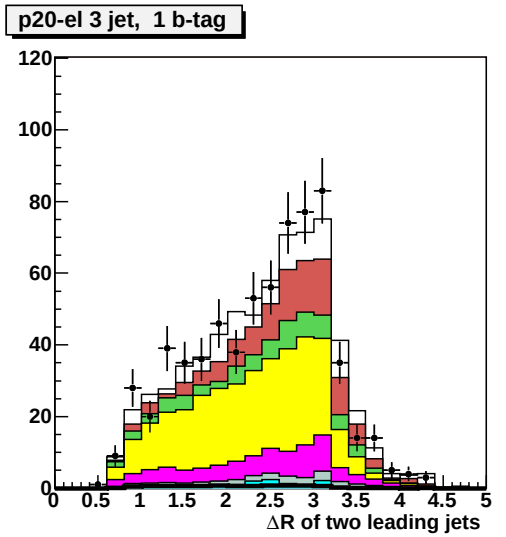

(f) Δ R between the two leading jets.

Figure 130: Kinematic distribution of RunIIb events in the electron channel with exactly three jets of which exactly one is tagged with the tight b tagging criterion.

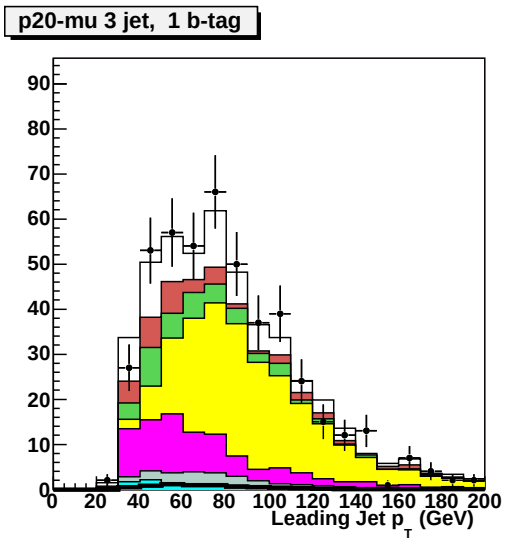

(a) Transverse momentum p_T of the leading jet.

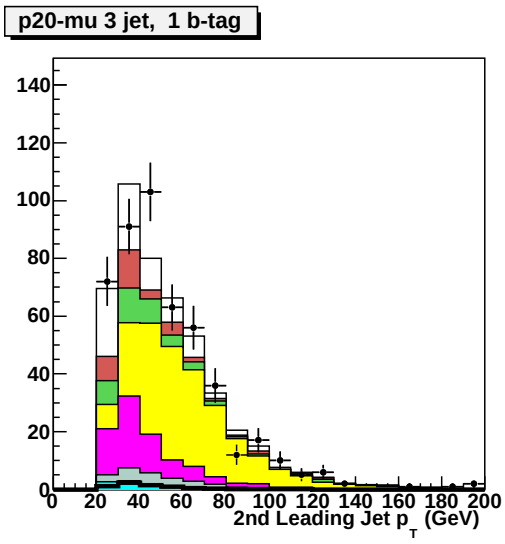

(b) Transverse momentum p_T of the second leading jet.

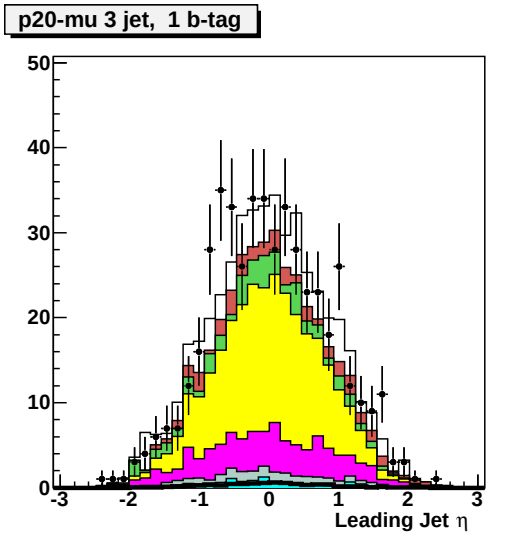

(c) Jet η of the leading jet.

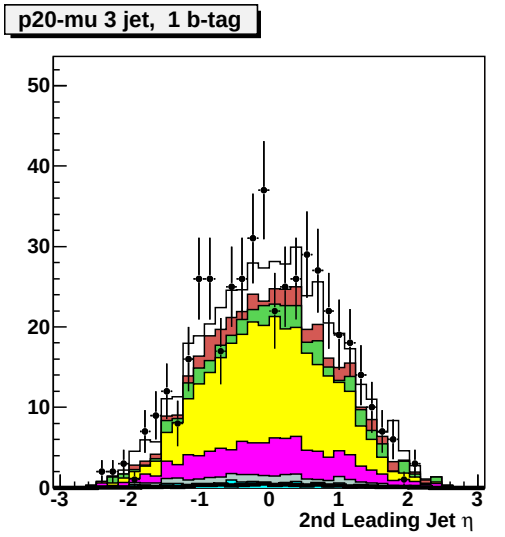

(d) Jet η of the second leading jet.

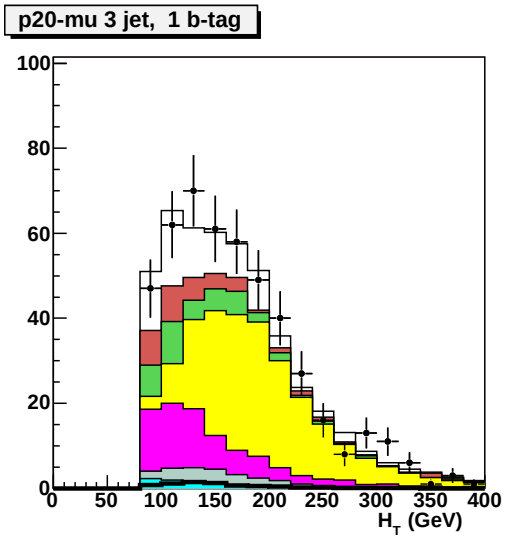

(e) Sum of the transverse jet momenta H_T.

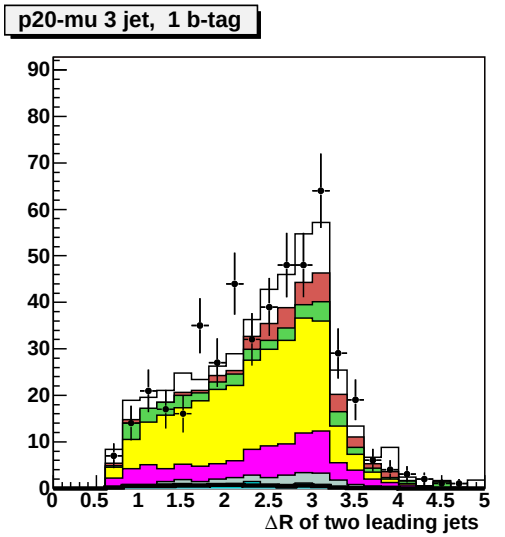

(f) Δ R between the two leading jets.

Figure 131: Kinematic distribution of RunIIb events in the muon channel with exactly three jets of which exactly one is tagged with the tight b tagging criterion.

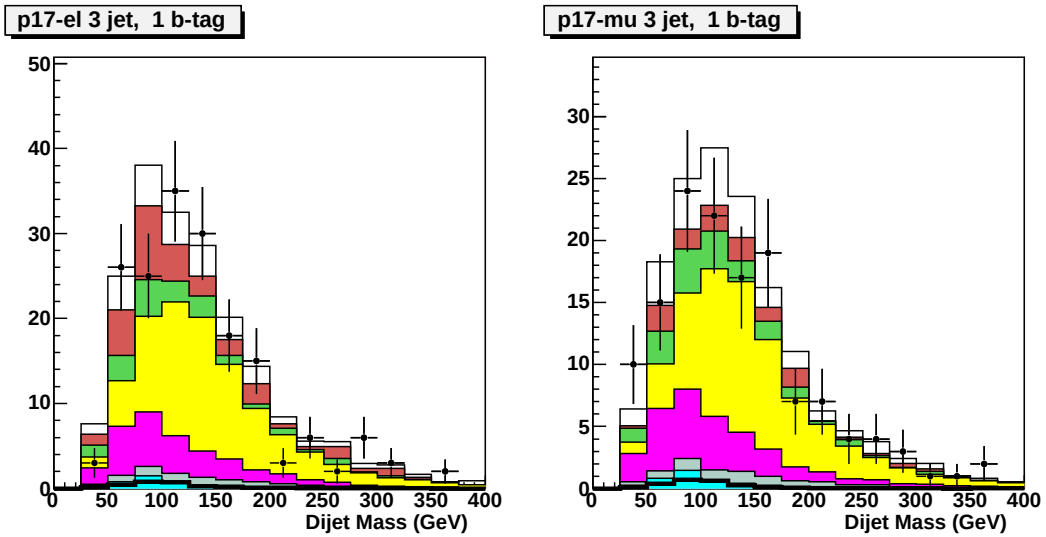

(a) Dijet mass distribution in the electron RunIIa channel.

(b) Dijet mass distribution in the muon RunIIa channel.

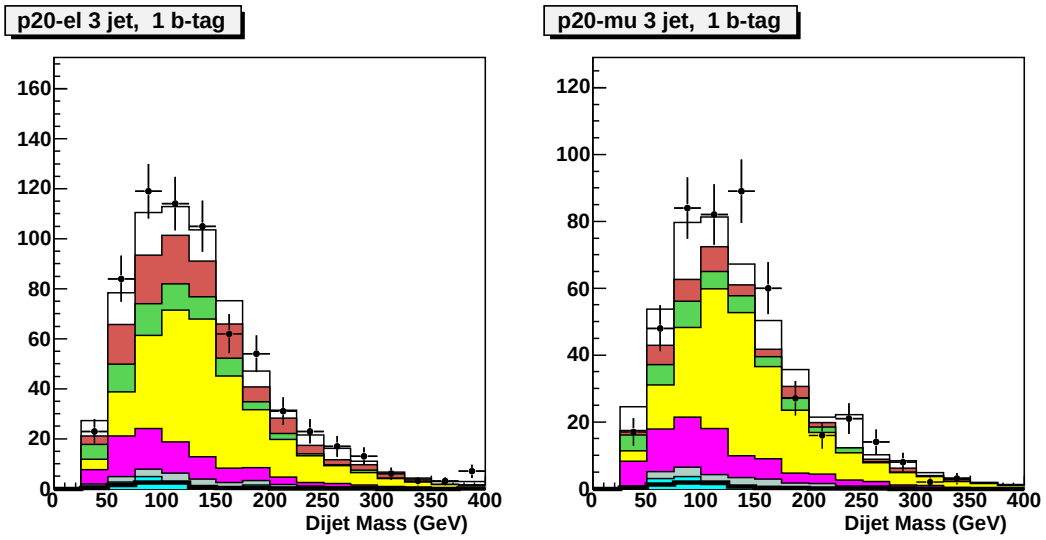

(c) Dijet mass distribution in the electron RunIIb channel.

(d) Dijet mass distribution in the muon RunIIb channel.

Figure 132: Distributions of the dijet mass in all analysis channels containig three jets in the final state of which exactly one is required to pass the tight b tagging criterion. Good agreement is achieved between data and simulation, including all MC backgrounds and the multijet background modeled from data.

A.4.3 *Double Tag*

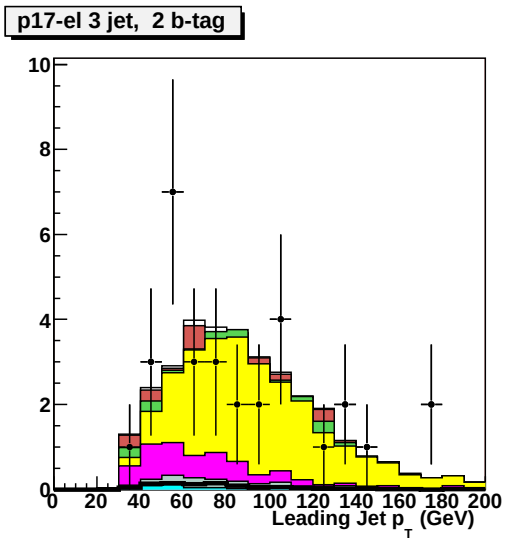

(a) Transverse momentum p_T of the leading jet.

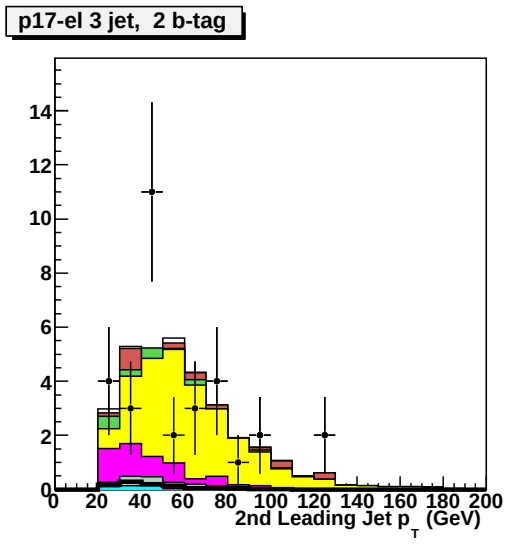

(b) Transverse momentum p_T of the second leading jet.

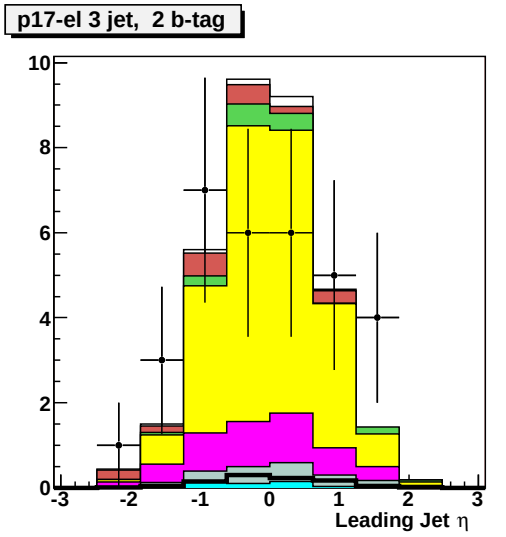

(c) Jet η of the leading jet.

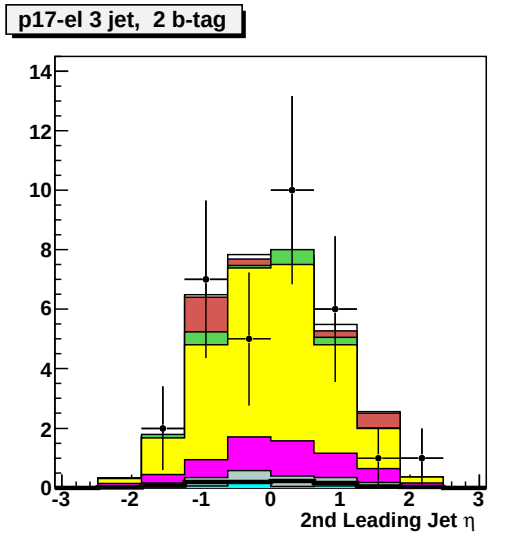

(d) Jet η of the second leading jet.

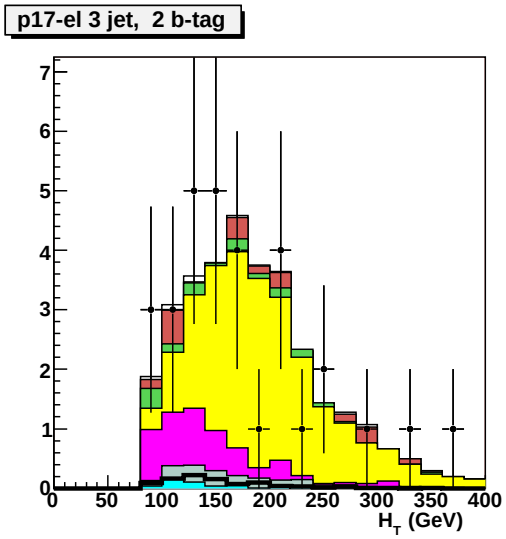

(e) Sum of the transverse jet momenta H_T.

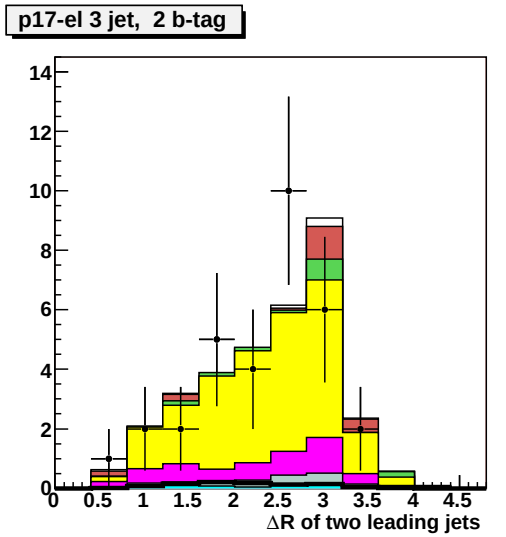

(f) ΔR between the two leading jets.

Figure 133: Kinematic distribution of RunIIa events in the electron channel with exactly three jets of which exactly two are tagged with the loose b-tagging criterion.

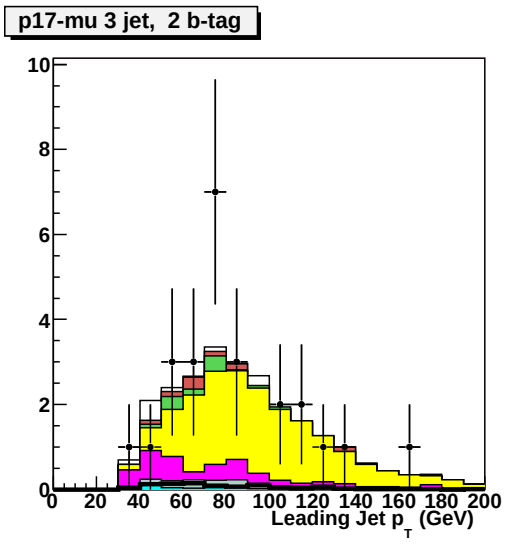

(a) Transverse momentum p_T of the leading jet.

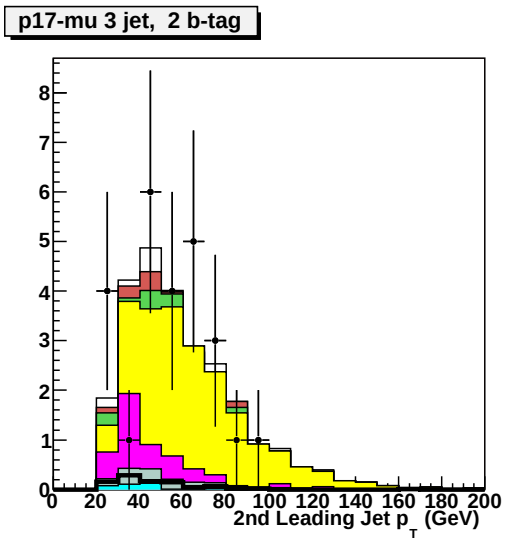

(b) Transverse momentum p_T of the second leading jet.

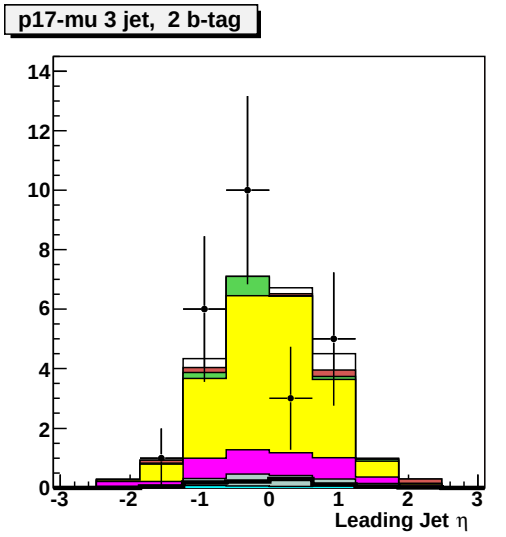

(c) Jet η of the leading jet.

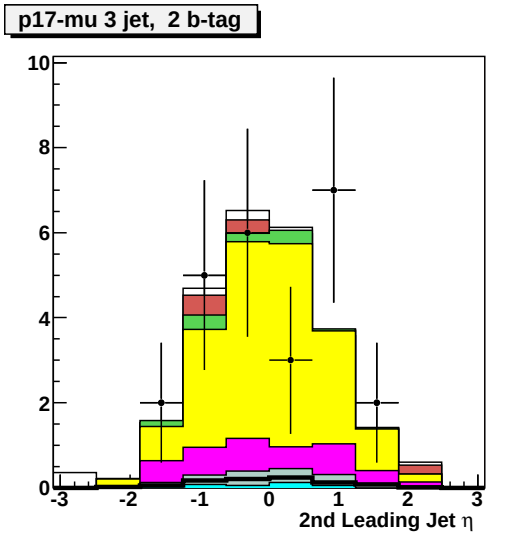

(d) Jet η of the second leading jet.

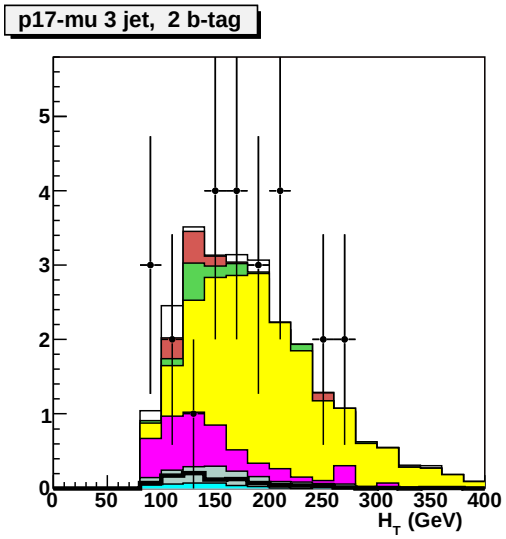

(e) Sum of the transverse jet momenta H_T.

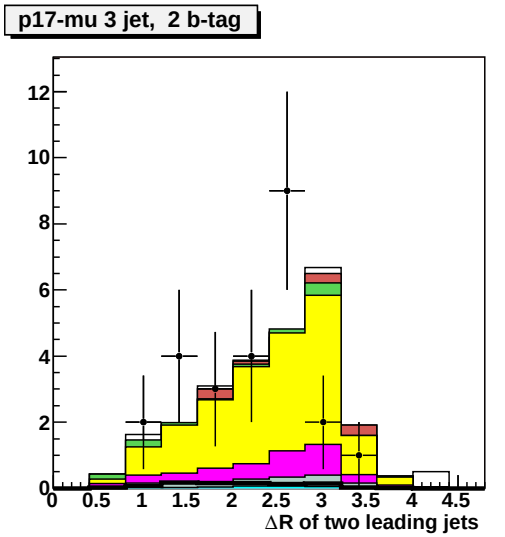

(f) ΔR between the two leading jets.

Figure 134: Kinematic distribution of RunIIa events in the muon channel with exactly three jets of which exactly two are tagged with the loose b-tagging criterion.

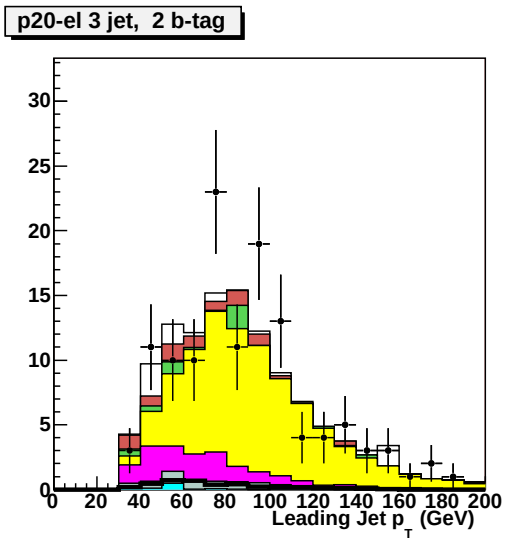

(a) Transverse momentum p_T of the leading jet.

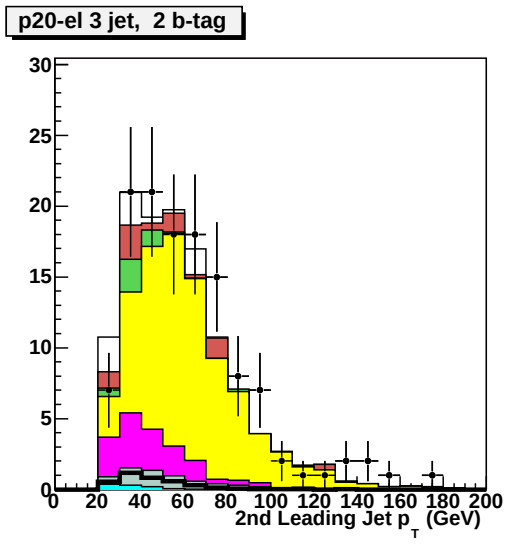

(b) Transverse momentum p_T of the second leading jet.

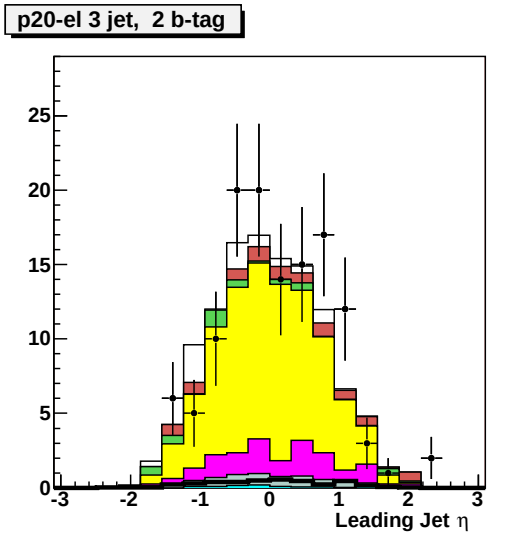

(c) Jet η of the leading jet.

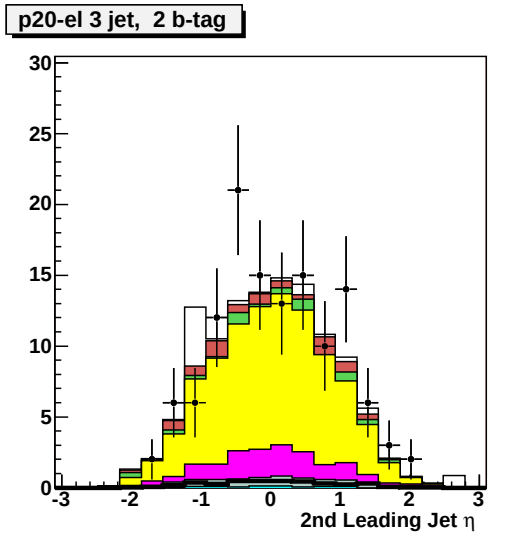

(d) Jet η of the second leading jet.

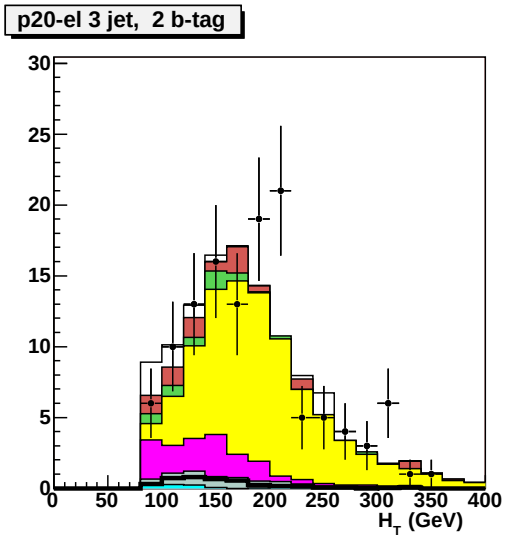

(e) Sum of the transverse jet momenta H_T.

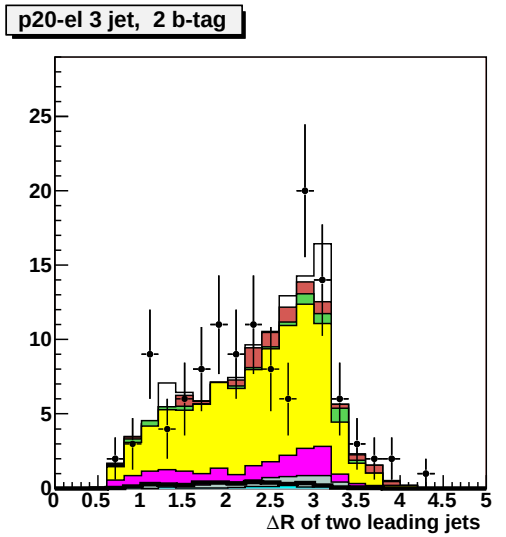

(f) ΔR between the two leading jets.

Figure 135: Kinematic distribution of RunIIb events in the electron channel with exactly three jets of which exactly two are tagged with the loose b tagging criterion.

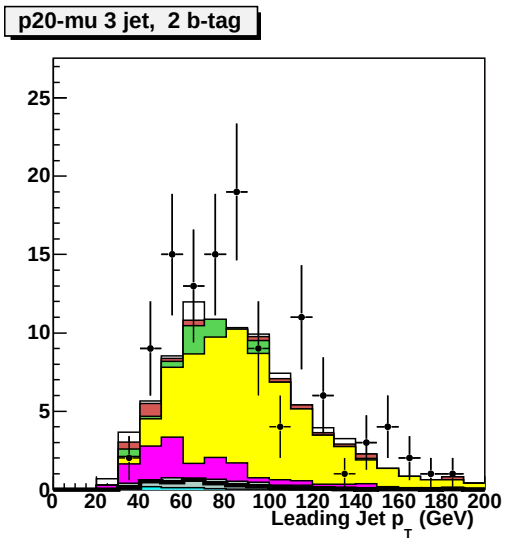

(a) Transverse momentum p_T of the leading jet.

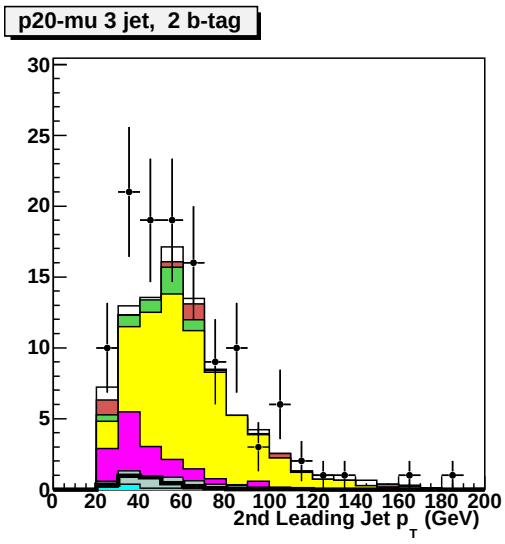

(b) Transverse momentum p_T of the second leading jet.

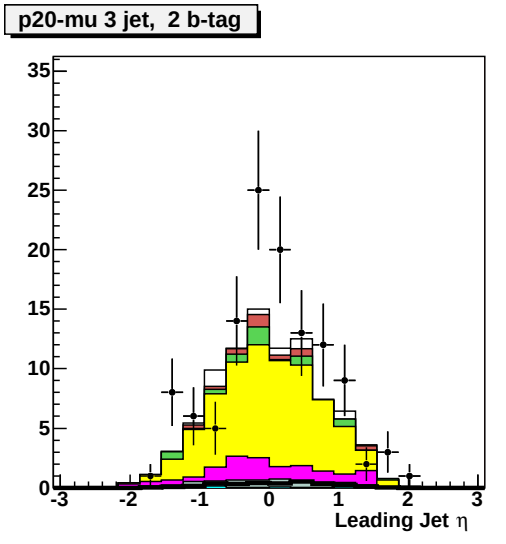

(c) Jet η of the leading jet.

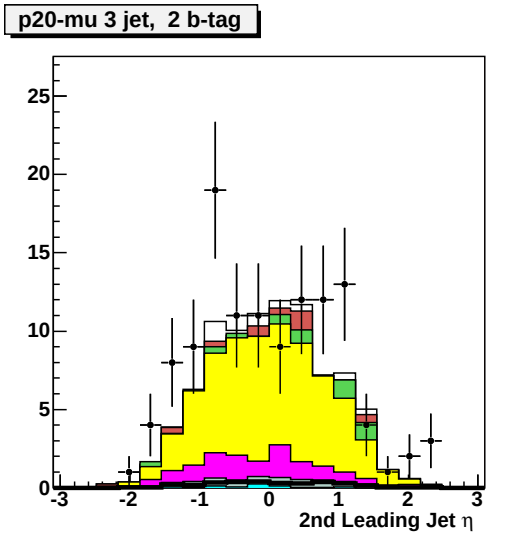

(d) Jet η of the second leading jet.

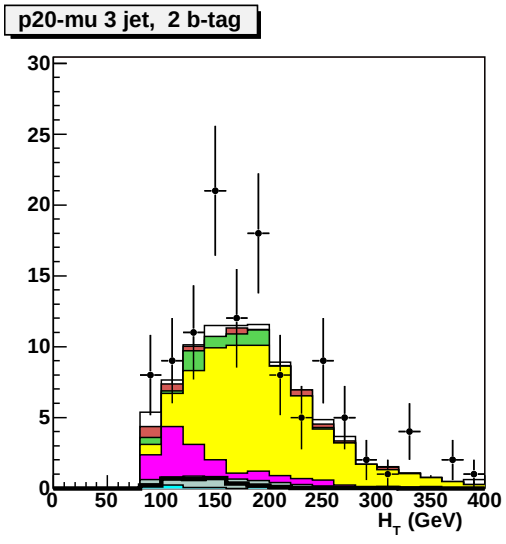

(e) Sum of the transverse jet momenta H_T.

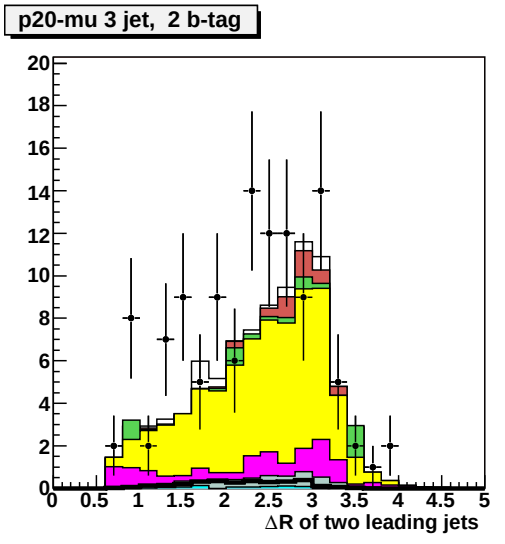

(f) ΔR between the two leading jets.

Figure 136: Kinematic distribution of RunIIb events in the muon channel with exactly three jets of which exactly two are tagged with the loose b tagging criterion.

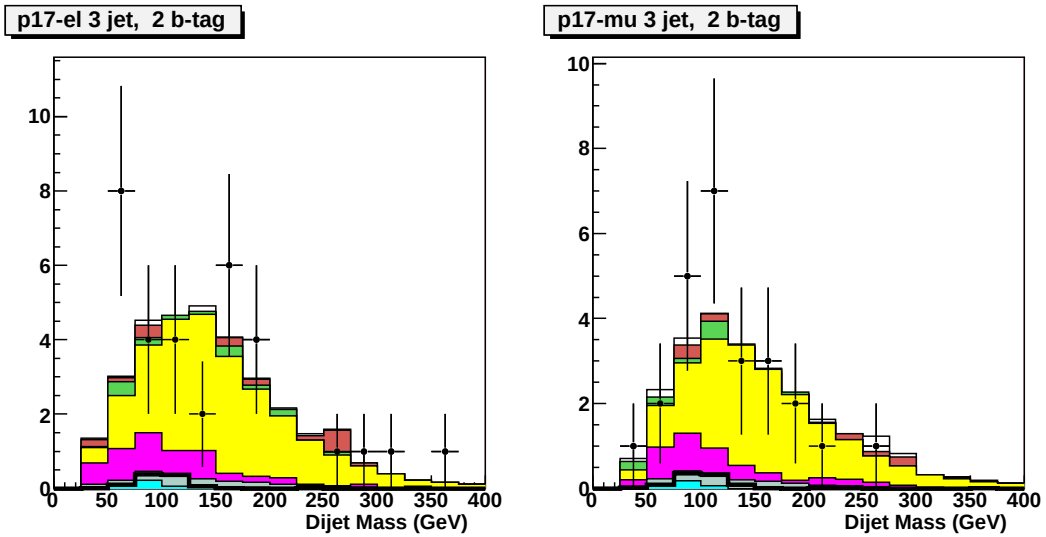

(a) Dijet mass distribution in the electron RunIIa channel.

(b) Dijet mass distribution in the muon RunIIa channel.

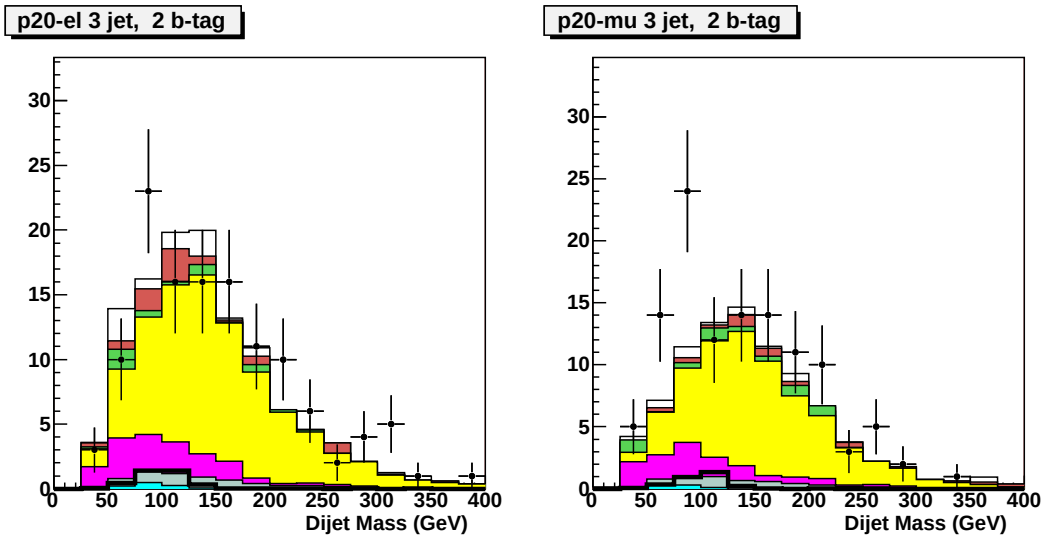

(c) Dijet mass distribution in the electron RunIIb channel.

(d) Dijet mass distribution in the muon RunIIb channel.

Figure 137: Distributions of the dijet mass in all analysis channels containig three jets in the final state of which exactly two are required to pass the loose b tagging criterion. Good agreement is achieved between data and simulation, including all MC backgrounds and the multijet background modeled from data.

A.5 COMBINED FIGURES FOR THREE JET EVENTS

Analogous to the figures of combinations of all events containing exactly two jets in the final state, already shown in Ch. 7, the following figures show the same combination of events for all events containing exactly three jets in the final state.

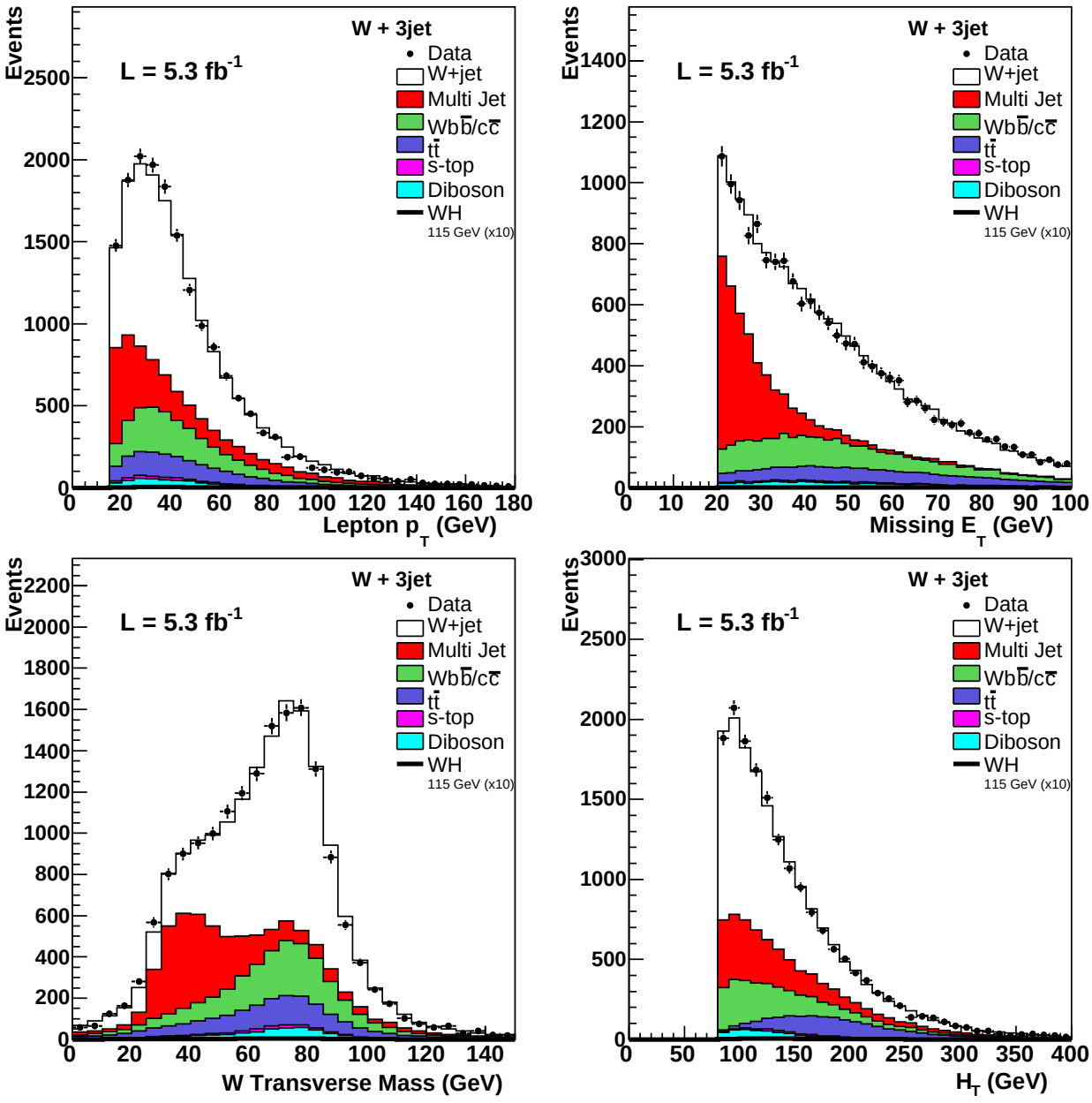

Figure 138: Kinematic distributions of the lepton p_T and $\not{E}_T$ (top row), W transverse mass and sum of the p_T of all jets (H_T) (bottom row) for the combination of all subsets with exactly three jets. No b tagging applied.

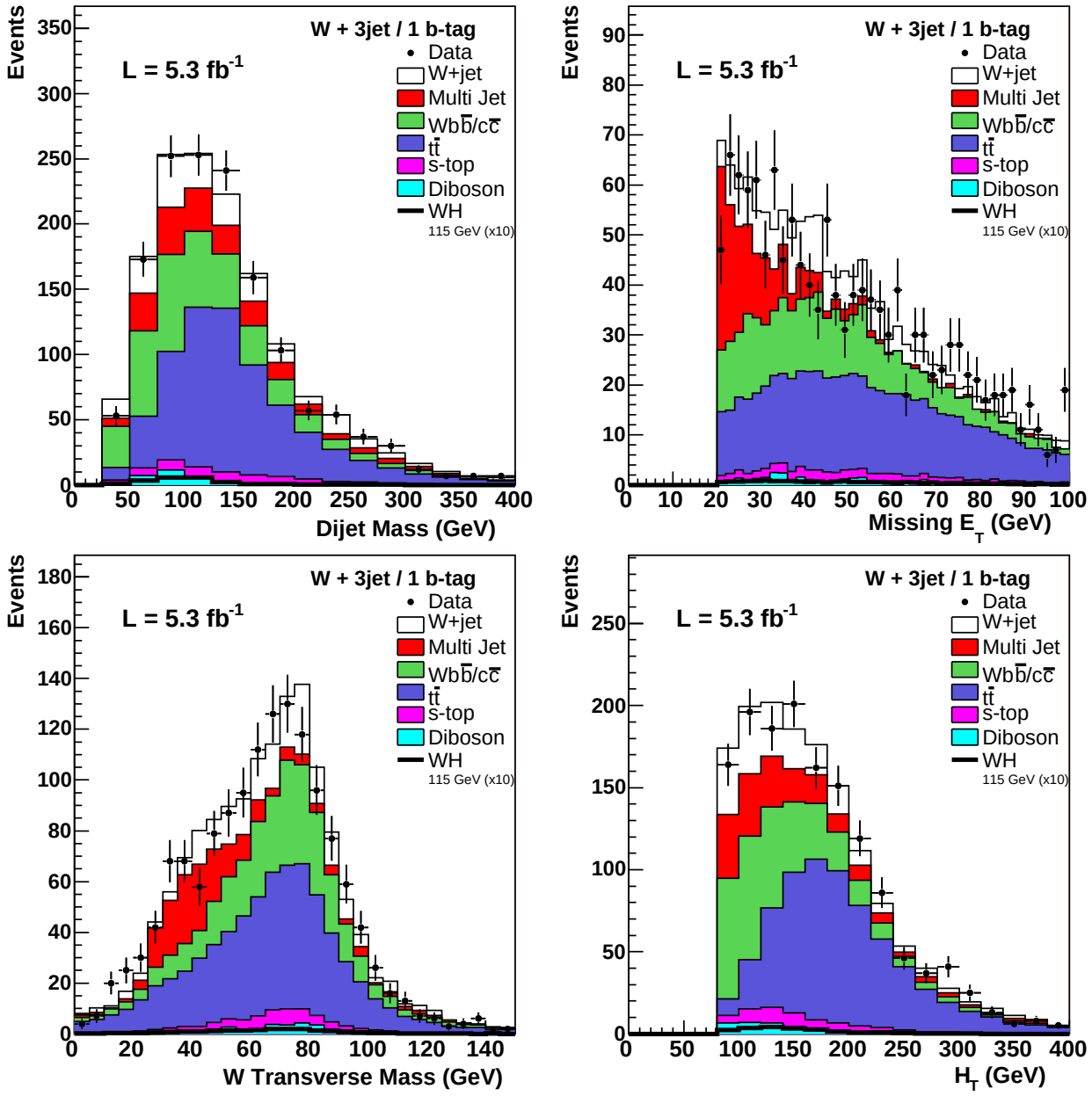

Figure 139: Kinematic distributions of the lepton p_T and $\not{E}_T$ (top row), W transverse mass and sum of the p_T of all jets (H_T) (bottom row) for the combination of all subsets with exactly three jets with exactly one tagged with the tight tagging criterion.

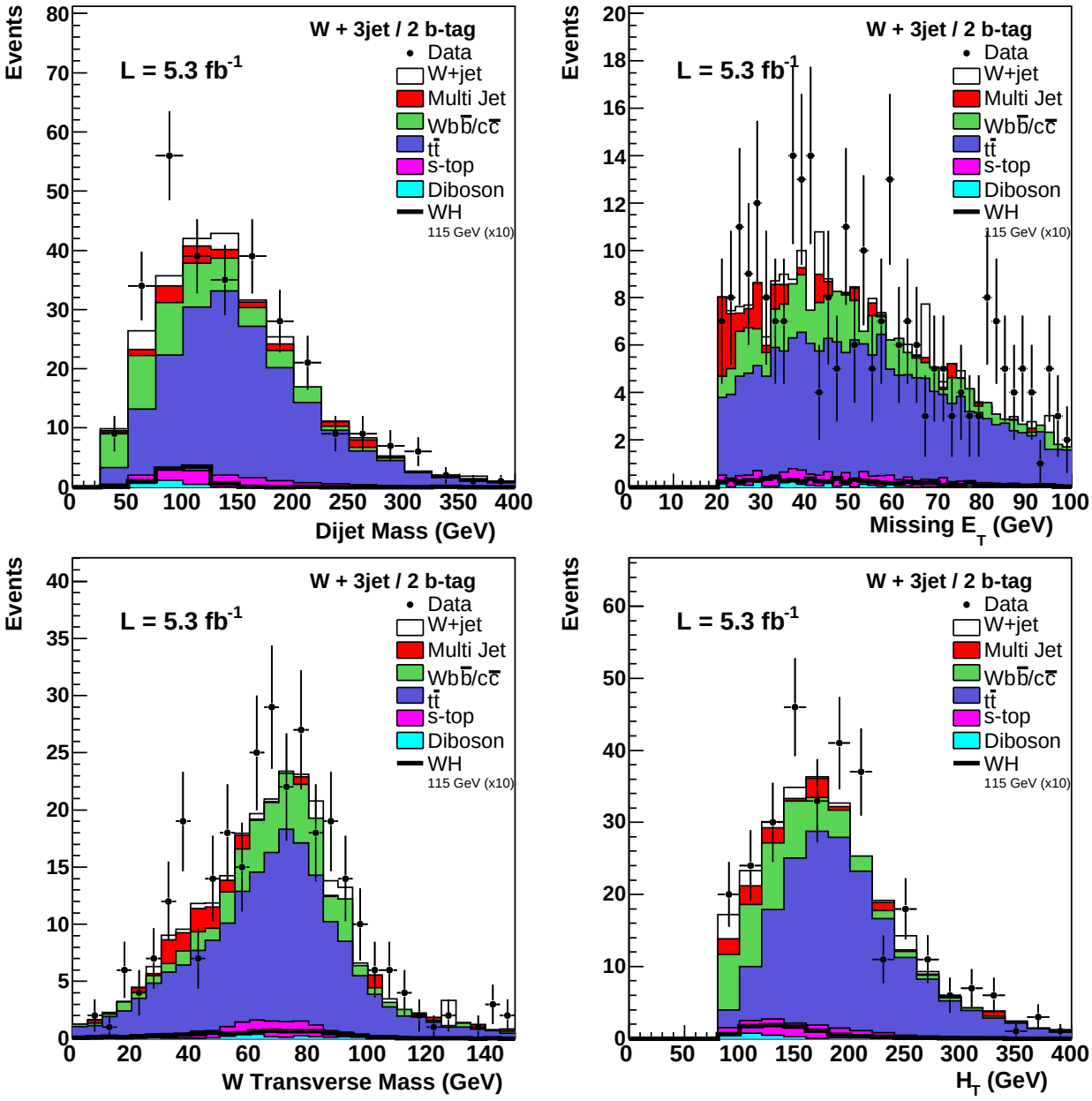

Figure 140: Kinematic distributions of the lepton p_T and $\not{E}_T$ (top row), W transverse mass and sum of the p_T of all jets (H_T) (bottom row) for the combination of all subsets with exactly three jets with exactly two tagged with the loose tagging criterion.

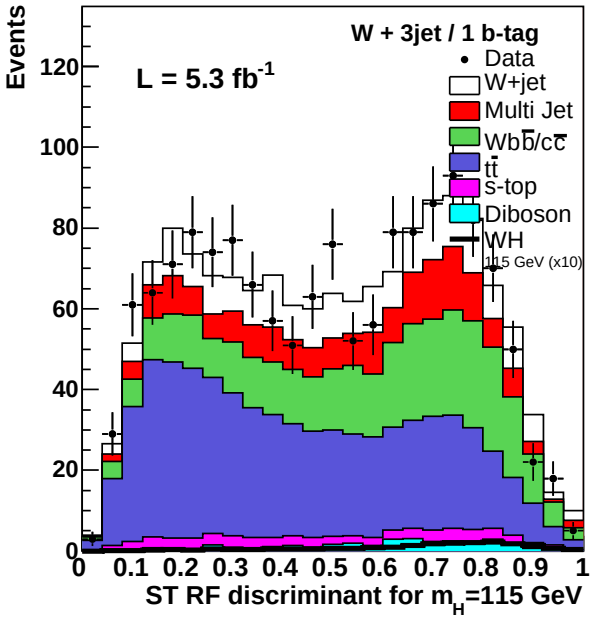

(a) Random Forest (single tag) trained and tested on the Single Tag

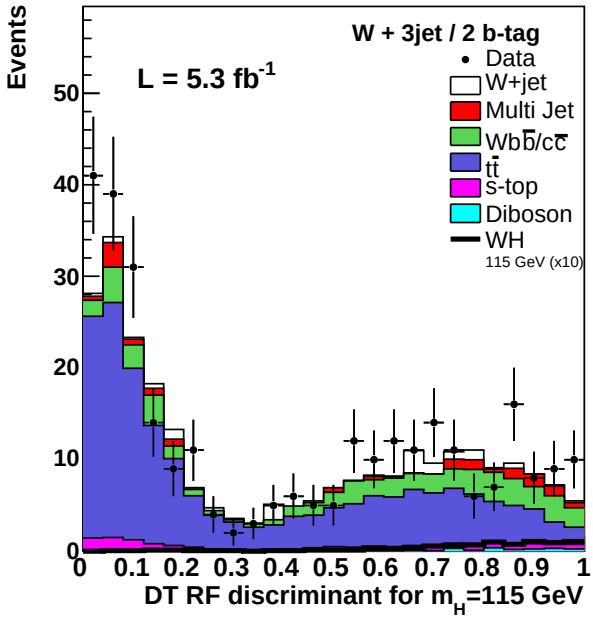

(b) Random Forest (double tag) trained and tested on the Double Tag

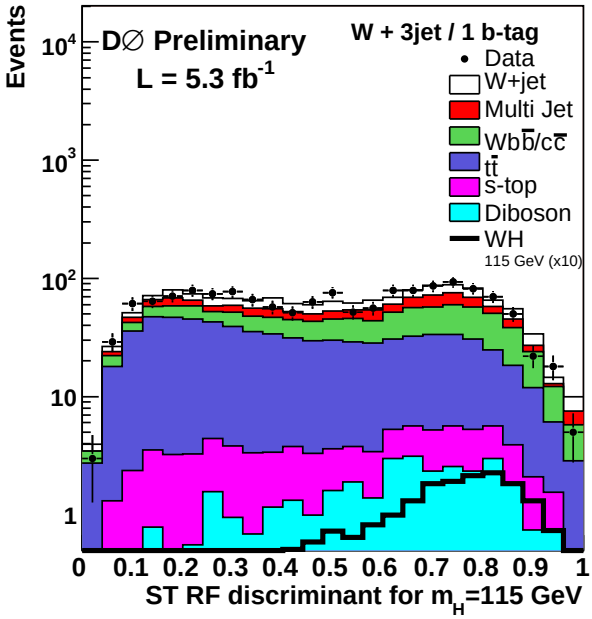

(c) Log Scale

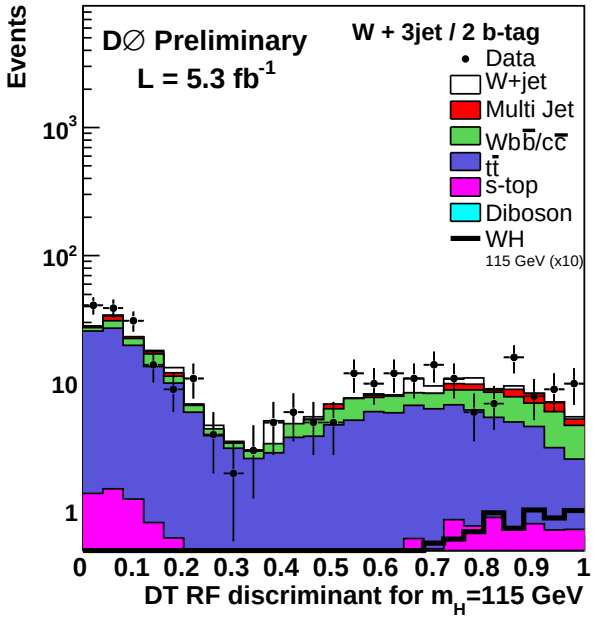

(d) Log Scale

Figure 141: Random forest output distributions for the combined three jet events (electron and muon, RunIIa and RunIIb). Left: RF trained and tested on the single tag sample. Right: RF tested and trained on the double tag sample. Top: Linear scale. Bottom: Log scale.

B

SYSTEMATIC UNCERTAINTY SIZE ESTIMATION

To estimate the size of each systematic uncertainty in the analysis, we vary each source of systematic uncertainty by $\pm 1\sigma$ (where σ is the size of the source of uncertainty, e.g. the jet energy scale correction). We re-perform a full analysis with the change in quantity of each source of uncertainty and then take the ratio of the obtained final distribution to our nominal distribution (this is done on the RF output distribution). This ratio is then a measure of the systematic uncertainty of the varied quantity. Exemplarily, the ratios are shown for all systematic uncertainties for events in the electron channel in the RunIIb sample with exactly two jets in the final state. See 7.4.2 for details on the systematic uncertainties.

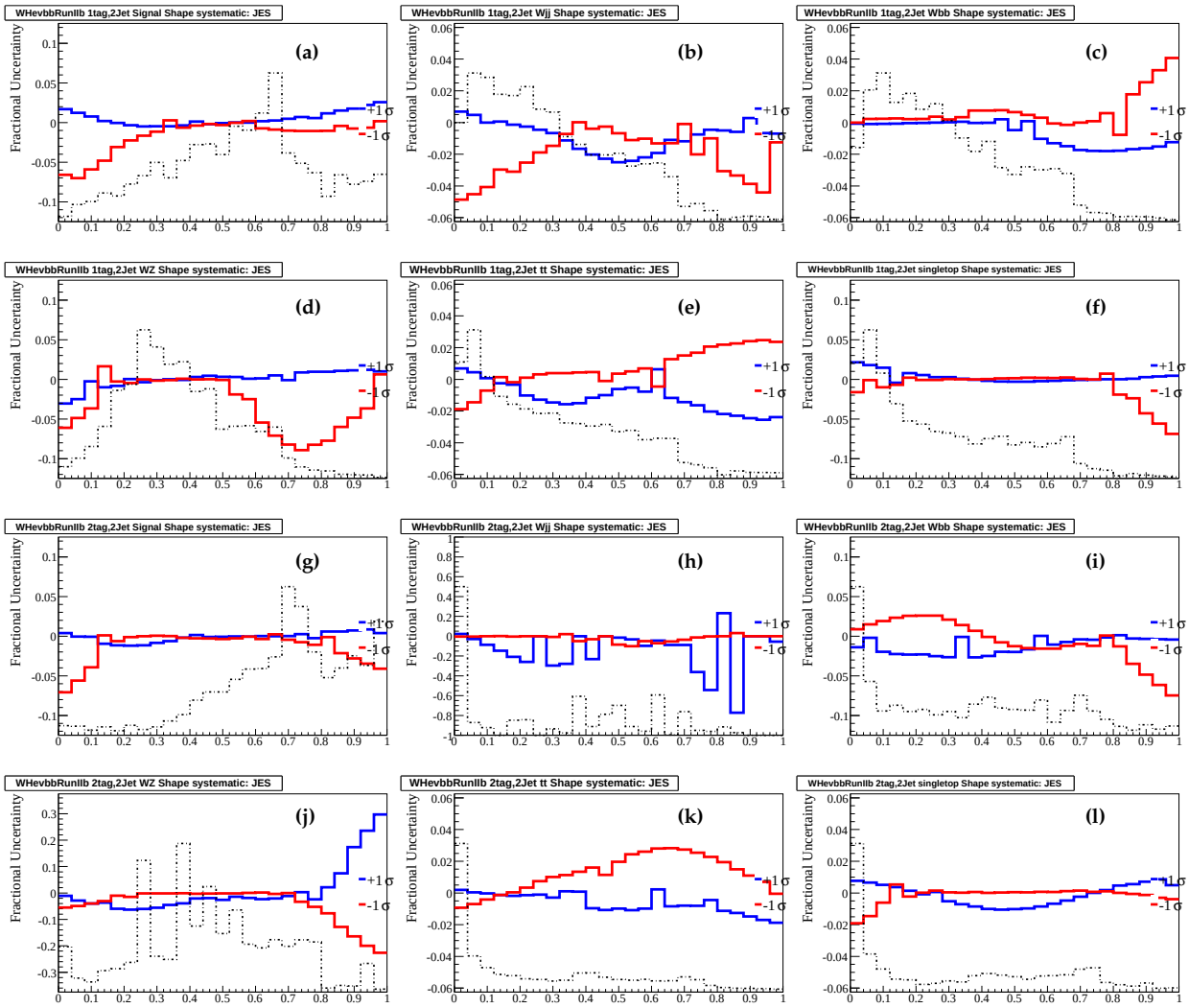

Figure 142: **Electron Systematics (2-jet)** Jet Energy Scale $\pm 1\sigma$ variation evaluated on the RF output. Fig. (a-f) are single tag samples, Fig. (g-l) are double tag samples. The dashed black line shows the distribution on which the systematic is evaluated. The blue (red) line represents the ratio to the $+1$ (-1) σ variation in each sample: Fig.(a,g) WH, (b,h) W+light jets, (c,i) W+heavy flavor jets, (d,j) Diboson, (e,k) $t\bar{t}$ and (f,l) single top.

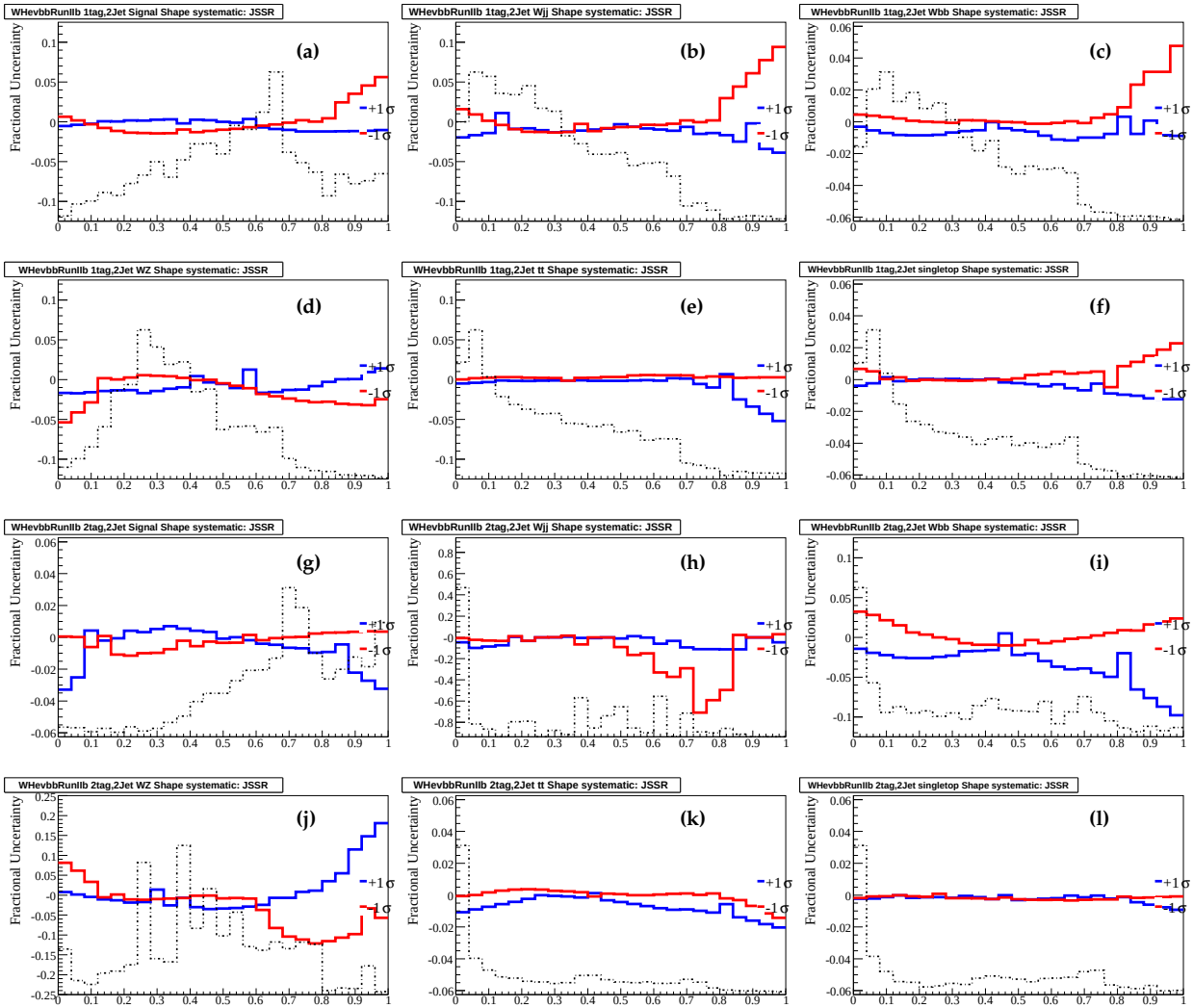

Figure 143: Electron Systematics (2-jet) **Jet Energy Resolution** $\pm 1\sigma$ variation evaluated on the RF output. Fig. (a-f) are single tag samples, Fig. (g-l) are double tag samples. The dashed black line shows the distribution on which the systematic is evaluated. The blue (red) line represents the ratio to the $+1$ (-1) σ variation in each sample: Fig.(a,g) WH, (b,h) W+light jets, (c,i) W+heavy flavor jets, (d,j) Diboson, (e,k) $t\bar{t}$ and (f,l) single top.

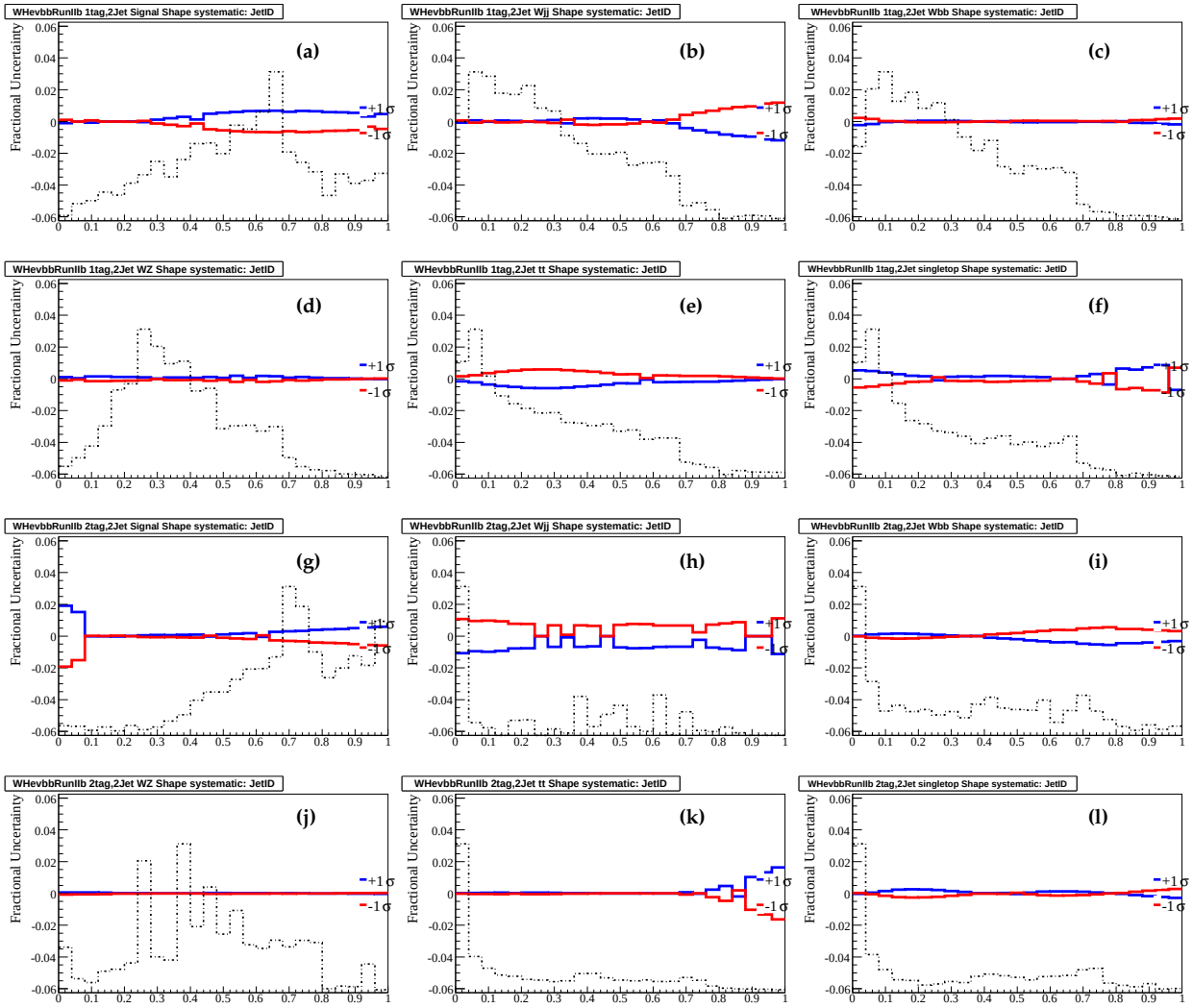

Figure 144: Electron Systematics (2-jet) **Jet identification efficiency** $\pm 1\sigma$ variation evaluated on the RF output. Fig. (a-f) are single tag samples, Fig. (g-l) are double tag samples. The dashed black line shows the distribution on which the systematic is evaluated. The blue (red) line represents the ratio to the $+1$ (-1) σ variation in each sample: Fig.(a,g) WH, (b,h) W+light jets, (c,i) W+heavy flavor jets, (d,j) Diboson, (e,k) $t\bar{t}$ and (f,l) single top.

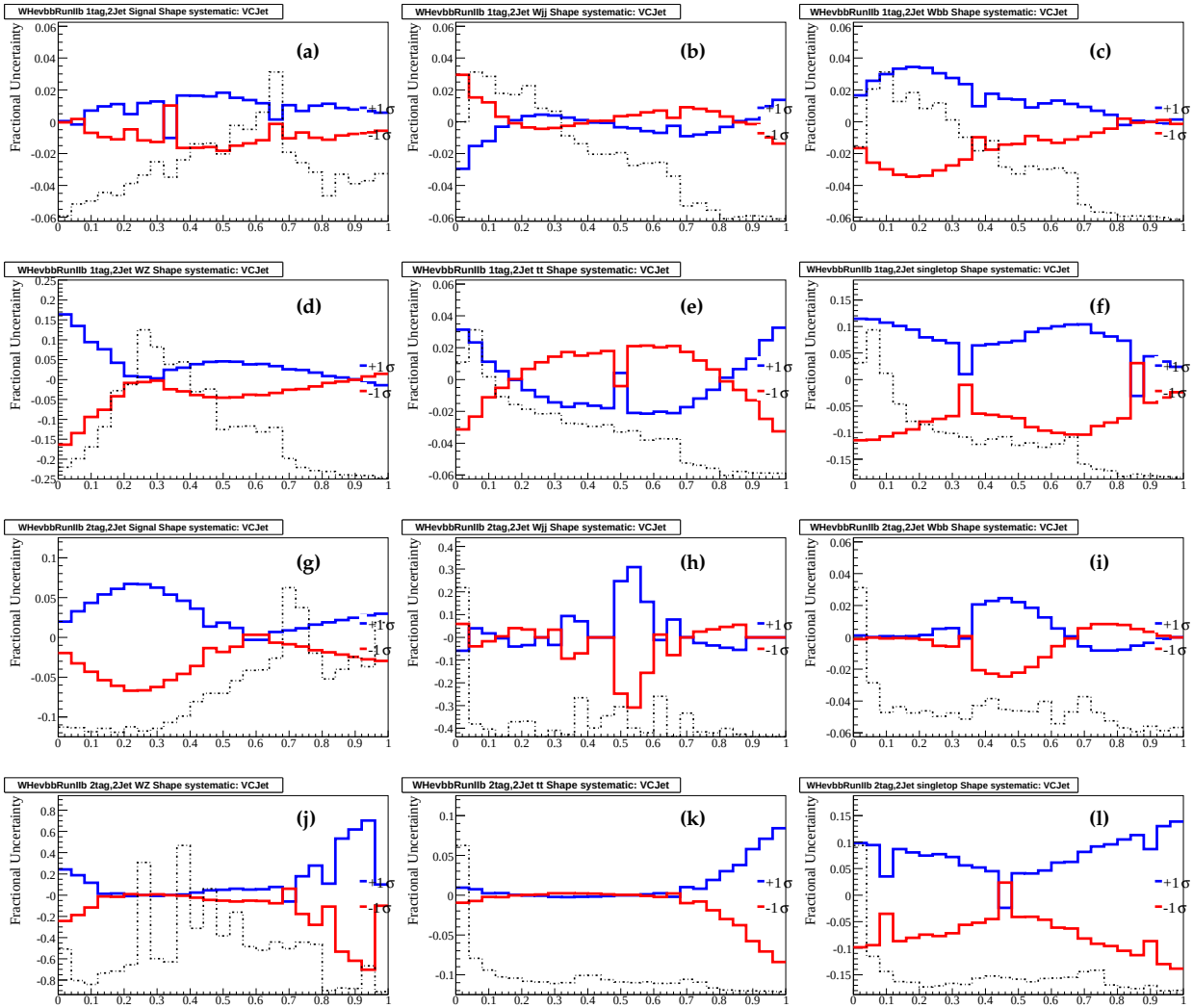

Figure 145: Electron Systematics (2-jet) **Vertex Confirmation** $\pm 1\sigma$ variation evaluated on the RF output. Fig. (a-f) are single tag samples, Fig. (g-l) are double tag samples. The dashed black line shows the distribution on which the systematic is evaluated. The blue (red) line represents the ratio to the $+1$ (-1) σ variation in each sample: Fig.(a,g) WH, (b,h) W+light jets, (c,i) W+heavy flavor jets, (d,j) Diboson, (e,k) $t\bar{t}$ and (f,l) single top.

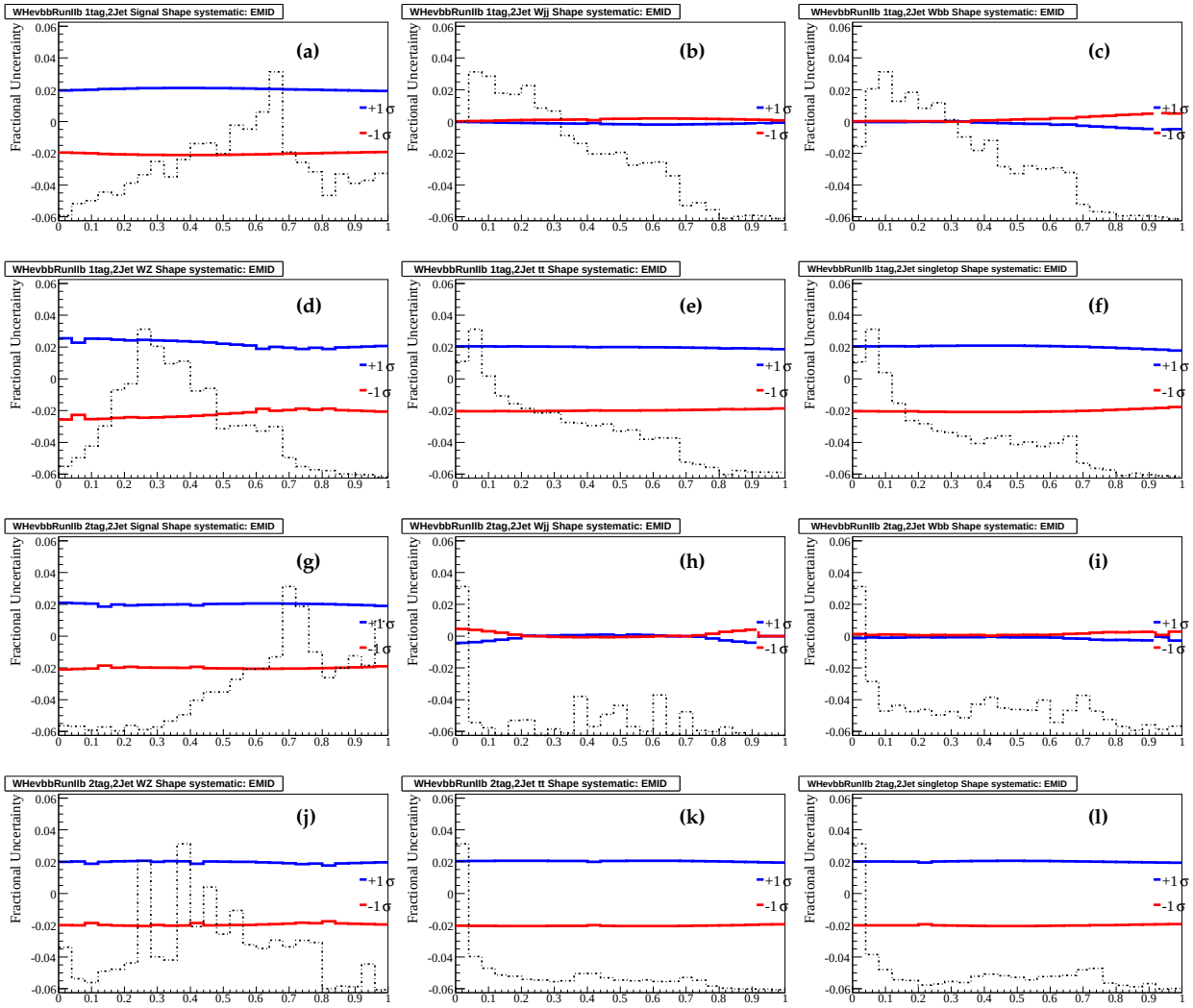

Figure 146: Electron Systematics (2-jet) **EM Identification** $\pm 1\sigma$ variation evaluated on the RF output. Fig. (a-f) are single tag samples, Fig. (g-l) are double tag samples. The dashed black line shows the distribution on which the systematic is evaluated. The blue (red) line represents the ratio to the $+1$ (-1) σ variation in each sample: Fig.(a,g) WH, (b,h) W+light jets, (c,i) W+heavy flavor jets, (d,j) Diboson, (e,k) $t\bar{t}$ and (f,l) single top.

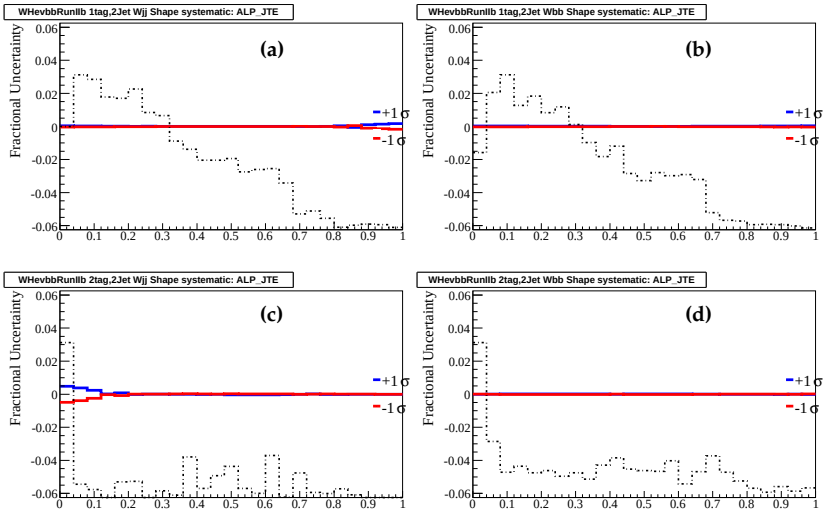

Figure 147: Electron Systematics (2-jet) **ALPGEN Jet η reweighting** $\pm 1\sigma$ variation for the RF output. Fig. a-b are for the single tag and c-d for the double tag sample. The dashed black line shows the distribution on which the systematic is evaluated. The blue line shows the $+1\sigma$, the red line shows the -1σ in each sample: Fig.(a,c) W+light jets, (b,d) W+heavy flavor jets.

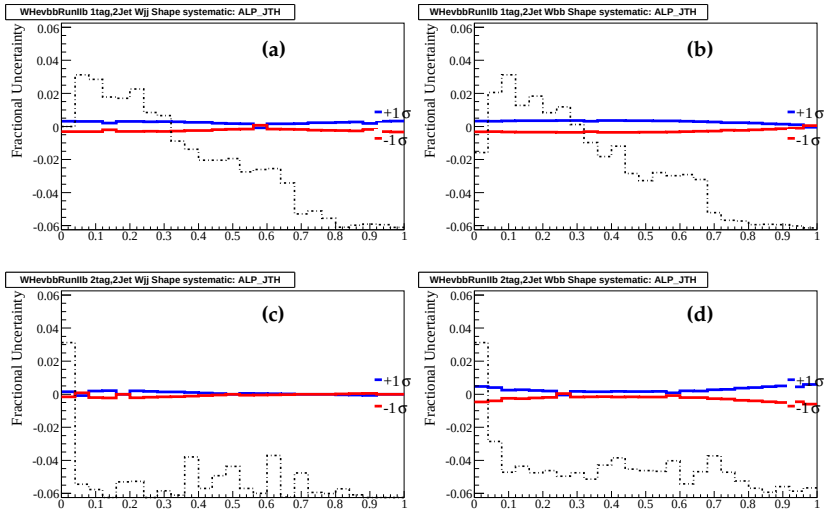

Figure 148: Electron Systematics (2-jet) **ALPGEN jet ICD reweighting** $\pm 1\sigma$ variation for the RF output. Fig. a-b are for the single tag and c-d for the double tag sample. The dashed black line shows the distribution on which the systematic is evaluated. The blue line shows the $+1\sigma$, the red line shows the -1σ in each sample: Fig.(a,c) W+light jets, (b,d) W+heavy flavor jets.

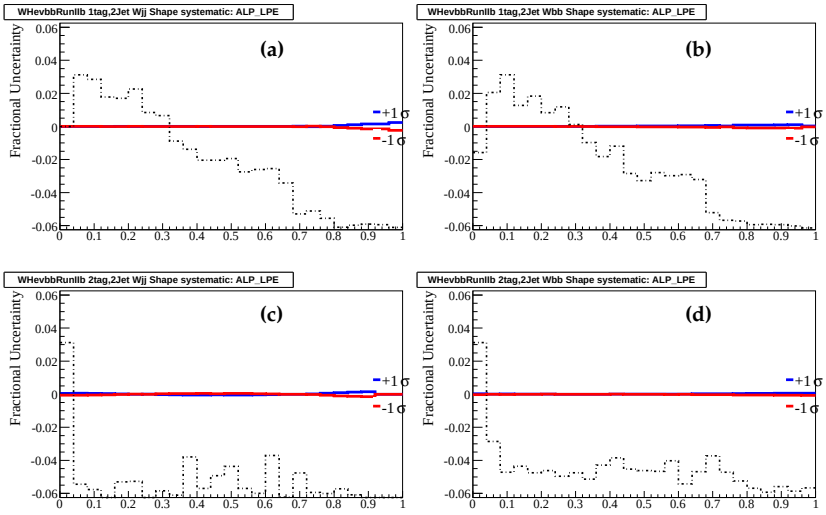

Figure 149: Electron Systematics (2-jet) **ALPGEN lepton η reweighting** $\pm 1\sigma$ variation for the RF output. Fig. a-b are for the single tag and c-d for the double tag sample. The dashed black line shows the distribution on which the systematic is evaluated. The blue line shows the $+1\sigma$, the red line shows the -1σ in each sample: Fig.(a,c) W+light jets, (b,d) W+heavy flavor jets.

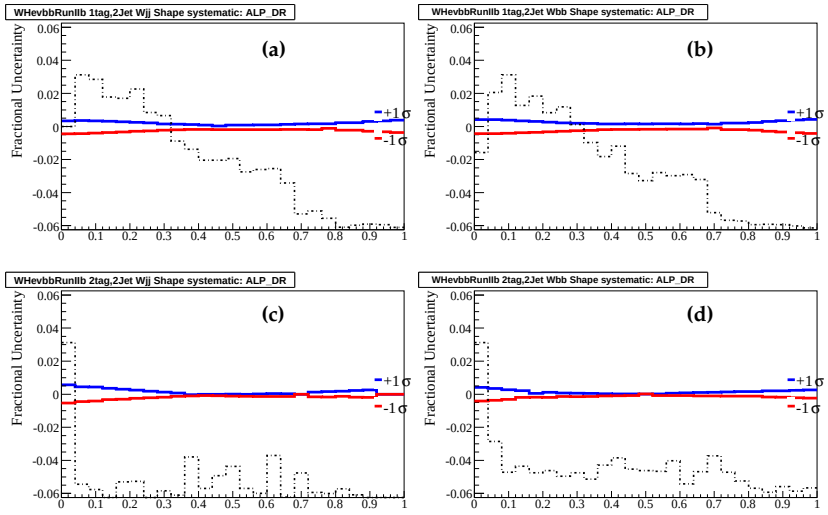

Figure 150: Electron Systematics (2-jet) **ALPGEN** ΔR **reweighting** $\pm 1\sigma$ variation for the RF output. Fig. a-b are for the single tag and c-d for the double tag sample. The dashed black line shows the distribution on which the systematic is evaluated. The blue line shows the $+1\sigma$, the red line shows the -1σ in each sample: Fig.(a,c) W+light jets, (b,d) W+heavy flavor jets.

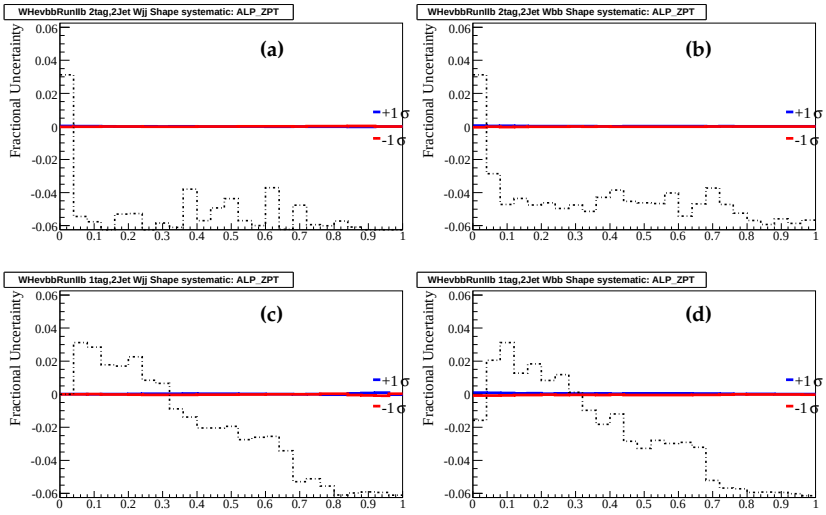

Figure 151: Electron Systematics (2-jet) **ALPGEN** Z p_T **reweighting** $\pm 1\sigma$ variation for the RF output. Fig. a-b are for the single tag and c-d for the double tag sample. The dashed black line shows the distribution on which the systematic is evaluated. The blue line shows the $+1\sigma$, the red line shows the -1σ in each sample: Fig.(a,c) W+light jets, (b,d) W+heavy flavor jets.

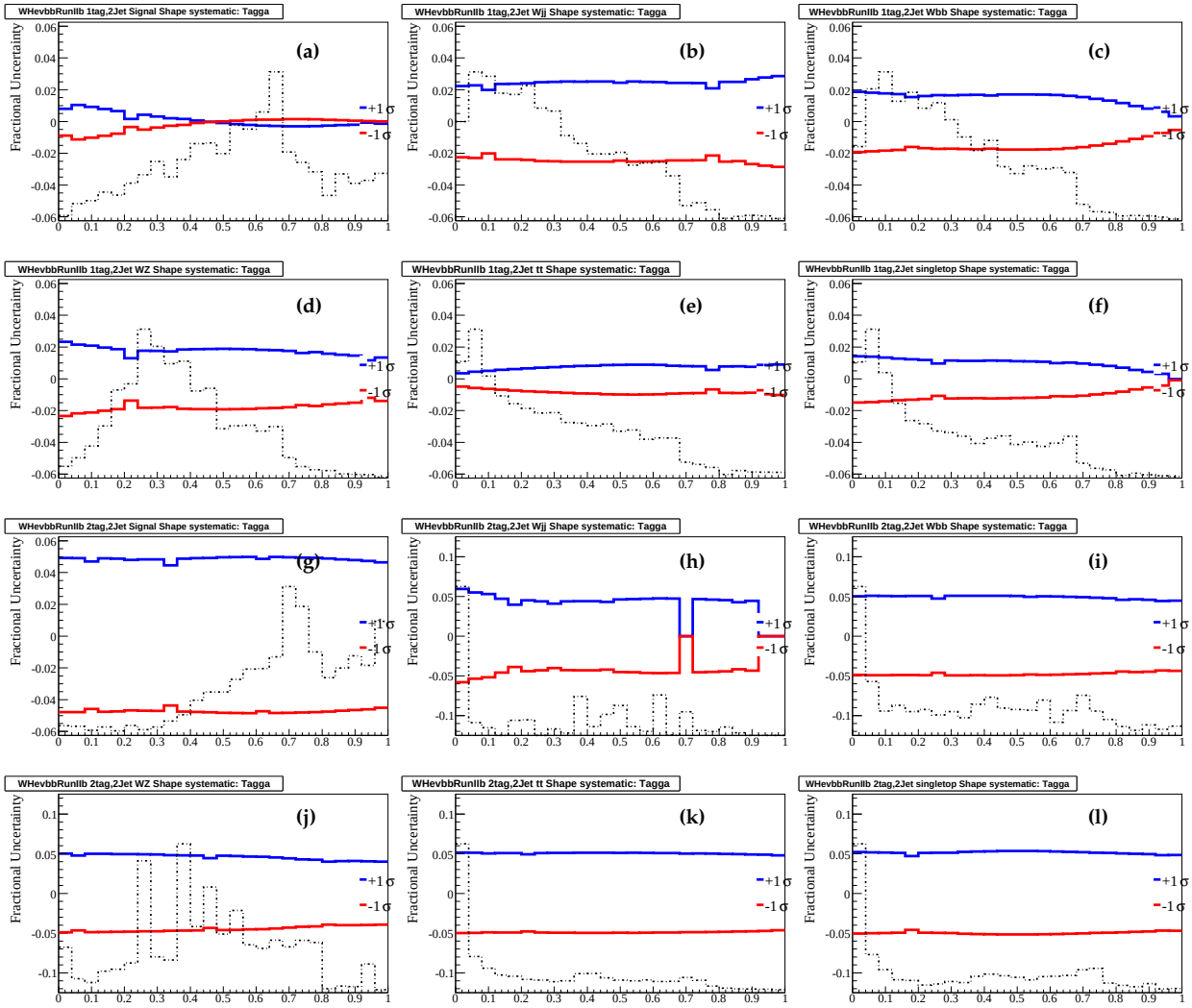

Figure 152: Electron Systematics (2-jet) **Taggability** $\pm 1\sigma$ variation evaluated on the RF output. Fig. (a-f) are single tag samples, Fig. (g-l) are double tag samples. The dashed black line shows the distribution on which the systematic is evaluated. The blue line shows the $+1\sigma$ variation, the red line shows -1σ variation in each sample: Fig.(a,g) WH, (b,h) W+light jets, (c,i) W+heavy flavor jets, (d,j) Diboson, (e,k) $t\bar{t}$ and (f,l) single top.

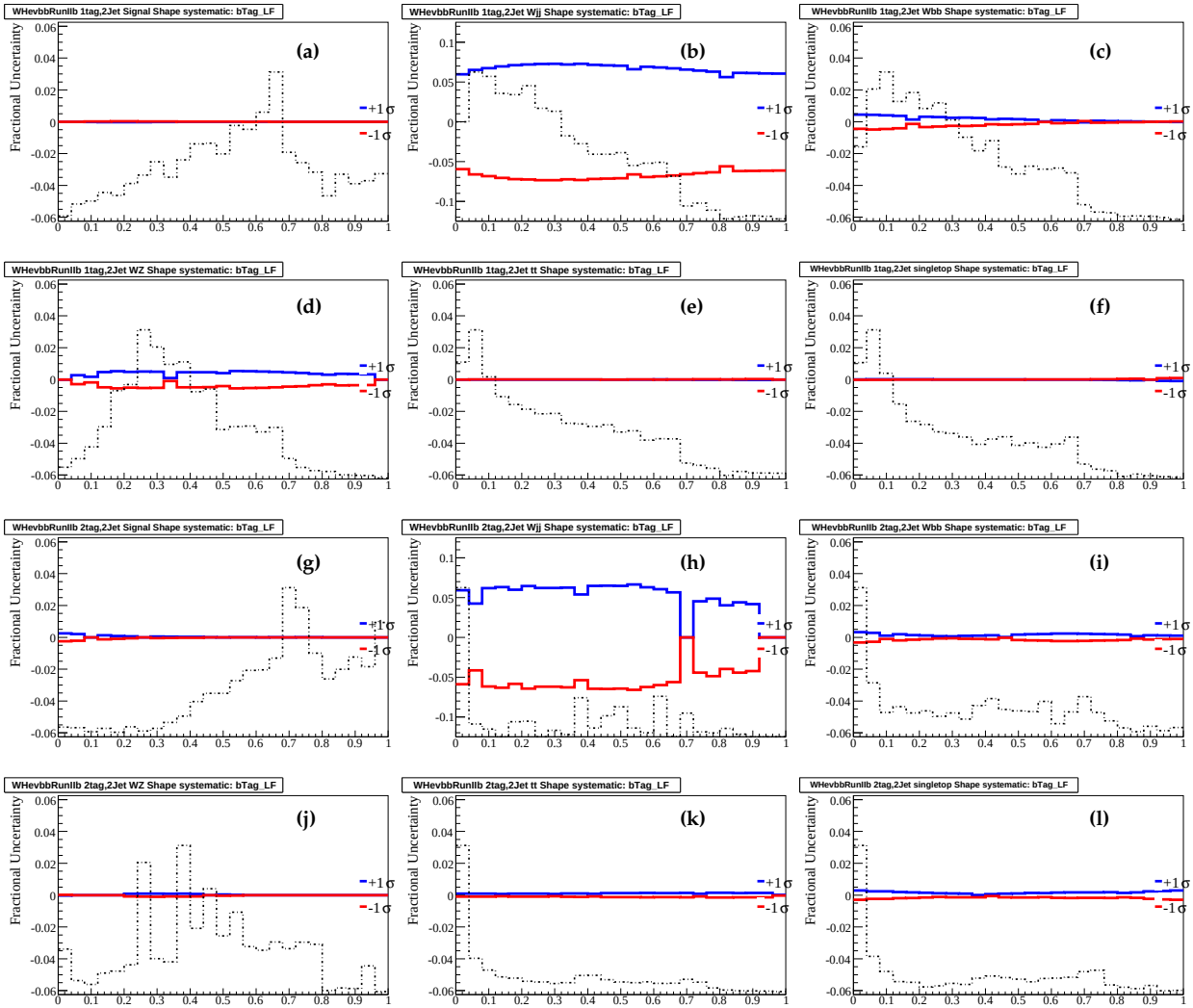

Figure 153: Electron Systematics (2-jet) **b jet identification** $\pm 1\sigma$ variation evaluated on the RF output. Fig. (a-f) are single tag samples, Fig. (g-l) are double tag samples. The dashed black line shows the distribution on which the systematic is evaluated. The blue line shows the $+1\sigma$ variation, the red line shows -1σ variation in each sample: Fig.(a,g) WH, (b,h) W+light jets, (c,i) W+heavy flavor jets, (d,j) Diboson, (e,k) $t\bar{t}$ and (f,l) single top.

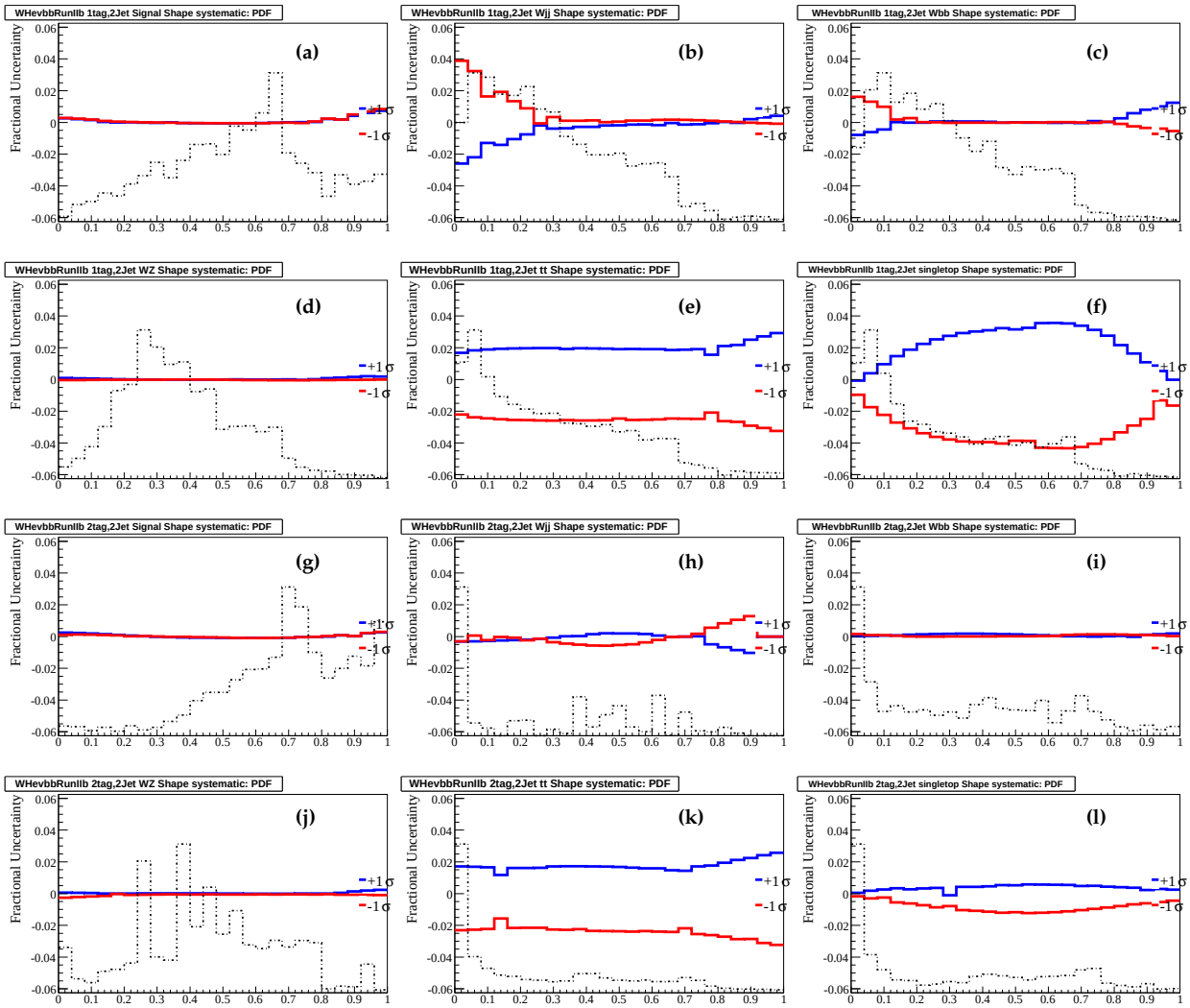

Figure 154: Electron Systematics (2-jet) **Variations of selected PDF uncerainties**. A total of 40 PDF variations are made, each contributing to the final set of systematics. The 18th PDF variation for signal, the 15th PDF variation for BG (one of largest shape changes) are shown: Fig. (a-f) are single tag samples, Fig. (g-l) are double tag samples. The dashed black line shows the distribution on which the systematic is evaluated. The blue line shows the $+1\sigma$ variation, the red line shows -1σ variation in each sample: Fig.(a,g) WH, (b,h) W+light jets, (c,i) W+heavy flavor jets, (d,j) Diboson, (e,k) $t\bar{t}$ and (f,l) single top.

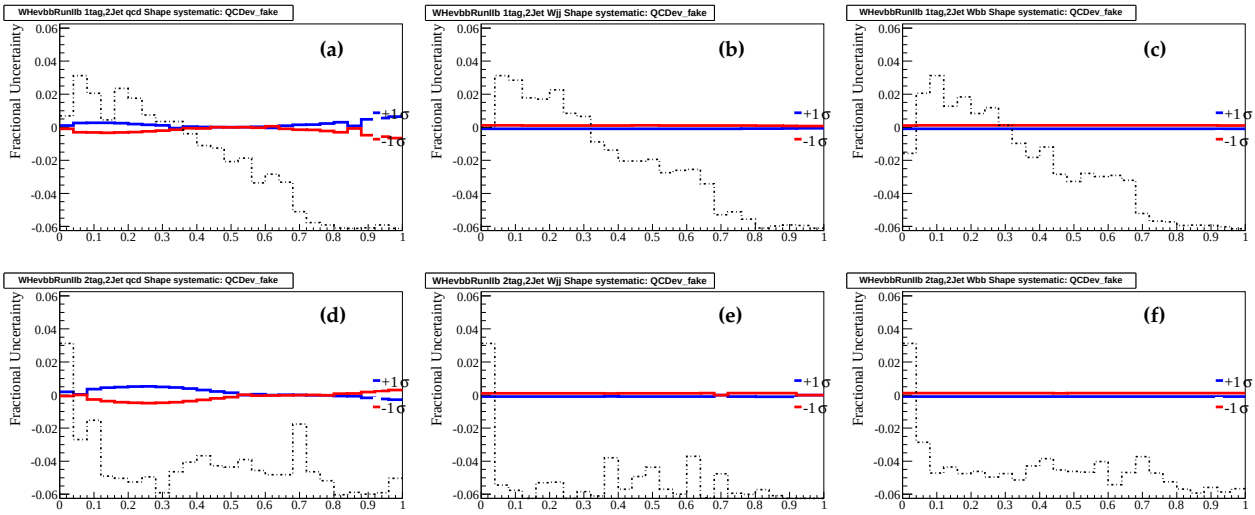

Figure 155: Electron Systematics (2-jet) **Multijet Misidentification Rate** $\pm 1\sigma$ variation for the RF output. Fig.a-c are for the single tag and d-f for the double tag sample. The dashed black line shows the distribution on which the systematic is evaluated. The red line shows $+1\sigma$, the blue line shows -1σ in each sample: Fig.(a,d) Multijet, (b,e) W+light jets, (c,f) W+$b\bar{b}$.

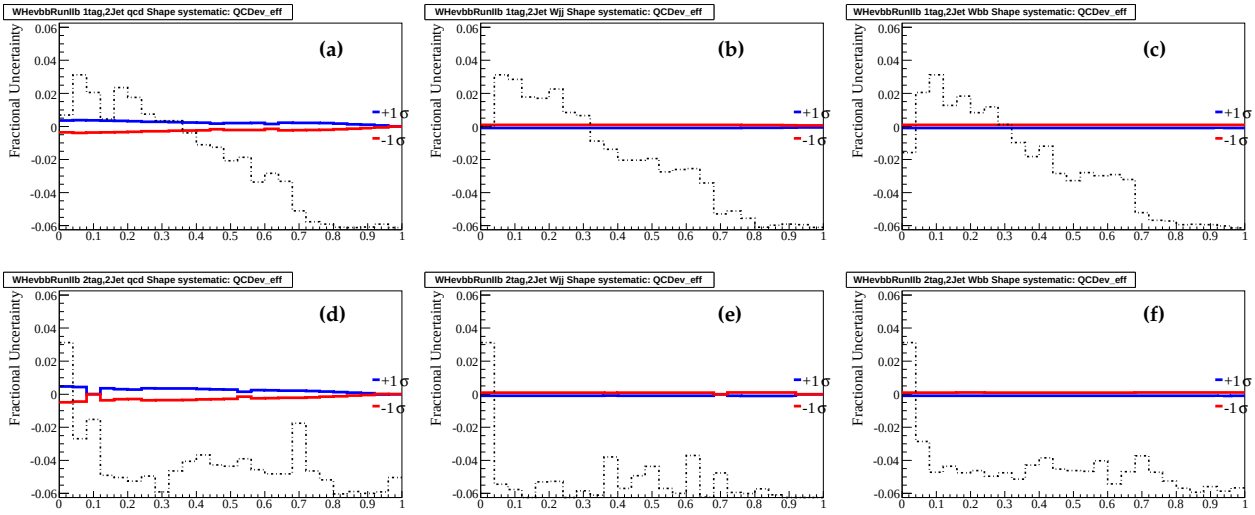

Figure 156: Electron Systematics (2-jet) **Multijet electron efficiency** $\pm 1\sigma$ variation for the RF output. Fig.a-c are for the single tag and d-f for the double tag sample. The dashed black line shows the distribution on which the systematic is evaluated. The red line shows $+1\sigma$, the blue line shows -1σ in each sample: Fig.(a,d) Multijet, (b,e) W+light jets, (c,f) W+$b\bar{b}$.

ABSTRACT

The Higgs mechanism of the Standard Model of particle physics provides a plausible and theoretically solid explanation for the origin of mass. It predicts at the same time the existence of a yet unobserved particle, the Higgs boson, with unknown mass from theory. The Higgs boson is strongly linked to the validity of the Standard Model at highest energies. This work outlines the three possible scenarios for the fate of the Standard Model at highest energies and their implications for theories of cosmological inflation. If the Higgs boson mass lies within a certain range the Standard Model could remain a valid theory up to the Planck scale. If in this case, the Higgs boson couples non-minimally to gravity, it could function as the particle responsible for cosmological inflation in the very early Universe.

A direct search for the Higgs boson could unveil its mass. The associated production of a Higgs boson with a W boson has the highest yields of production cross section times branching ratio in the region below 130 GeV at the Tevatron accelerator. We analyze a dataset of 5.3 fb^{-1} of Tevatron data accumulated by the DØ experiment, searching for a W boson that decays into a lepton and a neutrino, of which the latter is accounted for by missing energy in the detector. The Higgs boson decays into two b quarks which then hadronize and form jets. These jets can be identified by a neural network b tagging method. A Random Forest multivariate technique is then used to improve signal sensitivity. In the absence of a signal excess in our final data to simulation comparison, we set a limit on the production cross section times branching ratio of the Higgs boson in the WH channel of 0.533 pb at a mass of 115 GeV. This limit corresponds to a factor of 4.1 of the Standard Model prediction. Further limits are set for Higgs masses in a range of 100 - 150 GeV in steps of 5 GeV, the region where the WH channel is most sensitive. These results will be submitted for publication and contribute to the Tevatron combination of Higgs analyses.

RÉSUMÉ

Le mécanisme de Higgs du Modèle Standard (SM) peut expliquer l'origine de la masse. Il prédit également l'existence d'une particule non encore observée, le boson de Higgs, dont la masse n'est pas prédite par la théorie. Le boson de Higgs est fortement lié à la validité du SM à hautes énergies. On explique les trois scénarios pour l'évolution du SM et leurs implications pour les théories de l'inflation cosmologique. Si la masse du boson de Higgs se situe dans une certaine gamme, le SM pourrait rester une théorie valide jusqu'à l'échelle de Planck. Si le couplage du boson de Higgs à la gravité n'est pas minimal, il peut également être la particule responsable de l'inflation cosmologique. Pour rechercher le boson de Higgs au Tevatron, la production associée avec un boson W est l'un des canaux les plus sensibles pour une masse inférieure à 130 GeV. On analyse 5,3 fb-1 de données Do-Tevatron, en recherchant un boson W qui se désintègre en un lepton et un neutrino. Le boson de Higgs se désintègre en deux quarks b qui forment des jets qui peuvent être identifiés par un b tagger de réseau de neurones. Une analyse multivariée est utilisée pour améliorer la sensibilité au signal. En l'absence d'un excès de signal dans la comparaison données et simulation, on calcule une limite sur le produit (section efficace) x (rapport d'embranchement) dans le canal WH de 0,533 pb à une masse de 115 GeV à 95% niveau de confiance. Cette limite correspond à un facteur de 4,1 de la prédiction SM. D'autres limites sont calculées pour les masses dans une gamme de 100 à 150 GeV par pas de 5 GeV. Ces résultats seront soumis pour publication et contribuent à la combinaison d'analyses Higgs au Tevatron.